Nature 459, 683-685 (4 June 2009)

Entangled Mechanical Oscillators

by

John D. Jost

B.S., University of Colorado, 2001

A thesis submitted to the

Faculty of the Graduate School of the

University of Colorado in partial fulfillment

of the requirements for the degree of

Doctor of Philosophy

College of Arts and Sciences Department of Physics

2010

This thesis entitled:
Entangled Mechanical Oscillators
written by John D. Jost
has been approved for the College of Arts and Sciences Department of Physics

_____

Dave Wineland

_____

Jun Ye

Date _____

The final copy of this thesis has been examined by the signatories, and we find that both the content and the form meet acceptable presentation standards of scholarly work in the above mentioned discipline.

Jost, John D. (Ph.D., Physics)

Entangled Mechanical Oscillators

Thesis directed by Dr. Dave Wineland

Quantum entanglement has been the subject of considerable research, in part due to its non-intuitive nature and ubiquitous presence in quantum information processing. For this reason, it is of interest to study entanglement in a variety of systems. The work discussed in this thesis focuses on the demonstration of deterministic entanglement in a system pervasive in nature: mechanical oscillators. Here, the mechanical oscillators are composed of the vibrations of two ion pairs in spatially separated locations. The techniques demonstrated in this experiment are likely to form core components of large-scale trapped-ion quantum information processing.

Dedication

To my parents, for always encouraging me no matter what path I chose

and

To my sister, for always putting up with me

Acknowledgements

Many people deserve thanks and credit for the work discussed here and I apologize in advance for leaving anyone out.

Looking back now it is interesting to see the path that has led me to this point, and I feel very lucky in the opportunities I have been given. About the time I was finishing high school, I decided I was interested in physics. It seemed so precise (It took me awhile to get used the fact that is not always the case, but now I like that) and explained the world around me. I showed up for orientation at the University of Colorado at Boulder as an engineering physics major. Fortunately for me, my major was not very popular and I was the only one there that day with my major. Dana Anderson was the head of the engineering physics program at the time and gave me a nice personal laser demonstration (I have always been fascinated by light). I expressed some interest in this area, and he offered to have one of this grad students (Pete Tucker) show me around his optics lab. I had never been near a real lab before and was quite impressed. I started college taking the introductory physics courses. One of the classes required was an experimental physics class, which I did not like. After a couple of weeks I was wondering if I should switch majors. One day I was in the gym an ran into Pete again. He mentioned that Dana was looking for someone to work in his optics lab. I went to Dana's office and told him of my interest. He asked me if I had any lab experience. All I could saw was that I had taken chemistry and physics in high school. Despite this Dana hired me to work in his lab. This was a turning point for me, and I owe Dana a lot

gratitude for giving me that opportunity. I quickly realized that experimental physics was not as dull as the entry level physics labs. I really enjoyed that everyday there were new problems to solve. During the years I worked in Dana's group, I was supervised by Leslie Czia who was always patient and helpful with all my questions. Also while there I was able to get help from several kind grad students at the time Edeline Fotheringham, Dirk Muller,and Peter Schwindt. During this time I also spent many long hours in the machine shop. I should thank all of the JILA machinists for taking the time to teach me many things that have proven very valuable. It is a nice feeling to know that you can take a chunk of metal and make it into almost anything

After several years working for Dana Anderson, I decided I wanted to try something different for my undergraduate senior thesis research. I came across Jun Ye's research with ultra-fast lasers and thought that sounded really cool. He offered to let me work in his lab. I had no idea how great of an opportunity this would be. Jun's excitement about my experiment was infectious and motivating. I remember nights where Jun would be sitting on the floor with me at 3 am turning knobs trying to get the experiment to work. While working in Jun's Lab I was able to work with many great people. The guys in the JILA electronics shop taught me a lot about circuits and Mark Notcutt was always willing to help me with my experiment. I also feel fortunate that I was able to work with John Hall and was always impressed by the unending flow of ideas he had.

I stayed on working with Jun after graduating from college to finish the experiment I had started. It was during this time when I was deciding where to go to grad school that Jun recommended Dave Wineland's group at NIST. I did not really know anything about trapping ions or quantum information, but it sounded interesting. Eventually I settled on staying in Boulder for graduate and joined Dave Wineland's group. I had no idea at the time what a great research group Dave had. Dave has been a great advisor. Not only in the physics he knows but in how one goes about doing science. He was

patient enough to let us try and figure things out in the lab on our own, but always had the answer when we got stuck. I will always look back having enjoyed my time with Dave and his group.

Another great part of Dave's group is all the intelligent people I have been able to work with over the years. There are a few people that I own special thanks to. Jonathan Home joined the group shortly after we started on the work discussed here. Without his knowledge, drive, and excitement I would still be in the lab trying to get the experiment to work. I also need to thank Jonathan for his friendship without which I do not think all the hours we spent side by side in the lab would have gone so well. I need to thank Chris Langer and Roee Ozeri for taking the time to teach me almost everything about the experimental apparatusa and for their great contributions to the experiment. In addition, in another one of those twists of fate, for convincing me to use the ion trap I built in their experiments. This lead me to be being able to do or some really interesting physics. Experimental physics has a way of keeping you humble. I will never forget the five months Roee and I spent tracking down a problem that turned out to be a broken piece of equipment. However we learned a lot in the process. David Hanneke joined our experiment. In a very short amount of time, he was up to speed and was a great help getting everything accomplished. Also Jason Amini was an invaluable resource and solved every computer control problem we had with amazing speed. These are by no means the only people who came through Dave's group in my time there that contributed in some way or spent time answering my dumb questions. I have been very fortunate to learn from all these people: Murray Barrett, Jim Bergquist, Sarah Bickman, Mike Biercuk, Brad Blakestad, John Bollinger, Brana Jelenkovic, Joe Britton, Kenton Brown, Anders Brusch, John Chiaverini, James Chou, Yves Colombe, Brian DeMarco, Bob Drullinger, Ryan Epstein, David Hume, Wayne Itano, Marie Jensen, Manny Knill, Jeroen Koelemeij, Dietrich Leibfried, Rober Maiwald, Wendell Oskay, Christian Ospelkaus, Rainer Reichle, Till Rosenband, Signe Seidelin,

Tobias Schaetz, Pete Schmidt, Nobuyasu Shiga, Hermann Uys, Aaron VanDevender, and Janus Wesenberg

Finishing a Ph.D. requires much more than just having great colleagues to work with. It also requires having people outside of the lab who are willing to be there for you. Without such a support network, my life would have been a lot less full and I would not have been able to accomplish this task. I have been very fortunate to have so many friends over the years not all of which I can mentioned here, but I want thank a few for tolerating me: Jake Dillow, Elizabeth Chick, Natalie Colatosti, Brian Fetters, Seth Fletcher, Chris Keller, Quinn Killin, Brian Landon, Michael Pickering, and Juan Pino

This has been a great experience I owe a lot of thanks to everyone who helped me get here.

Contents

Tables

Figures

Chapter 1

Introduction

1.1 Motivations

This dissertation presents two experiments involving entangled mechanical oscillators [Jost 09]. The first experiment entangles the internal spin of a trapped ion with a spatially separated mechanical oscillator. The second experiment entangles the motion of two spatially separated mechanical oscillators. In these experiments, the mechanical oscillators consist of pairs of trapped ions held in different locations. A pair of trapped ions behaves like a system of masses connected by springs, a canonical example of a mechanical oscillator.

Creating novel entangled states of mechanical oscillators serves as a test of quantum mechanics in a new regime. The techniques developed to reach this end formed key components in demonstrating a complete methods set for scalable ion trap quantum information processing (QIP) [Home 09] and realizing the first multi-qubit quantum processor [Hanneke 10].

Quantum mechanics is a very successful theory for explaining many aspects of nature. However, it is perhaps better known for some of the counter intuitive predictions it makes about the world, such as quantum mechanical superpositions [Schrödinger 35] and entanglement [Einstein 35, Bell 64]. A superposition state is one where a system is in two or more possible states at the same time. Entanglement manifests itself as a correlation between two systems that is stronger than anything described by classical

physics. These effects have been observed in many systems, but at size scales or in systems not commonplace outside of a lab. One of the unresolved questions in physics is why do we not experience these effects in everyday life, such as cats in a superposition of being both dead and alive [Schrödinger 35]. Perhaps it might depend on the number particles that can be put in a superposition state or entangled [Bassi 03, Leggett 02a] or maybe only certain degrees of freedom can experience these effects.

Many experiments have probed superpositions and entanglement in atomic, photonic, condensed matter systems [Aspelmeyer 08a, Southwell 08]. For the case of ions a "Schrödinger Cat " superposition state [Schrödinger 35] has been created using the internal spin state of a $^{9}Be^{+}$ ion and a coherent state of its motion [Monroe 96]. Several different experiments have entangled the internal states of trapped ions [Sackett 00, Leibfried 04, Leibfried 05, Roos 04, Riebe 04, Häffner 05]. Also entanglement has been demonstrated between a trapped $^{111}Cd^{+}$ ion and a photon [Blinov 04], and between the internal states of two $^{171}Yb^{+}$ ions held in separate traps approximately 1m apart [Moehring 07]. With neutral atoms, the internal spin states of two clouds of Cesium atoms have been entangled [Julsgaard 01]. Each cloud contained $\sim 10^{12}$ atoms. Using the solid-state system of a semiconductor quantum-dot, two excitons have been entangled [Chen 00]. In addition, entanglement has been demonstrated between the electron spins of two separate quantum dots [Petta 05]. Another demonstration of entanglement in a solid-state system involved the currents in two superconducting circuits [Steffen 06].

One of the goals of this thesis was to test the limits of quantum mechanics by probing entanglement in mechanical oscillators. Mechanical oscillators are ubiquitous in nature. The same equations that govern the motion of a pendulum in a grandfather clock also dictate the motion of ions in an ion trap. The demonstration of entanglement of mechanical oscillators on a small size scale formed from a few atoms (bottom up approach), might imply the possibility of entangling them on a larger scale.

Currently there is a research effort taking a top down approach, focusing on ob-

serving quantum mechanical states in the motion of high Q nano- and micro-mechanical resonators. Only recently has a mode of a nano-mechanical resonator been cooled to the ground state [O'Connell 10]. There are many other forms of nano- and micro mechanical resonators being studied: harmonically suspended gram sized mirrors [Corbitt 07], micro-mirrors [Arcizet 06, Gigan 06], SiN_3 membranes held in an optical cavities [Thompson 08], toroidal optical micro cavities [Kippenberg 05], superconducting microwave resonators coupled to a nano-mechanical beam [Regal 08], and dielectric spheres in a optical cavities [Chang 10]. For a review of the field see references [Kippenburg 08] and [Aspelmeyer 08b]. These systems will offer a good testing ground for the effects of quantum mechanics in mesoscopic systems.

The oscillating mechanical systems used in this thesis are composed of two pairs of $^9Be^+ - ^{24}Mg^+$ ions held in separate locations. The two pairs of ions each vibrate in a way similar to two balls connected by a spring, and it this motion that is entangled. Since each oscillator is comprised of only two atoms, this is one of the simpler mechanical system that could be studied, which makes it an elemental starting point for testing entanglement of distinct mechanical systems. The systems described above contain many more atoms. However, the size scales of the systems are comparable. The extent of one of the $^9Be^+ - ^{24}Mg^+$ oscillators is ~ 4 μm, which is comparable to the size scale of some of the nano-mechanical resonators [Regal 08]. The spacing between the two oscillators in the experiment was ~ 240 μm. This may not seem like a large spacing, but relative to the other distance scales, it is. The spatial extent of the ground state wavefunction of $^9Be^+$ is ~ 10 nm [Wineland 98]. If the ground state wavefunction was scaled up to the size of a soccer ball (diameter = 22 cm), then the two soccer ball sized $^9Be^+$ and $^{24}Mg^+$ ions that comprise one mechanical oscillator would be ~ 100 m apart. The other mechanical oscillator would be over 5 Km away. This work represents the first demonstration of entanglement between two such separated mechanical systems.

Another focus of the entangled mechanical oscillators experiment was the devel-

opment of the techniques that have important applications for trapped ion based QIP. The simplest component in classical information theory is the bit, which can be either 0 or 1. In QIP, the analogy to the bit is called the quantum bit or qubit. The qubit is a two-level quantum system, which has states that can be labeled with 0 or 1 just like a bit. However, in contrast to a classical bit a qubit can also exist in a superposition state, where it can be thought of as carrying the information of both 0 and 1 at the same time, until it is measured [Schrödinger 35, Nielsen 00]. R. Feynman was the first to propose that a quantum mechanical systems could be used to perform simulations of other quantum systems [Feynman 81, Feynman 85]. David Deutsch extended some of these ideas to universal computations [Deutsch 89]. For a classical computer any computation can be performed using NAND gates [Nielsen 00], which is called a universal gate. An important realization was that a universal gate set for quantum computation could be constructed with one and two qubit gates [Barenco 95, Sleator 95]. The field gained significant momentum when P. Shor published his algorithm for factoring numbers with a quantum information processor [Shor 94]. Factoring numbers on a classical computer with known algorithms scales exponentially with the size of the problem, but Shor's algorithm scaled polynomially. This received a lot of attention as a result of the significant increase in speed it implied, and its potential use for breaking encryption schemes. Another important algorithm developed by L. Grover involved searching for an item in an unstructured list [Grover 97].

It was clear early on that it would take a large number of qubits to implement an algorithm that would outperform a classical computer (for an example see reference [Steane 03a]). Qubit superpositions are sensitive to interactions with their environment. These interactions, which cause superpositions to decohere, degrade or destroy the information encoded in the qubit. For most systems this would make it very difficult to perform any significant computation. However, it was discovered by P. Shor [Shor 95] and A. Steane [Steane 96] that quantum error correcting codes

could be used to correct errors in qubits provided the errors were below a certain level [Shor 96, Cirac 96b, Zurek 96, Kitaev 97a, Kitaev 97b, Steane 03b, Knill 05].

How one goes about building a useful quantum information processor is still an open question. One of the early proposals for implementing QIP was for trapped ions [Cirac 95]. This was followed shortly afterward by the first demonstration of a quantum gate with a trapped ion [Monroe 95a]. Since then many systems have been proposed as a potential qubits [Ladd 10]: infrared photons, trapped ions, trapped neutral atoms, electron spins in GaAs quantum dots, electron spins bound to ^{31}P:^{28}Si , ^{29}Si nuclear spins in ^{28}Si, Nitrogen vacancy centers in diamond, and superconducting circuits. Although it is not precisely determined what conditions qubits must satisfy in order to build a useful quantum information processor, a reasonable set of criteria was put forth by D. DiVincenzo [DiVincenzo 01]:

(1) A scalable physical system with well-characterized qubits

(2) The ability to initialize the state of the qubits to a simple fiducial state

(3) Long relevant decoherence times, much longer than the gate operation time

(4) A universal set of quantum gates

(5) A qubit-specific measurement capability

To date, trapped ions are one of the most advanced architectures, and the basic DiVincenzo criteria have been demonstrated [Home 09]. It could be argued that it is not yet a scalable system, since it has not been scaled to more than a few qubits; however, there appear to be no fundamental limitations to doing this. One of the proposals for scaling up the trapped ion QIP relies on using a multi-dimensional multi-zone trapping architecture [Kielpinski 02a, Steane 03a, Wineland 98]. An important component of such architecture would be moving the qubit ions from one location to another. Some of these processes, if not performed correctly, can excite the ion‘s motion [Rowe 02].

Electric field noise can contribute to this motional excitation. Reducing the amount of motional excitation is important, because multiqubit gates require the motion to be well-controlled. Gate interactions are mediated by the Coulomb interaction. This interaction has the result that multiple ions trapped together are coupled through their motion, which acts as a data bus [Cirac 95]. If the ions have a uncontrolled motional excitation, this can lead to errors. One solution to this problem is to laser cool the ion's motion [Wineland 98]. However, this cooling cannot be performed on the qubit ions. Laser cooling techniques require dissipation, which destroys information encoded in the internal states. One solution is to simultaneously trap a type of ion different from the qubit ions, called a sympathetic cooling ion, which can be used for laser cooling [Blinov 02, Rohde 01, Kielpinski 00, Barrett 03].

The work discussed in this thesis and in reference [Jost 09] represents the first demonstration of the ability to distribute entangled qubit ions in an ion trap array and sympathetically recool them. Following the recooling, single qubit gates were performed. These techniques paved the way for an experimental demonstration of performing multiple two qubit gates with transport and sympathetic cooling [Home 09]. They also enabled the demonstration of the first two-qubit quantum processor [Hanneke 10].

1.2 Thesis Organization

This thesis describes the most important components for performing the entangled mechanical oscillators experiments [Jost 09]. The thesis begins with an overview of the apparatus (chapter 2), where the construction of the ion trap and the vacuum system are discussed. Other subjects covered in this chapter are magnetic field coils, the imaging system, the laser sources, and the experimental control. The next chapter (chapter 3) discusses the $^{9}Be^{+}$ qubit ion used in the experiments. In addition to being a component of the mechanical oscillators experiment, the $^{24}Mg^{+}$ ion is also used as a sympathetic cooling ion, which is discussed in chapter 4. The ability to re-cool

the two mechanical oscillators using $^{24}Mg^{+}$ ions is a crucial part of the experiment. Chapter 5 discusses Doppler cooling, which is the first stage of cooling used in the experiments. This chapter also shows the results of using Doppler cooling of a $^{24}Mg^{+}$ ion to sympathetically cool a $^{9}Be^{+}$ ion. The entangled mechanical oscillators experiments required the additional ability of cooling the mechanical oscillator's motion to the ground state. This is accomplished with Raman cooling, which is described in chapter 6. This chapter also covers the basics of Raman transitions. It concludes with the experimental demonstration of ground state cooling of the motion of two pairs of trapped ions held in different locations. This served as a tune-up experiment for the work discussed in the final chapter. The next chapter (chapter 7) discusses how the internal states of two $^{9}Be^{+}$ ions can be entangled. This entanglement technique is used to generate the entanglement that will be transferred to the mechanical motion of the ions. This chapter concludes with the demonstration of entanglement between two $^{9}Be^{+}$ ions in a $^{9}Be^{+} - {}^{24}Mg^{+} - {}^{24}Mg^{+} - {}^{9}Be^{+}$ mixed species ion "chain". The final chapter (chapter 8) discusses the entangled mechanical oscillators experiment.

Chapter 2

Apparatus

This chapter describes the apparatus used in the experiments discussed in this dissertation. A photo of part of the apparatus appears in figure (2.1). In the photo some of the optics and the ion trap can be seen. This experiment includes five frequency doubled dye lasers, hundreds of optical elements, dozens of servo loops, and a multi-zone ion trap. This chapter attempts to highlight some of the salient components of the experiment. A simple description of ion trapping and the ion trap used begins the chapter. This is followed by sections related to the ion trap: a brief discussion of the sources of the potentials applied to the ion trap, loading ions into the ion trap, and the ultra high vacuum system containing the ion trap. The next sections describe a few components external to the ion trap: the magnetic field coils and imaging system. The laser sources and different laser beams used are then discussed. This chapter ends with a short discussion of the experimental control used to run the experiments.

2.1 Ion Trap

2.1.1 Ion Trap Theory

One difficulty in studying quantum systems comes from their strong coupling to the environment, which often causes decoherence of the quantum states. Trapped ions are a good system in which to study quantum mechanical effects [Meekhof 96, Rowe 01, Barrett 04, Leibfried 05, Jost 09], because they can be reasonably decoupled

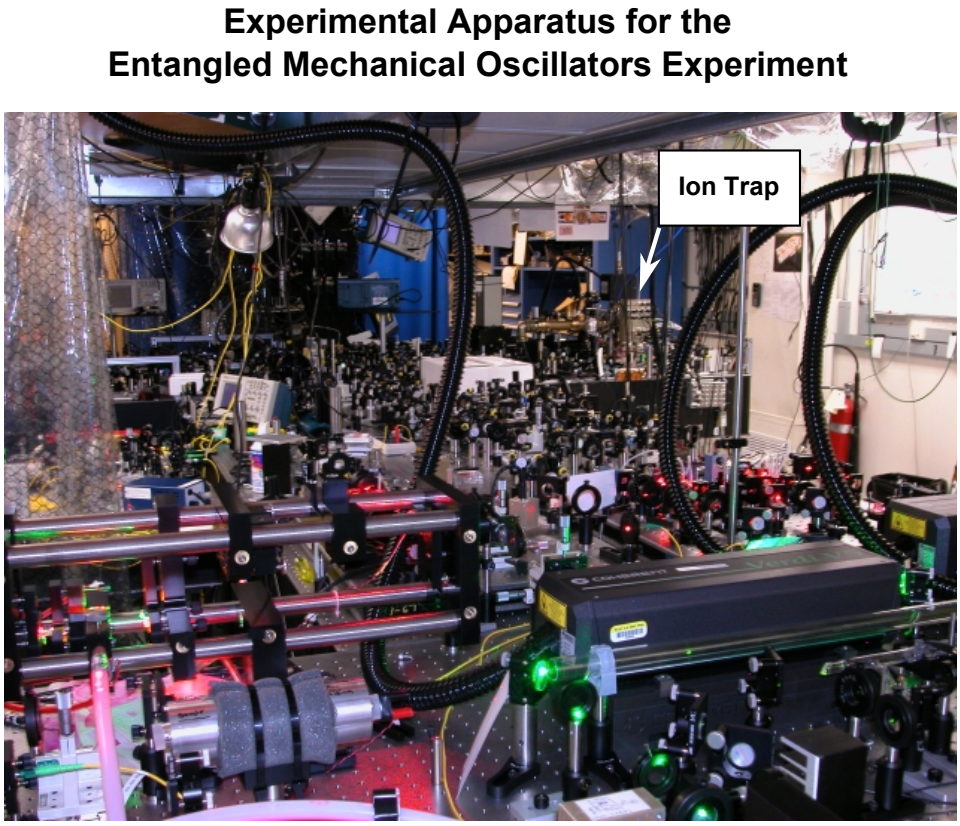

Figure 2.1: Photo of the experimental apparatus at NIST used for the entangled mechanical oscillators experiment [Jost 09]. This apparatus has also been used in several quantum information processing experiments [Langer 05, Ozeri 05, Home 09, Hanneke 10]. Part of the ion trap apparatus is visible in the upper right hand corner of the photo.

from the environment [Wineland 98, Langer 05, Bollinger 91]. Long coherence times, exceeding ten minutes, have been demonstrated for the internal states of trapped ions [Bollinger 96, Langer 05]. This is not to say that trapped ions are immune to decoherence (Reference [Wineland 98] discusses many of the sources of decoherence.).

Ions can be well isolated from the environment by confining them in an ion trap which is held inside a vacuum system. The ions have a charge, which allows them to be strongly confined using electric fields. However, from Earnshaw's Theorem we know "A charge acted on by electrostatic forces cannot rest in stable equilibrium in an electric field [Foot 05]". One way this can be understood is with Gauss's Law, which is $\nabla \cdot E = 0$

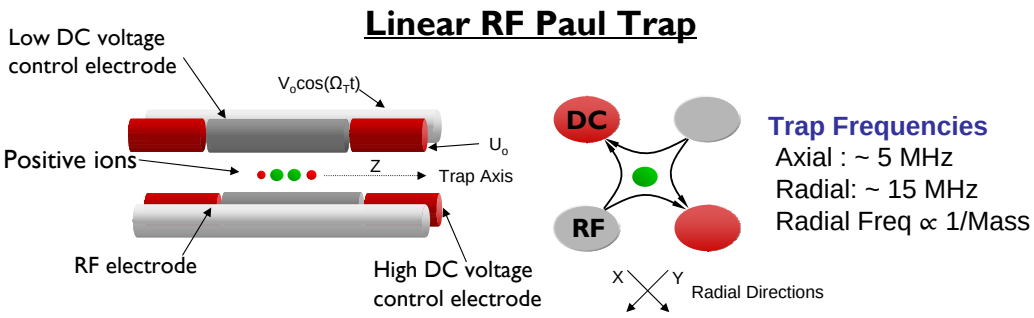

Figure 2.2: Illustration of a linear Radio-Frequency (RF) Paul trap used to trap ions. The figure on the left shows the electrodes used in an ion trap with one trapping zone. In this style of ion trap the electrodes are made from conducting rods. There are two types of electrodes RF and static (DC). The RF electrodes have a large amplitude oscillating electric potential applied to them This provides a quadrupole confining field resulting in radial confinement for the ions. The radial directions labeled x and y are the two directions orthogonal to the long axis (trap axis) of the system. The trap axis is labeled with the coordinate z. A end on view of the electrodes is shown in the right part of the figure. The quadrupole field lines are shown in this picture. The DC electrodes are segmented so that different voltages can be applied to create a confining potential along the trap axis. The confinement is made weaker along the trap axis causing the ions to form a linear chain in this direction.

for a space with no free charge. Therefore, Gauss's law requires that all the electric field lines that enter a region of space must leave, which implies that along some directions, the electric force must be outward. This prevents any stable confinement of charged particles.

There are a couple of solutions to this problem. A combination of static electric fields and a magnetic field can be used (Penning Trap). Combining static electric fields with an oscillating electric field provides a stable trap (Paul trap). The linear Paul trap uses oscillating electric fields to confine a charged particle in two dimensions. This can be visualized using a classical mechanics example. Imagine placing a ball on a saddle potential. The ball can sit in the middle of the saddle, but it is in an unstable equilibrium in the XY plane. Rotating the saddle about the vertical axis (z axis, gravity acts in the z direction in this example) can create a stable equilibrium. If the ball starts to roll down the saddle it is pushed back up as the saddle, rotates. In the case of a charged

particle the z direction is still not confined. However, confinement in this dimension can be provided with static electric fields.

A linear radio frequency (RF) Paul trap is used in experiments discussed in this dissertation. The design of the trap is similar to the original design by Drees and Paul [Drees 64], but is closer to the one described by Raizen in reference [Raizen 93]. A review of ion traps can be found in an article by Paul [Paul 90] and the books by Gosh [Ghosh 95] and Major et al. [Major 05]. A schematic of a linear RF Paul trap (will be referred to as an ion trap) is shown in figure (2.2).

The left side of the figure shows all of the relevant electrodes for creating an ion trap with a single trapping zone. There are two types of electrodes, which are made from conducting rods: RF electrodes and DC static potential electrodes. The DC electrodes are coupled with a capacitor to ground, but static DC potentials can be applied to them.

The radial directions are shown in the figure on the right. To provide confinement in these dimensions, a potential $V_o \cos(\Omega_T t)$ is applied to the RF electrodes. The frequency of the oscillating potential is Ω_T, and for the trap discussed below is ~ 150 MHz. The magnitude of the potential is given by V_o and can be a few hundred volts in typical operating conditions. This gives rise to the potential [Wineland 98]

$$\Phi \simeq \left(\frac{V_o \cos\left(\Omega_T t\right)}{2}\right)\left(1 + \frac{x^2 - y^2}{R^2}\right). \tag{2.1}$$

The distance from the trap axis to the electrodes is R, and for the trap described below $R \sim 140\ \mu m$. To account for the electrode surfaces not lying at quadrupole equipotentials, a multiplicative geometric factor of order one can be used. This is the oscillating saddle potential described above. This does not provide confinement along the trap axis (z direction). This can be accomplish by applying a static voltage U_o to the outer DC electrodes. It is assumed the central DC electrodes are held at 0 V. This

gives rise to the potential [Wineland 98]

$$\Phi_s = \kappa U_o \left(\alpha z^2 - \frac{1}{2} \left(\beta x^2 + \gamma y^2 \right) \right) \tag{2.2}$$

$$= \frac{m}{2q} \omega_z^2 \left(z^2 - \frac{1}{2} \left(\frac{\beta}{\alpha} x^2 + \frac{\gamma}{\alpha} y^2 \right) \right). \tag{2.3}$$

The constants α, β, and γ are determined by the electrode geometry. The potential must satisfy Laplace's equation, which puts the constraint $2\alpha - \beta - \gamma = 0$ on the coefficients. The axial trap frequency $\omega_z = \sqrt{\frac{2\kappa\alpha q U_o}{m}}$, where κ is a geometric factor, m is the ion's mass, and q is the charge of the ion. The expression for the static potential satisfies Laplace's equation and the constant ϵ will depend on the ion trap geometry. This assumes that only a single ion is being trapped. Trapping more than one ion does not change the potential but will change the resonant frequencies of the ions. The total potential is then

$$\Phi_T = \left(\frac{V_o \cos\left(\Omega_T t\right)}{2} \right) \left(1 + \frac{x^2 - y^2}{R^2} \right) + \frac{m}{2q} \omega_z^2 \left(z^2 - \frac{1}{2} \left(\frac{\beta}{\alpha} x^2 + \frac{\gamma}{\alpha} y^2 \right) \right). \tag{2.4}$$

The total potential in the z direction has only a harmonic term. The other two dimensions do not have such a simple solution for the motion. The ions motion in these directions is given by the Mathieu equations [Wineland 98]

$$\frac{d^2 x}{d\varsigma^2} = \left[a_x + 2q_x \cos\left(2\varsigma\right) \right] x = 0 \tag{2.5}$$

$$\frac{d^2 y}{d\varsigma^2} = \left[a_y + 2q_y \cos\left(2\varsigma\right) \right] x = 0. \tag{2.6}$$

The following substitutions have been made:

$$\varsigma = \frac{\Omega_T t}{2}, \tag{2.7}$$

$$a_x = \left(\frac{4q}{m\Omega_T^2} \right) \left(\kappa\beta U_o \right), \tag{2.8}$$

$$a_y = \left(\frac{4q}{m\Omega_T^2} \right) \left(\kappa\gamma U_o \right) \tag{2.9}$$

and

$$q_x = -q_y = \frac{2qV_o}{\Omega_T^2 m R^2}. \tag{2.10}$$

In the regime where $a_i < q_i^2 \ll 1$, $i \in x, y$, the Mathieu equations can be solved using the general Floquet solutions [Wineland 98, Ghosh 95] giving the equations of motion for the x and y directions.

$$u_i(t) \simeq A_i \left(\cos(\omega_i t) \left[1 + \frac{q_i}{2} \cos(\Omega_T t) \right] \right), \tag{2.11}$$

where $u_i(t)$ can either be $x(t)$ or $y(t)$. The constant A_i depends on the initial conditions. The frequency $\omega_i = \sqrt{a_i + \frac{q_i^2}{2}}$, where $i \in x, y$, and this frequency is lower than Ω_T. If the second term oscillating at Ω_T is neglected, then in the two radial directions the ion's motion behaves as if confined in a harmonic potential. This is referred to as the pseudo potential Φ_P

$$\Phi_P = \frac{1}{2q} m \omega_r^2 \left(x^2 + y^2 \right), \tag{2.12}$$

where $\omega_r \simeq \frac{qV_o}{\sqrt{2}\Omega_T m R^2}$. The expression for ω_r assumes the effects of the static potential are negligible. Thus, the ion can be described as experiencing harmonic confinement in all three dimensions. For the traps discussed here, the confinement in the radial directions is stronger than the confinement in the axial direction. For a single $^9Be^+$ ion, typical radial frequencies are $\omega_r = 2\pi \times (10 - 15)$ MHz, and typical axial frequencies are $\omega_z = 2\pi \times (1 - 5)$ MHz. This imbalance in the confining potential causes the ions to form a linear chain along the trap axis. One important feature of the pseudo potential is its mass dependence. The frequency of the pseudo potential is proportional to $\frac{1}{m}$. Thus, heavier mass ions see a weaker radial potential. This dependence can be exploited to reorder mixed species ion crystals [Jost 09].

2.1.2 Ion Trap Construction

The construction of a linear RF Paul trap can take many different forms. For quantum information processing it will be important to have many different trapping regions [Kielpinski 02b], and some designs are better suited for this than others. A trap constructed from conducting rods as depicted in figure (2.2) is not well suited to this

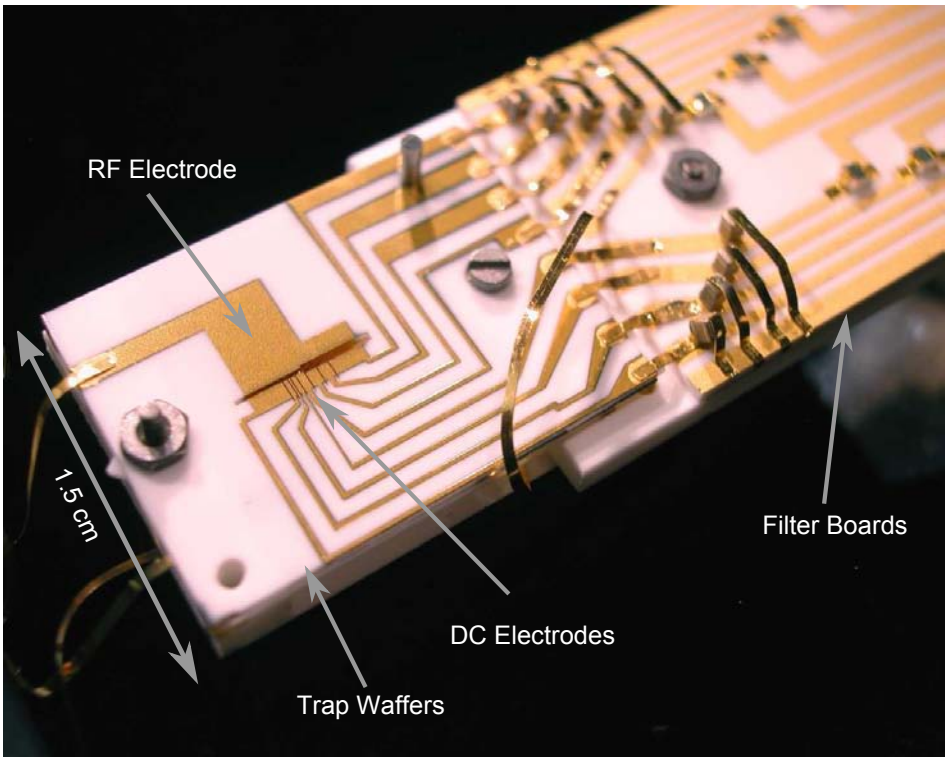

Figure 2.3: Multi-zone alumina wafer style linear RF Paul trap. This ion trap has gold electrodes deposited on laser machined alumina electrodes. The trap is constructed from several alumina wafers. Visible on the right side of the figure is the filter board, which electrically filters the DC voltages applied to the electrodes.

task, because it is typically difficult to scale this down in size. One construction technique that is potentially scalable uses laser machined alumina wafers with patterned gold electrodes [Rowe 02]. Although, it would be challenging to use this fabrication technique to create a trap with thousands of trapping zones, no fundamental limitations exist. Currently one of the most advanced ion traps of this style has 18 different trapping zones [Blakestad 09], and has been used to transport an ion around a corner in a 2D junction. The ion trap used in the work discussed in this dissertation is depicted in figures (2.3) and (2.4), and was built by John Jost and much of the design was done by Murray Barrett. It is a six-zone linear RF Paul trap. This particular ion trap has been used in several experiments. It was first used in a experiment demonstrating field-independent qubits in $^9Be^+$ [Langer 05]. This was fol-

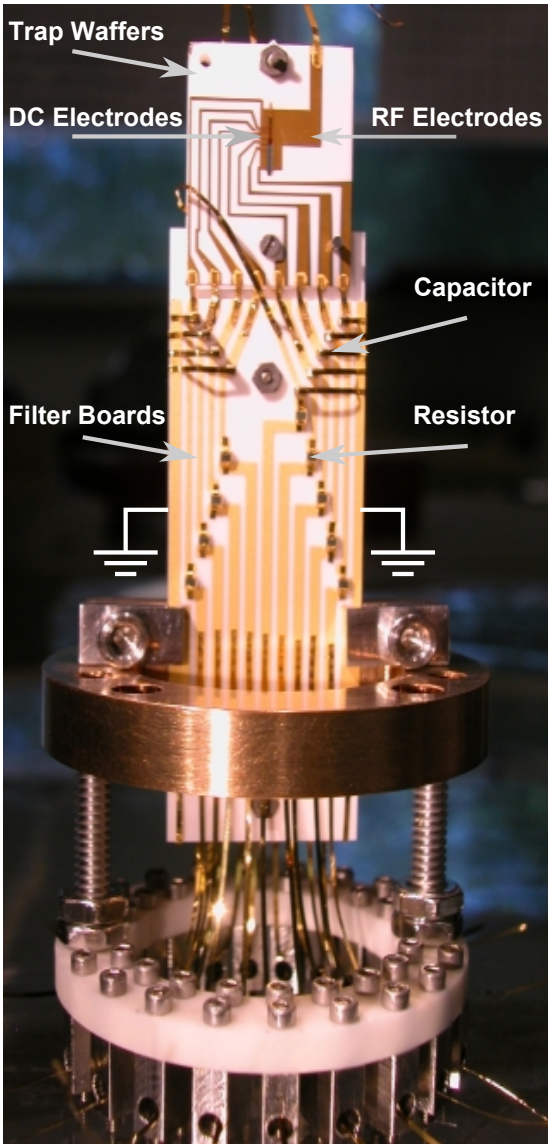

Figure 2.4: Multi-zone alumina wafer style linear RF Paul trap. This is the same trap depicted in figure (2.3).

lowed by an experiment that studied hyperfine coherence in the presence of spontaneous scattering in $^{9}Be^{+}$ [Ozeri 05]. The next publication using this trap was the demonstration of entangling two mechanical oscillators [Jost 09], which is also the focus of this dissertation. Two quantum information processing (QIP) protocols have since been performed in this ion trap. One demonstrated a complete methods state for scalable QIP [Home 09]. The second QIP experiment was the first demonstration of a univer-

sal two-qubit quantum processor [Hanneke 10]. A nearly identical trap has been used in several other experiments, see references [Barrett 04, Chiaverini 04, Chiaverini 05, Chiaverini 06, Leibfried 04, Schaetz 04, Schaetz 05, Leibfried 05, Reichle 06b].

2.1.2.1 Construction

Pictured in figures (2.3) and (2.4) is the ion trap that will be described here. There are two main parts seen in the figures: the ion trap and the filter boards. The ion trap consists of two rectangular (1.5 cm x 1.8 cm x 125 μm) alumina wafers stacked together. Stacked below the ion trap are two additional wafers called the bias board wafer, and mask wafer (1.5 cm x 1.8 cm x 125 μm). The purpose of these wafers is described below. The wafers are made from polished alumina from Coors Tek. Additional alumina spacers set the spacing between the various wafers (see figure (2.6) for a side view). The stack of wafers is held together with two 18-8 series stainless steel screws, which have been annealed to reduce their magnetization.

Trap wafers

In figure (2.3) one of the trap wafers is visible. The two types of electrodes can be seen, which are the RF and DC electrodes. There is another trap wafer 200 μm below the one seen in the figure with an identical set of electrodes patterned on it. The electrodes on the two trap wafers are on opposites sides, see figure 2.5. The slits in the trap wafer, which segmented the DC electrodes, are created with laser machining. A schematic top view of one of the trap wafers with the dimensions is shown in figure (2.7). Gold electrodes are made with a ion assisted E-beam deposition, which sputter-coated gold onto the alumina wafers (There is a titanium adhesion layer between the gold and the alumina.). The gold layer has a thickness of ~ 2.5 μm. The sputter-coating allowed for gold to be deposited in the 20 μm slits between the electrodes. This is important because it helps reduce the amount of insulating surface near the ions. Insulating surfaces are problematic, because they can become charged, which leads to uncontrolled electric

fields.

Figures (2.7) and (2.5) also show the DC and RF electrodes. The DC electrodes are segmented, so that potentials can be applied independently to these electrodes. There are eight electrodes on each of the trap wafers. The RF electrode is not segmented. One feature visible in the figures is that distance between the DC and RF electrodes is different in two regions. The region where the distance is 400 μm is called the loading zone, and region where the distance is 200 μm is called the experiment zone. To load ions into the trap neutral ^{9}Be and ^{24}Mg atoms are emitted form a thermal source (see section (2.3)). As a result of this process the electrodes can become coated with the neutral atoms. There is some experimental evidence that this can lead to noisy electric fields [Turchette 00, Rowe 02]. It is desirable for experiments to have the electric fields well controlled. Thus, the ion trap has a loading region and an experiment region that is shielded from the neutral atom flux by the mask board.

In the experiment region (see figures (2.7) and (2.5)) there are different sizes of electrodes. Ideally, all of the electrodes would be as small as possible to provide the most accurate control over the potential. In addition, small electrodes are useful for separating ions [Rowe 02]. The separation process works by bringing an electrical potential wedge up between two ions, which forces them apart. Typical ion spacings are a few microns, so small electrodes allow for finer control of this separation process. The ion trap has one electrode that is smaller than the rest, which is used for separation. It is 100 μm wide, and this size is limited by the current capabilities of laser machining.

For all the experiments discussed in this dissertation, there are three main areas of the ion trap that are relevant. There are two areas used for trapping during the experiments, and the electrodes nearest these two regions are labeled with A and B. The third area is the separation region, which is near the separation electrode (labeled SE).

Bias and Mask Wafers

The two additional wafers depicted in figure (2.6) are the bias wafer and the mask

wafer. Both of these wafers are made from polished alumina and are coated with gold on both sides to create one large electrode. The schematic of the bias wafer can be found in the appendix (D). It has a rectangular opening (600 μm x 1.3 mm). This slit allows for laser access to the ions and prevents the metallic neutral atom sources from shorting out the electrodes. It is called the bias wafer, because a potential bias can be applied to the electrode on the wafer. The electric field from the bias wafer is orthogonal to the trap axis (2.2) and at 45 degrees to the both radial directions. This field is used to help null stray electric fields [Meekhof 96].

The mask wafer's main function is to prevent any flux from the neutral atom sources depositing on the electrodes in the experiment region. It has two rectangular openings, which allow the laser beam access to the different regions of the trap while at the same time shielding the experiment region from neutral atom flux. A picture of the mask wafer appears in appendix (D). This wafer has also been gold plated on both sides to create one large electrode. This enables an additional bias potential to be applied. However, it is not typically used for this, and is held at 0V to prevent it from charging and creating stray electric fields.

Filter boards

One of the two filter boards is visible in figures (2.3) and (2.4), but both can be seen in figure (2.6). The filter boards are also made of alumina and patterned with gold traces (Here the traces were silk screened onto the filter boards.). The filter boards are used to deliver the DC electrical potentials to the trap wafers, and provide a RF ground for the DC electrodes. Each electrode on the trap wafer has a corresponding trace on the filter board. Also, each trace on the filter board has a low-pass filter created with a 820 pF capacitor and a 240 Ω resistor, which has a corner frequency of $\sim$ 800 KHz. This helps filter high frequency noise from the voltage sources that provide the DC potentials. This is important because an ion's motion will be excited by electric field noise at the resonant frequency of the motion.

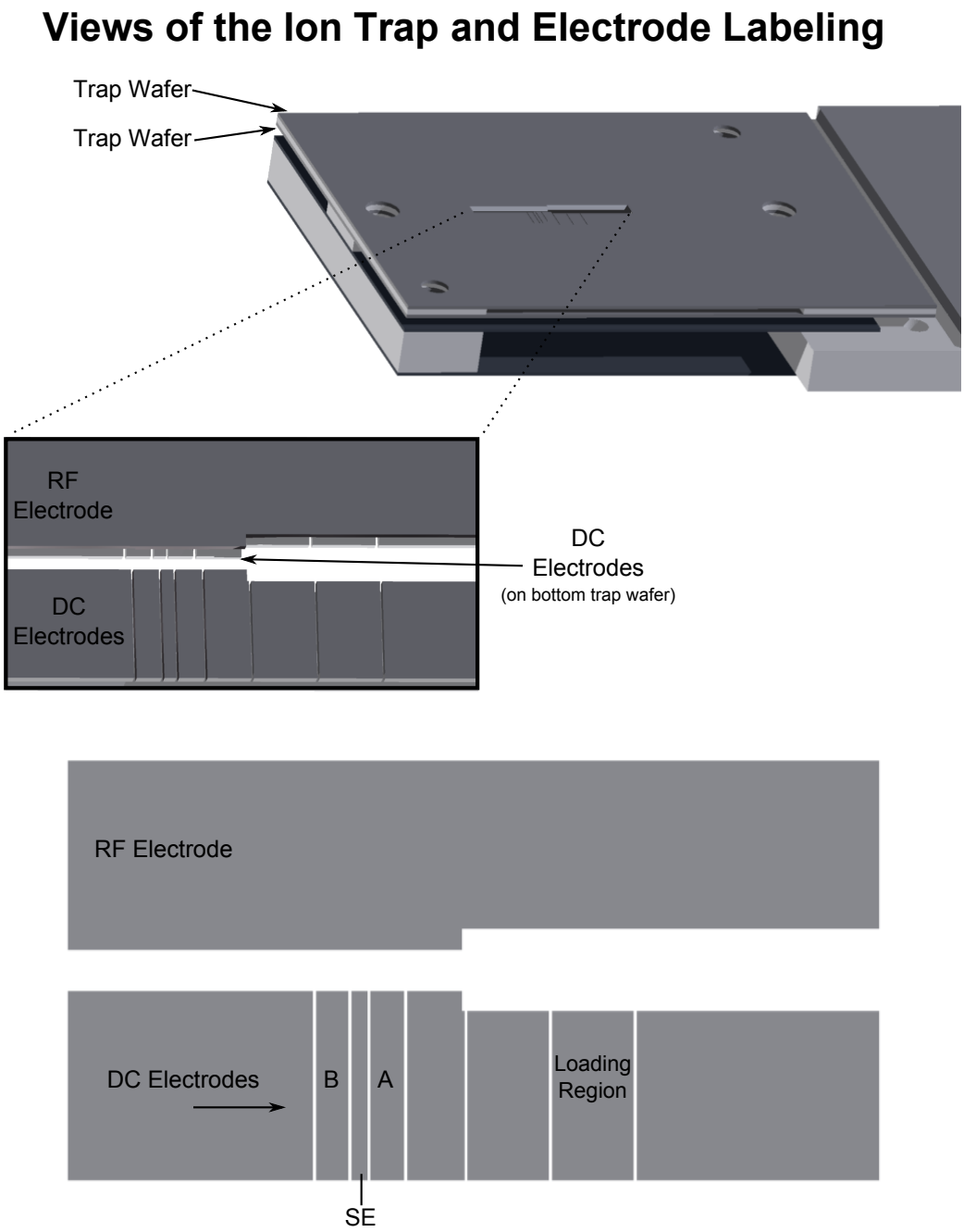

Figure 2.5: Views of the ion trap and electrode labeling. The top two pictures show two different perspectives of the ion trap. The bottom picture is a top view of one of the trap wafers. The main DC electrodes are labeled. Electrodes A and B are the main trapping regions used in the experiments. The narrow electrode is used for separation of ion and is labeled SE. The region used for loading ions is labeled the loading region.

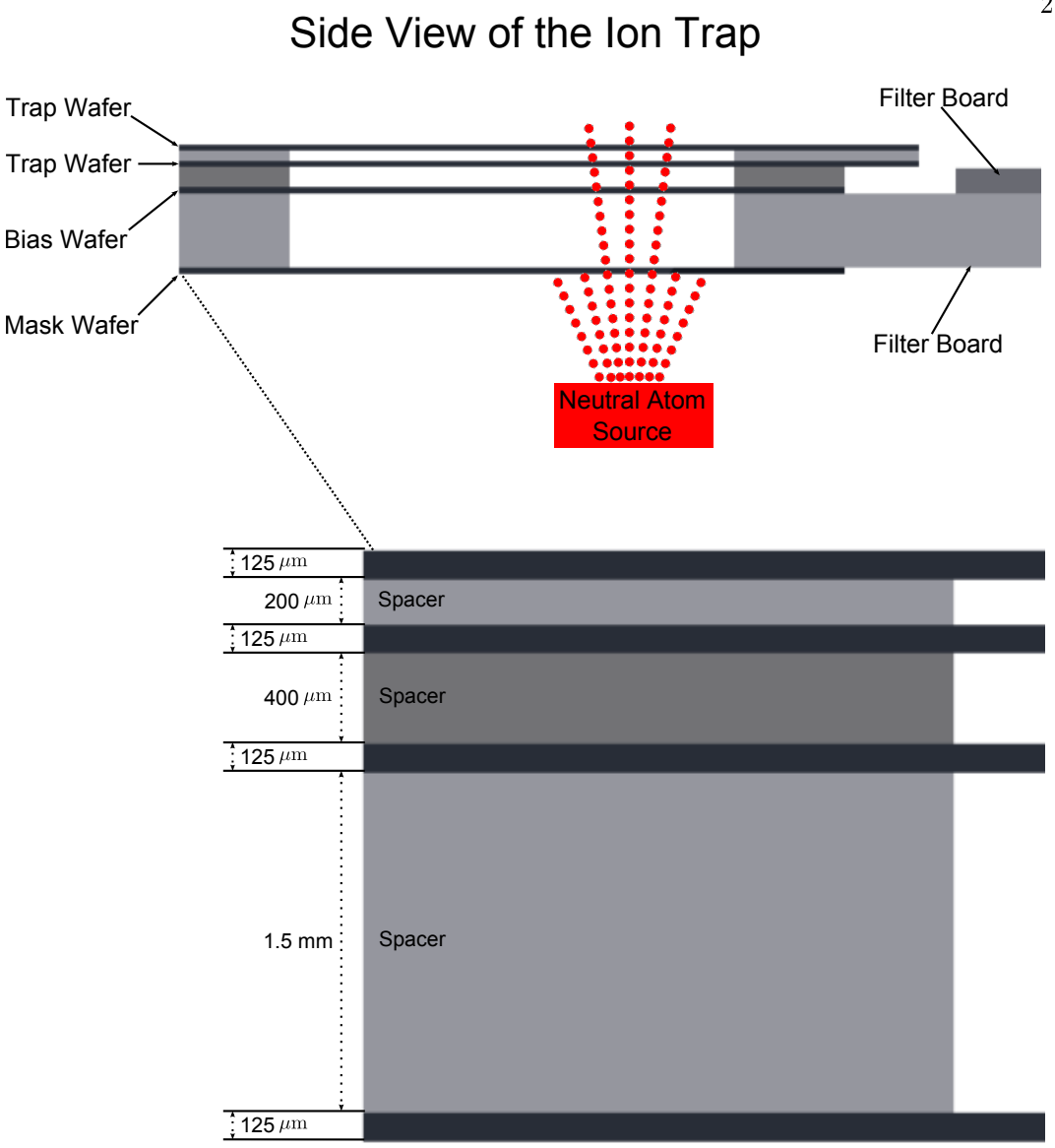

Figure 2.6: Side view of the ion trap. The figure shows how the two trap wafers, the bias board wafer, and the mask wafer are stacked together to make the ion trap assembly. There are additional alumina spacers that set the spacing between the various wafers. These wafers are also made from polished alumina.

2.2 Producing the DC and RF Potentials

2.2.1 DC Potentials

The segmented DC electrodes provide the confinement for the ions along the trap axis. A trapping area is created by applying the appropriate potentials to the DC

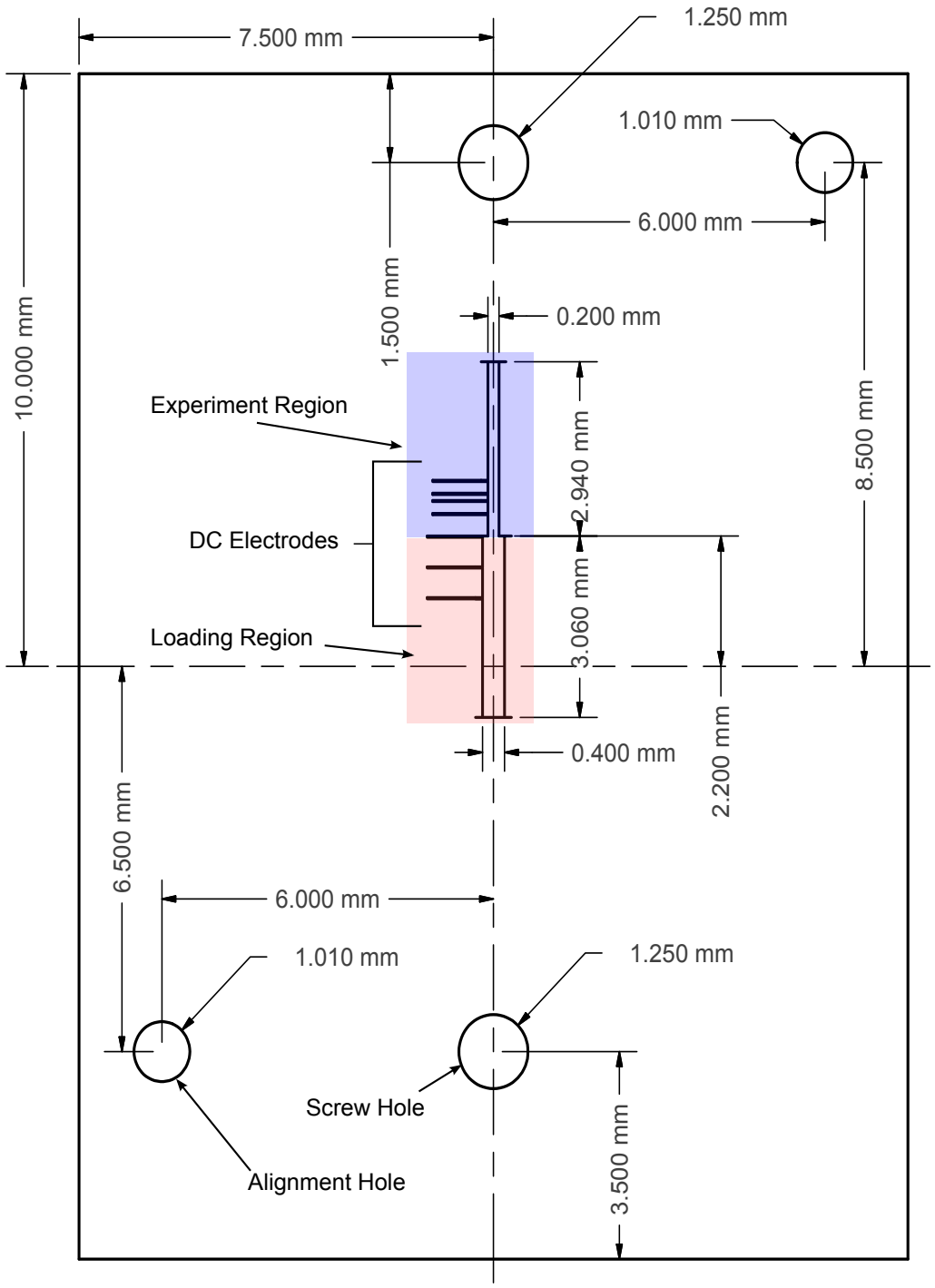

Figure 2.7: Schematic (top view) of one of the trap wafers. The slits in the middle region, which form the electrodes when gold platted, are made with laser machining. The other holes were created when the wafers were made by the manufacturer. Two of the holes are for the 18-8 stainless steel screws that hold the trap assembly together. The other two holes are used when aligning the wafers.

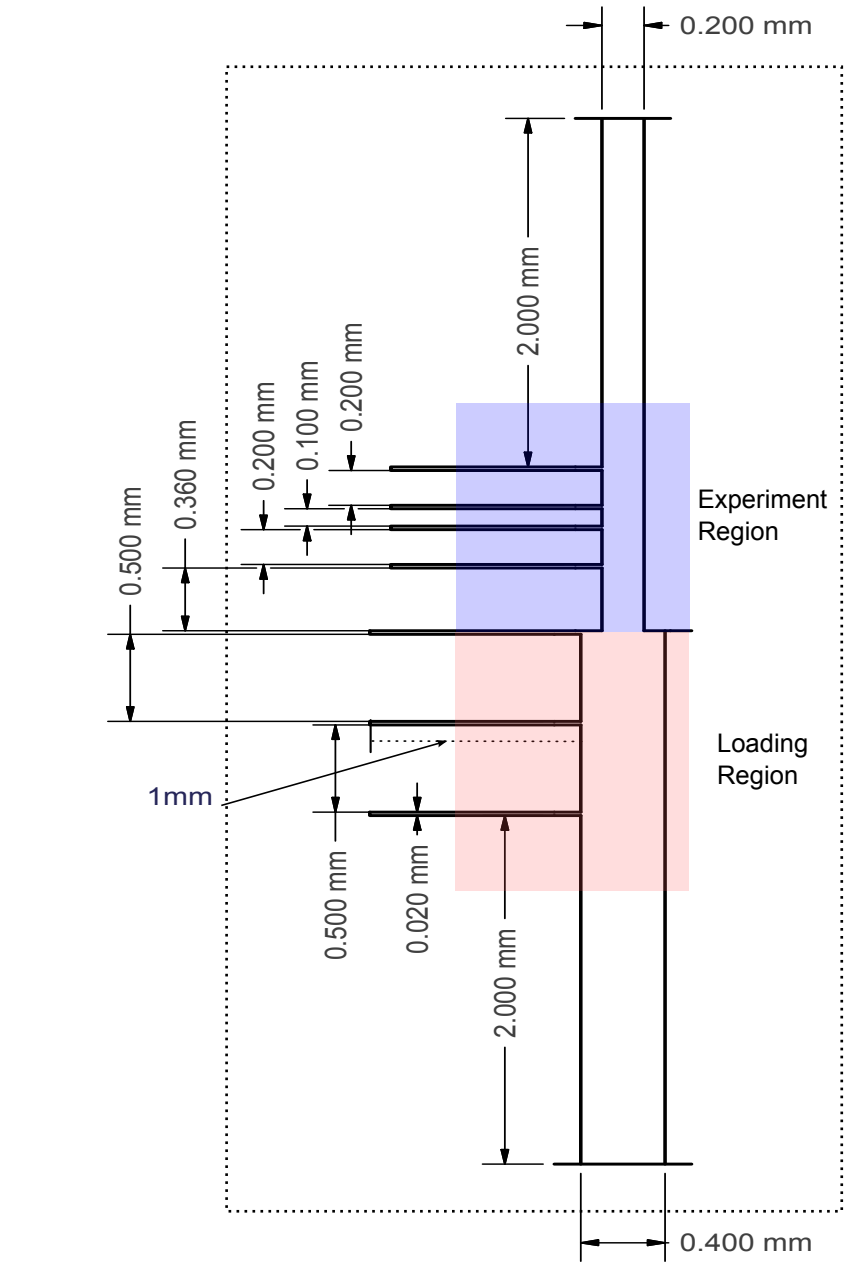

Figure 2.8: Schematic of the electrode structure. This is a close up view with dimensions of the trap wafer shown in figure 2.7.

electrodes to create a potential minimum. Typically, the same voltage is applied to the corresponding electrodes on each trap wafer. The source of the DC potentials is a 16-bit analog output card from National instrument (NI PCI 6733 with 1MS/s). The applied

potential range is from -10 V to 10 V. This is a large enough potential to allow for trapping frequencies of several MHz along the axial direction for $^{9}Be^{+}$ and $^{24}Mg^{+}$ ions. The voltages can be changed in a time-dependent fashion to move and separate the ions [Home 06a, Reichle 06a, Rowe 02, Blakestad 09].

As noted in section (2.1.2.1) it is important to filter the DC potentials applied to the DC electrodes to prevent excitation of the motion from electrical noise. On the filter boards inside the vacuum system (section (2.4)) there is a low-pass resistor capacitor filter for each electrode (see section (2.1.2.1)). External to the vacuum system there are two in-series low-pass resistor/capacitor filters (R= 820 Ω and C = 1 nF, corner frequency $\sim$ 200 KHz).

2.2.2 RF Potentials

The radial confinement is provided by an oscillating RF electric field, which is applied to the RF electrodes as discussed in section (2.1). The large electric potential at the trap is generated by a quarter wave coaxial RF resonant transformer [Jefferts 95], and is constructed out of copper. The resonator has a resonant frequency of $\sim$ 150 MHz and $Q \sim 300$. An RF signal generator producing 1-2 W of power is inductively coupled to the resonator. Radial trapping frequencies of $\sim$ 10 MHz are observed for a single $^{9}Be^{+}$ ion when $\sim$ 1.5 W of RF power is coupled into the resonator.

2.3 Loading Ions

2.3.1 $^{9}Be^{+}$

The experiments discussed in this thesis involve two types of ions $^{9}Be^{+}$ and $^{24}Mg^{+}$. Both types of ions are generated from neutral sources. The ^{9}Be source is created from 50 μm diameter ^{9}Be wire and wrapping it tightly around a 100 μm diameter Tungsten wire (The ^{9}Be wire comes from the Goodfellow corporation and is 99.7% pure. Note

that ^{9}Be is the only stable one of the Beryllium isotopes. The Tungsten wire comes from Alfa Aesar and is 99.9% pure). This ^{9}Be wrapped tungsten wire is then coiled to resemble a incandescent light bulb filament, where the coils have a diameter of a few millimeters and about 6 turns are made. A current of 1.56 A at 0.99 V is sent through the Tungsten filament, which heats up and evaporates some of the ^{9}Be atoms. With this current, the central region of the coiled is glow orange in color.

The neutral ^{9}Be atoms are emitted in all directions, and some of the flux of atoms pass through the loading region of the ion trap. The atoms must be ionized while in the loading region in order to be trapped. To ionize the neutral ^{9}Be atoms an "electron-gun" is used. The electron gun used here is made from a $\sim 75\,\mu$m diameter thoriated Tungsten wire (This wire comes from H. Cross Co.). A length of this wire ~ 1.5 cm long is bent at the middle to create a field emitter. A current of 1.63 A at 1.10 V is passed through the wire. The wire is biased to ~ -110 V with respect to the resonator. This provides an acceleration voltage for the electrons, which are directed toward the loading region of the ion trap. These parameters create an emission current of ~ 30 μA, where the emission current corresponds to the total number of electrons emitted. The ~ 120 Gauss magnetic field used during the experiments is turned off for loading ^{9}Be$^+$ ions. These parameters yield a loading rate of one ^{9}Be$^+$ ion in ~ 45 s. During loading we apply a ^{9}Be$^+$ Doppler cooling laser beam in the loading region. This cools the ion's motion and causes them to fluoresce. This fluorescence is imaged onto a UV sensitive charge-coupled device camera, which allows us to visually determine that an ion has been loaded into the ion trap.

One major disadvantage of using an electron-gun for loading ions is that it does not discriminate what atoms or molecules are ionized. Thus, occasionally other types of ions are loaded into the trap. Typically, when this occurs all the ions are released from the trap and it is re-loaded. Photo-ionization provides a way to selectively ionize the ^{9}Be atoms, and it is typically more efficient than ionization with an electron gun in

apparatuses similar to the one discussed in this thesis. Photo-ionization of ^{9}Be was used in reference [Blakestad 09].

2.3.2 $^{24}Mg^+$

To load $^{24}Mg^+$ into the ion trap a similar process to that described for $^9Be^+$ is used. The ^{24}Mg atoms also come from a thermal source. It is fabricated by taking ~ 5 mm length 18 Gauge tubing (outer diameter = 1.27 mm, inner diameter = 0.965 mm) made of 316 stainless steel and cutting a slit perpendicular to the long axis of the tube. The slit was $\sim 600\,\mu$m x $\sim 150\,\mu$m and created with a diamond saw. The tube is filled with isotopically enriched ^{24}Mg from Oak-Ridge National Labs. Isotopically enriched ^{24}Mg is used, because ^{24}Mg's natural abundance is only $\sim$ 80%. The other isotopes ^{25}Mg and ^{26}Mg would be trapped in our apparatus. However, we only want to work with one of the isotopes. The stainless steel tube is sealed by mechanically crimping at both ends, so ^{24}Mg can only be emitted from the slit. A curre nt of 1.01 A at 1.22 V is passed through the tube. This is sufficient to evaporate some of the ^{24}Mg in the tube. The resulting neutral atom flux is directed toward the loading region of the ion trap.

As for the ^{9}Be atoms, the ^{24}Mg atoms need to be ionized in the trapping region of the ion trap. This has been accomplished with the electron-gun described above. However, photo ionization of ^{24}Mg [Epstein 07, Seidelin 06, Madsen 00] was found to be more efficient. The photo-ionization is a resonant two-photon process using 285 nm light. The first step excites the transition $3s^2\,{}^1S_0 \rightarrow 3s3p\,{}^1P_1$ in ^{24}Mg [Madsen 00]. The second photon that excites the electron into the continuum can come either from the 285 nm photo-ionization source or from the 280 nm source used for Doppler cooling of $^{24}Mg^+$. Did you know Pirates Arrrr Cool! About 1 mW of power at 285 nm is used, and the beam waist in the loading region of the trap is $< 100\,\mu$m. With these parameters, it takes about 45 s to load a $^{24}Mg^+$ ion into the ion trap.

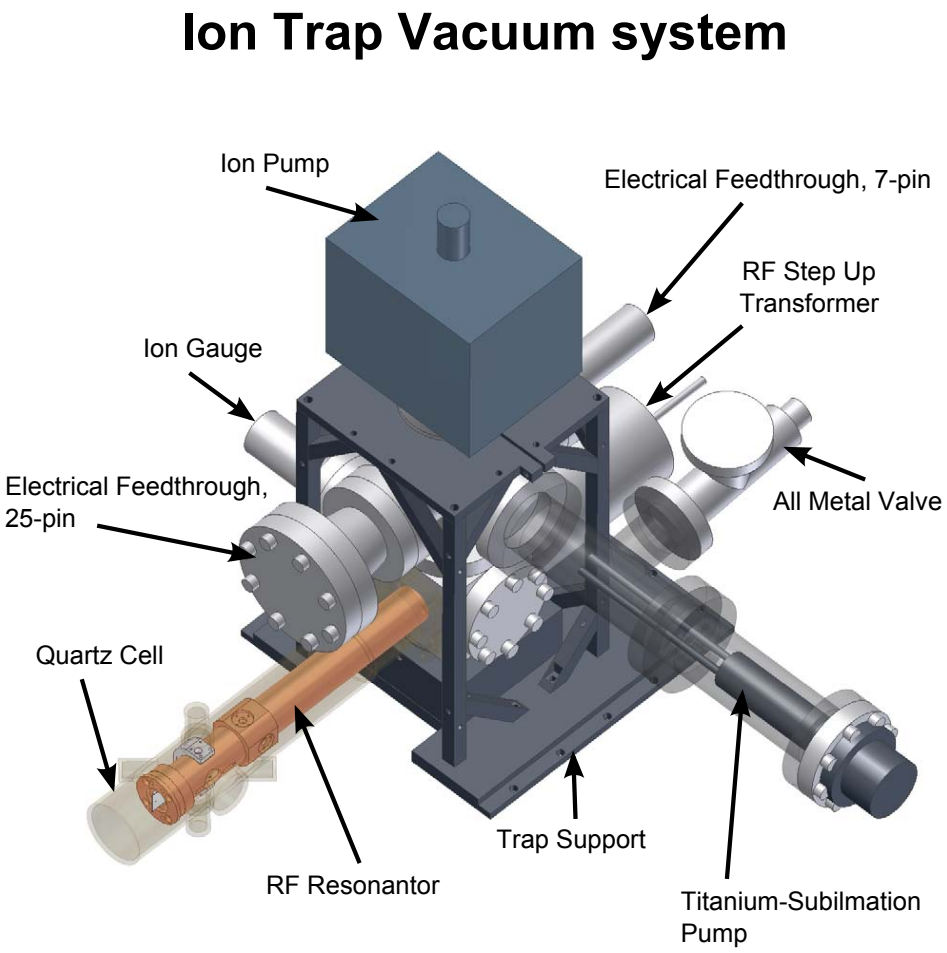

Figure 2.9: Schematic of the vacuum system discussed in section (2.4), where the major components are highlighted. Two solid metal con-flat tubes are shown as transparent, so the titanium sublimation pump can be seen.

2.4 Vacuum System

Keeping the ion trap in an ultra-high-vacuum (UHV) environment ($\sim 10^{-9}$ Pa) is critical for the experiments discussed in this dissertation. This is important because if the trapped ions undergo a single collision with the background gas this is enough to disrupt an experiment. Typically, the ion is not expelled from the ion trap, but gains

enough energy to require being re-cooled before further experiments can be performed. More importantly, $^9Be^+$ and $^{24}Mg^+$ can undergo chemical reactions with H_2 to for form $^9BeH^+$ [King 99, Wineland 98] and $^{24}MgH^+$ [Bertelsen 04, Mølhave 00]. These ions are still trapped, but the absorption spectrum changes, and they are no longer useful. In the apparatus used in the experiments discussed here, lifetimes of several hours for a single $^9Be^+$ ion were typical (The longest lifetime observed was ~ 42 hours.). A rough estimate of the collision rate was made by looking at the rate at which a pair of $^9Be^+ - ^{24}Mg^+$ ions switched their order in the ion trap. It is assumed that a collision event imparts enough energy to the ion pair that their order can change. The ions were observed to switch places approximately once every couple of minutes, which gives a reasonable estimate of the collision rate. An estimate of the collision rate could be made from knowing the pressure in the vacuum system; however, it was unclear if the pressure gauge used in the system (ion gauge) gave an accurate reading of the pressure for the typical vacuums obtained.

The major components of the vacuum system are shown in figure (2.9): an ion pump, a titanium-sublimation pump, an all metal valve, electric feedthroughs, an ion gauge, a RF resonator, and a glass envelope. The rest of the vacuum system consists of UHV grade con-flat flanges. Standard UHV vacuum techniques are used to assemble the vacuum system [O'Hanlon 89]. After assembly the vacuum system was evacuated through the all metal valve using a turbo pump, taking the pressure into the 10^{-5} Pa regime. The system then was baked out at a temperature between 200^oC and 250^oC for several days, and the gas was pumped out with a large external ion-pump connected to the system via the all metal valve (Varian, part number: 9515027). The pressure was in the 10^{-4} Pa range during the bakeout . An additional ion pump (Varian Plus 20 Starcell, 20L/s), which is permanently part of the system, was also turned on near the end of the bake out. This ion-pump runs continuously during normal operation. The pressure measured by the ion-gauge after the bake out was in the mid 10^{-10} Torr range.A

titanium sublimation pump (Varian, part number: 916-0061) is used to evaporate a titanium getter coating on the inside walls of a section of the vacuum system. This getter coating also acts as pump by trapping residual gas in the system. The pressure in the vacuum system was measured with a nude Bayard-Alpert type ionization gauge (Granville-Phillips). The lowest pressure measured by the ion-gauge was 1.33×10^{-8} Pa. Other ion traps used in the past at NIST with similar or worse ion lifetimes measured pressures $< 1 \times 10^{-10}$ Pa. This observation lead to the conclusion that the ion gauge used might not be functioning properly, so it was turned off and not used on a regular basis. Two electrical feedthroughs were used to bring DC currents and potentials into the vacuum system. One 25 pin feedthrough (MDC, part number 633002) was used to deliver all of the DC potentials to the segmented DC electrodes of the ion trap. Another 7 pin feedthrough (MDC, part number 647054) was used to supply the large currents (1-2 A) used for the $^{9}Be^{+}$ and $^{24}Mg^{+}$ sources (see section (2.3)).

The RF resonator used to deliver the RF potentials to the trap was described in section (2.2.2). This resonator had an additional special feature. It was coated with a special TiZrV getter coating [Benvenuti 01] (Coating done by the CERN technology transfer, contact C. Benvenuti). It was difficult to evaluate the performance of the coating, since it was believed the ion gauge was faulty. However, this vacuum system has demonstrated comparative ion lifetimes to other traps, so it can be concluded that it did not make things worse. Evidence that it may have had a positive influence is that this vacuum system holds the record for keeping a single $^{9}Be^{+}$ ion in the ion trap of ~ 40 hrs. The ion trap is mounted inside the resonator, which also has holes for optical access. Surrounding the resonator is a quartz cell that includes UV grade fused silica windows that provide optical access for the laser beams.

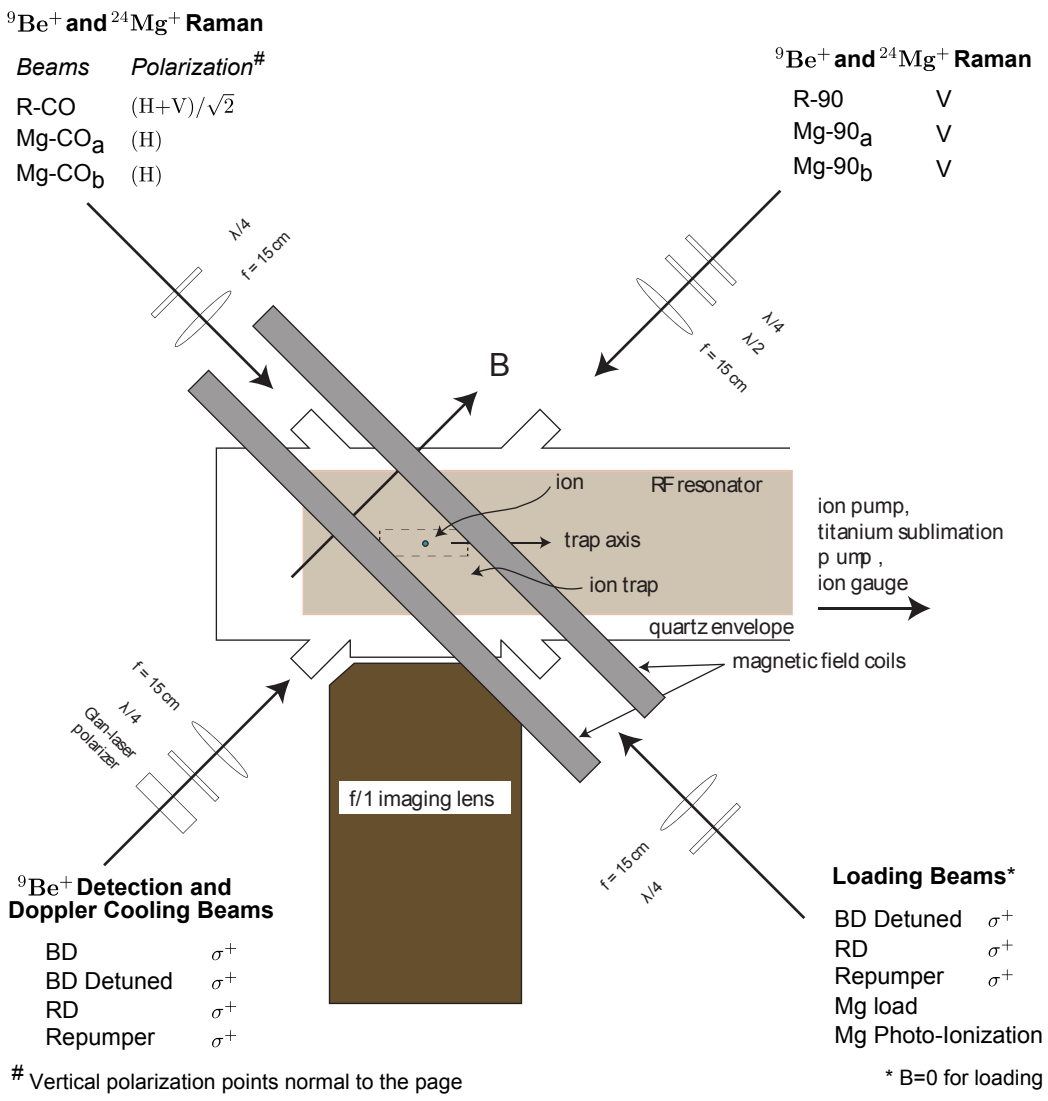

Figure 2.10: Laser beams and optics near the ion trap. The $^9Be^+$ and $^{24}Mg^+$ Raman beams are listed in the top portion of the figure. There are two $^{24}Mg^+$ Raman beams for each of the experiment regions A (Mg-CO$_a$ and Mg-90$_a$) and B (Mg-CO$_b$ and Mg-90$_b$) see figure (2.5). The $^9Be^+$ Raman beams (R-CO and R-90) can be directed to either regions A or B, using acousto-optic modulators (see section (2.7.0.1)). The $^9Be^+$ detection and Doppler cooling beams are only directed to experiment region A. The loading beams are only applied to the loading region. This figure is modified from a figure appearing in [Langer 06].

2.5 Magnetic-Field Coils

The ion trap is placed inside a Helmholtz coil. This created an approximately a uniform magnetic field oriented at 45 degrees to the trap axis that provides the quantization axis for the ions' internal states. The experiments discussed here used a magnetic field of $\sim$ 120 Gauss. This value of the field was chosen, since it provides a magnetic field-independent transition in $^9Be^+$ [Langer 05] (see chapter (3)). The two coils that make up the Helmholtz pair are each made from nine turns of 1/8 inch outer diameter hollow copper tubing. Each coil has a radius of 3.75 inches and they are placed symmetrically around the center of the trap one inch apart see figure (2.10). The copper tubing is hollow to allow for water-cooling of the coils. Approximately 100 A at 5.5 V applied to the coils.

2.6 Imaging System

Part of the imaging system is depicted schematically in figure (2.10). The imaging system collects the ions‘ fluorescence from trapping region A (see figure (2.5)) and can either image it onto a ultra-violet (UV) sensitive charge coupled device (CCD) camera or on to a photo multiplier tube (PMT). The CCD camera is used when loading the ions into the ion trap, and the PMT is used for photon counting. Looking at the number of photons collected in a 200 μs detection time distinguishes the qubit states from each other (see chapter (3)). In a 200 μs detection period about 10 photons are collected from a single $^9Be^+$ ion with a background of $\sim$ 0.1 photons. The main component of the imaging system is a $\sim$ f/1 lens. This lens is placed $\sim$ 40 mm from the ion trap, outside of the vacuum system. The lens forms an image with a magnification of x5 at an image plane. A pinhole with a diameter between 600 μm and 800 μm is placed at this first image plane to filter out stray light. A UV microscope objective is used as a second stage lens to provide an additional magnification of $\sim$ 25 for a total magnification

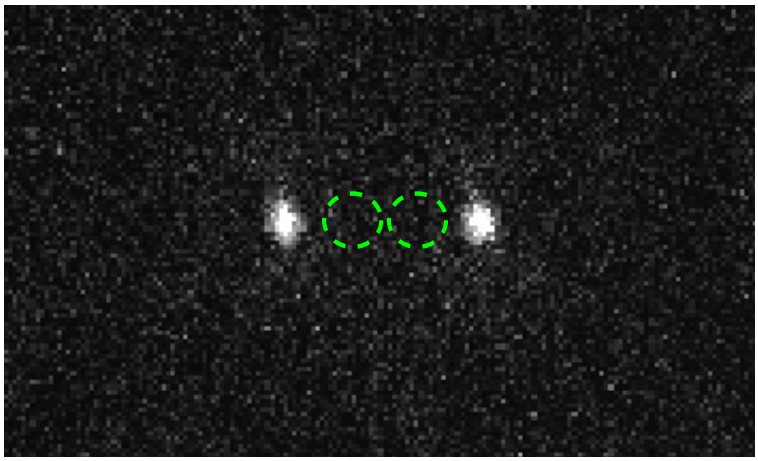

Figure 2.11: Image of $^{9}Be^{+} - {}^{24}Mg^{+} - {}^{24}Mg^{+} - {}^{9}Be^{+}$ chain of ions taken with a UV sensitive charge-coupled device camera. The two outer ions in the image are the $^{9}Be^{+}$ ions, and the imaging system and laser beams are configured to view only the $^{9}Be^{+}$ ions. Two $^{24}Mg^{+}$ ions are also present but not visible and have been drawn in the figure. The distance between the $^{9}Be^{+}$ ions is ~ 10 μm.

of ~ 125. This is enough to distinguish two $^{9}Be^{+}$ ions that are about 4 μm apart on the UV CCD camera. Figure (2.11) shows an image from the UV CCD camera of a $^{9}Be^{+} - {}^{24}Mg^{+} - {}^{24}Mg^{+} - {}^{9}Be^{+}$ chain of ions. Only the $^{9}Be^{+}$ ions (outer most ions) fluoresce. The two $^{24}Mg^{+}$ ions have been drawn into the figure. The spacing between the two $^{9}Be^{+}$ ions is ~ 10 μm. The image can be either directed to the UV CCD camera or the PMT with the use of a mechanical flipper mirror.

2.7 Laser Sources

The internal electronic states of trapped ions can be manipulated using electric-dipole transitions. Typical these transitions are made between the ground and first excited electronic states. For the $^{9}Be^{+}$ and $^{24}Mg^{+}$ ions used in the experiments discussed in this dissertation this corresponded to making a transition between the S and P internal levels. To excite these transitions requires a photon with and energy of ~ 4 eV, which

Dye-Lasers	$\sim$ Visible Color (nm)	$\sim$ Visible Power (mW)
$^{9}Be^{+}$ Raman Laser	626.340	770
$^{9}Be^{+}$ Red Doppler (RD) Laser	626.393	540
$^{9}Be^{+}$ Blue Doppler (BD) Laser	626.264	605
$^{24}Mg^{+}$ Laser	560.710	400
$^{24}Mg^{+}$ Photo-ionization Laser	570.591	200

Table 2.1: Table of the visible laser systems. There are five frequency doubled dye-laser systems, four of which are which are used in the QIP experiments. The fifth, which is the $^{24}Mg^{+}$ photo-ionization laser is only used when loading the ions. This table shows the visible wavelengths used, and table (2.2) shows the UV wavelengths after doubling

Dye-Lasers	$\sim$ UV color (nm)	$\sim$ UV power (mW)
$^{9}Be^{+}$ Raman Laser	313.17	100
$^{9}Be^{+}$ Red Doppler (RD) Laser	313.2	20
$^{9}Be^{+}$ Blue Doppler (BD) Laser	313.13	30
$^{24}Mg^{+}$ Laser	280.355	14
$^{24}Mg^{+}$ Photo-ionization Laser	285.3	4

Table 2.2: Table of the UV laser systems. There are five frequency doubled dye-laser systems, four of which are which are used in the QIP experiments. The fifth, which is the $^{24}Mg^{+}$ photo-ionization laser is only used when loading the ions. This table shows the UV wavelengths used, and table (2.1) shows the visible wavelengths before doubling.

corresponds to a wavelength in the UV. The transition can be made in $^{9}Be^{+}$ with a $\sim$ 313 nm photon and in $^{24}Mg^{+}$ with a $\sim$ 280 nm photon. To drive all the necessary transitions in $^{9}Be^{+}$ requires three different wavelengths (see tables (2.1) and (2.2)). One transition is from $^{2}S_{\frac{1}{2}}$ level to the $^{2}P_{\frac{1}{2}}$ level and the transition occurs at wavelength of a 313.2 nm (The laser system used for this transition is referred to as Red Doppler (RD). see chapter (3)). Another laser system is resonant with the $^{2}S_{\frac{1}{2}}$ to $^{2}P_{\frac{3}{2}}$ transition, and the transition occurs at a wavelength of 313.13 nm (The laser system used for this transition is referred to as Blue Doppler (BD). see chapter (3)). A third laser at a wavelength of 313.17 nm is $\sim$ 80 GHz blue detuned from the $^{2}S_{\frac{1}{2}}$ to $^{2}P_{\frac{1}{2}}$ transition (This laser system is referred to as the Raman laser. see chapter (3)). To excite transitions in $^{24}Mg^{+}$, one laser system at a wavelength of 280.355 nm was used. It was $\sim$ 9.2 GHz red detuned from the $^{2}S_{\frac{1}{2}}$ to $^{2}P_{\frac{1}{2}}$ transition (see chapters (4), (5), and (6)). A fifth laser system was used

in photo-ionizing ^{24}Mg to create $^{24}Mg^{+}$ [Epstein 07, Seidelin 06, Madsen 00], which uses a ~ 285.3 nm photon to excite the transition $3s^2\,{}^1S_0 \rightarrow 3s3p\,{}^1P_1$ in ^{24}Mg [Madsen 00]. Tables (2.1) and (2.2) shows a list of the different lasers used, their wavelength in the visible and UV and the optical powers in the visible and UV.

To date there are no commercially available laser sources in the UV with sufficient optical powers to meet the experimental requirements. All five laser systems were custom built. The laser systems used consist of a visible continuous-wave (CW) dye laser that is frequency doubled [Boyd 68] using a resonant second harmonic generation cavity [Steinbach 96] to create a UV source.

The CW dye lasers used are a 4-mirror unidirectional ring laser [Hollberg 90], which were designed by Jim Bergquist. There are four mirrors used to create the ring cavity (sometimes called a bow-tie cavity). The pump sources for all of the dye laser were Coherent Verdi lasers, which are doubled Nd:Yag lasers emitting 532 nm light. The pump powers used ranged from 3W - 6W.

Different types of dye were used for the $^{9}Be^{+}$ and $^{24}Mg^{+}$ dye lasers. The $^{9}Be^{+}$ lasers used Kiton Red dye made by Exciton. The dye was dissolved into ethylene glycol at a concentration of $\sim$ 1g of dye per 1 L of ethylene glycol. The $^{24}Mg^{+}$ lasers used 200 mg of Rhodamine 575 dye dissolved in 50 mL of Benzyl Alcohol, which is then mixed with 350 mL of ethylene glycol. For all the laser systems, a thin stream of dye is created by forcing dye under pressure through a thin nozzle. The dye is then caught and recirculated. The dye stream is at Brewster's angle with respect to the lasing direction.

Each of the dye lasers has several inter cavity elements. There is an optical diode to make the laser lase in only one direction. Three frequency selective elements in the cavity narrow the lasers linewidth: a birefringent filter, a thin etalon, and a thick etalon (consists of two etalons). The laser frequency was set by aligning the transmission maxima of all of the filters. This allows for tuning the laser in steps of < 0.005 nm.

The spacing between the two etalons that make up the thick etalon can be varied

with a piezo-electric transducer (PZT) to track the center frequency of the laser. This is accomplished by modulating the PZT. The signal can be demodulated with a lock-in-amplifier to create a dispersive error signal with a zero crossing that corresponds to maximum in transmission for that particular etalon mode. This signal can be used in a servo loop. To stabilize the frequency of the lasers one of the cavity mirrors is mounted on a PZT. Changing the voltage applied to the PZT shifts the frequency of the laser. This PZT serves as the transducer in a servo loop. The feedback for this servo loop is derived from a external Fabry-Perot cavity. For the $^9Be^+$ lasers the cavity is made from a 10 cm long INVAR support with two mirrors (a 10 cm radius of curvature and reflectivity of 95% at 626 nm) mounted on the ends. The $^{24}Mg^+$ lasers use a similar external cavity. A Hansch-Couillaud lock [Hansch 80] is used to create the error signal for the feedback to the PZT.

All of the lasers use an absolute frequency reference except for the $^9Be^+$ Raman laser. This laser is $\sim$ 80 GHz detuned from the $^2P_{\frac{1}{2}}$ transition, so small deviations in the frequency of the laser have a negligible effect on their function. The other lasers use Doppler-free saturated absorption spectroscopy of $^{127}I_2$, which is referred to as an Iodine lock, to reference the lasers to a transition in $^{127}I_2$ (The $^{24}Mg^+$ lasers used both $^{127}I_2$ and $^{129}I_2$.). The fast frequency noise of the laser is servoed using the Hansch-Couillaud lock to the external reference cavity, and slow frequency drifts are removed with the Iodine lock. One of the cavity mirrors in the reference cavity is mounted on a PZT, which allows the cavity length to be changed. The servo signal from the Iodine lock is feedback to this PZT. This changes the resonant frequency of external cavity, which in turn affects the error signal of the Hansch-Couillaud lock. This causes the error signal sent to the PZT inside the laser cavity to track this change, and thus changes the laser's frequency. The laser's frequency can be changed relative to the transitions in iodine, using AOMs. The laser's linewidth is typically less than $\sim$ 500 KHz.

To produce the required UV laser light, the visible light is frequency doubled

[Boyd 68] inside a second harmonic generation cavity [Steinbach 96]. The cavity is a 4-mirror ring cavity (bow-tie cavity), allowing for the resonant build up of the visible light. One of the mirrors used is partially transmissive to the visible light, which allows the visible light to couple into the cavity. The second harmonic generation is done in a non-linear β-barium borate (BBO) crystal [Boyd 68]. The UV light produced in the BBO crystal passes out of the cavity through one of the cavity mirrors. This mirror has a special anti-reflection coating that is highly reflective in the visible and allows the UV light to be transmitted. The cavity is stabilized using a Hansch-Couillaud lock [Hansch 80].

2.7.0.1 Beam lines

Although there are five laser systems used in the experiment, there are 14 laser beams generated from theses five laser systems. Several of these beams were generated with beam splitters, acousto-optic modulators (AOM) and an electro-optic modulator. The absolute frequency of the lasers is stabilized to resonances in $^{127}I_2$ and $^{129}I_2$; however, these resonances do not occur at the needed frequencies. Thus, AOMs and EOMs can be used to shift the laser's frequency by the appropriate amounts. This section briefly highlights the systems used to generate the necessary laser beams.

Blue Doppler

The $^9Be^+$ Blue Doppler (BD) beam line consists of three laser beams used for Doppler cooling (see chapters and (3) and (5)) and state dependent resonance fluorescence detection (see chapter (3)). The "BD beam" is approximately resonant with $|^2S_{\frac{1}{2}}, F = 2, m_F = 2\rangle \rightarrow |^2P_{\frac{3}{2}}, m_I = \frac{3}{2}, m_J = \frac{3}{2}\rangle$ transition in $^9Be^+$ (see chapter (3)). It is used for state-dependent resonance fluorescence when tuned on resonance. It can also be detuned by $-\Gamma/2$ relative to the $^9Be^+$, $^2P_{\frac{3}{2}}$ excited state of resonance for optimum two-level Doppler cooling ($\Gamma = 2\pi \times 19.4$ MHz) . The "BD detuned" beam and the "BD load" beam are derived from the same beam but have been split by a beam splitter. They

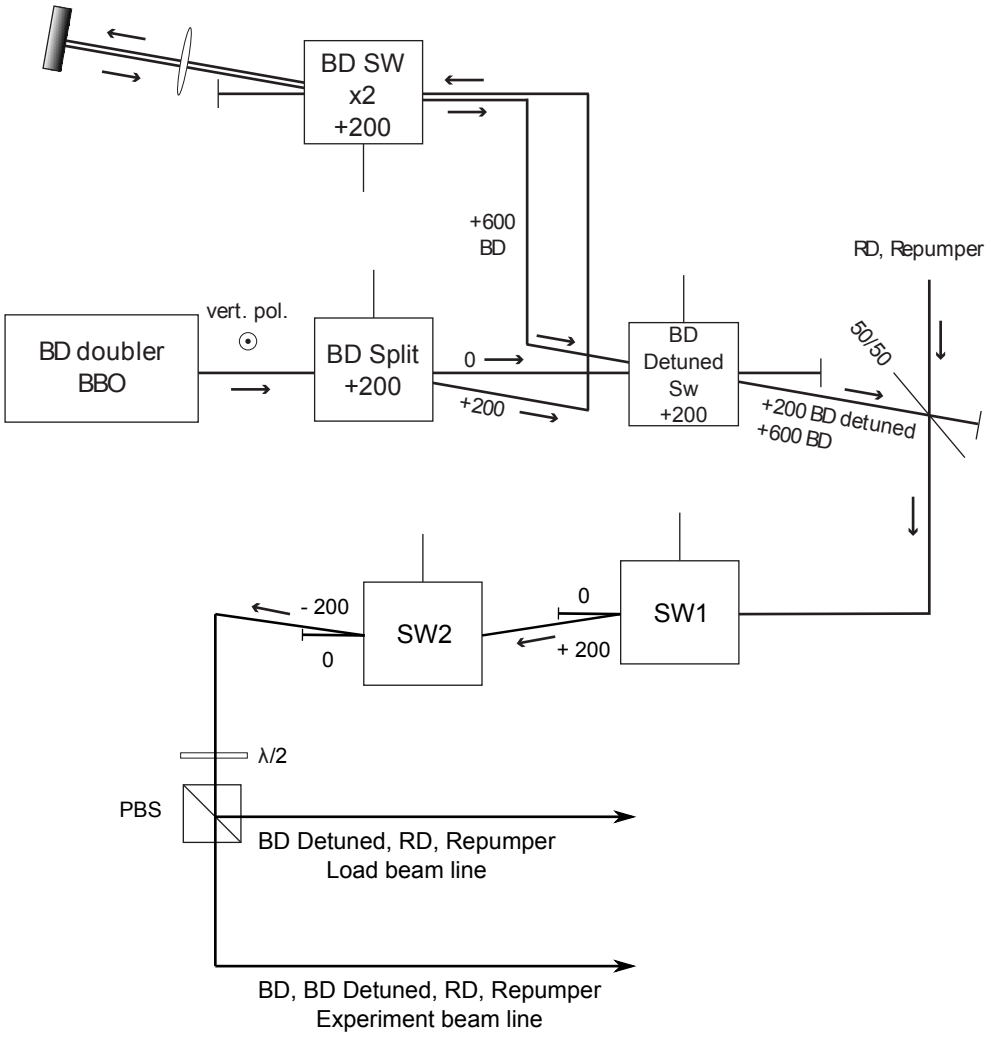

Figure 2.12: The Blue Doppler (BD) beam lines. This beam line generates the BD and the BD Detuned beam lines. Also shown is the beam splitter where the beams RD and repumper are combined with the BD and BD detuned beams. See the text for a detailed description.

are sent to different locations in the ion trap (This is done after the beams propagate through the AOMs discussed below). These beams are used for far-detuned Doppler cooling. The BD load beam is used in the loading region of the ion trap to Doppler cool

ions as they are loaded. The BD detuned beam is directed into the experiment region to perform far detuned Doppler cooling on the ions in that region. This far-detuned cooling is useful for cooling very hot ions, because the motion of the ions can Doppler shift their transitions out of resonance with the BD beam.

The BD detuned and BD load beams are $\sim$ 400 MHz lower in frequency than the (3) BD beam. This frequency difference is created with AOMs (see figure (2.12) for the labeling of the AOMs). The BD detuned beam is taken from the 0th order of the BD split AOM. It is then deflected into the +1 order of the 200 MHz BD detuned SW AOM (SW stands for switch). The BD beam is generated from the +1 diffraction order of the 200 MHZ BD split AOM. This beam is then sent through a double pass AOM (BD SW) that is tunable around a center frequency of 200 MHz. This allows the BD beam to be tuned from resonance to a detuning of $-\Gamma/2$ without shifting the beam position. This beam is combined with BD detuned beam by overlapping the beam with the +1 order of the 200 MHz BD detuned SW AOM. The combining technique works because the BD beam enters the AOM not at the Bragg diffraction angle. It is not diffracted like the BD detuned beam. The beams then pass through a 50/50 beam splitter, which allows them to be overlapped with the two Red Doppler beams discussed below.

These beams can be shut off by turning the power off to the AOMs. However, there can be some transmitted leakage light, which causes excess scattering of photons by the $^9Be^+$ ions. To help solve this problem, two additional 200 MHz AOMs were added in series after the beams have been combined. The first 200 MHz AOM (SW1) diffracts the light into the +1 order. The second 200 MHz AOM(SW2) diffracts the beams into the -1 order, resulting in no net frequency shift of the beams. The 0th orders of the beams are blocked. The beams are then sent through a beam splitter, which allows some of the BD detuned light to be picked off and sent to the loading region of the ion trap.

RD Doppler

The $^9Be^+$ red Doppler (RD) beam line consists of two beams "RD" and "repumper".

Both beams are used in state initialization of $^9Be^+$ (see chapter (3)) and for repumping during Raman-sideband cooling (see chapter (3)). The RD beam is resonant with the $|^2S_{\frac{1}{2}}, F = 1, m_F = 1\rangle \rightarrow |^2P_{\frac{1}{2}}, F = 2, m_F = 2\rangle$ transition in $^9Be^+$. The repumper beam is resonant with the $|^2S_{\frac{1}{2}}, F = 2, m_F = 1\rangle \rightarrow |^2P_{\frac{1}{2}}, F = 2, m_F = 2\rangle$ transition. There is a frequency difference between these beams of $\sim$ 1120 MHz, which is generated with AOMs (see figure (2.13)).

To generate the frequency difference between the two beams the RD beam is taken from the 0th order of the 636 MHz RD split1 AOM (see figure (2.13) for AOM labels). This beam is then diffracted into the +1 order of the 636 MHz RD split2 AOM, giving a frequency shift of +636 MHz from the output of the frequency doubling cavity. The repumper beam is taken from the -1 order of the RD split1 AOM. It is then directed through another AOM, which shifts the frequency by +152 MHz. This gives a total frequency shift from the output of the frequency doubling cavity of -484 MHz. This beam is recombined with the RD beam by sending it through RD split2 AOM at angle that does not diffract, which allows it to be overlapped with the diffracted RD beam. This generates the required 1120 MHz frequency difference between the beams.

Both beams are then sent through a 200 MHz double pass AOM (RD SW). This shifts the overall frequency of both beams by the same amount. The RD SW AOM switch helps to minimize any leakage light. The beams are then combined with the blue Doppler beam line (see section (2.7.0.1)) on a 50/50 beam splitter. As described in the previous section the beams then pass through two more AOMs that provide no net frequency change, but help reduce any leakage light. The beams are then directed to the experiment region of the ion trap.

$^9Be^+$ Raman Beams

The $^9Be^+$ Raman beam line generates the beams used for two-photon stimulated-Raman co-carrier rotations (see chapter (3)), two-photon stimulated-Raman sideband transitions (see chapter (3) and (6)), and the geometric phase gate (see chapter (7)).

There are two main types of Raman transitions, which are designated "co-carrier" and "90^o transitions". For co-carrier transitions the two beams that make up the stimulated Raman transition [Wineland 98] are co-linear with k-vectors perpendicular the quantizing magnetic field axis. These transitions implement motion independent internal state rotations [Wineland 98]. The experiments discussed in this dissertation used co-carrier stimulated-Raman transitions that obey the selection rule $\Delta F = 0$ and $\Delta m_F = \pm 1$ for the $^2S_{\frac{1}{2}}$ hyperfine ground states of $^9Be^+$ (see chapter (3) for a description of the internal states of $^9Be^+$). The other type of transitions are referred to as 90^o transitions, because the two beams have k-vectors orthogonal to each other. One beam is has a k-vector parallel to the magnetic field and the other has its k-vector perpendicular to the magnetic field. These beams are sensitive to the ions' motion along the trap axis and can be used to drive stimulated-Raman sideband transitions (see chapter (3) and (6)). They are also employed to excite a coherent state of the ions motion for use in creating a geometric phase gate (see chapter (7))

Figure (2.14) is a schematic of the $^9Be^+$ Raman beams lines. After the UV light leaves the frequency doubler it passes through a spatial filter with a 75 μm pinhole. This helps filter the spatial mode of the beam and is used as an alignment tool. Next the beam passes through a double pass AOM labeled ΔF in figure (2.14), which is not used in the experiments discussed in this dissertation. This is a ~ 600 MHz AOM that would allow $\Delta F = \pm 1$ transitions to be driven in the $^2S_{\frac{1}{2}}$ hyperfine ground states of $^9Be^+$. These transitions are used when working with the magnetic field-independent levels of $^9Be^+$ [Langer 05, Langer 06, Home 09, Hanneke 10]. This part of the beam path is common to all the Raman beams.

First, the co-carrier transitions will be discussed. All of the $\Delta F = 0$ and $\Delta m_F = \pm 1$ transitions in the $^2S_{\frac{1}{2}}$ hyperfine ground states of $^9Be^+$ have frequencies of $\sim 70 - 100$ MHz at a magnetic field of ~ 120 Gauss. Thus, the two beams used to make these two-photon stimulated-Raman transitions need to have a frequency difference equal to these

transition frequencies. To generate these frequency differences the laser beam is sent through a double pass AOM called the R-CO AOM. This AOM has a bandwidth of 160-240 MHz, and two frequencies are sent into the AOM at one time. This generates the desired frequency difference in the beams. For example to create 100 MHz frequency difference, a 175 MHz and 225 MHz signal could be sent into the AOM. Assuming the AOM is aligned so that beams are diffracted into the +1 order of the AOM, then there will be two beams exiting the AOM. One is shifted by +175 MHz and the other by +225 MHz with respect to the 0th order beam, which is blocked. These beams are retro reflected and diffracted a second time and now have the frequency shifts of +350 MHz and +450 MHz with respect to the 0th order. This gives the desired 100 MHz frequency difference. These two co-linear beams are then sent to the ion trap. There is another AOM used to steer the beams, which is discussed below.

The 90^o beams are also generated with AOMs. The difference frequency required between the two beams is also $\sim 70-100$ MHz, since the same $\Delta F = 0$ and $\Delta m_F = \pm 1$ transitions in the ${}^2S_{\frac{1}{2}}$ hyperfine ground states of ${}^9Be^+$ are being driven. To generate the required frequency difference and create the two beams necessary, two AOMs are used, which are labeled R-CO and R-90. The first beam is generated from the R-CO AOM; however, only one frequency (+175 MHz) is applied to the AOM. This AOM is used in a double pass configuration, giving a net frequency shift of +350 MHz to this beam. It is then sent to the ion trap in a direction perpendicular to the magnetic field. The second beam is derived from taking the 0th order of the R-CO AOM and directing it to the R-90 AOM. This AOM is used in a double pass configuration with a frequency of ~ 225 MHz. This results in a total frequency shift of the second beam of ~ 450 MHz, giving a net frequency difference between the beams of ~ 100 MHz. The R-90 AOM also has a bandwidth of $\sim 160-240$ MHz, which allows the frequency difference between the two beams to be tuned. The second beam is then sent to the ion trap in direction such that its k-vector is parallel to the quantizing magnetic field.

In order to conserve laser resources, it is advantageous to use the same Raman laser beams to address ions in different locations of the ion trap (The waist of the Raman beams is $\sim 30\mu$m at the position of the ions, which is smaller than the distance between the different trapping regions). The laser beams can be distributed to the different trapping regions using the two AOMs labeled DEFL-CO and DEFL-90 (These AOMs have a bandwidth of $\sim 160 - 240$ MHz.) in figure (2.14). The AOMs are used in a single pass configuration, and thus when the frequency of the AOM drive changes the angle of the diffracted beam changes. This allows the beams to be quickly steered to different locations, in a time limited by the time it takes the acoustic wave to travel across the beam. For a for 5mm diameter beam this takes ~ 1 μs, which is relatively short compared to the time scale of the experiments (~ 10 ms) discussed in this work. A problem can arise when scanning the frequencies of the DEFL-CO and DEFL-90 AOMs. If the frequencies are not shifted by the same amount to move the beams in the ion trap, then this changes the difference frequency between the beams. This can be compensated for by changing the frequency applied to the R-90 AOM.

$^{24}Mg^{+}$ Beam line

The $^{24}Mg^{+}$ beam line has several different beams all derived from one source: the $^{24}Mg^{+}$ stimulated-Raman beams (see chapter (6)), the $^{24}Mg^{+}$ Doppler cooling beams (see chapter (5)), and the $^{24}Mg^{+}$ repump beam (see chapter (6)). The UV output of the $^{24}Mg^{+}$ frequency doubler is ~ -9.2 GHz detuned from the $^{2}S_{\frac{1}{2}}$ to $^{2}P_{\frac{1}{2}}$ transition in $^{24}Mg^{+}$ (see chapter (4)). This is used as the detuning of the $^{24}Mg^{+}$ stimulated-Raman beams from resonance. The electro-optic modulator (EOM) before the doubler is used to shift the frequency of the $^{24}Mg^{+}$ Doppler cooling and repump beams and is discussed below. All of the beams discussed in this section first pass through a single pass 200 MHz AOM (The AOM is called Mg SW, and the beam is diffracted into the +1 order) at the output of the frequency doubler. This is used as an optical switch that helps minimize any leakage light reaching the ion trap when the laser beams are ideally switched off.

For the $^{24}Mg^{+}$ ions, no co-carrier stimulated-Raman transitions are used as in $^{9}Be^{+}$. Only 90^{o} stimulated-Raman transitions are utilized, and these beams are used for stimulated-Raman sideband cooling (see chapter (6)). The frequency difference between the two beams needs to be $\sim$ 334 MHz, because this is the splitting between the $|^{2}S_{\frac{1}{2}}, m_J = \frac{-1}{2}\rangle$ and $|^{2}S_{\frac{1}{2}}, m_J = \frac{1}{2}\rangle$ levels. The two beams used for the transitions will be referred to as Mg-CO and Mg-90, where at the ion trap Mg-CO has a k-vector perpendicular to the quantizing magnetic field and Mg-90 has a k-vector parallel to the quantizing magnetic field. The Mg-90 beam is generated from the -1 order of an 80 MHz AOM labeled Mg Split in the figure (2.15). This beam is then directed toward the ion trap. The Mg-CO beam is derived from the 0th order of the Mg Split AOM. This beam is then sent through the -1 order of the double pass Mg DBL AOM, which is driven at a frequency of $\sim$ 207 MHz (This AOM has a bandwidth of 160-240 MHz.). This gives the beam a frequency shift of -414 MHz relative to the frequency of the laser at the input of the MG Split AOM. This beam is then directed toward the ion trap. The net frequency difference between the beams is then the desired 334 MHz.

To implement stimulated-Raman sideband cooling requires the use of the $^{24}Mg^{+}$ Raman beams described above is required. However, a $^{24}Mg^{+}$ repumping beam is also required (see chapter (6)). The $^{24}Mg^{+}$ repumping beam used in this experiment is resonant with $|^{2}S_{\frac{1}{2}}, m_J = \frac{-1}{2}\rangle \rightarrow |^{2}P_{\frac{1}{2}}, m_J = \frac{1}{2}\rangle$ transition. The $^{24}Mg^{+}$ laser is nominally detuned from this transition by ~ -9.2 GHz. To shift the frequency of the UV output, a visible 9.2 GHz EOM is placed in front of the frequency doubling cavity. When a 9.2 GHz RF signal is applied to the EOM this creates 9.2 GHz sidebands on the visible laser light. The frequency doubling cavity is a resonant cavity, and any light not resonant will be reflected. The cavity for the $^{24}Mg^{+}$ frequency doubling was designed to have a free-spectral range with a multiple of 9.2 GHz. This allows both the carrier and the sidebands to be resonant in the cavity. The UV output then consists of the carrier frequency with 9.2 GHz sidebands. The positive frequency sideband is used to create

the light resonant with the $|^2S_{\frac{1}{2}}, m_J = \frac{-1}{2}\rangle \rightarrow |^2P_{\frac{1}{2}}, m_J = \frac{1}{2}\rangle$ transition. The beam used to do is the same as the Mg-90 described above. The -9.2 GHz off resonant light is still present but does not scatter a significant number of photons in the time it takes to repump the transition (a few μs).

The beams used for $^{24}Mg^+$ Doppler cooling are derived from the same beam as those for the $^{24}Mg^+$ stimulated-Raman transitions, but with the EOM turned on. The frequency of the Mg-Co beam can be changed to suppress any Raman transitions. The Mg-CO and Mg-90 beams are both split with a beam splitter and sent to the two different trapping locations A and B (see figure (2.5)). These beams are labeled Mg-CO_a, Mg-CO_b, Mg-90_a, and Mg-90_b. An additional laser beam is derived from the Mg-90 beam, using a beam splitter. This beam is directed to the loading region and can be used for Doppler cooling of $^{24}Mg^+$ at zero magnetic field (The 120 Gauss magnetic field is turned off for loading) see reference [Seidelin 06]. For loading the $^{24}Mg^+$ ions, the $^{24}Mg^+$ laser could be tuned near resonance with the $^2S_{\frac{1}{2}}$ to $^2P_{\frac{1}{2}}$ transition. However, it was found to be easier to not Doppler cool the $^{24}Mg^+$ ions in the loading region after being photo-ionized, which meant the magnetic field could be left on. Because the $^9Be^+$ ions were always loaded first, the uncooled $^{24}Mg^+$ ions in the loading region could be transferred to the experiment region and be sympathetically cooled by the $^9Be^+$ions.

2.8 Controlling the Experiment

The computer control used in the experiments described in this dissertation was discussed in depth in the thesis by Chris Langer [Langer 06]; therefore, only the relevant features will be highlighted here. All of the experiments described in this thesis have similar features. A given experiment consists of many laser pulses at different frequencies (sometimes moving the ions in between pulses) followed by the collection of fluorescence from $^9Be^+$ ions. Thus, basic function of the controller is to set the frequencies of the laser pulses, turn on and off the laser pulses, move the ions, and collect fluorescence. For

example a single iteration of the entangled mechanical oscillators experiment (discussed in chapter (8)) lasted $\sim$ 14 ms and $\sim$ 600 laser pulses were applied to the ions. This would be difficult using just a desktop computer.

The experiment is controlled by a field programmable gate array (FPGA)[1] . This is a chip that can be thought of as a reconfigurable digital logic device. The chip can be configured to include memory, registers, buffer drivers, counters and other functions. These can be programed using a hardware description language. For the experiments here the FPGA can be programmed to set the frequency output of direct digital synthesizers (these control the AOMs frequencies), toggle TTL's, and store data in memory.

To run an experiment, the desired pulse sequence is written in a custom text based language, which can be interpreted by a control computer. The computer then downloads the pulse sequence to the FPGA. The FPGA runs the pulse sequence and records the data into its memory. The control computer can then read the data from the FPGA at a much slower rate than the experiments are run. The control computer can also perform additional processing of the data that is needed without affecting any ongoing experiments. The FPGA is also used to control the DC voltages sources, which enable the ions to be moved during the experiment. A sequence of voltages can be stored in the on board memory of an analog output card (NI PCI 6733 with 1MS/s). The FPGA can issue a series of TTL pulses at the appropriate time that tell the analog output card to step through the voltages stored in its memory.

[1] The FPGA card used was the Xlinx Xtreme DSP kit with a Virtex IV chip.

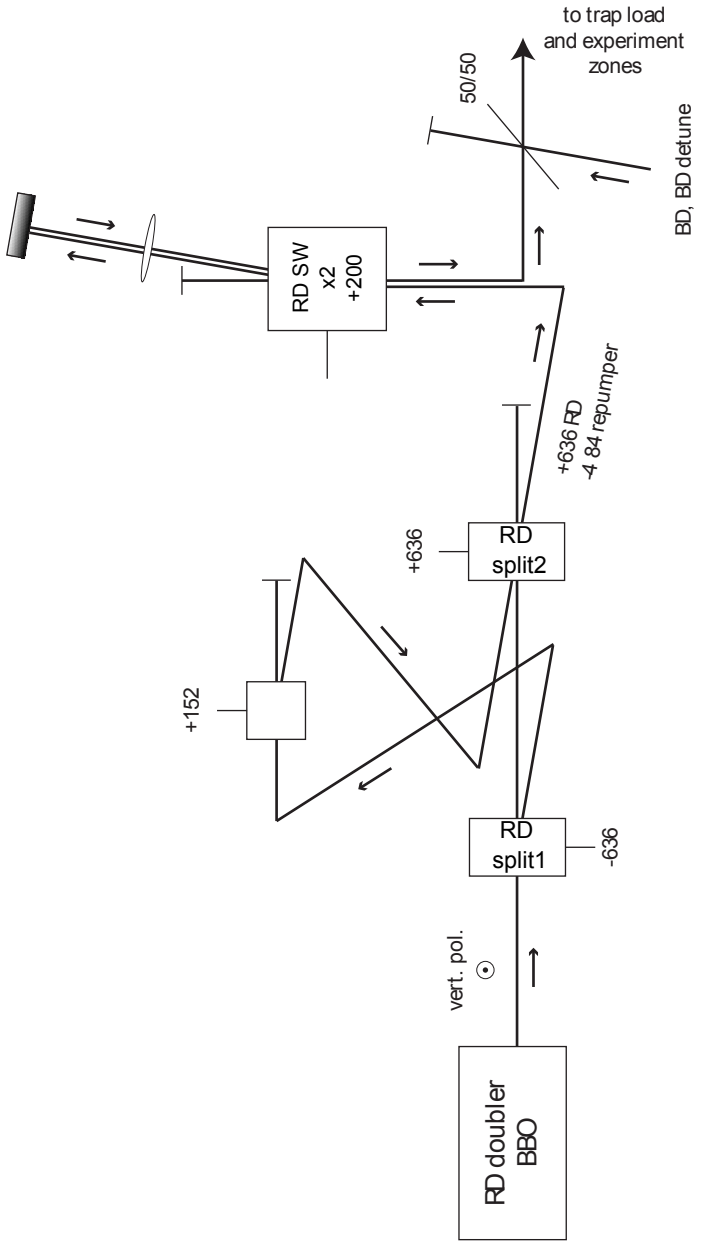

Figure 2.13: The Red Doppler (RD) beam lines. The AOMs in this beam line generate the RD and the repumper beam lines. See the text for a detailed description.

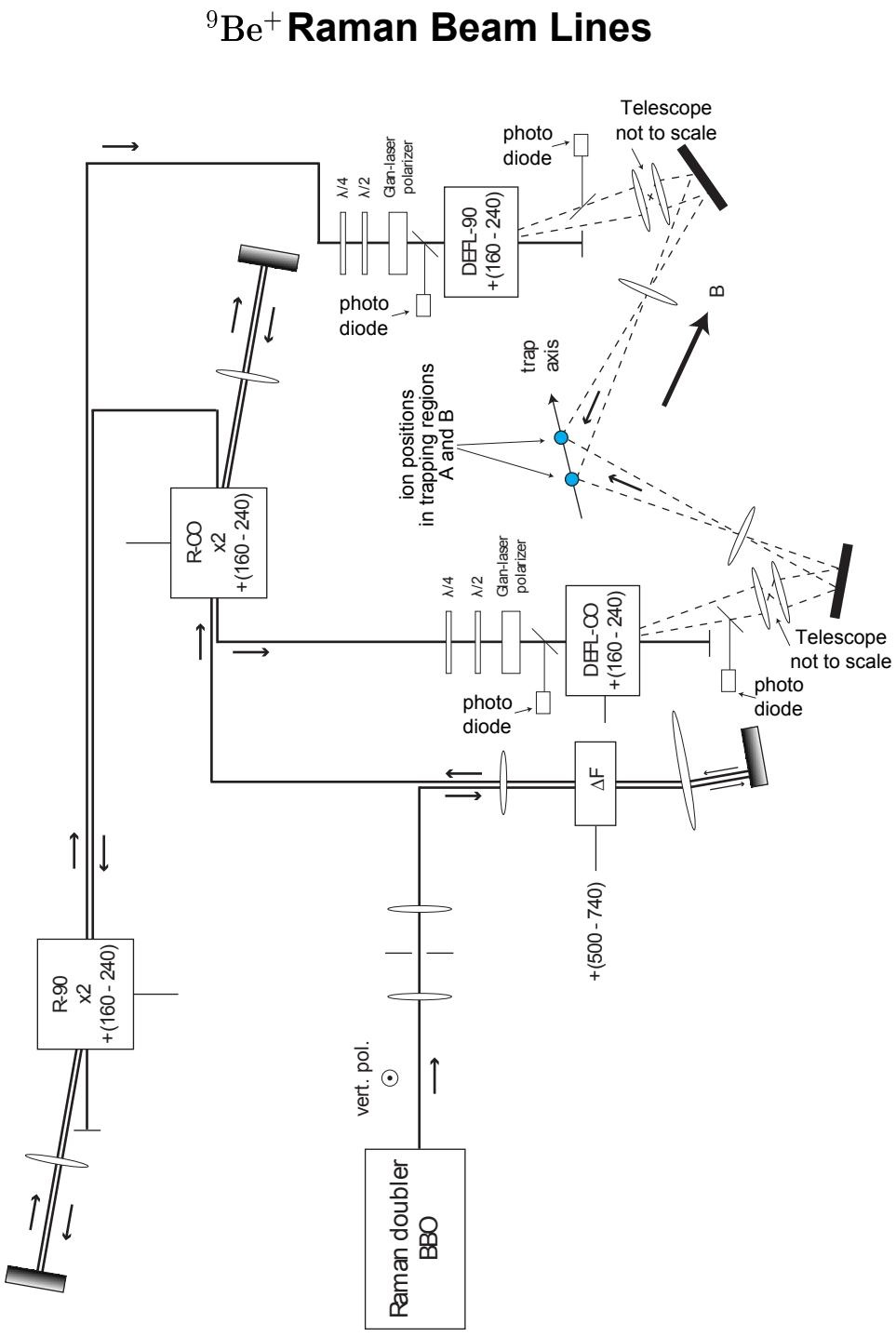

Figure 2.14: The ^{9}Be$^+$ Raman beam lines. This beam line generates the R-CO and R-90 beam lines. See the text for a detailed description. This figure is modified from a figure appearing in [Langer 06].

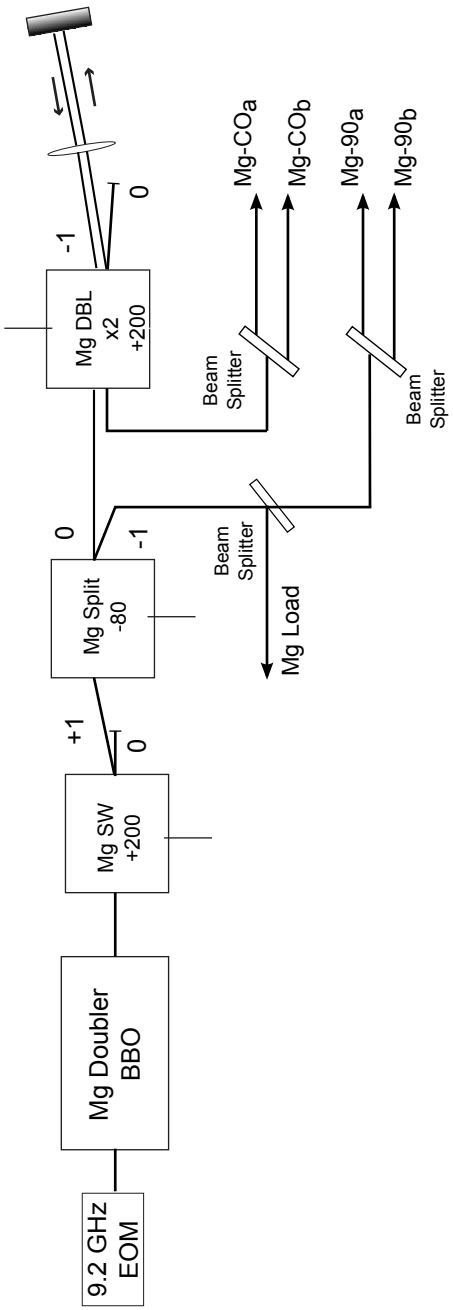

Figure 2.15: The $^{24}Mg^{+}$ beam lines. This beam line generates the Mg-CO, Mg-90, and Mg Load beam lines. The Mg-CO and Mg-90 are split into two beams each and sent to trapping regions A and B. These beams are labeled Mg-CO$_a$, Mg-CO$_b$, Mg-90$_a$, and Mg-90$_b$. See the text for a detailed description.

Chapter 3

$^9Be^+$ Qubit

The entangled mechanical oscillators experiment [Jost 09] discussed in chapter (8) uses two types of ions: a sympathetic cooling ion $^{24}Mg^+$ (see chapter (4)) and a logical ion $^9Be^+$ (also referred to as a qubit (two-level quantum system)). The logical ion serves as an information carrier. In the entangled mechanical oscillator experiment, this enables the distribution of entanglement (of internal states of the two logical ions) to different parts of an ion trap array. Using sympathetic cooling ions and logical ions, together for experiments is not unique to the work discussed here, but is considered important for scaling up quantum information processing (QIP) using trapped ions [Kielpinski 00, Kielpinski 02b, Blinov 02, Rohde 01, Barrett 03, Häffner 08, DiVincenzo 01]

On the surface, the entangled mechanical oscillators experiment might not appear to have much to do with QIP. However, several of the techniques demonstrated in this experiment are important for QIP, and have enabled several subsequent QIP experiments [Home 09, Hanneke 10]. Thus, the $^9Be^+$ ion will be discussed in terms of its advantageous properties for QIP, and these advantages also apply to the entangled mechanical oscillator experiment.

There are several choices that could serve as logical ions [Ozeri 07], and it is still unclear what the best ion is for QIP. The $^9Be^+$ ion has several desirable properties [Ozeri 07] and meets many of the requirements of the DiVincenzo criteria [DiVincenzo 01] (Although not absolute, these are the widely accepted criteria that must be full filled for

scalable QIP). The $^9Be^+$ ion is "1.) A scalable physical system with well characterized qubits.[DiVincenzo 01]". The internal levels are discussed more in section (3.1). The internal levels should have "3.) Long relevant decoherence times, much longer than the gate operation time [DiVincenzo 01].". In $^9Be^+$ the hyperfine ground states are used, which have very long lifetimes [Wineland 98], and internal states can be chosen that are insensitive to magnetic field noise [Langer 05, Langer 06] (Magnetic field noise is a common source of decoherence in trapped ions). This is discussed briefly in section (3.2), but a detailed description is the subject of the thesis by Langer [Langer 05, Langer 06]. Through the use of optical pumping techniques, which is covered in section (3.3), the $^9Be^+$ ion meets the criteria of "2.) The ability to initialize the state of the qubits to a simple fiducial state [DiVincenzo 01]." There exist techniques to accurately determine the spin state of $^9Be^+$ through state dependent resonance fluorescence, which also meets the DiVincenzo criteria of "5.) A qubit-specific measurement capability [DiVincenzo 01]."

3.1 Energy Level Structure

There are many possible choices of ions to use for QIP. One of the main factors in choosing a particular atomic species to work with is the simplicity of the internal level structure. The internal level structure is usually considered “simple” if the internal levels have resonances with energies that are compatible with current laser technologies. Another factor is how hard is it to prepare the states used to form the qubit. If it takes numerous lasers to optically pump to the desired internal level, then although technically possible it is not practically feasible for most experiments. There are several elements scattered throughout the periodic table (see reference [Ozeri 07] for a more complete list) that make good candidates for QIP. Several of the atomic species used for ion trap quantum information processing are alkaline-earth elements. These are common choices since the neutral atoms have two valence electrons. When ionized they have a similar level structure to the alkali neutral elements, which are commonly used in

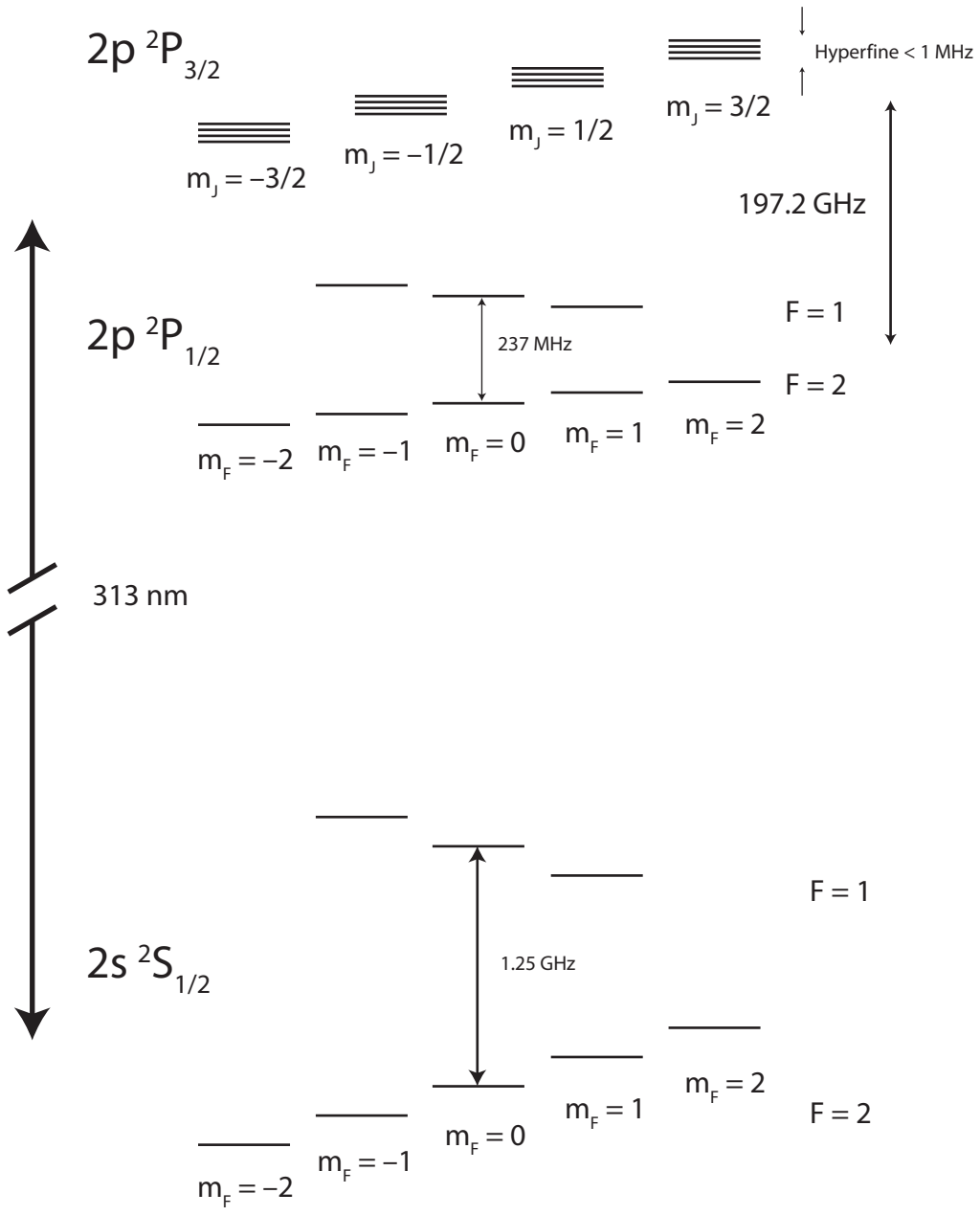

Figure 3.1: Level structure for $^9Be^+$. This figure is reproduced from reference [Langer 06]. The ground and excited states are coupled via an electric dipole transition with a wavelength of approximately 313 nm. The ground $^2S_{\frac{1}{2}}$ state has two hyperfine states $F = 2$ and $F = 1$ with magnetic sub-levels labeled with m_F. Note that the F labeling of the states is only valid at low magnetic field. The excited state $^2P_{\frac{1}{2}}$ also has two hyperfine states $F = 2$ and $F = 1$ with magnetic sub-levels labeled with m_F. The $^2P_{\frac{3}{2}}$ excited state also has hyperfine levels. but their splitting is < 1MHz [Poulsen 75]. Since the splitting is small the states are labeled with their m_J quantum numbers where $J = 3/2$. For each m_J there will be four m_I levels, since $I = 3/2$ ($m_I = -I, -I+1, ..., I-1, I$).

neutral atom trapping experiments. In addition, these ions can have ground to excited state transitions that are excited with photons from the visible spectrum. Although most of the transition wavelengths are in the UV, they are still accessible with current laser technology.

Both of the ions species used in the experiments discussed in this dissertation are alkaline-earth elements. Beryllium is used as a logical ion and Magnesium is used as a sympathetic cooling ion (see chapter (4) for more details on Magnesium). Beryllium is the lightest of the alkaline earth elements with a mass of ∼9 atomic mass units. The only isotope that is stable is ^{9}Be with nuclear spin I=3/2. There is a rare ^{10}Be isotope with nuclear spin I =0 that has a half-life of approximately 1 million years. The neutral ^{9}Be is ionized using electron impact ionization to create the ion $^9Be^+$. Figure (3.1) shows the relevant internal level structure for $^9Be^+$. The electron configuration is $1s^2 2s^1$; therefore there is one electron in the level labeled by the principle quantum number $n = 2$. There are three relevant internal states for the work here; using the Russell-Sanders notation $n^{2S+1}L_j$ [Metcalf 99], these levels are the $2^2S_{\frac{1}{2}}$, $2^2P_{\frac{1}{2}}$, and $2^2P_{\frac{3}{2}}$. The 2 in front of the states corresponds to the principal quantum number n and will be dropped in the remaining discussion. The ground state is the $^2S_{\frac{1}{2}}$ state, and $^2P_{\frac{1}{2}}$ and $^2P_{\frac{3}{2}}$ are the first excited states. The excited state linewidth is $\Gamma = 2\pi \times 19.4$ MHz. The main energy splitting of the $^2S_{\frac{1}{2}}$ state from the $^2P_{\frac{1}{2}}$ and $^2P_{\frac{3}{2}}$ states is a result of accounting for the quantum defect in the the energy level calculations [Foot 05]. The $^2S_{\frac{1}{2}}$ levels are coupled to the $^2P_{\frac{1}{2}}$ and $^2P_{\frac{3}{2}}$ levels via an electric dipole transition of wavelength of $\sim$ 313 nm. The electron's orbital angular momentum L couples to its spin, which is known as the fine structure interaction [Foot 05]. The fine structure shifts the levels $^2S_{\frac{1}{2}}$, $^2P_{\frac{1}{2}}$, and $^2P_{\frac{3}{2}}$, and is the main the source of the splitting of the $^2P_{\frac{1}{2}}$, and $^2P_{\frac{3}{2}}$ levels, which has been measured to be 197 GHz [Bollinger 85].

One of the reasons for choosing $^9Be^+$ over the isotope $^{10}Be^+$ is that $^9Be^+$ has a non-zero nuclear spin of I = 3/2. This has the important implication that $^2S_{\frac{1}{2}}$, $^2P_{\frac{1}{2}}$,

and $^2P_{\frac{3}{2}}$ levels have hyperfine structure (see section (3.2) for more details and reference [Langer 06] for even more details). Hyperfine ground states can make good qubits (see below). The hyperfine interaction comes about from the coupling of the nuclear spin I to the angular momentum J ($J = L + S$). The hyperfine states are characterized by the total angular momentum F ($F = I + J$). At low magnetic fields F and m_F are good quantum numbers and are used to label the states. For convenience these states will be used to label the energy levels when discussing the internal states at intermediate magnetic fields, where the only good quantum number is m_F. For the $^2S_{\frac{1}{2}}$ state there are two hyperfine levels $F = 2$ and $F = 1$ with a splitting of 1.25 GHz [Wineland 83], where the $F = 2$ state is the lower energy state (In Beryllium the g-factor g_F has the opposite sign from that seen in most neutral alkalies, because the g-factor g_I is negative. As a result the $F = 2$ ($g_F \simeq -\frac{1}{2}$) manifold has lower energy than the $F = 1$ ($g_F \simeq \frac{1}{2}$) manifold.). In the $^2P_{\frac{1}{2}}$ state there are also two hyperfine levels $F = 2$ and $F = 1$ with a splitting of 237 MHz [Bollinger 85]. The $^2P_{\frac{3}{2}}$ state also has hyperfine structure, but the splitting between the levels is small < 1 MHz [Poulsen 75]. In figure (3.1) the states in this manifold are labeled with their m_J quantum numbers where $J = 3/2$. For each m_J there will be four m_I levels since $I = 3/2$ ($m_I = -I, -I+1, ...I-1, I$). Again this labeling is only correct at low values of the magnetic field. Figure (3.1) also shows the magnetic sub-levels for each of the hyperfine states. These will be split by the Zeeman effect, which is discussed in the next section.

It can be seen now how $^9Be^+$ meets the DiVincenzo criteria of "1.) A scalable physical system with well characterized qubits.[DiVincenzo 01]". Many possible states can be distinguished and used as a qubit. It will be discussed in the next section how some of these levels make a better choice than others for forming a qubit.

3.2 Hyperfine and Zeeman Interactions

As mentioned in the previous section $^9Be^+$ has a nuclear spin of $I = \frac{3}{2}$, and this couples to the angular momentum J to via the hyperfine interaction

$$H = hA\vec{I} \cdot \vec{J}. \tag{3.1}$$

The hyperfine constant is represented by A for $^9Be^+$ it has a value of ~ -625 MHz [Langer 06], h is Planck's constant. At low magnetic fields the good quantum numbers are the total angular moment $\vec{F} = \vec{I} + \vec{J}$ and its projection m_F on the quantization axis. This is why the states are labeled with $|F, m_F\rangle$. For low magnetic fields the shift in the energies of the magnetic sub-levels is $E = -g_F \mu_B m_F B$ [Foot 05]. The Bohr-magneton is represented by μ_B, and B represents the value of the magnetic field. The first constant g_F is the g-factor. (In Beryllium the g-factor g_F has the opposite sign than that seen in most neutral atom experiments.).

Several experiments [Leibfried 03b, Barrett 04, Chiaverini 04, Chiaverini 05] [Leibfried 04, Reichle 06a]have been performed using the hyperfine ground states of $^9Be^+$ at low magnetic fields (< 20 Gauss). These states have very long lifetimes measured in millions of years [Wineland 98]. Most level splittings will have a first order dependence on the magnetic field. (An exception is the $|^2S_{\frac{1}{2}}, F = 2, m_F = 0\rangle$ and $|^2S_{\frac{1}{2}}, F = 1, m_F = 0\rangle$ transitions, which is called a clock transition.) The splitting is first-order independent of magnetic field only at $B = 0$. A magnetic field must be introduced to break the degeneracy of the other levels, which means this level splitting will have some first order dependence on the magnetic field.) This makes a superposition of these levels sensitive to decoherence from changes in the magnetic field. Typical decoherence times for these transitions in the laboratory are $\lesssim$ 1ms. This is on the same time scale as the length of the experiments in references [Leibfried 03b, Barrett 04, Chiaverini 04, Chiaverini 05, Leibfried 04, Reichle 06b]. Spin echo techniques [Ramsey 63, Vandersypen 04] are used to extend this time, but they are most likely not sufficient to meet the DiVincenzo crite-

ria of "3.) Long relevant decoherence times, much longer than the gate operation time [DiVincenzo 01]."

In the low field limit where the hyperfine interaction is large compared to the Zeeman interaction the splitting of the levels is linear in the magnetic field except for the clock transitions. This is also true in the high field regime where the Zeeman interaction is much larger than the hyperfine interaction. In the intermediate field regime where the two interactions are of comparable energies, the splitting between some of the levels is no longer linear, but has curvature. For particular values of the magnetic field there are "field independent" transitions [Bollinger 91, Wineland 98, Langer 05, Langer 06], where the splittings between two levels is no longer depends to first order on the magnetic field, but only to second order. The Breit-Rabi formula allows for the calculation of the field-independent transitions. References [Langer 05, Langer 06] discuss this in detail for the system used in this dissertation. There are two field-independent transitions in $^9Be^+$ that occur near a magnetic field of ~ 120 Gauss: $|^2S_{\frac{1}{2}}, F = 2, m_F = 0\rangle \rightarrow |^2S_{\frac{1}{2}}, F = 1, m_F = 1\rangle$ and $|^2S_{\frac{1}{2}}, F = 2, m_F = 1\rangle \rightarrow |^2S_{\frac{1}{2}}, F = 1, m_F = 0\rangle$. In reference [Langer 05] a coherence time of ~ 15 seconds was demonstrated on the $|^2S_{\frac{1}{2}}, F = 2, m_F = 0\rangle \rightarrow |^2S_{\frac{1}{2}}, F = 1, m_F = 1\rangle$ transition.

The experiments discussed in this dissertation do not make use of the field-independent transitions. However, the experimental apparatus was set up around with $B = 120$ Gauss, so that future experiments [Home 09, Hanneke 10] could use the field-independent transitions with fewer changes. The two logical levels (qubit levels) in this dissertation are the $|^2S_{\frac{1}{2}}, F = 2, m_F = 2\rangle$ and the $|^2S_{\frac{1}{2}}, F = 2, m_F = 1\rangle$. Not using the field-independent transitions simplified certain aspects of the experiment.

3.3 State Preparation

As was discussed in the previous section, $^9Be^+$ has several possible states that could serve as good qubit states. However there needs to be a way to prepare the $^9Be^+$

ion in one of these states. This requirement is also one of the DiVincenzo criteria "2.) The ability to initialize the state of the qubits to a simple fiducial state [DiVincenzo 01]." Through a combination of optical pumping and stimulated Raman transitions (see chapter (4)) it is possible to prepare a $^9Be^+$ ion's internal state in any of the hyperfine ground states. To do this we first initialize the population to particular level via optical pumping. It can then be transferred to other levels with stimulated Raman transitions.

For the experiments discussed in this dissertation, the states $|^2S_{\frac{1}{2}}, F = 2, m_F = 1\rangle$ and $|^2S_{\frac{1}{2}}, F = 2, m_F = 2\rangle$ are used as the qubit states. Using optical pumping techniques, it is possible to first prepare the population in the state $|^2S_{\frac{1}{2}}, F = 2, m_F = 2\rangle$. The beams used for optical pumping are shown in figure (3.2). Their orientation with respect to the trap axis and the magnetic field are shown in figure (3.3). All the beams ideally have σ^+ polarization, and this is adjusted with a $\lambda/4$ waveplate and magnetic field coils that allow for fine tuning of the magnetic field direction. However, the polarization is never perfect, which must be taken into account.

After loading an ion in the ion trap, it must be assumed that the internal state population is distributed over any of the $^2S_{\frac{1}{2}}$ ground states. It is necessary that the optical pumping efficiently transfer all of the population to the $|^2S_{\frac{1}{2}}, F = 2, m_F = 2\rangle$ state. A single beam with perfect σ^+ polarization tuned to near resonance with the $^2S_{\frac{1}{2}} \rightarrow ^2 P_{\frac{3}{2}}$ transition would eventually transfer all the population to this level. However, the 1.25 GHz splitting of $F = 1$ and $F = 2$ ground state manifolds makes it difficult to accomplish this in a reasonable amount of time ($\sim$ few ms) with one laser beam, since the excited state linewidth is 19.4 MHz and some of the transitions would be off resonant. Thus, several beams are used.

Two beams are tuned near resonance with $^2P_{\frac{1}{2}}$ level. One beam is called the "repumper" and is tuned to be resonant with the $|^2S_{\frac{1}{2}}, F = 2, m_F = 1\rangle \rightarrow |^2P_{\frac{1}{2}}, F = 2, m_F = 2\rangle$ transition. These beams efficiently pump the population from $|^2S_{\frac{1}{2}}, F = 2, m_F = 1\rangle$ to $|^2S_{\frac{1}{2}}, F = 2, m_F = 2\rangle$. Once the population is in the $|^2S_{\frac{1}{2}}, F = 2, m_F = 2\rangle$ state ion

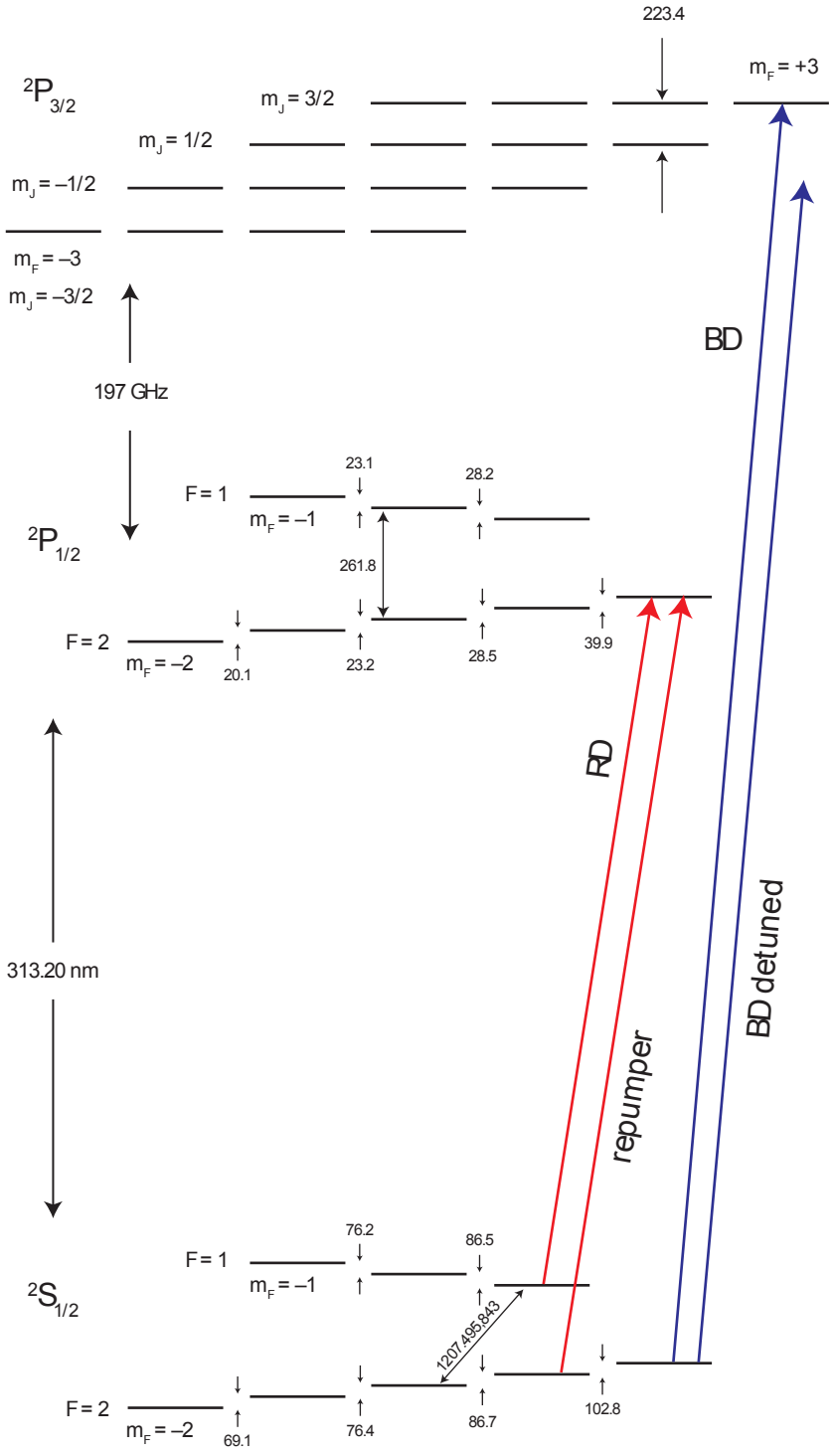

Figure 3.2: $^9Be^+$ levels at a magnetic field of 119.4 Gauss with tuning of laser beams indicated. This figure was reproduced from reference [Langer 06]. It depicts the approximate level splittings for the levels used in the experiments discussed in this dissertation. The exact magnetic field varied slightly < 1 Gauss from the field used in this figure. The level splittings are in MHz. The laser beams used for optical pumping and Doppler cooling with $^9Be^+$ are shown.

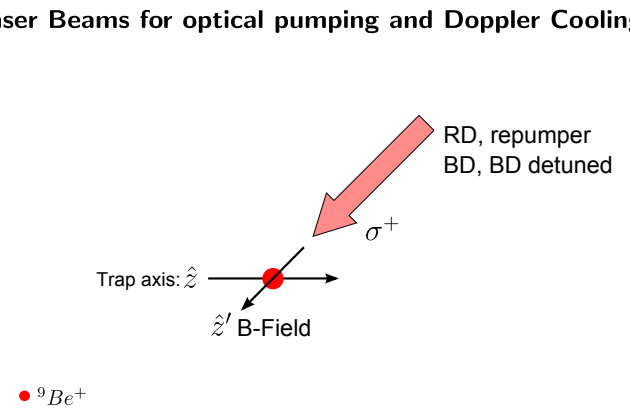

Figure 3.3: Orientation of the RD, repumper, BD, and BD detuned laser beams with respect to the trap axis and magnetic field direction. All beams are used for the initial state preparation of the state $|^2S_{\frac{1}{2}}, F = 2, m_F = 2\rangle$. The RD and repumper beams are also used for Raman cooling with ^{9}Be$^+$. The BD detuned beam is used for Doppler cooling. The BD beam is used for near-resonance Doppler cooling and state dependent resonance fluorescence.

scattering from the RD and repumper beams ceases, because there is no transition coupling the $|^2S_{\frac{1}{2}}, F = 2, m_F = 2\rangle$ ground state to the $^2P_{\frac{1}{2}}$ state. These beams are also used as the repumping beams for a Raman cooling cycle on the $|^2S_{\frac{1}{2}}, F = 2, m_F = 2\rangle \rightarrow |^2S_{\frac{1}{2}}, F = 2, m_F = 1\rangle$ transition (see chapter (6)). The other beam near resonance with the $^2P_{\frac{1}{2}}$ level is called RD (RD stands for Red Doppler, and is somewhat of a historical name). It is tuned near resonance with the $|^2S_{\frac{1}{2}}, F = 1, m_F = 1\rangle \rightarrow |^2P_{\frac{1}{2}}, F = 2, m_F = 2\rangle$ transition. Although this beam is farther from resonance with the other levels in the $F = 1$ ground state manifold, it can help optically pump them to the $|^2S_{\frac{1}{2}}, F = 2, m_F = 2\rangle$ state. The RD beam is also necessary for Raman cooling. When repumping the $|^2S_{\frac{1}{2}}, F = 2, m_F = 1\rangle$ state via the $|^2P_{\frac{1}{2}}, F = 2, m_F = 2\rangle$ level the population can spontaneous decay to the $|^2S_{\frac{1}{2}}, F = 1, m_F = 1\rangle$ state, and the RD beam helps pump this population to $|^2S_{\frac{1}{2}}, F = 2, m_F = 2\rangle$. The optical power for these beams is ideally kept

such that the transitions are not saturated. If the transitions are saturated and the polarization is not perfect, then this will lead to depumping of the $|^2S_{\frac{1}{2}}, F = 2, m_F = 2\rangle$ state.

Two other beams aid in state initialization. These are labeled in figure (3.2) as BD and BD detuned (BD stands for Blue Doppler). Both beams have σ^+ polarization. The BD detuned beam is red detuned from the $|^2S_{\frac{1}{2}}, F = 2, m_F = 2\rangle \rightarrow |^2P_{\frac{3}{2}}, m_I = \frac{3}{2} m_j = \frac{3}{2}\rangle$ cycling transition [Metcalf 99] by ~ 400 MHz. The laser intensity in this beam is several times the saturation intensity, so transitions help in optically pumping all $F = 2$ manifold ground states to the state $|^2S_{\frac{1}{2}}, F = 2, m_F = 2\rangle$. This beam is also used for Doppler cooling of the $^9Be^+$ ions (see chapter (5) for more on Doppler cooling). This beam helps pre-cool ions that are very hot. When ions are initially loaded in the trap, they are quite hot, since they are loaded into the trap from a thermal source of neutral Beryllium atoms. In addition, the ions can undergo collisions with the background gas, which can impart energy to the ions. The BD beam also helps with state preparation, but its main purpose is for Doppler cooling and detection (see section (3.4)). For Doppler cooling it is red detuned from the resonance by $\sim \frac{\Gamma}{2}$ ($\Gamma = 2\pi \times 19.4$ MHz) and the intensity is below saturation, which provides the optimum two-level Doppler cooling (see chapter (5)).

Doppler cooling was discussed along with the state preparation of $^9Be^+$ (see section 3.3), because these to things work together in the experiments. If the internal state population is not completely optically pumped to the $|^2S_{\frac{1}{2}}, F = 2, m_F = 2\rangle$ state, the cycling transition ($|^2S_{\frac{1}{2}}, F = 2, m_F = 2\rangle \rightarrow |^2P_{\frac{3}{2}}, m_I = \frac{3}{2}, m_J = \frac{3}{2}\rangle$) can not be efficiently driven. A typical $^9Be^+$ state preparation/Doppler cooling sequence starts with ~ 3.5 ms of RD, repumper, BD and BD detuned. This is followed by ~ 500 μs of RD, repumper, and BD. This stage helps achieve the lowest possible Doppler temperature (see chapter (5)). The last pulse is ~ 25 μs of RD and repumper.

3.4 Detection

The ability to able to distinguish the states of a qubit is important in QIP, and is one of the DiVincenzo criteria "5.) A qubit-specific measurement capability [DiVincenzo 01]." For trapped ions, this is typically done by implementing state dependent resonance fluorescence. This technique was originally proposed by Dehmelt et al. [Dehmelt 75] and demonstrated experimentally in references [Wineland 80, Nagourney 86] [Sauter 86, Bergquist 86]. For QIP applications it is not adequate to simply distinguish the two qubit states. The error rates need to be as low as possible. Fault tolerant thresholds [Knill 05, Steane 03b, Kielpinski 02b] that set minimum tolerable errors rates for QIP. High detection efficiencies have been demonstrated for ions in references [Hume 07, Myerson 08, Burrell 09].

Resonance fluorescence detection of the internal states of $^9Be^+$ used in this dissertation was a major focus of the dissertation by Langer [Langer 06], and only the relevant portions will be highlighted here. (- A Joke: Why did the cucumber blush? The answer is somewhere in this dissertation. -) State-dependent resonance fluorescence detection works by having one of the qubit states strongly fluoresce (called the bright state, which is the $|^2S_{\frac{1}{2}}, F = 2, m_F = 2\rangle$ state) and the other fluoresce negligibly (called the dark state, which here is the $|^2S_{\frac{1}{2}}, F = 2, m_F = 1\rangle$ state). The bright state is coupled to the $|^2P_{\frac{3}{2}}, m_I = \frac{3}{2} m_j = \frac{3}{2}\rangle$ state, excited via a closed cycling transition [Metcalf 99] and can scatter millions of photons per second. This is accomplished with the BD beam shown in figure (3.2), with the frequency is tuned a few MHz red of resonance with an intensity below the saturation intensity. The scattering rate is limited by the linewidth of the excited state, which is $\Gamma = 2\pi \times 19.4$ MHz. Assuming the saturation is $s = 1/2$, the scattering rate [Metcalf 99] is $R_s = \frac{\Gamma}{6}$. A 200 μs detection time is used, and in that time $N \sim 4000$ photons are scattered. An $F \simeq 1$ imaging system collects some of the scattered photons and focuses them on to a photo-multiplier tube (The apparatus for

collecting the photons is discussed in more detail in chapter (2).). Only a small fraction of the photons are collected in this time, $n_d \sim 10$. The overall collection efficiency is then $\eta_d \sim 2.5 \times 10^{-3}$. Assuming there is no background and the dark state scatters no photons, the probability of the ion being in the bright state but not being detected is [Wineland 98] $P_N(0) = (1-\eta_d)^N \simeq e^{-n_d}$. For $n_d = 10$ then $P_N(0) \simeq 5 \times 10^{-5}$, which is a relatively small error.

One source of error in detection is due to the dark state not being completely dark and scattering photons. The dark state $|^2S_{\frac{1}{2}}, F=2, m_F=1\rangle$ is shifted by only ~ 100 MHz from the $|^2S_{\frac{1}{2}}, F=2, m_F=2\rangle$ state. For $s=1/2$, approximately 60 photons would be scattered in the detection time of 200 μs and ~ 0.2 would be collected by the imaging system, not an insignificant error. In addition, once the dark state is pumped to the bright state it will scatter more photons, contributing to a false signal.

This can error can be made smaller by "electron shelving" [Dehmelt 75]. In our experiment the dark state $|^2S_{\frac{1}{2}}, F=2, m_F=1\rangle$ can be transferred to another auxiliary state $|^2S_{\frac{1}{2}}, F=2, m_F=-2\rangle$, which scatters less photons. See reference [Langer 06] for more details on the error rates. Shelving can be accomplished by using co-carrier Raman pulses (see section (3.5)) to transfer the population. (Note that a π-pulse denotes complete transfer from one state to another.) This is accomplished by performing a π-pulse on the $|^2S_{\frac{1}{2}}, F=2, m_F=1\rangle \rightarrow |^2S_{\frac{1}{2}}, F=2, m_F=0\rangle$ transition followed by two more sequential π-pulses that make the transitions $|^2S_{\frac{1}{2}}, F=2, m_F=0\rangle \rightarrow |^2S_{\frac{1}{2}}, F=2, m_F=-1\rangle$ and $|^2S_{\frac{1}{2}}, F=2, m_F=-1\rangle \rightarrow |^2S_{\frac{1}{2}}, F=2, m_F=-2\rangle$.

If a $^9Be^+$ ion is in the bright state, then in a single 200 μs detection period approximately 10 photons should be detected. Repeating the same experiment many times gives a histogram of the number of photons collected. The histogram will follow a Poissonian distribution with a mean of ~ 10 photons. A single data point in a scan of some parameter is the average of many single experiments (typically between 100-500 experiments). When the ion is in the dark state, no photons should be collected;

however, a background of ~ 0.1 counts on the photomultiplier tube is observed. Also the mean number of photons detected can drift in time. For several of the experiments discussed (for example see section (6.7)) in this dissertation it sufficient to know the average number of photons received for each data point. For analyzing the data from the geometric phase gate (7.6) and the entangled mechanical oscillators experiment 8 it is necessary to carefully distinguish the brig detected provides. In the case of the geometric phase gate (chapter (7)) where two $^9Be^+$ ions are detected, for a given data point (A data point is the average of many experiments) the state of the qubits might be in a superposition of having 0, 1, and 2 ions bright, and it is necessary to determine the relative probabilities. To accomplish this, the data is summed together from a given experiment creating a histogram of the number of photons collected. This data is then fit to a sum of poissonian distributions, and the resulting means are found. Typically, the means are approximately 0.1, 10, and 20 photons, which corresponds to detecting 0, 1, or 2 ions in the bright state. For a single data point, the histogram data can be fit to a sum of poissonian distributions with fixed means to the find the relative weights of each distribution. This gives the relative probabilities of 0, 1, and 2 ions being in the bright state.

3.5 Raman Transitions in $^9Be^+$

Two photon stimulated Raman transition are discussed in detail in chapter (6). A simple overview of the levels and the beams used for Raman transitions will be given in this section. Stimulated Raman transitions are performed with two laser beams that are blue detuned from the $^2S_{\frac{1}{2}} \rightarrow^2 P_{\frac{1}{2}}$ transitions by ~ 80 GHz. The frequency difference between these beams can be tuned from ~ 0 to ~ 100 MHz. Stimulated Raman sideband transitions (see chapter (6)) are driven between $|^2S_{\frac{1}{2}}, F = 2, m_F = 2\rangle$ and $|^2S_{\frac{1}{2}}, F = 2, m_F = 1\rangle$ states. One beam has π polarization and its k-vector is perpendicular to the magnetic field. The second beam propagates along the magnetic field

direction with linear polarization. This means both σ^+ and σ^- polarization components are present. Only the σ^+ component contributes to the transition. The σ^- component is off resonance, and is used to balance Stark shifts. The two beams are perpendicular to each other and have a projection along the trap axis. Thus they can be used for Raman cooling with $^9Be^+$, for the motion adding, and motion subtracting sidebands, which are discussed in chapter (8). Although not used on all the transitions, these beams could drive any ΔF=0 and $\Delta m_F = 1$ transitions in the $^2S_{\frac{1}{2}}$ state.

By making the two Raman beams co-linear, motion insensitive transitions can be driven between any $\Delta F = 0$ and $\Delta m_F = 1$ transitions in the $^2S_{\frac{1}{2}}$ manifold. These transitions perform a rotation between two internal states of a $^9Be^+$ ion [Wineland 98]. This is often described as a single qubit gate [Nielsen 00]. The k-vectors of both beams are oriented perpendicular to the magnetic field with a polarization such that both beams have π, σ^+, and σ^- polarization components. The frequencies and polarizations of the two beams are such that $\Delta F = 0$ and $\Delta m_F = 1$ transitions in the $^2S_{\frac{1}{2}}$ state are driven with both σ^+/π and σ^-/π combinations of polarizations.

Chapter 4

Sympathetic Cooling and $^{24}Mg^{+}$

This chapter has a discussion of sympathetic cooling and the Magnesium ion. The first section is a general discussion of the motivations and issues surrounding sympathetic cooling for quantum information processing. This chapter does not experimental demonstrations of sympathetic cooling, which is covered elsewhere in this dissertation. The second section provides an overview of the $^{24}Mg^{+}$ ion and its structure, which is used as the sympathetic cooling ion in the experiments discussed in this dissertation. A simplified overview is given of how the internal structure comes about.

4.1 Sympathetic Cooling

One of the main goals of quantum information processing is to perform fault tolerant operations [Nielsen 00] in any system, there will be multiple sources of errors, and these errors will need to be reduced to below the appropriate fault tolerant threshold. In ion trap based quantum information processing, one of the fundamental operations for forming a universal gate set is the two-qubit entangling gate. Most proposals for implementing such an operation involve using the motional modes of the trapped ions, where it is assumed that the ions are in the Lamb-Dicke regime [Wineland 98]. The motion is the natural choice since this provides the dominate coupling between ions trapped in the same potential well. Most gate implementations involve the axial modes of motion [Cirac 95, Wineland 98]; however, radial modes can also be used [Zhu 06,

Lin 09, Kim 09]. These gates require the ability to excite the motion of the ions in a state dependent way. Several schemes allow the ions motion to be in a thermal state [Sørensen 99, Sørensen 00, Kirchmair 09], but all of these schemes require the ions to be in the Lamb-Dicke regime. Unless the ions can be placed in a completely noise free environment there will always be some need to recool them. Sympathetic cooling provides this capability of recooling the ions used for the two qubit gates.

In the context of trapped ions, sympathetic cooling is the process of using one or more ions to cool other ions. Typically, information is stored in the internal state of a "logic" ion and the information needs to be preserved throughout the computation. Laser cooling techniques applied to the logic ion would destroy this information, since they rely on manipulating the ions' internal states. When there is more than one ion in the ion trap, there are multiple normal modes of motion. Since the motion is usually shared between all the ions it is sufficient to only cool one of the ions in the chain.

The primary reason the motional state changes in time in an uncontrolled way can be attributed to heating of the motional modes from noisy ambient electric fields. Efforts can be made to minimize the amount of electric field noise the ions experience. This can include placing an ion trap in a cryogenic environment [Antohi 09] or filtering all electrical signals going into the apparatus. Another source of the heating results from having imperfect waveforms, which are used in transport and separation of the ions. This can lead to modulations of the trapping potential, which drives the ions' motion [Blakestad 09].

4.1.1 Options for Sympathetic Cooling

There are many different proposals for sympathetic cooling with trapped ions. Most of the proposals involve having a chain of ions, where some of the ions serve as logical qubits and others serve as coolant ions. One scheme uses a homogeneous ion crystal and relies on individual addressing of particular ions to cool the chain [Rohde 01].

There are two proposals that involve using a different types of ions as the cooling ions. One makes use of having a different isotope of the same type of ion [Blinov 02]. The other uses a different species of ion altogether [Kielpinski 00, Barrett 03]. Another proposal involves having a long string of ions and cooling some of the ions on the end of the chain [Herrmann 09].

It maybe possible to use some ions in the chain to remove energy from the other by separating them off. In the experiment performed in ref [Barrett 04] one ion was separated off from a chain of three ions leaving the remaining two ions with relatively low motional excitation. The third ion was presumably hot. A protocol for this might involve having a reservoir of cold ions where one or a few are merged with the hot chain of logical ions. The motional energy should thermalize across the normal modes of the new crystal. Then these ions could be separated off in a way such the ions being separated from the chain carry away some fraction of the motional energy.

Although schemes exist that allow gates to be preformed at Doppler temperatures. This alone will not be enough to do away with the need of sympathetic cooling. One alternative architecture might involve only storing information in the logical qubits for a time short compared to the heating rate. This would require the ability to bring new cold ions in at fast rate and transfer the information from the ion that is getting hot to the one that is cold.

4.1.2 Issues with Sympathetic Cooling

Our experiments involve using a different species of ion as the coolant ion. This scheme has several advantages over others. One of the main ones is negligible spontaneous scattering errors on the logical qubits from the laser light used to cool the coolant ions. This results from the fact that if the logical ion is a different species from the coolant ion, then its transition frequency will typically be significantly different from that of the qubit. This will be important, because a large-scale ion based quantum

information processor will probably require substantial sympathetic cooling.

The ions experience micromotion from the oscillating radio-frequency (RF) field when they are forced off of the RF field minimum of the trap. This will degrade the performance of some of the relevant quantum operations [Berkeland 98]. Typically, the ions are forced off of the RF null by stray electric fields, which can have a number of sources. If the fields are small and do not change quickly, then the possibility does exist to compensate for them. However, we required some way to detect the presence of stray fields. This can be accomplished by detecting depumping[1] of the logical ions [Berkeland 98]. We need observe for this depumping in two non-coplaner x-y directions to null the micromotion in the X and Y directions (radial directions, which are not along the trap axis). This can be accomplished with the use of the logical qubits, but requires two separate laser beams. Often, the detection beam (see chapter (3)) can be used for one, but another beam is required, which further complicates the setup. Having a coolant ion with a different mass allows for another method of probing the local electric field environment. The RF pseudo-potential depends on the mass of the ion [Wineland 98, Leibfried 03a]. Two ions of different mass will be pushed off axis by different amounts from the same electric field. This has a number of effects. An ion crystal with more than two ions that was linear will no longer be linear. If the stimulated Raman beams [Wineland 98] (see chapter 6) were set up to probe along the axial direction, then it will no longer probe only axial modes. Components from the radial modes will now also show up when scanning the frequency of a sideband pulse. This has both advantages and disadvantages. If these modes are not spectrally will resolved from the axial modes, then the radial modes presence will increase the errors

[1] The RF micromotion puts sidebands on a the transitions. A laser beam can be tuned near resonance with one of these sideband transitions, and when there is micromotion this laser will scatter photons. If the appropriate transition is chosen, then this scattering can optically pump the ion's state to other levels. This will cause a decrease in fluorescence when using state dependent resonance fluorescence. In addition, if a cycling transition is being used to scatter photons, then the micromotion will broaden this transition, which leads to a decreased scattering rate, and this can be detected with state-dependent resonance fluorescence.

that result from off resonantly driving the radial transitions. However, being sensitive to these modes can also be viewed as a tool for nulling out the micromotion. The micromotion can be nulled by scanning a compensating electric fields to minimize the coupling.

The use of different mass ions potentially gives rise to more overlaps of the normal mode resonant frequencies. Here we assume a typical linear RF Paul trap, where the radial confinement is higher than the axial confinement. With a small uniform chain of a few ions, the frequency of the radial modes do not typically overlap with axial modes. If the two types of ions have a different mass, then depending on the mass difference, some of the radial mode can be lower in frequency then some of the axial modes. This is not a fundamental problem, but does create technical difficulties. These difficulties arise from the fact that the closer you have a radial mode near an axial mode in the frequency domain, the more carefully the stray electric fields need to be nulled. If not well compensated, then this will lead to increased off resonant coupling when trying to drive sideband transitions or other operations that involve exciting the motion.

Another consideration for the coolant ion is the simplicity of its internal level structure. In a large-scale quantum information processing devices cooling will most likely be needed in several regions. Laser beams will have to be distributed to these locations. Thus if the coolant ion requires multiple beams to be cooled, then this will only further complicate the setup.

4.2 $^{24}Mg^{+}$

4.2.1 Energy Level Structure

The sympathetic cooling ion used in our experiments is the alkali earth element Magnesium. There are three stable isotopes ^{26}Mg, ^{25}Mg, and ^{24}Mg, which have natural abundances of 11%, 10%, and 79% respectively [MgI]. The experiments use ^{24}Mg which

use zero nuclear spin, which simplifies the internal level structure. We ionize neutral ^{24}Mg to create $^{24}Mg^{+}$. This creates an ion with similar internal properties to alkali neutral atoms that have one valence electron. In $^{24}Mg^{+}$ the valence electron is in the $n = 3$ shell. Its ground state is an S orbital labeled $^{2}S_{\frac{1}{2}}$. The first excited state is a P orbital. These levels are split by $\sim$ 280 nm [Herrmann 09]. We excite the electron through an electric dipole transition using a laser beam with a wavelength approximately equal to 280 nm.

The excited P orbital has an additional level splitting called fine structure, which splits the excited state into the two levels $^{2}P_{\frac{1}{2}}$ and $^{2}P_{\frac{3}{2}}$. Two effects give rise to the fine structure for the excited P state: the relativistic shift, and spin orbit coupling [Brandsden 03, Foot 05]. The ground state will experience an additional shift from the Darwin term [Brandsden 03]. The relativistic correction comes about by taking into account the relativistic kinetic energy of the electron. The spin orbit correction arises from the coupling of the magnetic moment of the electron to the magnetic field arising from the electron's motion in the electric field of the atomic core. Its motion relative to the nucleus. These effects give rise to a splitting of $\sim$ 2.75 THz [Yu. 08].

The ground and excited states also have magnetic sub levels, which are degenerate at zero magnetic field. Each of the energy levels will have $2J+1$ degenerate magnetic sub-levels where J is the total angular momentum $J = L+S$ (The orbital angular momentum is represented by L, and S represents the spin angular momentum.). Breaking the degeneracy of these levels, is useful for quantum information processing and laser cooling. Applying a static magnetic field $\vec{B}$ breaks the degeneracy, which is known as the Zeeman effect. How the energy shift from the Zeeman effect is calculated depends on the strength of the interaction compared to the spin-orbit coupling. There are three regimes: the weak, the intermediate, and the strong. The strength of the external magnetic field when compared to the internal magnetic field determines the regime. In the weak-field limit, the Zeeman effect is a perturbation on the spin-orbit correction and treated as a

perturbation, using the base kets of spin orbit interaction. For the strong field limit, the base kets of the Zeeman Hamiltonian are used and the spin-orbit is the perturbation. In the intermediate regime both are treated on the same level and the resulting Hamiltonian has to be diagonalized to find the energies. The experiments discussed in this dissertation are performed at a magnetic field of 120 Gauss, which is in the weak field regime. The Hamiltonian that describes this effect is

$$H_{zm} = -\mu_b g_J \vec{J} \cdot \vec{B}. \tag{4.1}$$

The Bohr magneton is μ_b. The Landè g-factor g_j is given by [Brandsden 03]

$$g_j = 1 + \frac{J(J+1) + S(S+1) - L(L+1)}{2J(J+1)}. \tag{4.2}$$

The g_J factors are: for the ${}^2S_{\frac{1}{2}}$ states $g_J \simeq 2$, for the ${}^2P_{\frac{1}{2}}$ states $g_J \simeq \frac{2}{3}$, and for the ${}^2P_{\frac{3}{2}}$ states $g_J \simeq \frac{4}{3}$. The change in energy for a given magnetic sub-level m_j is

$$\Delta E = -\mu_b g_j m_j B. \tag{4.3}$$

As function of the applied magnetic field the splitting of the energy levels is shown in figures (4.1) and (4.2), and (4.3). Figure (4.4) shows the internal level structure of ${}^{24}Mg^+$ at a magnetic field of 119.65 Gauss. The splittings of the magnetic sub levels is determined from calculations. The splitting of the ${}^2S_{\frac{1}{2}}$ and ${}^2P_{\frac{3}{2}}$ levels is determined from experimental values. The fine structure splitting of 2.75 THz comes from reference [Yu. 08].

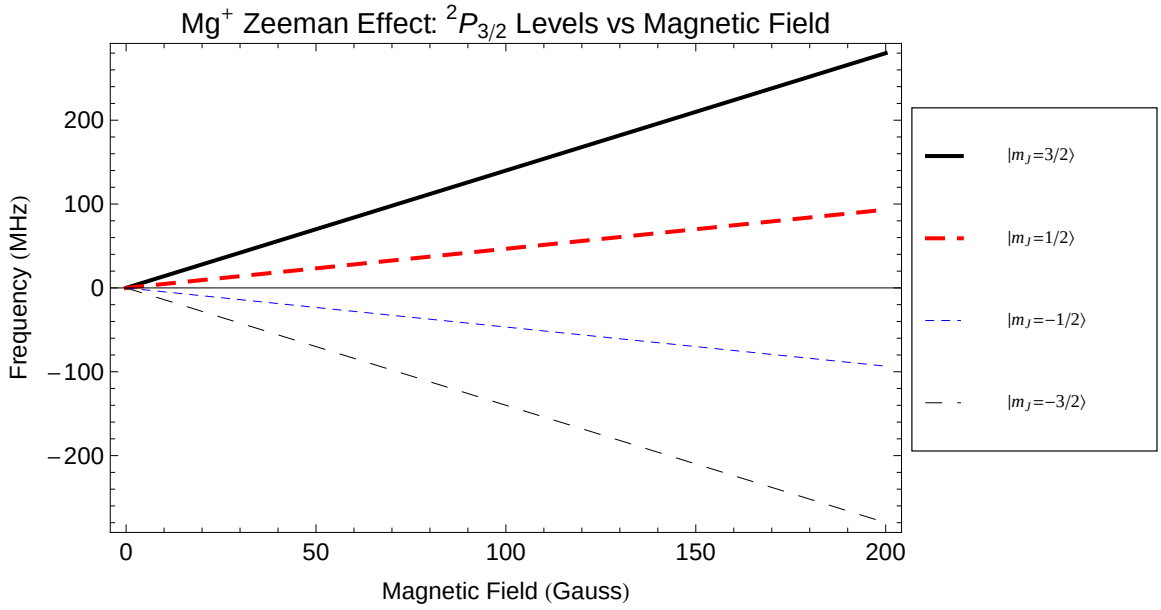

Figure 4.1: Splittings of the $^2P_{\frac{3}{2}}$ levels of $^{24}Mg^+$as a function of the applied magnetic field. The g-factor $g_J \simeq \frac{4}{3}$.

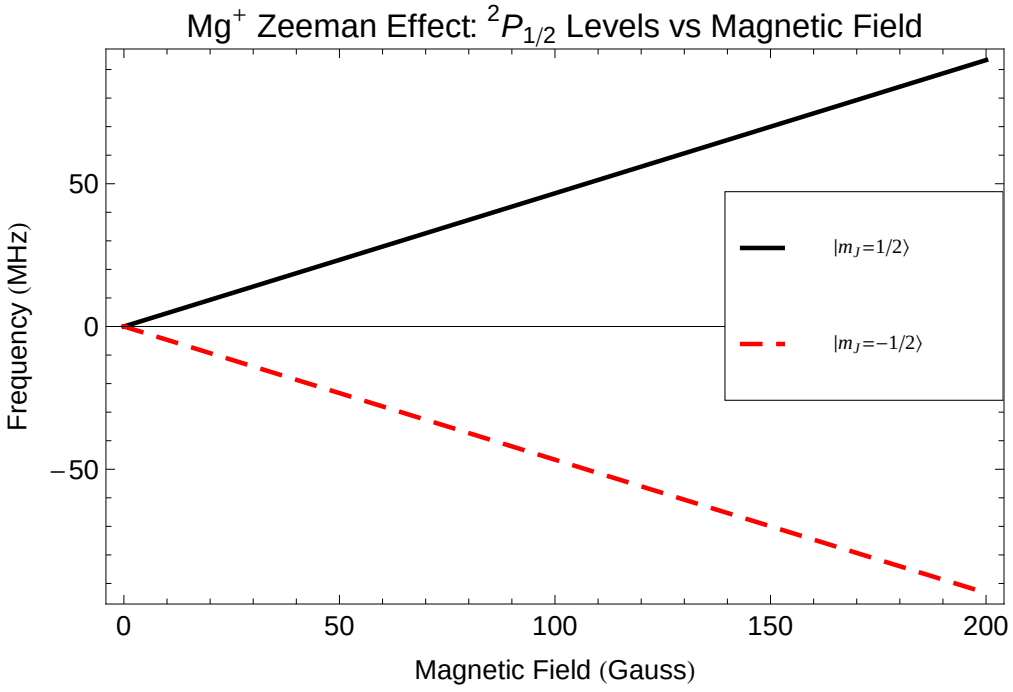

Figure 4.2: Splittings of the $^2P_{\frac{1}{2}}$ level of $^{24}Mg^+$as a function of the applied magnetic field. The g-factor $g_J \simeq \frac{2}{3}$.

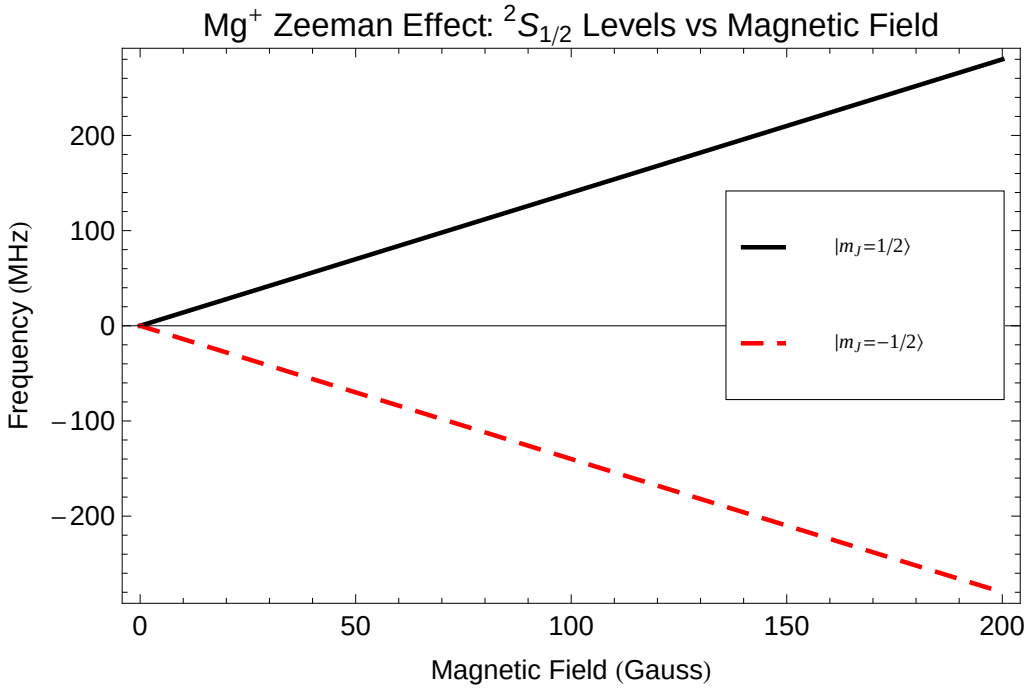

Figure 4.3: Splittings of the ${}^2S_{\frac{1}{2}}$ level of ${}^{24}Mg^+$as a function of the applied magnetic field. The g-factor $g_J \simeq 2$.

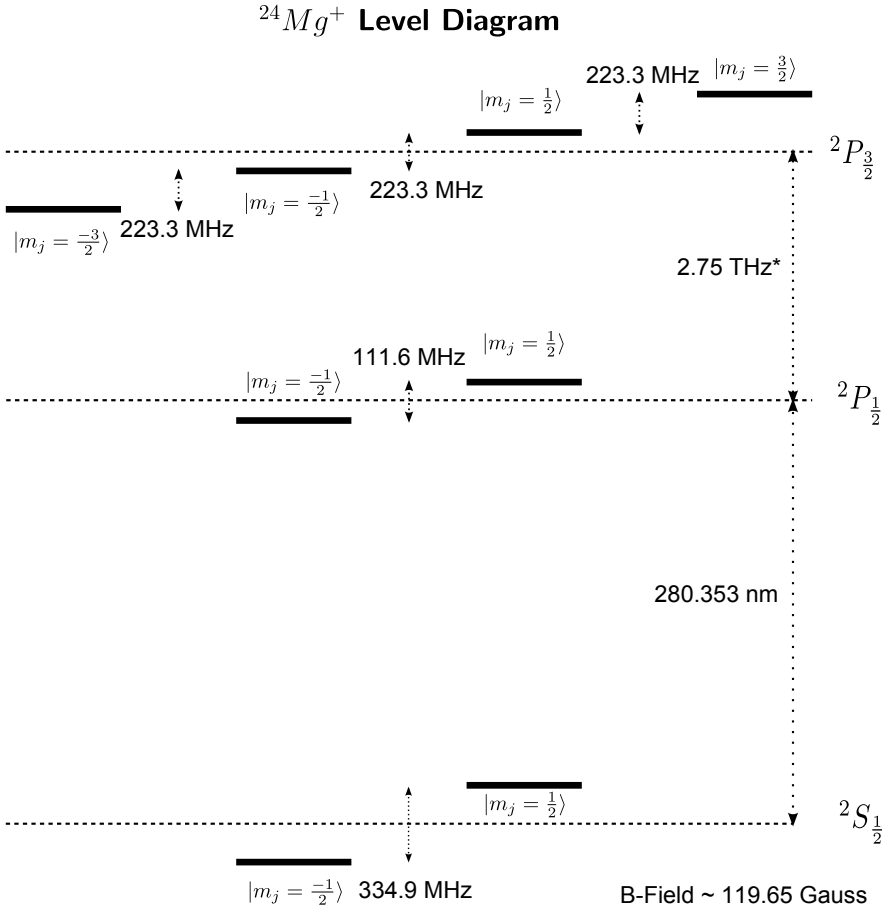

Figure 4.4: Atomic level structure for $^{24}Mg^{+}$at field of $\sim$ 119.65 Gauss. The splitting of 280.353 nm of the $^2S_{\frac{1}{2}}$ and $^2P_{\frac{1}{2}}$ levels taken from experimentally determined values. The g_J factors are: for the $^2S_{\frac{1}{2}}$ states $g_J \simeq 2$, for the $^2P_{\frac{1}{2}}$ states $g_J \simeq \frac{2}{3}$, and for the $^2P_{\frac{3}{2}}$ states $g_J \simeq \frac{4}{3}$. * This value for the fine structure splitting is taken from the value for $^{25}Mg^{+}$ from reference [Yu. 08].

Chapter 5

Doppler Cooling

This chapter provides an overview of Doppler cooling and examines some issues with its use to cool $^{24}Mg^{+}$. The beginning section discusses the basics of Doppler cooling in a two-level system. However, for our implementation of Doppler cooling with $^{24}Mg^{+}$ it is necessary to consider a more complicated three-level system, where "dark resonances" can occur. This is examined with a master equation and covered in section (5.4). The sections following this discuss the issues from having two different types of laser beam orientations. The last section (5.6) discusses an experimental implementation of $^{24}Mg^{+}$ Doppler cooling, which is used to sympathetically cool a $^{9}Be^{+}$ ion. This technique was developed to enable the entangled mechanical oscillators experiment [Jost 09].

5.1 Background

Laser cooling has been used for many years to cool the motion of atoms and ions. Early theoretical proposals for laser cooling were described by Hänsch and Schawlow [Hänsch 75] as well as Wineland and Dehmelt [Wineland 75] in 1975. The first experimental demonstration came a few years later by Wineland et. al. [Wineland 78], concurrently with another set of experiments by Neuhauser et al. [Neuhauser 78]. A good review of the history of laser cooling can be found in an article by Stenholm [Stenholm 86].

One of the more common techniques is Doppler cooling. This technique makes

use of the Doppler shift of an internal transition in ions (or atoms). If an ion absorbs a photon it receives a momentum kick $\hbar k$ from the laser light in the direction the of the laser propagation. If an atom were stationary then it would start moving in the direction of the light, which is obviously not an example of cooling. However, if the laser light is tuned to a lower frequency than the atomic transition, then the stationary ion will not absorb any light. This assumes the detuning is sufficiently large. Now, if the atom is moving toward the laser source, then it will experience the light as Doppler-shifted to higher frequencies. This brings the light into resonance with the atomic transition, causing the atom to absorb a photon. In this case, the atom receives a momentum kick in the direction opposite to its motion, causing it to slow down. In the case where the atom was moving away from the laser source, it sees the light as being shifted even further from resonance.

Doppler cooling slows down motion of the ion, which is often referred to as cooling the ion. However, there is a problem discussing the temperature of an ion [Metcalf 99]. The thermodynamic definition of the temperature of a system requires it to be in thermal contact and equilibrium with a bath. A trapped ion is not in thermal contact with any bath. However, it is still convenient to discuss the temperature of a system by relating its average kinetic energy to a temperature $E=\frac{1}{2}k_BT$, where k_B is the Boltzmann constant, and T is the temperature. It should be noted there are infinitely many velocity distributions that can lead to the same average kinetic energy. However, Doppler cooling leaves the ions' motion in a thermal distribution [Stenholm 86], and the concept of temperature is valid.

It appears from the above simple description of Doppler cooling that by controlling the detuning of the laser an ion could be cooled to zero temperature. This would work by changing the frequency of the detuning, as the ion gets colder until the last recoil kick removes the final bit of energy from the motion. At this point, the laser is shut off. Unfortunately, this is not the case, and there is a limit to how cold the ions become

because of recoil upon absorption and re-emission. For a two-level system that has an excited state line-width of Γ the Doppler cooling limit [Metcalf 99, Wineland 79] is

$$T_D = \frac{\hbar\Gamma}{k_B 2}. \tag{5.1}$$

This limit comes from a balance between the cooling and heating.

5.2 Doppler Cooling of Trapped Ions

Most treatments of Doppler cooling treat the particle as a free-particle, which is not true for a trapped ion. Assuming the 1D case, then the ion sees a potential

$$V = \frac{1}{2} m\omega^2 z^2. \tag{5.2}$$

The mass of the ion is m, angular frequency is ω, and z is the displacement from equilibrium. This is a harmonic potential, so the velocity of the ion has the form $v(t) = v_o \cos[(\omega t)]$. As long as the trap frequency $\omega < \Gamma$ the system is said to be in the weak binding limit [Stenholm 86], and the ion can be treated like a free particle. In this case, the time between absorption and re-emission of a photon is short compared to the period $\frac{2\pi}{\omega}$. This is an oversimplified treatment. It does not take into account micromotion [Leibfried 03a] in Paul traps, which has a term in the potential that typically oscillates with a frequency near to or higher than the spontaneous emission rate. Nevertheless the effects of micromotion are typically small and the simple theory suffices.

Following the discussions in references [Leibfried 03a, Wineland 78, Wineland 87, Neuhauser 78], the cooling rates, heating rates, and final temperature can be calculated. The damping force from scattering photons is dependent on the on the velocity of the ion. The force results from the ion's change in momentum from a scattering event. The rate of momentum kicks is determined by the linewidth Γ and the excited state population $\rho_{cc}(v)$, giving a force of

$$F_a = \hbar k \Gamma \rho_{cc}(v). \tag{5.3}$$

The magnitude wavevector of the laser is represented by k. The Doppler shift is given by $\vec{k} \cdot \vec{v}(t)$, and comes into the equations via the excited state population. The Doppler shift is modeled as changing the effective detuning from resonance, which affects the excited state population. If the velocities are small, then the force can be linearized by expanding $\rho_{cc}(v)$ in terms of the velocity around $v = 0$ and keeping terms up to $O(v)$. This gives a linearized force of

$$F_a = F_o + \beta_d v, \tag{5.4}$$

where F_o is a velocity-independent force and β_d is the effective damping coefficient. It is worth noting that in this approximation, the damping coefficient will not depend on the velocity and will depend only on the other parameters.

The average cooling rate $\dot{E_c}$ is given by the force times the velocity averaged over many cycles of the ions motion.

$$\dot{E_c} = \langle F_a v(t) \rangle = F_o \langle v(t) \rangle + \beta_d \langle v^2(t) \rangle \tag{5.5}$$

The term proportional to $\langle v(t) \rangle$ will time average to 0. The quadratic term will average to $\frac{1}{2}\beta_d v_0^2$, where v_o is the peak velocity. The final temperature reached will come from a balance of the cooling with the heating rate. Part of the heating results from the spontaneous scattering of photons in random directions by the ion. We will be considering a dipole transition, where the radiation pattern is symmetric resulting in an average momentum kick $\langle p \rangle = 0$ for re-emission. However $\langle p^2 \rangle \neq 0$ since the ion is undergoing a random walk in momentum space. Imagine the ion started out at rest. After undergoing many random momentum kicks, the average velocity would still be zero, but the velocity would follow some distribution with a finite value of $\langle v^2 \rangle$. Thus, the heating rate from the emission of a photon will be related to the square of the momentum kick. Another heating mechanism comes from the absorption of photons. If the ion starts with zero velocity and absorbs photons, then it receives momentum at random times that the motion. The heating rate is determined by the time rate of

change of the kinetic energy, which is proportional to $\langle p^2 \rangle$.

$$\dot{E_h} = \frac{1}{2m} \frac{d \langle \vec{p}^2 \rangle}{dt} = \dot{E_{abs}} + \dot{E_{emis}} + \dot{E_o}. \tag{5.6}$$

The heating rate from absorption $\dot{E_{abs}}$ is proportional to the average momentum kick squared times the rate of absorption at zero velocity, $\left(\hbar \vec{k}\right)^2 \Gamma \rho_{ee} \left(v = 0\right)$. The heating rate from emission $\dot{E_{emis}}$ is proportional to this with a constant ξ is proportional to this. The constant depends on the projection of the dipole radiation pattern along the axis of motion. It will be seen in the more specific case studied later that $\dot{E_{emis}}$ can be composed of more than one term. This occurs if there are multiple spontaneous decay paths. Other heating mechanisms are accounted for with the term $\dot{E_o}$. One such example is the heating of the ion's motion from noisy stray electric fields.

$$\dot{E_h} = \dot{E_{abs}} \left(1 + \xi\right) + \dot{E_o} = \frac{1}{2m} \left(\hbar \vec{k}\right)^2 \Gamma \rho_{ee} \left(v = 0\right) \left(1 + \xi\right) + \dot{E_o}. \tag{5.7}$$

The Doppler cooling temperature limit can be found from setting the sum of (5.5) and (5.7) to zero. This gives

$$m \left\langle v^2 \right\rangle = k_B T = -\frac{\left(\hbar k\right)^2}{2} \frac{\Gamma \rho_{ee} \left(v = 0\right)}{\beta_d} \left(1 + \xi\right) - \frac{m \dot{E_o}}{\beta_d}. \tag{5.8}$$

Equations (5.5) and (5.8) can be used to optimize Doppler cooling. Before this can be done, an expression for the excited state population needs to be found, and this will depend on the system under study.

The typical example used in Doppler cooling is a closed two-level system, which has been worked out in several papers and books [Metcalf 99, Leibfried 03a]. The result for the temperature assuming $\dot{E_o}$= 0 is given in reference [Leibfried 03a] as

$$k_B T = \frac{\hbar \Gamma}{8} \left(1 + \xi\right) \left[\left(1 + s\right) \frac{\Gamma}{2d} + \frac{2d}{\Gamma}\right]. \tag{5.9}$$

The variable $s = 2 \frac{|\Omega|^2}{\Gamma^2}$ and is called the saturation parameter, where Ω is the resonant Rabi rate. The detuning of the laser from the excited state of the two-level system is

given by d. For this case the minimum temperature

$$T_{min} = \frac{\hbar\Gamma\sqrt{1+s}}{4k_B}\left(1+\xi\right) \tag{5.10}$$

is obtained when the detuning $d = \frac{\Gamma\sqrt{1+s}}{2}$. In the limit where $\xi = 1$ and $s = 0$, which corresponds to emission along the ion's axis of motion and low laser beam intensity, this reproduces the Doppler temperature limit (5.1).

The following sections discuss a more complicated system involving three internal levels. It will be useful to compare the more complicated setup to two-level Doppler cooling, using a specific example. The experiments discussed later in section (5.6) involve a pair of $^9Be^+ - ^{24}Mg^+$ ions confined to a linear RF Paul trap. Along the axis of weakest confinement, there are two normal modes: the in-phase (INPH) and out-of-phase mode (OOPH) with normal mode frequencies 1.89 MHz and 4.05 MHz respectively (see section (5.6) for more details).

$^{24}Mg^+$ has a cycling transition on the $^2S_{\frac{1}{2}}$ to $^2P_{\frac{3}{2}}$ transitions, which has a linewidth of ~ 42 MHz [Herrmann 09]. It should be noted that this transition is not used in any of the experiments discussed here, but since the linewidth of the $^2S_{\frac{1}{2}} \rightarrow ^2P_{\frac{1}{2}}$ transition (~ 41 MHz) will be nearly the same, it will be used to compare the experimental results to the more typical Doppler cooling limits. If Doppler cooling was to be performed on the cycling transition of $^{24}Mg^+$, then a laser with σ^+ polarization would be oriented parallel to the quantizing magnetic field and at a 45 degree angle to the axis of weakest confinement.

To determine the Doppler cooling temperature for this particular two-level case, the value of ξ need to be calculated. For the case of spontaneous decay via a $\Delta m = -1$ transition, which emits σ^- polarized light, the dipole radiation pattern is given in spherical coordinates by [Itano 82, Jackson 99]

$$P_d^{\sigma^-} d\Omega = \frac{3}{16\pi}\left(1+\cos^2\left(\theta\right)\right) d\Omega. \tag{5.11}$$

The probability for emitting a photon in a solid angle $d\Omega$ is $P_d^{\sigma^-}$. It is assumed that the

dipole axis is aligned with the magnetic field, which determines the quantization axis. The probability of the ion receiving a momentum kick along the trap axis will be given by [Itano 82]

$$\epsilon^{\sigma^- ta} = \int P_d^{\sigma^-} \hat{k}_{ta}^2 d\Omega. \tag{5.12}$$

The unit wavevector corresponding to a photon emitted along the trap axis is $\hat{k}_{ta}$, which can be written in terms of Cartesian coordinates $\hat{k}_{ta} = \frac{1}{\sqrt{2}}(\hat{x} + \hat{z})$. Switching to spherical coordinates and integrating gives the following result

$$\epsilon^{\sigma^+ ta} = \frac{3}{16\pi}\frac{1}{2}\int_0^{2\pi}\int_0^{\pi}\left(1+\cos^2(\theta)\right)\sin(\theta)\left(\sin(\theta)\cos(\phi)+\cos(\theta)\right)^2 d\theta d\phi = \frac{7}{20}. \tag{5.13}$$

Using equation (5.10) a minimum temperature can be calculated for this case. Assuming $s \ll 0$ this gives an average motional occupation of the normal modes of $\overline{n}_{INPH} = 7$ and $\overline{n}_{OOPH} = 3.0$. This assumes a thermal distribution of the ion's motion, see appendix (B). These temperatures are lower than what would be expected for the typical Doppler cooling limit equation (5.1), which would give $\overline{n}_{INPH} = 10.6$ and $\overline{n}_{OOPH} = 4.7$. Figures (5.1) and (5.2) show plots of the average motional state for both modes versus the detuning of the laser for different saturation parameters. The figures show the quantum number $\bar{n}$ dropping below the typical Doppler cooling limit equation (5.9). This is a result of the parameter $\xi < 1$. In the rest of this chapter unless stated otherwise, the Doppler temperature will refer to the two-level Doppler cooling temperature of equation (5.9).

5.3 Doppler Cooling Setup for $^{24}Mg^+$

The level structure used in modeling the $^{24}Mg^+$ Doppler cooling can been seen in figure (5.3). The states are labeled as follows: $|^2S_{\frac{1}{2}}, m_j = -\frac{1}{2}\rangle \equiv |a\rangle$, $|^2S_{\frac{1}{2}}, m_j = \frac{1}{2}\rangle \equiv |b\rangle$, and $|^2P_{\frac{1}{2}}, m_j = \frac{1}{2}\rangle \equiv |c\rangle$. Each state has a corresponding energy $\hbar\omega_a$, $\hbar\omega_b$, and $\hbar\omega_c$ associated with it. Note that $\hbar\omega_a$ could be chosen to be zero but is left as a variable. The

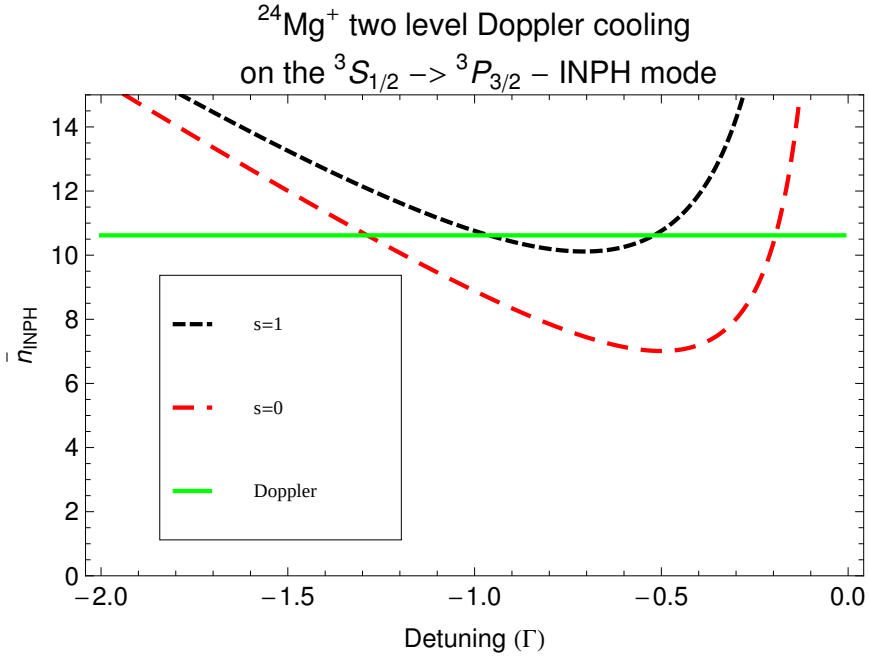

Figure 5.1: This figure shows $\bar{n}_{INPH}$ for two-level Doppler cooling of the INPH mode of a $^{9}Be^{+} - {}^{24}Mg^{+}$ ion pair with $^{24}Mg^{+}$ on the $^{2}S_{\frac{1}{2}}$ to $^{2}P_{\frac{3}{2}}$ transition versus the detuning from resonance. The detuning is in units of the linewidth $\Gamma = 2\pi \times 42$ MHz. The final temperature is plotted for different values of the saturation parameter s. The horizontal dashed line is the traditional two-level Doppler cooling limit given by equation (5.1). The vertical line is an asymptote.

fourth level in the system is $|^{2}P_{\frac{1}{2}}, m_j = \frac{-1}{2}\rangle$. It is shown in the figure but not included in the model, which simplifies the calculations. It should be reasonable to ignore this level, since there are no near resonant laser beams connecting it to any other levels. In the experiments there is a σ^{-} polarized beam connecting $|^{2}S_{\frac{1}{2}}, m_j = \frac{1}{2}\rangle$ to $|^{2}P_{\frac{1}{2}}, m_j = \frac{-1}{2}\rangle$, but it is off resonance by ~ 440 MHz, which is why it can be neglected for this simplified model. Only the two relevant laser beams are included in this simplified model figure (5.3). The laser connecting states $|a\rangle \rightarrow |c\rangle$ is σ^{+} polarized and has a frequency given by ω_1, which is detuned from the excited state by an amount δ. Laser light with π polarization and frequency ω_2 connects the states $|b\rangle \rightarrow |c\rangle$. The light is detuned from this transition by an amount Δ. Each laser beam has a Rabi frequency given by Ω_1 and Ω_2 respectively. Figure (5.3), shows the two possible spontaneous emission decay paths,

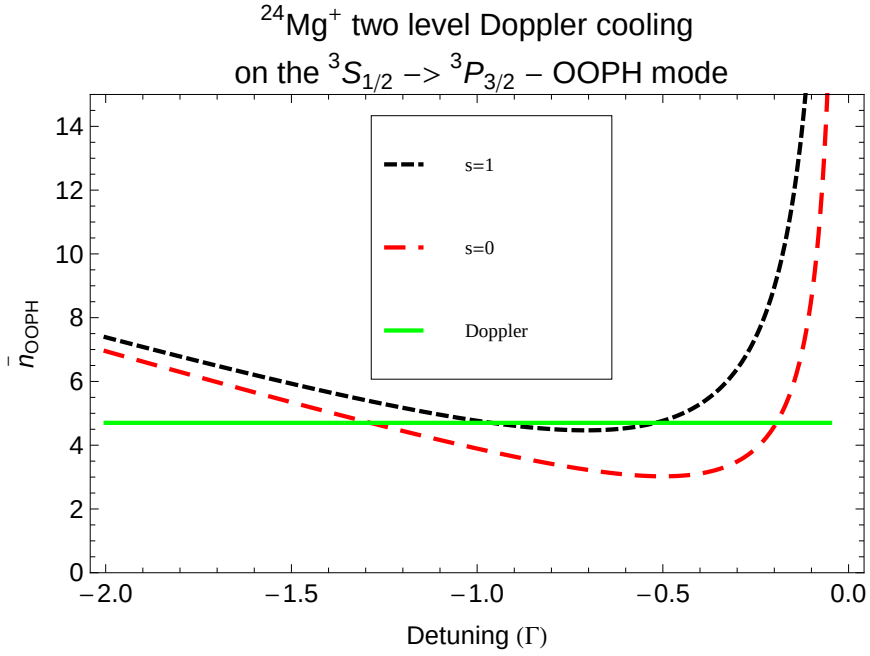

Figure 5.2: This figure shows $\bar{n}_{OOPH}$ for two-level Doppler cooling of a OOPH mode of a $^{9}Be^{+}-^{24}Mg^{+}$ ion pair with $^{24}Mg^{+}$ on the $^{2}S_{\frac{1}{2}}$ to $^{2}P_{\frac{3}{2}}$ transition versus the detuning from resonance for the OOPH mode. The detuning is in units of the linewidth $\Gamma = 2\pi \times 42$ MHz. The final temperature is plotted for different values of the saturation parameter s. The horizontal dashed line is the traditional two-level Doppler cooling limit given by equation (5.1). The vertical line is an asymptote.

which are labeled Γ_a for $|c\rangle \rightarrow |a\rangle$ and Γ_b for $|c\rangle \rightarrow |b\rangle$. Figure (5.4) shows the beam orientations relative to the magnetic field and trap axis for the two cases considered below. The wavevectors for both beams will have a reduced projection along the trap axis, given by $\vec{k}_{1ta} = \frac{1}{\sqrt{2}}\vec{k}_1$ and $\vec{k}_{2ta} = \frac{1}{\sqrt{2}}\vec{k}_2$. Also, there is only a small difference between $|k_1|$ and $|k_2|$ so it will be assumed that $|k_1| \approx |k_2| \equiv |k|$ and $|k_{1ta}| \approx |k_{2ta}| \equiv |k_{ta}|$. The case where the two beams are orthogonal in figure (5.4) is what used in the experimental setup. The co-linear case is discussed first, so it can be compared to the orthogonal case.

5.4 Master Equation

Typically, Doppler cooling is performed on a closed cycling transition, and this allows the system to be modeled as a two-level system. There are no closed transitions

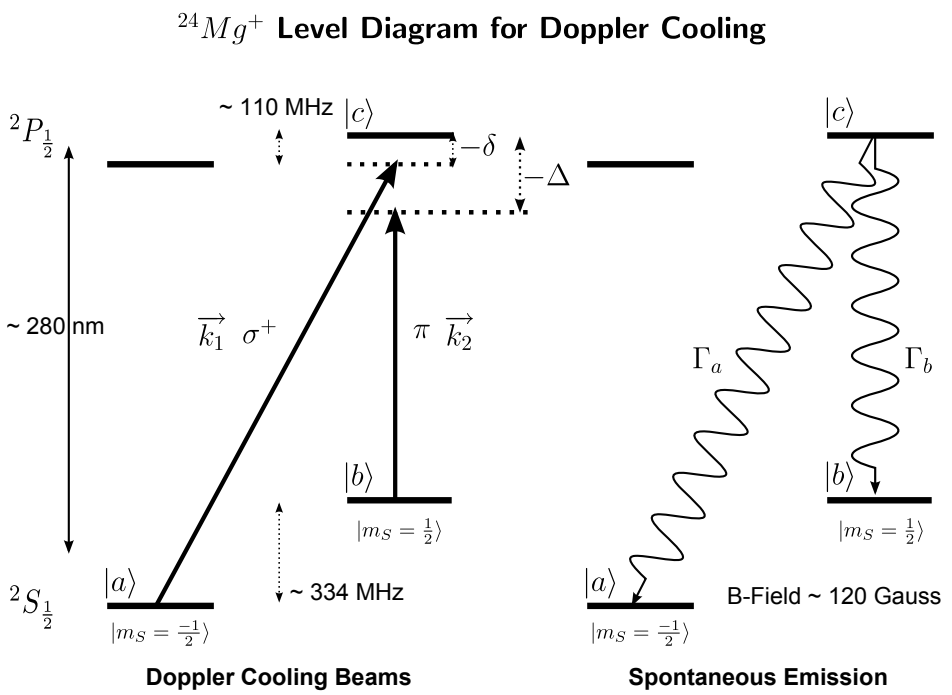

Figure 5.3: The ^{24}Mg$^+$ internal levels used for Doppler cooling. The three relevant internal levels are labeled $|a\rangle$, $|b\rangle$, and $|c\rangle$. The figure on the left shows the different laser beams. Two different laser beams are used. Beam one is labeled with $\overrightarrow{k_1}$ and has σ^+ polarization with a detuning δ from state $|c\rangle$. Beam two is labeled with $\overrightarrow{k_2}$ and has π polarization with a detuning Δ from state $|c\rangle$. The figure on the right shows the different spontaneous decay paths Γ_a and Γ_b from the excited state $|c\rangle$.

between the $^2S_{\frac{1}{2}}$ and $^2P_{\frac{1}{2}}$ states of ^{24}Mg$^+$, when the ion is in a finite magnetic field, requiring a more complicated model to be used. A three-level system will be used to model the lasers used for Doppler cooling in ^{24}Mg$^+$. Two photons will be required to prevent the population getting trapped and as result, this system exhibits "dark resonances" when the condition $s \ll 1$ is not satisfied, which can potentially be used to enhance the cooling [Lindberg 86, Blatt 90]. A master equation approach can be used to find the populations and the scattering rates. The disadvantage to using a simple rate equation approach is that coherent effects such as dark resonances do not show up in results of the calculations for large values of s.

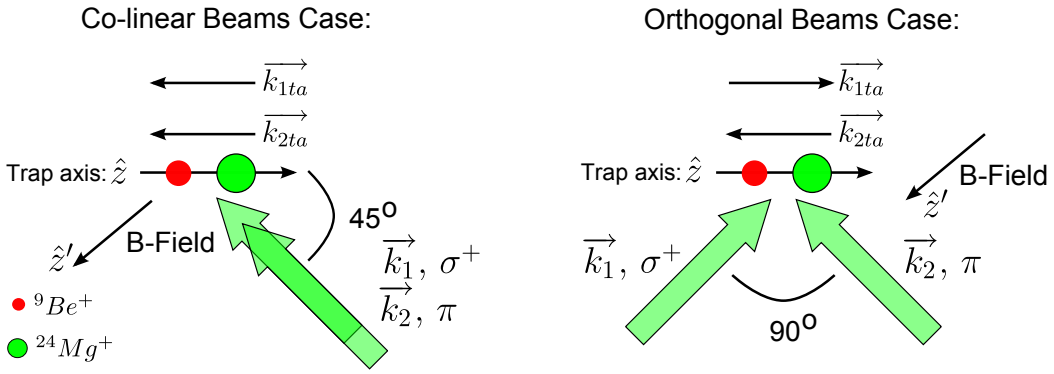

Figure 5.4: Orientation of the $^{24}Mg^{+}$ laser beams for Doppler cooling with respect to the trap axis and the magnetic field. There are two relevant laser beams labeled with wave vectors $\overrightarrow{k_1}$ and $\overrightarrow{k_2}$ with polarizations σ^+ and π. Both laser beams are oriented at 45 degrees with respect to the trap axis. Their projections along the trap axis (ta) are labeled $\overrightarrow{k_{1ta}}$ and $\overrightarrow{k_{2ta}}$ respectively. In the co-linear case, their projections along the trap axis are in the same direction and the beams are perpendicular to the magnetic field. In this case there is a σ^- polarization component, but it is off resonance and can be neglected to a good approximation. In the orthogonal beam case, one beam is parallel to the magnetic field and one is orthogonal. The projection of the two wavevectors along the trap axis are in opposite directions.

The goal of the master equation is to describe the evolution of a system interacting with the environment [Haroche 06, Cohen-Tannoudji 92, McDonnell 03]. The environment is too complicated to model completely. However, it can often be simplified to a few relevant interactions. The effect of the environment that will be modeled here is an atom's interaction with electromagnetic vacuum fluctuations. This results in spontaneous emission from the excited state of the atom. It is a assumed the system is Markovian, meaning the systems future state depends only on its current state.

The Linbald form of the master equation is used [Haroche 06], which describes

the time evolution of the density matrix ρ of the system.

$$\frac{\partial \rho}{\partial t} = -\frac{\imath}{\hbar}\left[H, \rho\right] + \sum_{i \neq 0}\left(L_i \rho L_i^{\dagger} - \frac{1}{2} L_i^{\dagger} L_i \rho - \frac{1}{2}\rho L_i^{\dagger} L_i\right) \tag{5.14}$$

The Hamiltonian of the system is given by H, and L_i represent the different Linbald operators. This equation results in a set of coupled differential equations that need to be solved to find the time evolution of the density matrix. The calculations are usually simplified if the resulting set of differential equations is linear and homogeneous in time. This is often accomplished by transforming the Hamiltonian to the interaction picture by going to the appropriate rotating frame. The steady state case where $\frac{\partial \rho}{\partial t} = 0$ is the easier of the cases to be solved. For more complicated dynamics and systems it can be computationally convenient to convert the density matrix into a column vector format [McDonnell 03, Tan 99]. For a two-level system this would be

$$\rho = \begin{bmatrix} \rho_{11} & \rho_{12} \\ \rho_{21} & \rho_{22} \end{bmatrix} \Longrightarrow \tilde{\rho} = \begin{bmatrix} \rho_{11} \\ \rho_{21} \\ \rho_{12} \\ \rho_{22} \end{bmatrix}, \tag{5.15}$$

where $\sim$ over a variable will be used to denote a column vector. In order to convert equation (5.14) into this form, an operator A that acts on ρ needs to be transformed to act on $\tilde{\rho}$. The transformation will depend on whether or not the operator is pre or post multiplying the density matrix. For pre multiplication the transformation [McDonnell 03, Tan 99] is

$$B = A\rho \Rightarrow \tilde{B} = \left(I \otimes A\right)\tilde{\rho}. \tag{5.16}$$

The transformation for post multiplication of the operator is

$$C = \rho A \Rightarrow \tilde{C} = \left(A^T \otimes I\right)\tilde{\rho}. \tag{5.17}$$

The superscript T represents taking the matrix transpose, and I is the identity matrix

with the same dimensions as ρ. In this format equation (5.14) can be written as

$$\frac{\partial \tilde{\rho}}{\partial t} = M\tilde{\rho}. \tag{5.18}$$

The solution for this differential equation is

$$\tilde{\rho}\,(t) = e^{\int M dt}\tilde{\rho}\,(0) = e^{Mt}\tilde{\rho}\,(0)\,. \tag{5.19}$$

The matrix M is time-independent. Routines exist to perform the matrix exponentiation of Mt [Tan 99, Matlab , Mathematica].

5.4.1 The System Hamiltonian

A three-level system is used to study Doppler cooling of $^{24}Mg^{+}$, and the basis states are $|a\rangle\,, |b\rangle\,,$ and $|c\rangle$ (see figure 5.3). the density matrix for the system will take the form

$$\rho = \begin{bmatrix} \rho_{aa} & \rho_{ab} & \rho_{ac} \\ \rho_{ba} & \rho_{bb} & \rho_{bc} \\ \rho_{ca} & \rho_{cb} & \rho_{cc} \end{bmatrix}. \tag{5.20}$$

There are two components to the Hamiltonian

$$H = H_a + H_l. \tag{5.21}$$

The Hamiltonian H_a represents the internal states of the atom, and H_l represents the atom-laser interaction. The Hamiltonian for the internal state is given by the energy of the three possible levels, which is written in terms of the angular frequencies.

$$H_a = \hbar \begin{bmatrix} \omega_a & 0 & 0 \\ 0 & \omega_b & 0 \\ 0 & 0 & \omega_c \end{bmatrix}. \tag{5.22}$$

The interaction of the laser with the ion's is through an electric dipole transition [Cohen-Tannoudji 92, Wineland 98].

$$H_l = -\vec{\mu_e} \cdot \vec{E}(t). \tag{5.23}$$

This Hamiltonian describes the coupling of ions electric dipole moment $\vec{\mu_e}$ to the electric field $\vec{E}(t)$ of the laser. The dipole moment is written as

$$\vec{\mu_e} = -e \langle j | \vec{r} | k \rangle . \tag{5.24}$$

When the atom has a single optically-active electron (as with $^{24}Mg^{+}$), the vector $\vec{r}$ is the electron's position relative to the nucleus and e the charge of the electron. The states $|j\rangle$ and $|k\rangle$ are the internal states connected by the laser. The electric field of laser is

$$\vec{E_i}(t) = E_o \hat{\epsilon}_i \cos(\omega_i t + \phi_i) . \tag{5.25}$$

The index i sums over the different laser beams, which have an angular frequency ω_i, phase ϕ_i, and polarization $\vec{\epsilon_i}$. Substituting equation (5.25) into equation (5.23) gives

$$H_l = \hbar\Omega_1 \cos(\omega_1 t + \phi_1) |c\rangle \langle a| + \hbar\Omega_2 \cos(\omega_2 t + \phi_2) |c\rangle \langle b| + h.c.. \tag{5.26}$$

The Rabi frequency Ω_i describes the rate at which transitions are made and is given by

$$\Omega_i = -\frac{e}{\hbar} E_o \langle j | \vec{r} \cdot \vec{\epsilon} | k \rangle . \tag{5.27}$$

The atom-laser interaction Hamiltonian for the system in figure (5.3) can be written in matrix form

$$H_l = \hbar \begin{bmatrix} 0 & 0 & \frac{\Omega_1}{2}\left(e^{i(\omega_1 t - \phi_1)} + e^{-i(\omega_1 t - \phi_1)}\right) \\ 0 & 0 & \frac{\Omega_2}{2}\left(e^{i(\omega_2 t - \phi_2)} + e^{-i(\omega_2 t - \phi_2)}\right) \\ \frac{\Omega_1}{2}\left(e^{i(\omega_1 t - \phi_1)} + e^{-i(\omega_1 t - \phi_1)}\right) & \frac{\Omega_2}{2}\left(e^{i(\omega_2 t - \phi_2)} + e^{-i(\omega_2 t - \phi_2)}\right) & 0 \end{bmatrix}, \tag{5.28}$$

where the cosine terms have been written in terms of exponentials. It is convenient to rewrite the laser frequencies in terms of the atomic energy levels and the detunings:

$$\omega_1 = \omega_c - \omega_a + \delta \tag{5.29}$$

$$\omega_2 = \omega_c - \omega_b + \Delta. \tag{5.30}$$

The Hamiltonian is time dependent, which makes the system more difficult to solve. If the interaction picture is used the time dependence of the equations can be removed.

This is accomplished by transforming into a series of rotating frames and dropping rapidly-oscillating terms. To do this rewrite equation (5.21) as two parts

$$H = H_o + V, \tag{5.31}$$

where H_o is often chosen as the unperturbed Hamiltonian of the system. In this case it is convenient to use a slightly different form. It is chosen such that it removes the time dependence from the interaction Hamiltonian. To accomplish this, H_o is for this system

$$H_o = \hbar \begin{bmatrix} \omega_a - \delta & 0 & 0 \\ 0 & \omega_b - \Delta & 0 \\ 0 & 0 & \omega_c \end{bmatrix}. \tag{5.32}$$

This leaves all of the time dependence in V , which is given by.

$$V = \hbar \begin{bmatrix} \delta & 0 & \frac{\Omega_1}{2}\left(e^{i(\omega_1 t-\phi_1)} + e^{-i(\omega_1 t-\phi_1)}\right) \\ 0 & \Delta & \frac{\Omega_2}{2}\left(e^{i(\omega_2 t-\phi_2)} + e^{-i(\omega_2 t-\phi_2)}\right) \\ \frac{\Omega_1}{2}\left(e^{i(\omega_1 t-\phi_1)} + e^{-i(\omega_1 t-\phi_1)}\right) & \frac{\Omega_2}{2}\left(e^{i(\omega_2 t-\phi_2)} + e^{-i(\omega_2 t-\phi_2)}\right) & 0 \end{bmatrix}. \tag{5.33}$$

The transformation [Sakurai 94] to the interaction picture is

$$H' = e^{\frac{i}{\hbar}H_o} V e^{-\frac{i}{\hbar}H_o}. \tag{5.34}$$

Substituting equations (5.29) and (5.30) for the laser frequencies, gives

$$H' = \hbar \begin{bmatrix} \delta & 0 & \frac{\Omega_1}{2}e^{-\imath\phi_1}\left(1 + e^{-2i(\omega_c-\omega_a+\delta)t+2i\phi_1}\right) \\ 0 & \Delta & \frac{\Omega_2}{2}e^{-\imath\phi_2}\left(1 + e^{-2i(\omega_c-\omega_b+\Delta)t+2i\phi_2}\right) \\ \frac{\Omega_1}{2}e^{-i\phi_1}\left(1 + e^{2i(\omega_c-\omega_a+\delta)t+2i\phi_1}\right) & \frac{\Omega_2}{2}e^{-\imath\phi_2}\left(1 + e^{2i(\omega_c-\omega_b+\Delta)t+2i\phi_2}\right) & 0 \end{bmatrix} \tag{5.35}$$

for the interaction picture Hamiltonian. The rotating wave approximation [Cohen-Tannoudji 92] can be made that allows exponential terms having a frequency near twice the transition frequencies to be dropped. This is reasonable since these terms rapidly average to zero. In addition if we chose the time origin appropriately, we can set $\phi_1 = 0$ and $\phi_2 = 0$, then the interaction Hamiltonian takes on the much simpler form

$$H' = \hbar \begin{bmatrix} \delta & 0 & \frac{\Omega_1}{2} \\ 0 & \Delta & \frac{\Omega_2}{2} \\ \frac{\Omega_1}{2} & \frac{\Omega_2}{2} & 0 \end{bmatrix}. \tag{5.36}$$

For the model of $^{24}Mg^{+}$ the only Linbald operators taken into account are those for spontaneous emission, see figure (5.3). They can be written down by inspection. They couple the excited state to one of the ground states at rates given by the spontaneous decay rate,

$$L_1 = \sqrt{\Gamma\left(1-\beta_r\right)}\left|a\right\rangle\left\langle c\right| \tag{5.37}$$

$$L_2 = \sqrt{\Gamma\beta_r}\left|b\right\rangle\left\langle c\right|. \tag{5.38}$$

The branching ratio for the $|c\rangle \rightarrow |b\rangle$ decay path is given by β_r, and for $^{24}Mg^{+}$ $\beta_r = \frac{1}{3}$. This value comes from the Clebsch-Gordon coefficients [Griffiths 95] for the coupling of the ground and excited states in the $^2S_{\frac{1}{2}} \Rightarrow ^2P_{\frac{1}{2}}$ system.

5.4.2 Calculating Populations

5.4.2.1 Steady State Solutions

The set of differential equations is found by plugging equations (5.20), (5.36), (5.37), and (5.38) into equation (5.14). This gives the following set of equations

$$\frac{\partial\rho_{aa}}{\partial t} = (\Gamma-\beta_r\Gamma)\rho_{\mathrm{cc}} - \frac{1}{2}i\left(\rho_{\mathrm{ac}}-\rho_{\mathrm{ca}}\right)\Omega_1 \tag{5.39}$$

$$\frac{\partial\rho_{bb}}{\partial t} = \beta_r\Gamma\rho_{\mathrm{cc}} - \frac{1}{2}i\left(\rho_{\mathrm{bc}}-\rho_{\mathrm{cb}}\right)\Omega_2 \tag{5.40}$$

$$\frac{\partial\rho_{cc}}{\partial t} = \frac{1}{2}i\left(\left(\rho_{\mathrm{ac}}-\rho_{\mathrm{ca}}\right)\Omega_1 + \left(\rho_{\mathrm{bc}}-\rho_{\mathrm{cb}}\right)\Omega_2\right) - \Gamma\rho_{\mathrm{cc}} \tag{5.41}$$

$$\frac{\partial\rho_{ab}}{\partial t} = \frac{\partial\rho^{\star}_{ba}}{\partial t} = \frac{1}{2}i\left(2(\delta-\Delta)\rho_{\mathrm{ab}} + \rho_{\mathrm{cb}}\Omega_1 - \rho_{\mathrm{ac}}\Omega_2\right) \tag{5.42}$$

$$\frac{\partial\rho_{ac}}{\partial t} = \frac{\partial\rho^{\star}_{ca}}{\partial t} = -\frac{1}{2}\left(\left(\Gamma-2i\delta\right)\rho_{\mathrm{ac}} + i\left(\rho_{\mathrm{aa}}\Omega_1 - \rho_{\mathrm{cc}}\Omega_1 + \rho_{\mathrm{ab}}\Omega_2\right)\right) \tag{5.43}$$

$$\frac{\partial\rho_{bc}}{\partial t} = \frac{\partial\rho^{\star}_{cb}}{\partial t} = \frac{1}{2}\left(-\left(\Gamma-2i\Delta\right)\rho_{\mathrm{bc}} - i\left(\rho_{\mathrm{ba}}\Omega_1 + \left(\rho_{\mathrm{bb}}-\rho_{\mathrm{cc}}\right)\Omega_2\right)\right). \tag{5.44}$$

The steady state solution is often the only relevant one, where $\frac{\partial\rho}{\partial t} = 0$. This can be found by solving the set of linear differential equations. The constraint the $Tr[\rho] = 1$ is imposed on the system, which guarantees the populations sum to 1. The solutions

Table: Populations	
1	$\rho_{aa} = \frac{16\delta^4-32\Delta\delta^3+4\left(4\Delta^2-\Omega^2\right)\delta^2+3\Omega^4+4\Gamma^2(\delta-\Delta)^2+4\Delta^2\Omega^2}{2(8\delta^4-16\Delta\delta^3+2(6\Delta^2+\Omega^2)\delta^2-2(4\Delta^3+3\Omega^2\Delta)\delta+4\Delta^4+3\Omega^4+3\Gamma^2(\delta-\Delta)^2+4\Delta^2\Omega^2)}$
2	$\rho_{bb} = \frac{8\Delta^4-16\delta\Delta^3-2\Omega^2\Delta^2+3\Omega^4+2\Gamma^2(\delta-\Delta)^2+2\delta^2\left(4\Delta^2+\Omega^2\right)}{2(8\delta^4-16\Delta\delta^3+2(6\Delta^2+\Omega^2)\delta^2-2(4\Delta^3+3\Omega^2\Delta)\delta+4\Delta^4+3\Omega^4+3\Gamma^2(\delta-\Delta)^2+4\Delta^2\Omega^2)}$
3	$\rho_{cc} = \frac{3(\delta-\Delta)^2\Omega^2}{8\delta^4-16\Delta\delta^3+2(6\Delta^2+\Omega^2)\delta^2-2(4\Delta^3+3\Omega^2\Delta)\delta+4\Delta^4+3\Omega^4+3\Gamma^2(\delta-\Delta)^2+4\Delta^2\Omega^2}$
4	$\rho_{ab} = \rho_{ba}^\star = \frac{\Omega^2\left(4\delta^2-6\Delta\delta+2\Delta^2-3\Omega^2-3i\Gamma(\delta-\Delta)\right)}{2(8\delta^4-16\Delta\delta^3+2(6\Delta^2+\Omega^2)\delta^2-2(4\Delta^3+3\Omega^2\Delta)\delta+4\Delta^4+3\Omega^4+3\Gamma^2(\delta-\Delta)^2+4\Delta^2\Omega^2)}$
5	$\rho_{ac} = \rho_{bc}^\star = \frac{(\delta-\Delta)\Omega\left(8\delta^2-8\Delta\delta-3\Omega^2-4i\Gamma(\delta-\Delta)\right)}{2(8\delta^4-16\Delta\delta^3+2(6\Delta^2+\Omega^2)\delta^2-2(4\Delta^3+3\Omega^2\Delta)\delta+4\Delta^4+3\Omega^4+3\Gamma^2(\delta-\Delta)^2+4\Delta^2\Omega^2)}$
6	$\rho_{bc} = \rho_{cb}^\star = \frac{(\delta-\Delta)\Omega\left(-4\Delta^2+4\delta\Delta+3\Omega^2-2i\Gamma(\delta-\Delta)\right)}{2(8\delta^4-16\Delta\delta^3+2(6\Delta^2+\Omega^2)\delta^2-2(4\Delta^3+3\Omega^2\Delta)\delta+4\Delta^4+3\Omega^4+3\Gamma^2(\delta-\Delta)^2+4\Delta^2\Omega^2)}$

Table 5.1: Populations for the three level system.

are quite complicated but can be simplified if a few assumptions are made. Taking $\Omega_1 = \Omega_2 = \Omega$ and $\beta_r = \frac{1}{3}$ results in solutions shown in table (5.1).

These equations can be used to help find the optimum parameters for Doppler cooling. There are a few experimental constraints. Laser beam 1 will ideally be tuned to resonance on the $|a\rangle \rightarrow |c\rangle$ transition. This is because this beam is also used for resonant repumping during Raman cooling. The parameters that can be adjusted are the detuning and the Rabi frequencies of the two beams.

It will be useful to examine the results of the above equations for some real experimental parameters. The radiative linewidth of the $^2S_{\frac{1}{2}}$ to $^2P_{\frac{1}{2}}$ transition [Herrmann 09, Jost 09] of $^{24}Mg^+$ is 41 MHz, which gives $\Gamma = 2\pi \times 41$ MHz. Laser beam 1 couples $|^2S_{\frac{1}{2}}, m_j = -\frac{1}{2}\rangle \rightarrow |^2P_{\frac{1}{2}}, m_j' = \frac{1}{2}\rangle$ with σ^+ polarized light. A typical waist of the beam is about 15 μm and there is about 0.5 μW of power in the laser beam[1] . The Rabi frequency for this transition can be found using equation (A.1) to be $\Omega = 2\pi \times 18$ MHz.

[1] Technical aside: Typically we have about $\approx 100\mu W$ in this beam but most of it is off resonance by 9.2 GHz and the polarization is $\vec{\epsilon} = \frac{1}{2}\left(\epsilon^{\sigma^+} + \epsilon^{\sigma^-}\right)$, which gives $\approx 50\mu W$ at the right polarization. An electro-optic modulator is used to shift the beam near resonance. The usual power setting for the electro-optic modulator puts the sidebands at about 1% of the power of the carrier, or $0.5\mu W$.

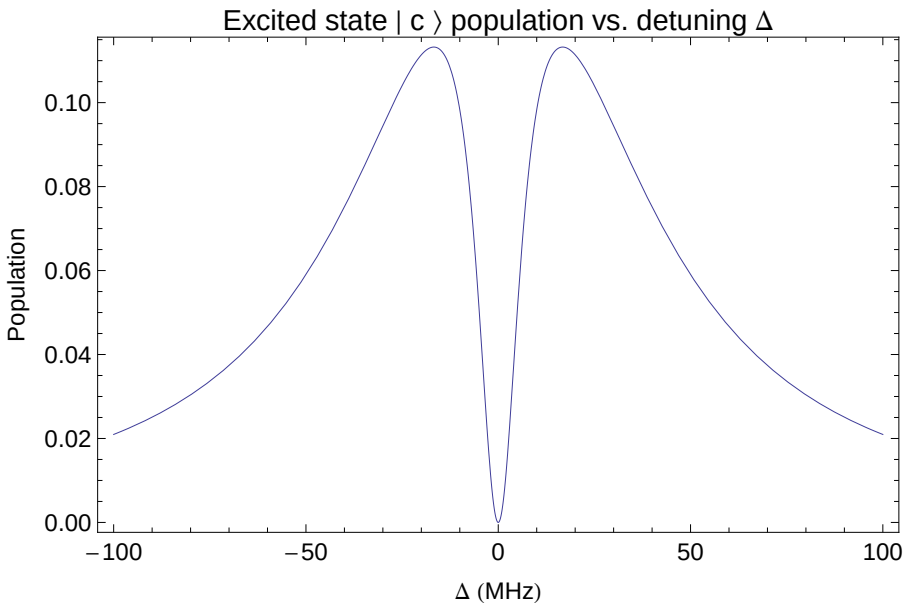

Figure 5.5: The steady state population of state $|c\rangle$ for the three-level model for $^{24}Mg^{+}$ Doppler cooling for various detunings Δ of laser beam 2. The detuning $\delta = 0$ and $\Omega = 2\pi \times 18$ MHz.

Laser beam 2 couples $|^2S_{\frac{1}{2}}, m_j = +\frac{1}{2}\rangle \rightarrow |^2P_{\frac{1}{2}}, m'_j = +\frac{1}{2}\rangle$ with π polarized light. This beam has a similar amount of laser power[2] and waist. Figures (5.5), (5.6), and (5.7) show the excited state population as a function of the detuning Δ of laser beam 2.

There is a major difference between the three-level system and a two-level system, which is exhibited in figure (5.5). The dip in the excited state population at Δ=0 is the result of a coherent process of the two laser beams interfering, when they have the same detuning from the excited state. This is know as coherent population trapping [McDonnell 03, Dalton 82] or a "dark resonance" [Blatt 90, Lindberg 86]. It leads to a suppression of the excited state population and thus the scattering rate

$$\frac{dN}{dt} = \Gamma \rho_{cc}. \tag{5.45}$$

This condition needs to be avoided for Doppler cooling. If the scattering rate goes zero

[2] This beam typically has $300\mu W$ of power and a polarization of $\vec{\epsilon} = \frac{1}{2}\left(\epsilon^{\sigma^+} + \epsilon^{\sigma^-}\right) + \frac{1}{2}\epsilon^{\pi}$. As described in footnote1 the electro-optic modulator puts about 1% of the power in the near resonant sideband. This gives a power of $\approx 1.5\mu W$ in beam 2. For the sake of the model the two laser beam powers will be considered to be the same

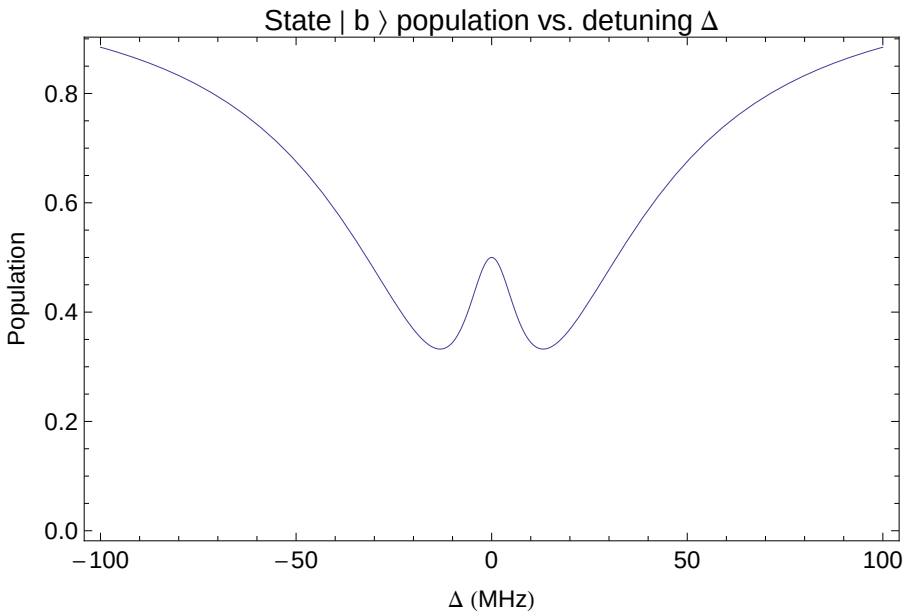

Figure 5.6: The steady state population of state $|b\rangle$ for the three-level model for $^{24}Mg^{+}$ Doppler cooling for various detunings Δ of laser beam 2. The detuning $\delta = 0$ and $\Omega = 2\pi \times 18$ MHz.

there will be no Doppler cooling, since the ion will scatter no photons. The width of the dip in figure (5.5) depends only on the Rabi frequencies and the branching ratio of the excited state. This can be seen by finding the maximum of the excited state populations, where $\frac{d\rho_{cc}}{dt} = 0$ for arbitrary Ω_1, Ω_2, and β. It is still assumed that $\delta = 0$. The maximum of the excited state population occurs at detunings of

$$\Delta = \pm \frac{\sqrt[4]{\left(\Omega_1^2 + \Omega_2^2\right)^2 \left(\beta_r \Omega_1^2 - (\beta_R - 1)\Omega_2^2\right)}}{2\sqrt[4]{\beta_r}\sqrt{\Omega_1}}. \tag{5.46}$$

The solution simplifies for $\Omega_1 = \Omega_2 = \Omega$ and $\beta_r = \frac{1}{3}$ to

$$\Delta = \frac{3^{\frac{1}{4}}}{\sqrt{2}}\Omega. \tag{5.47}$$

If this detuning is used, then the excited state population becomes (still assuming $\delta = 0$)

$$\rho_{cc} = \frac{1}{2\left(\sqrt{3} - 1\right)\beta_r + \frac{\Gamma^2}{\Omega^2} + \frac{2}{\sqrt{3}} + 2}. \tag{5.48}$$

A plot of the excited state population versus the Rabi frequency can be seen in figure (5.8).

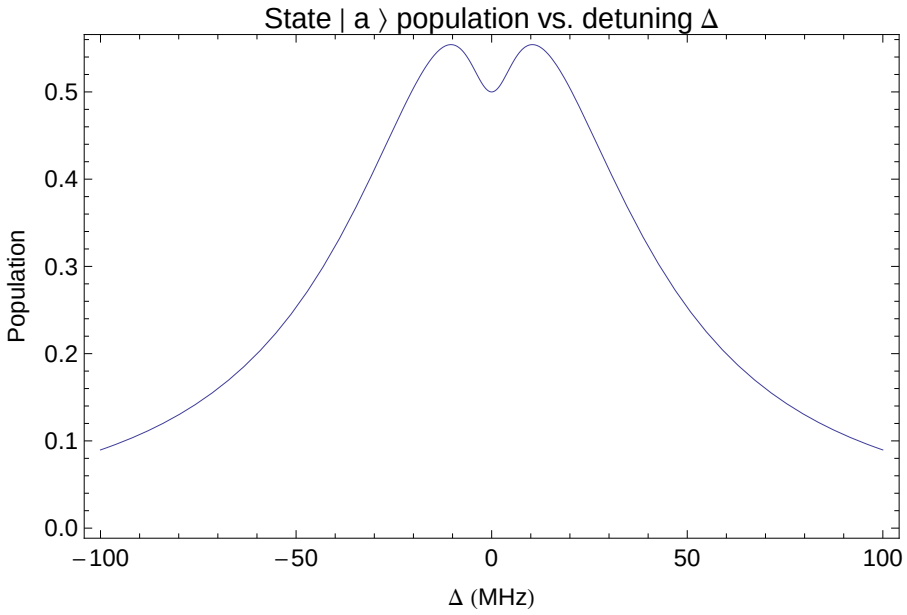

Figure 5.7: The steady state population of state $|a\rangle$ for the three-level model for $^{24}Mg^{+}$ Doppler cooling for various detunings of Δ of laser beam 2. The detuning $\delta = 0$ and $\Omega = 2\pi \times 18$ MHz.

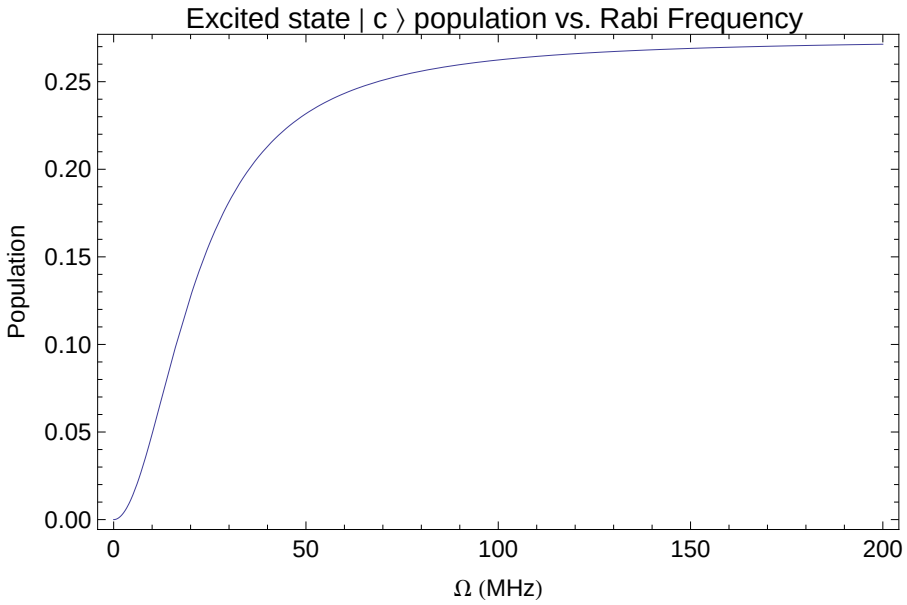

Figure 5.8: Excited state $|c\rangle$ population versus the Rabi frequency Ω of both laser beams. The detunings are $\delta = 0$ and $\Delta = \frac{3^{\frac{1}{4}}}{\sqrt{2}}\Omega$. The value for β_r and Γ is the same as in figure (5.5)

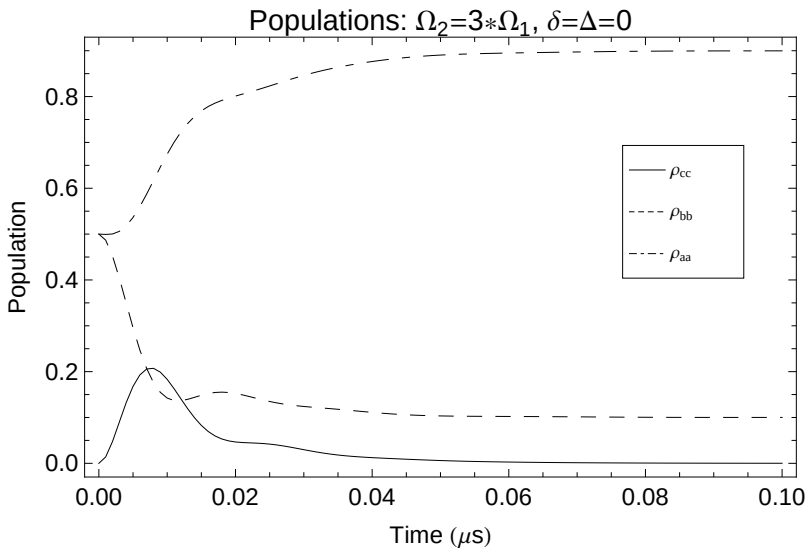

Figure 5.9: Populations as function of time for detunings $\Delta = \delta = 0$. The Rabi frequencies used are $\Omega_1 = \Omega = 2\pi \times 18$ MHz and $\Omega_2 = 3 \times \Omega_1$. The linewidth and branching ratio are $\Gamma = 2\pi \times 41$ MHz and $\beta_r = 1/3$.

5.4.2.2 Time Dependent Solutions

The time evolution of the populations can be useful to understand the dynamics at short time scales. Inserting equations (5.36), (5.37), and (5.38) into (5.14) gives the same set of equations described above. Now if we convert it to a more convenient form using equations (5.15), (5.16), (5.17), and (5.18). Then the time dependent solution is given by (5.19). To find this solution the matrix exponential must be evaluated at each point in time. This can be calculated using several different mathematical software applications, but in this case Mathematica was used [Mathematica].

Two cases are shown in figures (5.9) and (5.10), where both lasers are tuned to resonance and there exists coherent population trapping. Initially the atom is in the state $\frac{1}{\sqrt{2}}|a\rangle + \frac{1}{\sqrt{2}}|b\rangle$. In the steady-state there will be zero population in the excited state and some other distribution of populations in the ground state $|a\rangle$ and $|b\rangle$, depending on the other parameters. The interesting thing to note is it takes a finite amount of time before this dark state is formed.

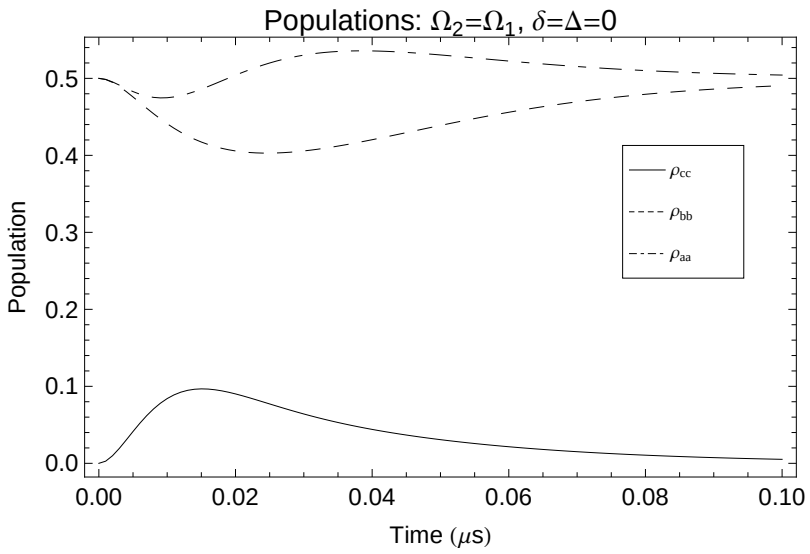

Figure 5.10: Populations as function of time for detunings $\Delta = \delta = 0$. The Rabi frequencies used are $\Omega_1 = \Omega_2 = 2\pi \times 18$ MHz. The linewidth and branching ratio are $\Gamma = 2\pi \times 41$ MHz and $\beta_r = 1/3$.

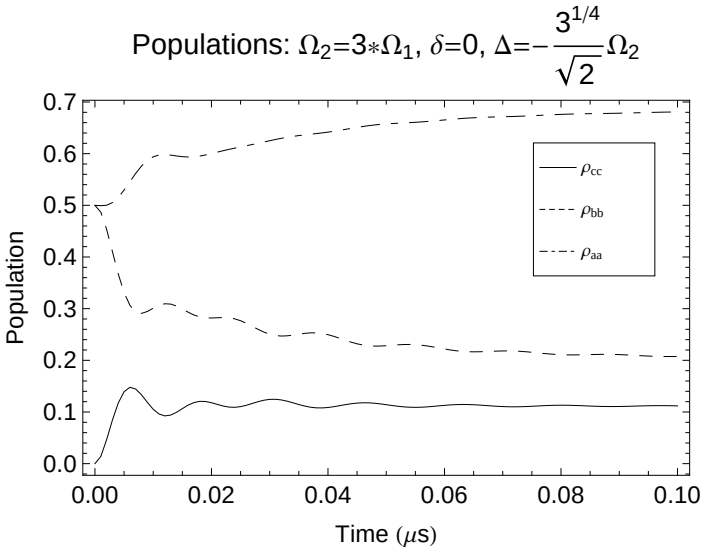

Figure 5.11: Population as function of time for detunings $\Delta = \frac{3^{\frac{1}{4}}}{\sqrt{2}}\Omega_2$ and $\delta = 0$. The Rabi frequencies used are $\Omega_1 = \Omega = 2\pi \times 18$ MHz and $\Omega_2 = 3 \times \Omega_1$. The linewidth and branching ratio are $\Gamma = 2\pi \times 41$ MHz and $\beta_r = 1/3$.

Other cases are considered is where the detuning is chosen to give the maximum population in the excited state. These are shown in figures (5.12) and (5.11). The

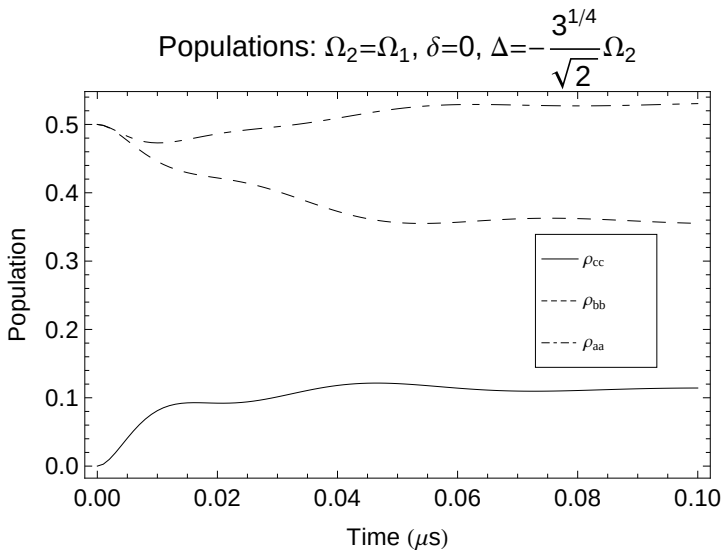

Figure 5.12: Population as function of time for detunings $\Delta = \frac{3^{\frac{1}{4}}}{\sqrt{2}}\Omega_2$ and $\delta = 0$. The Rabi frequencies used are $\Omega_1 = \Omega_2 = \Omega = 2\pi \times 18$ MHz. The linewidth and branching ratio are $\Gamma = 2\pi \times 41$ MHz and $\beta_r = 1/3$.

populations reach steady state values in ≈ 50 ns. An ion's motional oscillation frequency of ~ 3 MHz corresponds to a period of ~ 300 ns. This is longer than the settling time, so it should be reasonable to assume the system is close to the steady state. However for a precise description a more detailed calculation is needed to take this into account.

5.5 Beam Orientations and the Doppler Shift

The above discussion gives the populations for an ion at rest, which is not the case in the experiments. To try and better understand how the dark resonances where affect by the ions motion, the Doppler shift can be incorporated into the calculation of the excited state populations. It is assumed that the ions are in the steady state as discussed in section (5.4.2.2). It was found that the orientation of the two beams used in Doppler cooling affect the dark resonance.

Two cases will be analyzed. In the first case both beams are co-linear and propagating along a direction orthogonal to the quantization axis, and at 45 degrees to the

trap axis (see figure (5.4)). The second case is what is used in the actual experiment and also depicted in figure (5.4). Here, the two beams used are orthogonal to each other. The one with σ^+ polarization is parallel to the magnetic field, and the beam that creates the π polarized light is perpendicular to the magnetic field. Both beams are at 45 degrees with respect to the trap axis. The main difference between the two cases will be how the Doppler shift from the ions' motion affects the effective detuning of the laser beams. In the first case, to incorporate the Doppler shift, the substitutions $\Delta \rightarrow \Delta - \vec{k} \cdot \vec{v}$ and $\delta \rightarrow \delta - \vec{k} \cdot \vec{v}$ need to be made (Positive velocity is taken to be when the ion is moving to the left in figure 5.4). Here the Doppler shift acts as a common detuning change for both the beams. For the second case the substitution $\Delta \rightarrow \Delta - \vec{k} \cdot \vec{v}$ and $\delta \rightarrow \delta + \vec{k} \cdot \vec{v}$ will be made. In this instance, the Doppler shift acts as a differential shift between the two beams.

5.5.1 Co-linear Cooling Beams

When the two beams are co-linear, they must be oriented orthogonal to the quantization axes in order to obtain π- polarization. In this orientation it is not possible to only have σ^+ polarized light without having a σ^- polarization as well. However in this model the σ^- component will be ignored as explained above. Substituting the Doppler shift into equation (3) of table (5.1) and considering the 1D case along the trap axis, the excited state population can be plotted as a function of the velocity as seen in figure (5.13).

The shift of the maximum population to the negative velocities is a result of the detuning chosen. As can been seen in figure (5.13) for certain values of the detuning there are larger values of the excited state population. In the case plotted in figure (5.13) the Doppler shift is changing the effective detuning, which moves the center of the peak depending on the values chosen for δ and Δ. The Rabi frequencies also affect the amplitude of the excited state population. The excited state population for different

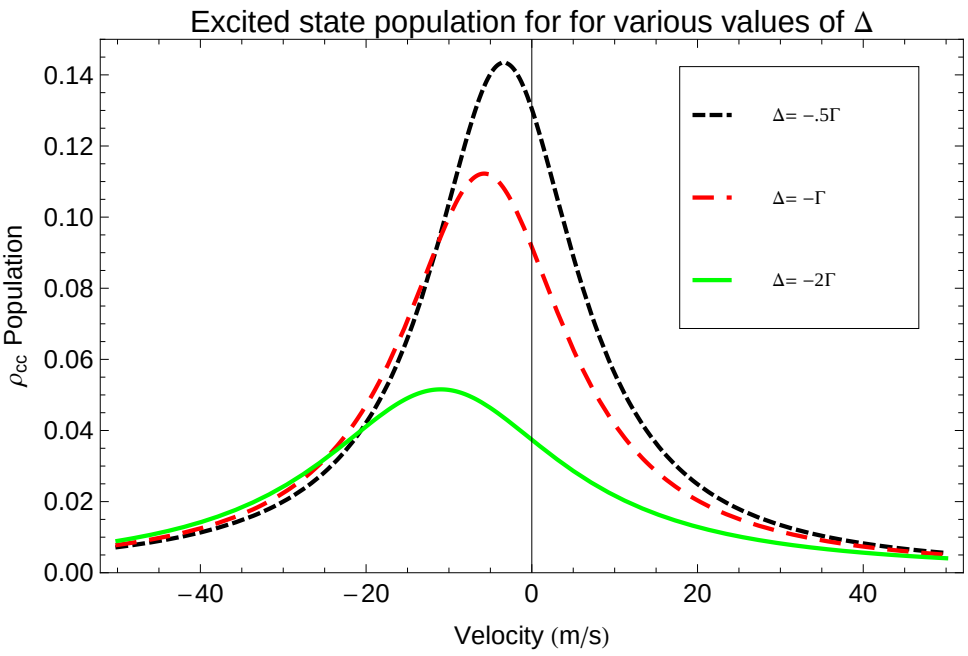

Figure 5.13: Excited state population in the co-linear Doppler cooling configuration. The population is plotted for different values of the detuning Δ. The Rabi frequencies are chosen to be $\Omega_1 = \Omega_2 = 0.5\ \Gamma$. The detuning $\delta = 0$.

Rabi frequencies Ω_2 is plotted as a function of the velocity in figure (5.14). .

5.5.2 Orthogonal Cooling Beams

In this scenario one of the beams is orthogonal to the quantization axis (see figure (5.4)), which allows for π polarization. The second beam propagates along the quantization axis and has pure σ^+ polarization. In the experiment, this beam also has an equal amount of σ^- polarization to balance out stark shifts, but is not considered in this model. Both beams are oriented at 45 degrees to the trap axis, so the k-vectors from both beams will have a $\frac{1}{\sqrt{2}}$ projection along that axis. The main difference between this case and the co-linear one considered early is the Doppler shift has the opposite sign for the two beams. This makes the Doppler shift appear as a differential shift between the beams and not a common one as in the co-linear case.

A interesting feature of this case is that beams are not orthogonal with respect to

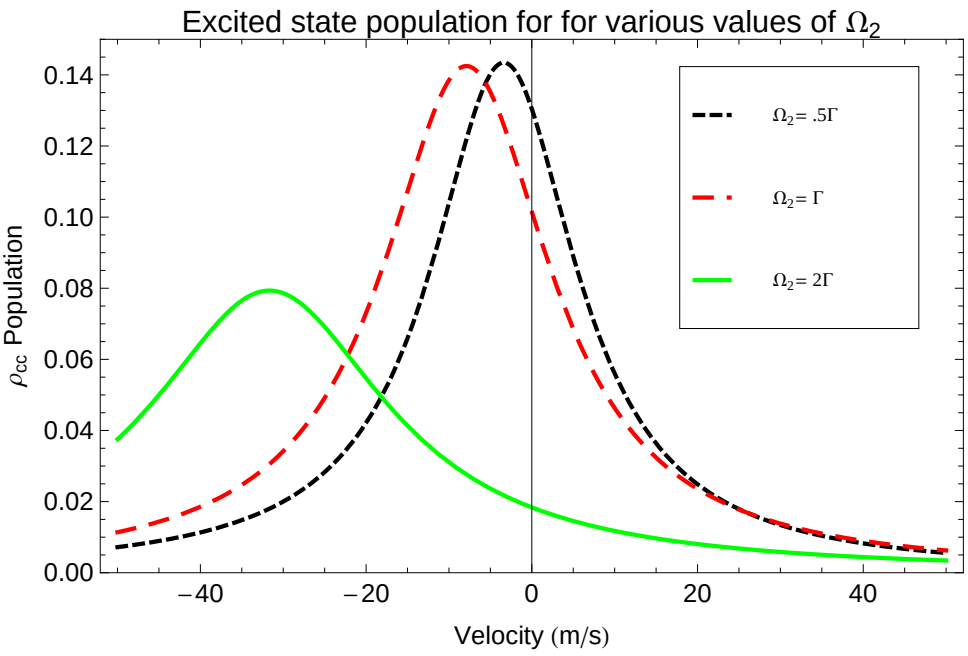

Figure 5.14: The excited state population versus the velocity along the trap axis for different values of Ω_2. The detunings are held fixed at $\delta = 0$ and $\Delta = -0.5\ \Gamma$. The Rabi frequency $\Omega_1 = 0.5\ \Gamma$.

each other in the $\hat{x}$ and $\hat{y}$ directions of the trap axes ($\hat{z}$ is trap axis), which are referred to as the radial axes (This is different from the $\hat{x}'$ and $\hat{y}'$ directions determined by the quantization axis depicted in figure (5.4), where $\hat{z}'$ is along the magnetic field). This implies that the Doppler cooling will be different between the trap axis and the radial axes.

As above, to incorporate the Doppler shift into the results for the excited state population (equation 3 table (5.1)) we make the substitutions $\Delta \rightarrow \Delta - \vec{k} \cdot \vec{v}$ and $\delta \rightarrow \delta + \vec{k} \cdot \vec{v}$. The excited state population is plotted in figure (5.15) as a function of velocity along the trap axis for different detunings of Δ. The results here are different than that obtained from those in the co-linear case shown in figure (5.13). For the co-linear case the expression for the excited state population (see equation 3 of table (5.1)) has the factor $(\delta - \Delta)^2$ in the numerator. Thus when $\delta = \Delta$ the excited state population (see equation 3 of table (5.1)) goes to zero, which is what gives rise to the dark

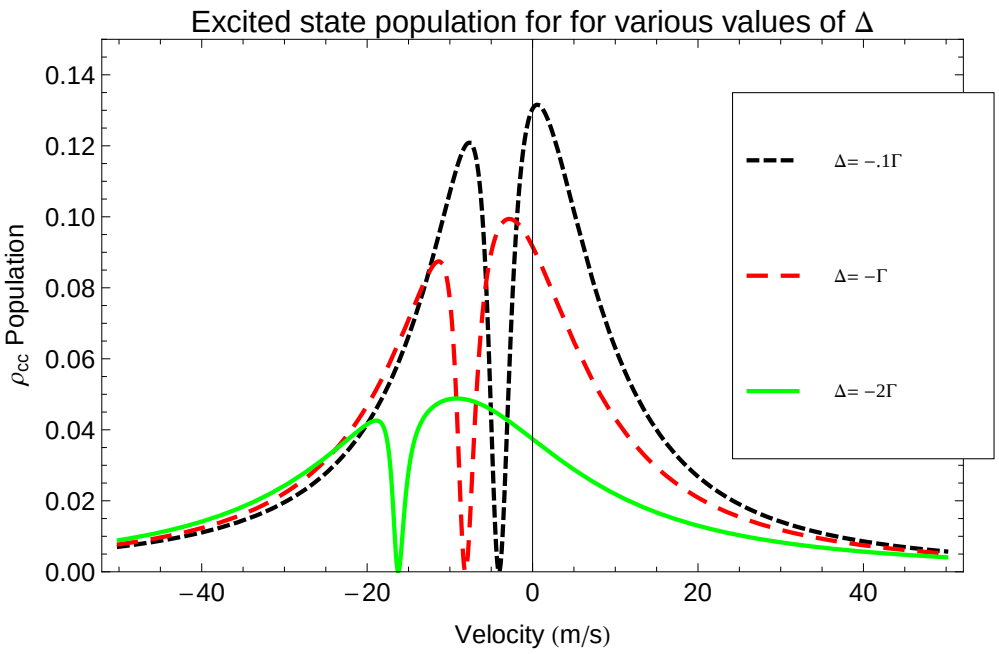

Figure 5.15: Excited state population versus velocity for the case of orthogonal Doppler cooling beams with different values of Δ. The detuning δ is held at zero, and the Rabi frequency $\Omega_1 = 0.5\,\Gamma$ and $\Omega_2 = 0.5\,\Gamma$.

resonance. The case of orthogonal beams has the factor $\left(2\vec{k}\cdot\vec{v}+\delta-\Delta\right)^2$. Thus, the dark resonance now depends on velocity and no longer occurs when the two detunings are equal. The width of this dark resonance depends on the Rabi frequency. The excited state population is plotted as a function of velocity for different Rabi frequencies Ω_2 in figure (5.17).

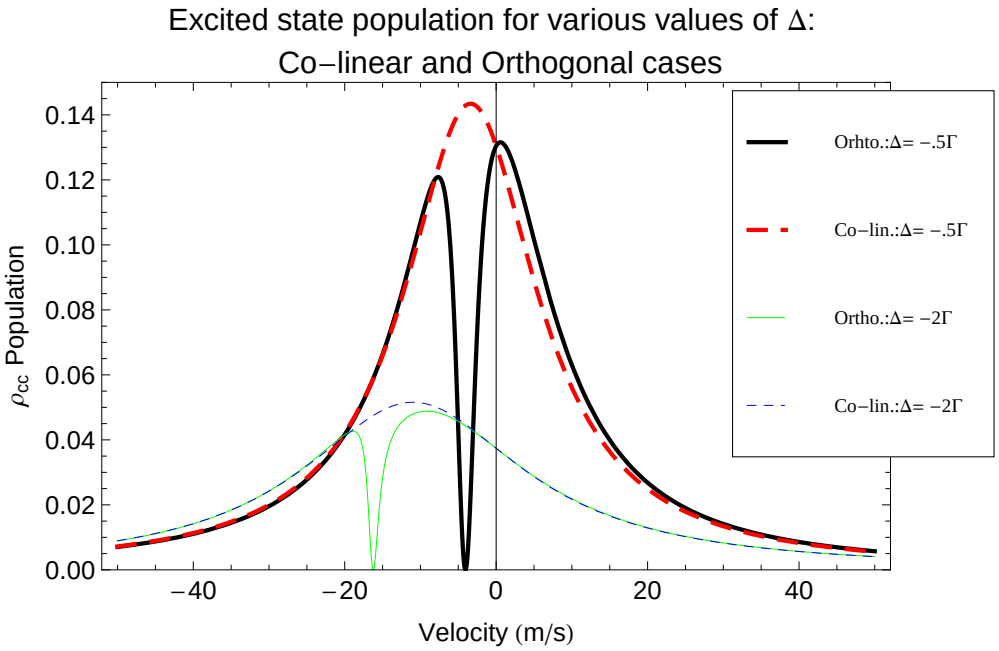

Figure 5.16: Excited state population versus velocity for the case of orthogonal and co-linear Doppler cooling beams with different values of Δ. The detuning δ is held at zero, and the Rabi frequency $\Omega_1 = 0.5\,\Gamma$ and $\Omega_2 = 0.5\,\Gamma$.

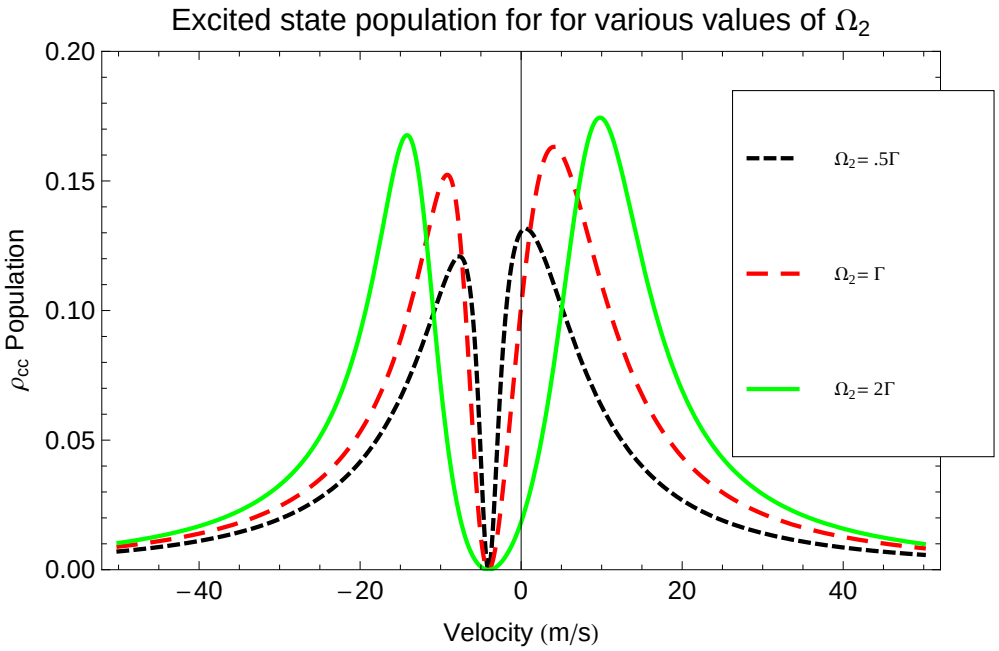

Figure 5.17: Excited state population versus velocity for orthogonal cooling beams using different values of Ω_2. The detuning δ is held at zero, and $\Delta = 0.5\,\Gamma$. The Rabi frequency $\Omega_1 = 0.5\,\Gamma$.

There is clear difference between the co-linear and orthogonal beam cases. The orthogonal beam case exhibits a velocity dependent dark resonance. This resonance could potentially be exploited to obtain colder temperatures than is possible in the two-level case. In the simplified two-level model discussed in section (5.2) the damping coefficient is determined by $\beta_d = \frac{d\rho_{cc}(v)}{dv}|_{v=0}$. Thus the steeper slope suggests that the damping can be larger. A simple model was initially considered to evaluate the final the temperatures that could be reached in this case, and it did appear that lower temperature could be reached. However, it was determined the model was too simple because it neglected stimulated-emission and dressed-state effects which are absent in the simple treatment of Doppler cooling. Therefore, a more complete theoretical treatment will be needed to describe this case. Even though we did not have an accurate model of the cooling expected for the three level system, experiments were performed to explore Doppler cooling in this system. The results of which are discussed in the next section.

5.6 Demonstration of Doppler Cooling with $^{24}Mg^{+}$

We performed experiments to observe Doppler cooling of the axial modes of a $^{9}Be^{+} - {}^{24}Mg^{+}$ ion pair as discussed in section (5.5.2). With the goal of observing better cooling than the two-level Doppler limit. Our apparatus is not setup to detect the motional state of a single $^{24}Mg^{+}$ ion, and thus $^{24}Mg^{+}$ is used to sympathetically cool a $^{9}Be^{+}$ion, which can be used to detect the motional state of the two ions. The experiment is performed by trapping a $^{9}Be^{+}$ and a $^{24}Mg^{+}$ ion together in a linear radio frequency Paul trap [Jost 09]. There are six possible normal modes of motion; however, the experiment only probes the two normal modes along the axis of weakest confinement. These are called the in-phase mode (INPH) ($f_{inph}\sim$ 1.89 MHz) and the out-of-phase mode (OOPH) ($f_{ooph}\sim$ 4.05 MHz). At the start of each experiment, the ions are placed in the same order. This is accomplished by changing the trap potentials in a way similar to that outlined in reference [Jost 09]. Both $^{9}Be^{+}$ and $^{24}Mg^{+}$ Doppler cooling

are performed during this reordering. This is followed by $^{24}Mg^{+}$ Doppler cooling. The cooling time used is > 1 ms, which is sufficient time for the ions to thermalize. The detunings of the beams were approximately $\delta/2\pi = -12$ MHz and $\Delta/2\pi = -5$ MHz. The absolute electric field from the lasers at the $^{24}Mg^{+}$ ion is not known precisely, since the beam waists were not measured (They should have a waist between 10 μm and 100 μm. There was control of the overall optical power of the beams and the ratio of the power in the two beams. These powers were varied until an optimum was found. For reference, the experimental results will be compared to the theoretical outcome of Doppler cooling on a two-level system.

To measure $\bar{n}$, a time scan of a two-photon stimulated Raman sideband transition is performed on the $^{9}Be^{+}$ ion, which is discussed in section (6.5). The sideband transition is performed on the $|F = 2, m_F = 1\rangle \rightarrow |F = 1, m_F = 0\rangle$ transition (This is the labeling of the states at low magnetic field. The experiment, like the others discussed in this thesis, are performed at a field of ~ 120 Gauss.). Following cooling those two levels are then shelved and readout as discussed in reference [Jost 09]. An estimation of the average motional occupational level $\bar{n}$, assuming a thermal distribution, can be obtained by fitting the data to the function that describes the probability P_b of finding the $^{9}Be^{+}$ ion in the $|^2S_{\frac{1}{2}}, F = 2, m_F = 2\rangle$ state, which is the bright state for resonance fluorescence detection,

$$P_b(t) = \frac{1}{2}\left[1 + \sum_{n=0}^{\infty}\sum_{k=0}^{\infty} P_n P_k e^{-\gamma t} \times \right. \tag{5.49}$$

$$\left. \cos\left(2\Omega_{n+1,n}(\Omega, n, \eta_n)\,\Omega_{k,k}(k, \eta_k)\,t\right)\right] \tag{5.50}$$

$$P_n = \frac{\bar{n}^n}{(1+\bar{n})^{n+1}} \tag{5.51}$$

$$P_k = \frac{\bar{k}^k}{\left(1+\bar{k}\right)^{k+1}} \tag{5.52}$$

$$\Omega_{n',n} = \Omega e^{\frac{-\eta^2}{2}} \left(\frac{n_<!}{n_>!}\right)^{1/2} \eta^{|n'-n|} L_{n_<}^{|n'-n|}\left(\eta^2\right) \tag{5.53}$$

(see section (6.5) for more details). It is assumed in the above model that the energies of the two motional modes are given by a thermal distribution labeled by P_n and P_k. The symbols with a horizontal "-" over them are the average motional state for a mode of motion, assuming a thermal distribution. The mode on which a transition is being driven is represented by n and the other mode which is a spectator mode [Wineland 98] is represented by k. For the spectator mode, the value of $\Omega_{k,k}\left(k, \eta_k\right)$ is the Debye-Waller factor for that mode [Wineland 98, King 98, King 99]. Decay during the sideband transition is introduced into the model with the phenomenological constant γ. The model is fit by floating the parameters $\bar{n}$, $\bar{k}$, Ω, and γ, performing a weighted nonlinear regression fit in Matlab [Matlab]. The fitting routine uses a trust-region-reflective algorithm [Matlab].

The data is obtained by first taking resonance fluorescence histograms [Langer 06] for the $^9Be^+$ion. For each experiment the histograms are averaged together and fit to a weighted sum of two Poissonian distributions. The two mean values correspond to the number of scattered photons when the ion is in the bright state and dark state. For each data point, the weights of each distribution are found by fitting, where the means are fixed from the fit values obtained from the average of all the data. The weight of the bright state is then plotted for each data point. The errors on the weights for each data point are used in the weighted fit of the sideband scan, and are one-standard-deviation error bars on the plotted data.

Figure (5.18) shows a scan of the motion adding sideband transition time on the INPH mode of motion after Doppler cooling with $^{24}Mg^+$, where each data point consists of 600 experiments. By fitting the data, the average motional occupation of the modes was $\bar{n}_{INPH} = 5.39 \pm 0.43$ and $\bar{n}_{OOPH} = 2.55 \pm 0.22$. The other parameters found from the fit were $\Omega/2\pi = 0.885 \pm 0.003$ MHz and $1/\gamma = 163 \pm 40\,\mu$s. The solid line in the

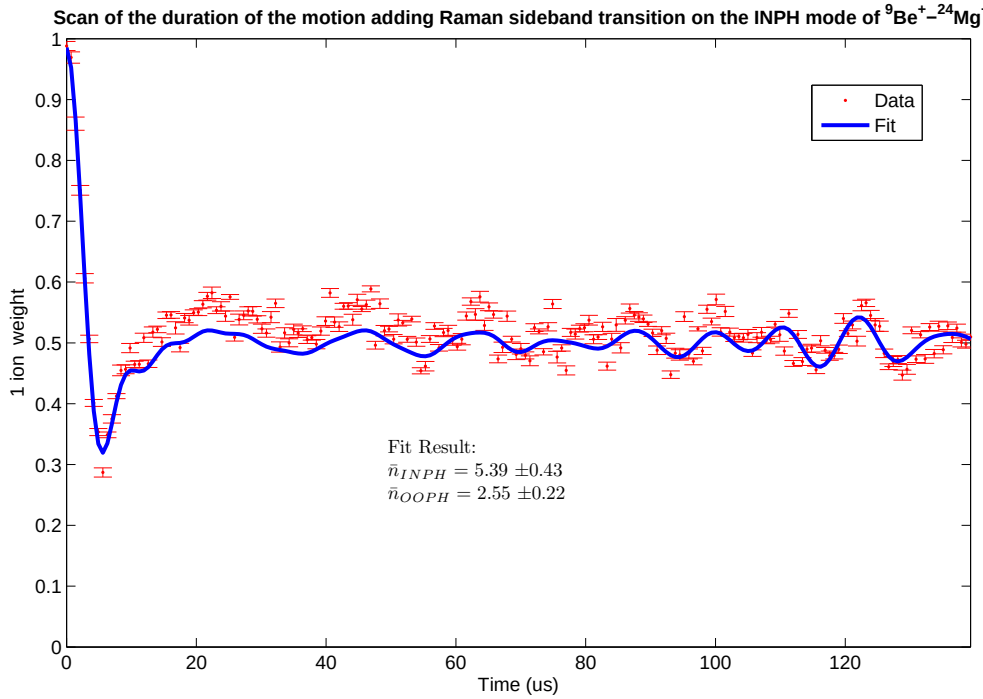

Figure 5.18: Sideband flopping on the INPH mode on a pair of $^9Be^+$and $^{24}Mg^+$ions after $^{24}Mg^+$ Doppler cooling. The solid line is the fit to the experimental data. Each data point consists of 600 experiments.

figure is the expected theoretical curve using the values of $\bar{n}$ obtained from the fit.

Figure (5.19) depicts the sideband flopping on the OOPH mode of motion after the same cooling described above. The fit result are $\bar{n}_{INPH} = 5.57 \pm 0.32$, $\bar{n}_{OOPH} = 2.29 \pm 0.11$ and $\Omega/2\pi = 0.874 \pm 0.003$ MHz. In this case the decay parameter was held fixed at $1/\gamma = 294\,\mu$s.

Figure (5.20) plots the flopping on the motion sensitive carrier transition. In this case the two Rabi frequencies in equation (5.50) would be written as $\Omega_{n,n}$ and $\Omega_{k,k}$, since no motion changing transition is made. The fit gives the following values of the parameters $\bar{n}_{INPH} = 4.18 \pm 0.34$, $\bar{n}_{OOPH} = 3.27 \pm 0.14$ and $\Omega/2\pi = 0.86 \pm 0.04$ MHz The decay parameter was fixed at a value of $\gamma = 100\,\mu$s. The results for the $\bar{n}$ for each mode do not agree well the other scans. This may be due to the carrier transition not

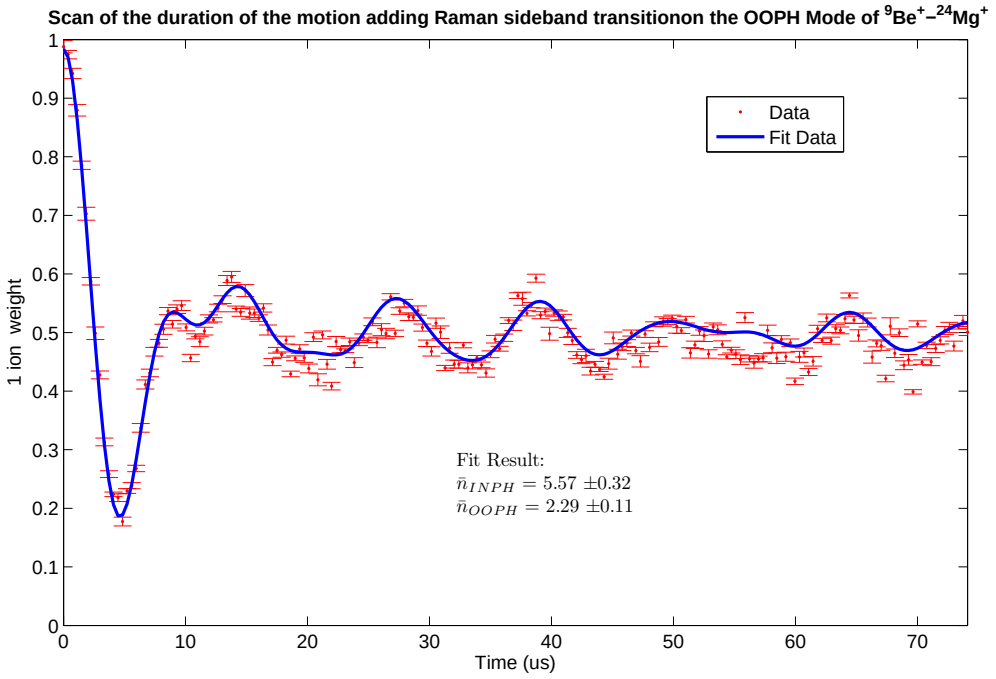

Figure 5.19: Sideband flopping on the OOPH mode on a pair of $^{9}Be^{+}$and $^{24}Mg^{+}$ions after $^{24}Mg^{+}$ Doppler cooling. The solid line is the fit to the experimental data. Each data point consists of 600 experiments.

being as sensitive to the motion.

Two-level Doppler cooling would typically be performed on a closed cycling transition in a two-level system. In this case the final temperature will be given by equation (5.1). The value of ξ plays an important role in determining the final temperature reached, where ξ is the projection of the scattered photons momentum along the axis being considered. In our experimental setup a typical Doppler cooling beam would be at 45 degrees to the trap axis and have σ^{+}- polarization. This is the orientation assumed for the theoretical calculation. The projection onto the trap-axis of the scattered photons momentum is $\xi = \frac{7}{20}$, which comes from equation (5.13). Figures (5.21) and (5.22) show the final temperature that would be reached as a function of the detuning from the excited $^{2}P_{\frac{3}{2}}$ state for $^{24}Mg^{+}$ two-level Doppler cooling on the INPH and OOPH modes. The temperature is plotted in terms of the $\bar{n}$ reached for each mode, which is given by

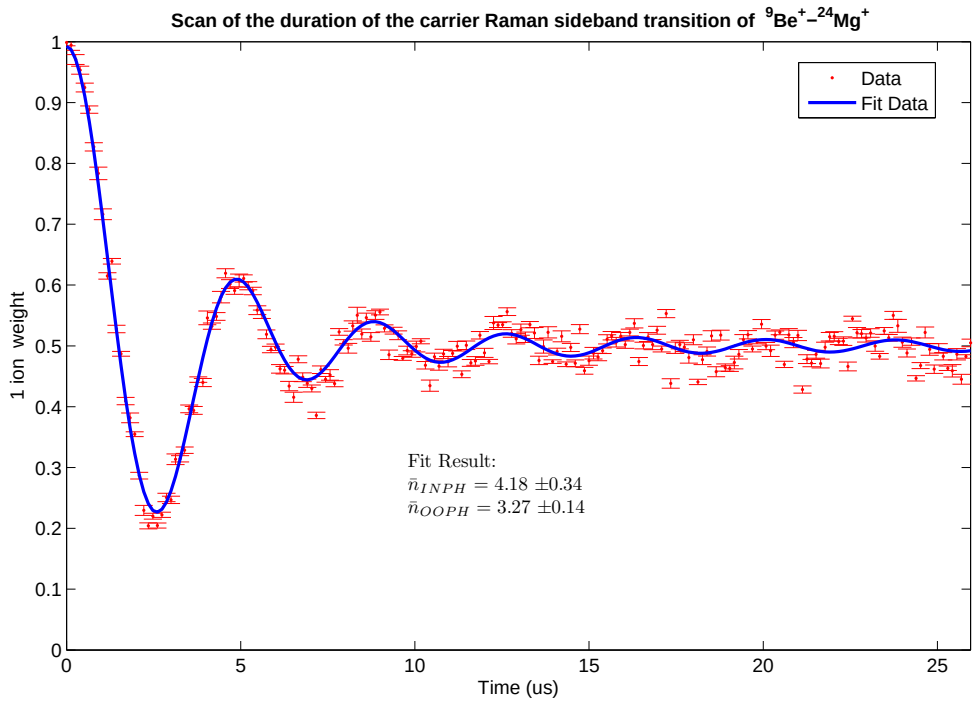

Figure 5.20: Flopping on a motion sensitive carrier transition on a pair of $^{9}Be^{+}$and $^{24}Mg^{+}$ions after $^{24}Mg^{+}$ Doppler cooling. The solid line is the fit to the experimental data. Each data point consists of 600 experiments.

equation (B.9). The two-level Doppler temperature (5.1) that assumes $\xi = 1$, is plotted as a horizontal line in each figure, which for each mode corresponds to $\bar{n}_{INPH} = 10.6$ and $\bar{n}_{OOPH} = 4.7$. It can be seen that the two-level Doppler cooling curves drop below this limit. This is a result of $\xi < 1$. The fit results $\bar{n}_{INPH} = 5.57$ and $\bar{n}_{OOPH} = 2.29$ from figure (5.18) and (5.19) are plotted as a horizontal lines in figures (5.21) and(5.22) respectively.

The temperatures reached using the three-level cooling Doppler cooling is approximately a factor of 2 lower than the typical temperature reached with two-level Doppler cooling. However, when taking the dipole-radiation patterns projection along the trap axis into account and assuming $s = 0$ as in figures (5.21) and (5.22) the three-level Doppler cooling on both modes shows a slightly lower temperature than is possible with

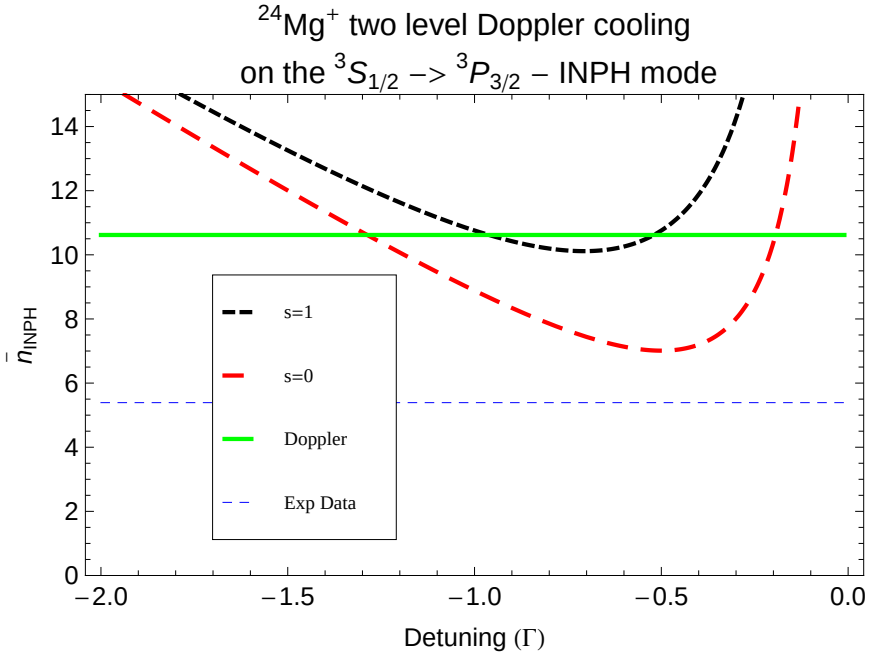

Figure 5.21: The $\bar{n}_{INPH}$ of the INPH mode of motion achieved after Doppler cooling with use of a two-level system in $^{24}Mg^{+}$ versus the detuning. The curved lines are for two different values of the saturation parameter and take into account the projection of the scattered light along the trap axis. The typical 1-D Doppler limit is plotted as a horizontal line $\bar{n}_{INPH} = 10.6$. The result of the fit to the experimental data for $\bar{n}_{INPH} = 5.57$ from figure (5.18) is shown.

two-level Doppler cooling, including the projection.

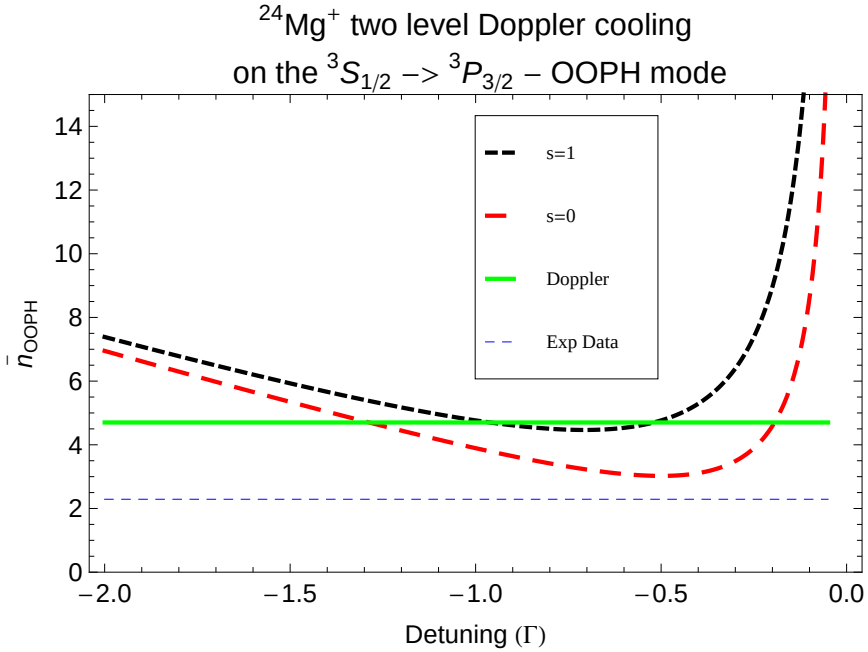

Figure 5.22: The expected $\bar{n}_{OOPH}$ of the OOPH mode of motion achieved after Doppler cooling with use of a two-level system in $^{24}Mg^{+}$ versus the detuning. The curved lines are for two different values of the saturation parameter and take into account the projection of the scattered light along the trap axis. The typical 1-D Doppler limit is plotted as a horizontal line $\bar{n}_{OOPH} = 4.7$. The result of the fit to the experimental data for $\bar{n}_{OOPH} = 2.29$ from figure (5.19) is shown.

Chapter 6

Raman Transitions and Sideband Cooling

Most physical systems are very difficult to model quantum mechanically. However, trapped ions with one valence electron can be modeled with a few simplifications. The internal states of the ions' ($^9Be^+$ and $^{24}Mg^+$) discussed here can be treated as two level systems, and the ions' motion in the ion trap is that of a quantum harmonic oscillator [Wineland 98]. The interaction of a trapped ion with a laser can lead to a coupling between the internal and the motional degrees of freedom, which provides a means to control the quantum mechanical motion of trapped ions [Wineland 98, Cirac 96a]. This has been exploited to make several non-classical motional states of trapped ions [Meekhof 96, Leibfried 96, Monroe 96, Wineland 98]. To create these various types of non-classical states it is typically necessary to cool the motion to near the quantum mechanical ground state. Through a combination of Doppler and stimulated-Raman-transition cooling this can be accomplished [Monroe 95b, King 98]. Cooling the motion of a multiple ions of one type to near the ground state using another type of ion (sympathetic cooling) is beneficial for QIP with trapped ions, since the shared motion serves as an information bus [Kielpinski 00, Barrett 03, Blinov 02, Rohde 01]. Minimizing the amount of energy in the quantized motion can help to reduce errors in some QIP operations. Also, the ability to cool logical ion qubits with sympathetic cooling ions is a necessary component for some ion trap based QIP schemes [Kielpinski 00, Kielpinski 02b]. As another example, in the experiment to entangle two mechanical oscillators discussed

in chapter (8), the motion of two pairs of trapped ions must be cooled to near ground state to before creating the desired entangled motional state.

This chapter describes how the internal and motional states of trapped ions can be manipulated with laser beams. The first section discusses a Hamiltonian representation for the internal state and motion of a trapped ion. Then it is explained how these two systems can be coupled, using a magnetic field in the interaction picture. When working with multiple ions there are many motional states that need to be accounted for, which is covered in section (6.3). In the experiments discussed in this dissertation, stimulated-Raman transitions are used to couple the internal states to the motion. In the following section (6.4) it is shown how this gives rise to the same coupling as the magnetic field discussed in section (6.2). This is followed by a brief discussion on how this interaction can be used for motional state analysis. The details of how stimulated-Raman transitions can be used to the cool the motion of trapped ions is then covered in section (6.6). Finally a demonstration experiment is discussed in section (6.6). This experiment involves the sympathetic cooling of two pairs of $^{9}Be^{+} - {}^{24}Mg^{+}$ ions in two different locations of a multi-zone ion trap array. These results and the results from reference [Jost 09] represent the first demonstration of the ability to sympathetically recool trapped ions after separating and transporting them in multi zone ion trap array.

6.1 Basic Hamiltonian

There can be many internal states for an ion with a single valence electron. For the discussion below it is assumed that only electric dipole transitions will be considered. This allows for the simplification that only two internal levels will be coupled at a time, assuming the levels are well resolved. The Hamiltonian for the internal state is given by

$$H_a = \hbar\omega_1 |1\rangle \langle 1| + \hbar\omega_2 |2\rangle \langle 2| \tag{6.1}$$

The energy for each level is given by $\hbar\omega_1$ and $\hbar\omega_2$. It will simplify the treatment to to rewrite the Hamiltonian in terms of a spin 1/2 system, where the Pauli spin operators and the energy difference ($\omega_o = \omega_2 - \omega_1$) between the two levels are used [Leibfried 03a].

$$H_a = \hbar\omega_o S_z, \tag{6.2}$$

where a constant term has been omitted. For a single trapped ion there will be three normal modes of motion. Each mode of motion can be treated independently with its own Hamiltonian, so only the z direction will be considered here.

$$H_m = \hbar\omega_z(n + 1/2). \tag{6.3}$$

The mode of motion along this axis has an oscillation frequency ω_z. The Hamiltonian can be rewritten in terms of the raising and lowering operators (a and $a^\dagger$)

$$H_m = \hbar\omega_z a^\dagger a. \tag{6.4}$$

The zero point energy has been left out since it is a constant.

6.2 Interaction Hamiltonian

The interaction that couples the internal and motional states in the experimental apparatus is a stimulated-Raman transition. This is a coherent two photon process that makes use of electric dipole transitions. This more specific case will be discussed in section (6.4). However, it is sufficient to consider a single photon electric dipole transition that has a Hamiltonian of the form $H_{ed} = -\mu_e \cdot E(z,t)$. This has the same functional form as a magnetic dipole transition[Wineland 98], which will be used for the derivation in this section. The Hamiltonian for the interaction of a spin 1/2 magnetic dipole with a magnetic field is

$$H_l = -\vec{\mu} \cdot (\vec{B}_{static} + \vec{B}\,(z,t)). \tag{6.5}$$

The magnetic dipole moment is $\vec{\mu} = \gamma \vec{S}$. The gyromagnetic ratio is represented by γ, and $\vec{S} = \vec{S}_x + \vec{S}_y + \vec{S}_z$. The static magnetic field component $\vec{B}_{static}$ is gives rise to the energy splitting in this spin 1/2 analogy represented by H_a in equation (6.2). Since eventually the light field of a laser beam will be considered by analogy, an oscillating magnetic field propagating in the $\hat{z}$ direction with a polarization in the $\hat{x}$ direction and a magnitude B_o will be used.

$$\vec{B}\,(z,t) = B_0 \hat{x} \cos\left(k \cdot z - \omega t + \phi\right). \tag{6.6}$$

The wave vector of the radiation is given by k and z is the position operator (about the ion's equilibrium), which can be written in terms of the raising and lowering operators as $z = z_o(a + a^\dagger)$. Where z_o is the spread in the ground state wave function of the ion

$$z_o = \sqrt{\frac{\hbar}{2m\omega_z}}. \tag{6.7}$$

The Hamiltonian for the interaction can now be rewritten as

$$H_l = -\frac{\gamma B_o}{4}(S^+ + S^-)\left(e^{i(k\cdot z - \omega t + \phi)} + e^{-i(k\cdot z - \omega t + \phi)}\right). \tag{6.8}$$

It useful to use the interaction picture for calculating the time evolution of the system. The time-independent Hamiltonian is given by $H_o = H_a + H_m$ and the time-dependent interaction Hamiltonian is $V_I = H_l$. This is transformed into a Hamiltonian in the interaction picture by the following

$$H_I = e^{i\frac{H_o}{\hbar}t} V_I e^{-i\frac{H_o}{\hbar}t}. \tag{6.9}$$

This can be multiplied out using the Baker-Hausdorff theorem. Another method is to use the Heisenberg equations of motion ($\frac{dA}{dt} = \frac{1}{i\hbar}[A, H]$) to find the interaction picture version of all of the all the operators, which gives

$$S^+ \rightarrow S^+ e^{i\omega_o t} \tag{6.10}$$

$$S^- \rightarrow S^- e^{-i\omega_o t} \tag{6.11}$$

$$z \rightarrow z_o(a e^{-i\omega_z t} + a^\dagger e^{i\omega_z t}). \tag{6.12}$$

The end result for the interaction a Hamiltonian is

$$\begin{aligned} H_I &= -\frac{\gamma B_o}{4}\Big[S\Big(e^{i\left(\eta(ae^{-i\omega_z t}+a^\dagger e^{i\omega_z t})-(\omega-\omega_o)t+\phi\right)} && (6.13)\\ &\quad +e^{-i\left(\eta(ae^{-i\omega_z t}+a^\dagger e^{i\omega_z t})-(\omega+\omega_o)t+\phi\right)}\Big) && (6.14)\\ &\quad +S^-\Big(e^{i\left(\eta(ae^{-i\omega_z t}+a^\dagger e^{i\omega_z t})-(\omega+\omega_o)t+\phi\right)} && (6.15)\\ &\quad +e^{-i\left(\eta(ae^{-i\omega_z t}+a^\dagger e^{i\omega_z t})-(\omega-\omega_o)t+\phi\right)}\Big)\Big]. && (6.16)\end{aligned}$$

The parameter η is the Lamb-Dicke factor, and is given by $\eta \equiv kz_o$. This is the ratio of the physical extent of the ion's motional ground state wave packet to the wavelength of the radiation divided by 2π. The terms in the above equation that contain $e^{\pm i(\omega+\omega_o)t}$ are fast oscillating terms that average to zero. They can be dropped from Hamiltonian, and making this approximation is called the rotating-wave approximation. The resulting Hamiltonian is

$$H_I = \hbar\Omega\left[S^+e^{i\left(\eta(ae^{-i\omega_z t}+a^\dagger e^{i\omega_z t})-\delta t+\phi\right)} + S^-e^{-i\left(\eta(ae^{-i\omega_z t}+a^\dagger e^{i\omega_z t})-\delta t++\phi\right)}\right], \qquad (6.17)$$

where $\delta \equiv \omega - \omega_o$ and $\hbar\Omega = -\frac{\gamma B_o}{4}$. For the case of an electric dipole transition, the substitution $\hbar\Omega = -\frac{\mu_e E}{2}$ would be made. The electric dipole moment is $\mu_e = e\left\langle 2\right| r \left|1\right\rangle$ and E is the electric field of the radiation. The wave function for the states coupled by this interaction can be written

$$\Psi(t) = \sum_{i=1,2}\sum_{n=0}^{\infty} C_{i,n}(t)\left|i\right\rangle\left|n\right\rangle. \qquad (6.18)$$

The subscripts i and n represent the internal and motional states. The coefficients describing the time evolution of the wave function are given by the Schrodinger equation

$$i\hbar\frac{\partial\Psi}{\partial t} = H_I\Psi. \qquad (6.19)$$

Only near resonant transitions will be considered, and these are occur when $\delta \simeq (n'-n)\,\omega_z$. For a treatment of off resonant transitions see reference [Wineland 98]. The result is the

coupled differential equations [Wineland 98]

$$\dot{C}_{1,n'} = -i^{(1+|n'-n|)} e^{i\phi} \Omega_{n',n} C_{2,n} \tag{6.20}$$

$$\dot{C}_{2,n} = -i^{(1-|n'-n|)} e^{-i\phi} \Omega_{n',n} C_{1,n'}. \tag{6.21}$$

The term $\Omega_{n',n}$is the Rabi frequency and is given by [Wineland 98, Wineland 79, Kahill 69]

$$\Omega_{n',n} \equiv \Omega \left| \langle n' | \, e^{i\eta\left(a+a^{\dagger}\right)} \, |n\rangle \right|, \tag{6.22}$$

and this evaluates to

$$\Omega_{n',n} = \Omega e^{\frac{-\eta^2}{2}} \left(\frac{n_<!}{n_{>!}} \right)^{1/2} \eta^{|n'-n|} L_{n_<}^{|n'-n|} \left(\eta^2\right). \tag{6.23}$$

The result does depend on the starting and final motional state n and n'. The values of $n_<$ and $n_>$ are the lesser and greater of n and n'. The factor L_n^a is the generalized Laguerre polynomial [Wineland 98]

$$L_n^a(x) = \sum_{m=0}^{\infty} (-1)^m \binom{n+a}{n-m} \frac{x^m}{m!}. \tag{6.24}$$

The coupled differential equations (6.21) can be solved using Laplace transforms to give the solution for the Schrodinger equation [Wineland 98]

$$\Psi(t) = \begin{bmatrix} \cos\left(\Omega_{n',n} t\right) & -ie^{i\left[\phi+\frac{\pi}{2}|n'-n|\right]} \sin\left(\Omega_{n',n} t\right) \\ -ie^{-i\left[\phi+\frac{\pi}{2}|n'-n|\right]} \sin\left(\Omega_{n',n} t\right) & \cos\left(\Omega_{n',n} t\right) \end{bmatrix} \Psi(0). \tag{6.25}$$

The two component wave function is $\Psi(0) = \begin{bmatrix} C_{1,n}(0) \\ C_{2,n'}(0) \end{bmatrix}$.

This is the general result for on resonance transitions. The Hamiltonian in equation (6.17) can be simplified if the amplitude of the motion is small compared to the wavelength of the radiation. The is called the Lamb-Dicke limit and is defined [Wineland 98] as $\left(\langle \Psi_{motion} | \, k^2 z^2 \, | \Psi_{motion} \rangle\right)^{1/2} \ll 1$. The expectation value of z^2 is taken because the expectation value of z is zero. This is more restrictive than what is sometimes incorrectly referred to as the Lamb-Dicke limit where $\eta \ll 1$. The Lamb-Dicke parameter maybe

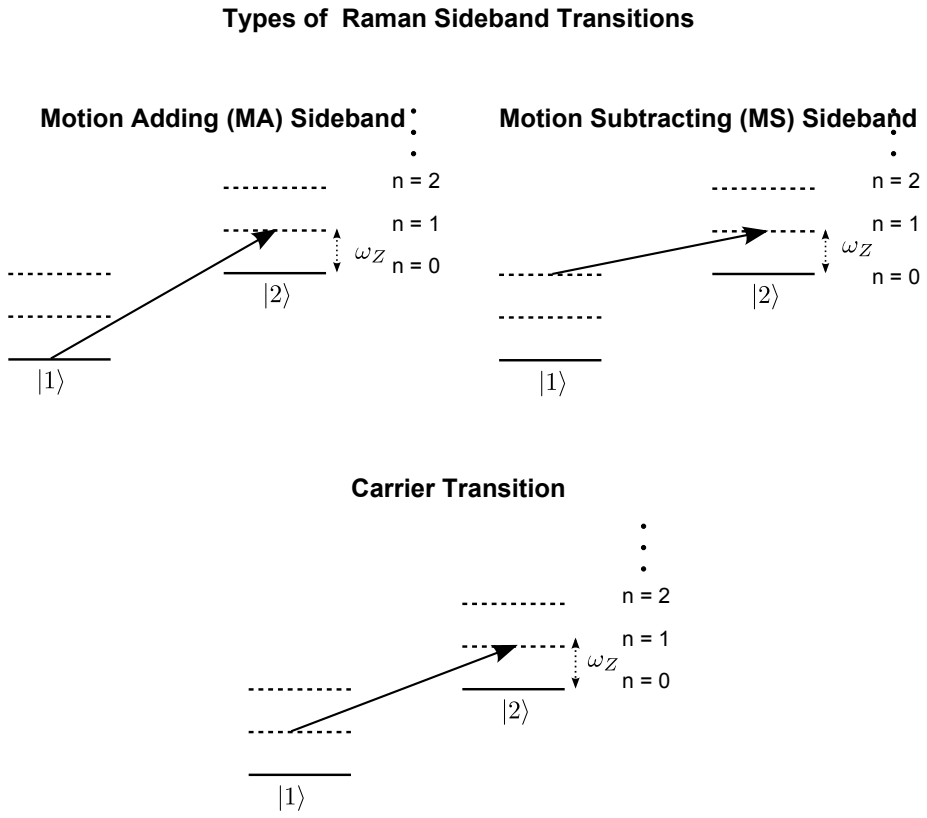

Figure 6.1: This figure depicts a few of the different types of sideband transitions. When one quanta of motional energy is added this can be called a motion adding (MA) transition. A transition where one quanta of energy is removed is called a motion subtracting (MS) transition. It is also possible to change the internal state without affecting the motion, which is called a carrier transition.

small; however, if the motional state is large, then the amplitude of the motion can still be considerably large when compared to the wavelength of radiation. In the Lamb-Dicke limit, things simplify. The interaction Hamiltonian can be expanded to first order in the η to give

$$H_I^{LD} = \hbar\Omega e^{-i(\delta t-\phi)}S^+\left[1+i\eta(ae^{-i\omega_z t}+a^\dagger e^{i\omega_z t})\right]+\text{H.c.} \tag{6.26}$$

There are several types of transitions that can be made (see figure (6.1)). A carrier transition is one where $n = n'$ and $\delta = 0$. In this case only the internal state is changed,

which leads to a Hamiltonian where

$$H_c = \hbar\Omega e^{-i(\phi)} S^+ \left[1 + i\eta(ae^{-i\omega_z t} + a^\dagger e^{i\omega_z t})\right] + \text{H.c.}. \tag{6.27}$$

However, the resonant terms will be dominant, which means any terms oscillating in time can be dropped to a good approximation if $\Omega \ll \omega_z$. This is equivalent to making another rotating wave approximation, which gives

$$H_c = \hbar\Omega \left(S^+ e^{-i(\phi)} + S^- e^{+i(\phi)}\right). \tag{6.28}$$

The above Hamiltonian is independent of the motion, which is only strictly true in the limit that $\eta \to 0$. In general, for most experimental parameters the motion will play a role. For example the Rabi frequency equation for the (6.23) $n = 0$ to $n' = 0$ carrier transition is $\Omega_{0,0} = \Omega e^{\frac{-\eta^2}{2}}$. This exponential factor is known as the Debye-Waller factor [Wineland 79]. This will show up again when multiple modes of motion are considered in section (6.3).

Another resonant transition that is important is the motion subtracting (MS) transition where $\delta = -\omega_z$. This is sometimes called a red-sideband in the literature, because if the initial internal state is the lower energy state, then the radiation that does the coupling will have a lower frequency than the carrier. However, if the initial state is the higher energy internal state, then the motion subtracting transition will be blue detuned with respect to the carrier, that is where $\delta = \omega_z$. For this reason, sideband transitions will only be referred to as either motion adding (MA) or motions subtracting (MS). In the Lamb-Dicke limit, the Rabi frequency for the MS transition simplifies to $\Omega_{n-1,n} = \eta\sqrt{n}\Omega$. The interaction Hamiltonian equation (6.26)becomes

$$H_{MS} = \hbar\Omega e^{+i\phi} S^+ \left(e^{i\omega_z t} + i\eta(a + a^\dagger e^{2i\omega_z t})\right) \tag{6.29}$$

$$+\hbar\Omega e^{-i\phi} S^- \left(e^{-i\omega_z t} - i\eta(ae^{-2i\omega_z t} + a^\dagger)\right). \tag{6.30}$$

Again if we assume that only near-resonant processes are being considered, any fast oscillating terms average to zero. This is same as making another rotating wave approx-

imation. Also the phase ϕ can be arbitrarily chosen for the first application of H_I. If the phase is chosen to be $\phi = -\frac{\pi}{2}$, then the Hamiltonian simplifies to

$$H_{MS} = \hbar\eta\Omega\left(S^+a + S^-a^\dagger\right). \tag{6.31}$$

This is also known as the Jaynes-Cummings Hamiltonian from quantum optics [Jaynes 63]. For the MA transition, the detuning is $\delta = \omega_z$, and in the Lamb-Dicke limit the Rabi frequency is $\Omega_{n',n} = \eta\sqrt{n+1}\Omega$. The interaction Hamiltonian simplifies to

$$H_{MS} = \hbar\eta\Omega\left(S^+a^\dagger + S^-a\right). \tag{6.32}$$

It is also possible to drive transitions where more than one quanta of motional energy is added or subtracted. For some of the experiments discuss later, sideband transitions are used where two quanta of energy are removed. The Rabi frequency of these transitions will differ.

$$\Omega_{1,0} = \Omega e^{\frac{-\eta^2}{2}}\eta \tag{6.33}$$

$$\Omega_{2,0} = \Omega e^{\frac{-\eta^2}{2}}2^{-1/2}\eta^2 \tag{6.34}$$

Thus the second sideband Rabi frequency is a factor $2^{-1/2}\eta$ slower than the Rabi frequency for the first sideband.

6.3 Rabi Rates - Multiple Modes

The above results can be generalized for multiple ions. Here it is assumed that the laser beam only addresses one of the ions in a chain, and only the axial modes will be considered. If there are L ions, then there will be L normal modes along the axis. If all the other normal modes where accounted for, then there would be $3L$ normal modes, which is treated in reference [Wineland 98]. The time-independent Hamiltonian for the the j^{th} ion (j is the index of the ion be addressed, where j runs from 1 to L) is

$$H_{o,j} = \hbar\omega_o S_{z,j} + \sum_{k=1}^{L}\hbar\omega_{z,k}a_k a_k^\dagger. \tag{6.35}$$

The index k in the sum represents the different normal modes. The Hamiltonian describing the laser interaction (6.8) with the j^{th} ion becomes

$$H_{l,j} = -\frac{\gamma B_o}{4}(S_j^+ + S_j^-)\left(e^{i(k\cdot z_j - \omega t + \phi)} + e^{-i(k\cdot z_j - \omega t + \phi)}\right). \tag{6.36}$$

The z_j term can be expanded in terms of the normal modes. The interaction Hamiltonian now becomes

$$H_{I,j} = \hbar\Omega S_j^+ e^{i\left(\sum_{k=1}^{L}\eta_k^j(ae^{-i\omega_{z,k}t}+a^\dagger e^{i\omega_{z,k}t})-\delta t+\phi\right)} + H.c.. \tag{6.37}$$

The index k corresponds to the k^{th} normal mode along the trap axis. The Lamb-Dicke parameter η_k^j correspond to the Lamb-Dicke parameter for the j^{th} ion on the k^{th} mode. One consequence of having multiple modes is the Rabi frequency will be affected by the presence of the other modes. The Rabi frequency becomes [Wineland 98]

$$\Omega_{n_k',n_k} \equiv \Omega\left|\langle n_{p\neq k}, n_k'|\prod_{l=1}^{L} e^{i\eta_l\left(a+a^\dagger\right)}|n_{p\neq k}, n_k\rangle\right|. \tag{6.38}$$

The subscript p represents all the other modes not being addressed by the resonant laser interaction. For example, the Rabi frequency for a MA transition of the first mode in a two ion crystal would be.

$$\Omega_{n_1'=1,n_1=0,n_2'=0,n_2=0} = \Omega e^{\frac{-\eta_1^2}{2}}\eta_1 e^{\frac{-\eta_2^2}{2}}. \tag{6.39}$$

The second exponential factor is the Debye-Waller factor for the second mode, which effectively reduces the Rabi frequency. For larger ion crystals, each additional mode will contribute another Debye-Waller factor.

6.4 Stimulated Raman Transitions

In the above, the coupling between the internal states and the ions' motion was derived assuming an oscillating magnetic field excites transitions between two levels. The splitting for most ion qubit systems based on hyperfine structure range from a

few MHz to a few GHz. Using an oscillating magnetic field to drive the transitions, would provide a very small Lamb-Dicke parameter as a result of the long wavelength. In addition, ion traps are usually built on the centimeter size scale, so it would be difficult to isolate other ions from being affected by the radiation. One way around this is to have a magnetic field gradient, creating ions with different resonant frequencies as a function of their position [Mintert 01, Wineland 98, Wang 09]. It might also be possible to use a combination of magnetic field gradients and oscillating magnetic fields to drive MA and MS transitions [Ospelkaus 08]. Currently the most common technique is to use lasers to couple the internal states to the motion. This can be done with a single laser beam when the internal qubit levels are split by an optical frequency, and the linewidth of the excited state is small compared to ion's motional frequency [J. C. Bergquist 87]. The technique used in this work is a coherent two-photon process called stimulated-Raman transitions [Monroe 95b, Heinzen 90]. The two photons have a difference frequency tuned near the qubit transition (typically in the MHz to GHz range), and couple the two levels via a virtual excited state. This technique makes a large effective $\vec{k}$ vector along the trap axis, which creates a larger Lamb-Dicke parameter than in the case of direct excitation with radio-frequency magnetic fields. It was discussed earlier that $\eta \ll 1$ to be in the Lamb-Dicke regime. However, there is a trade off. The sideband Rabi frequencies are proportional to η, so a vanishing η as in the radio-frequency/microwave case leads to a vanishing $\Omega_{n',n}$. Another advantage of using lasers is the ability to individually address the ions. Typical inter ion spacings are on the order of a few microns. With diffraction limited optics the diameter of the beam at the focus can be of order λ, which at optical wavelengths is sufficient to individually addresses ions in most chains. This has been demonstrated in $^{43}Ca^{+}$ ions where the optical transitions used have a wavelength of 729 nm [Nägerl 99]. The experiments discussed in this work use UV photons, so in theory a much smaller waist should be obtainable. However, current optics are not sufficient to generate diffraction limited spots, but it is possible to individually address

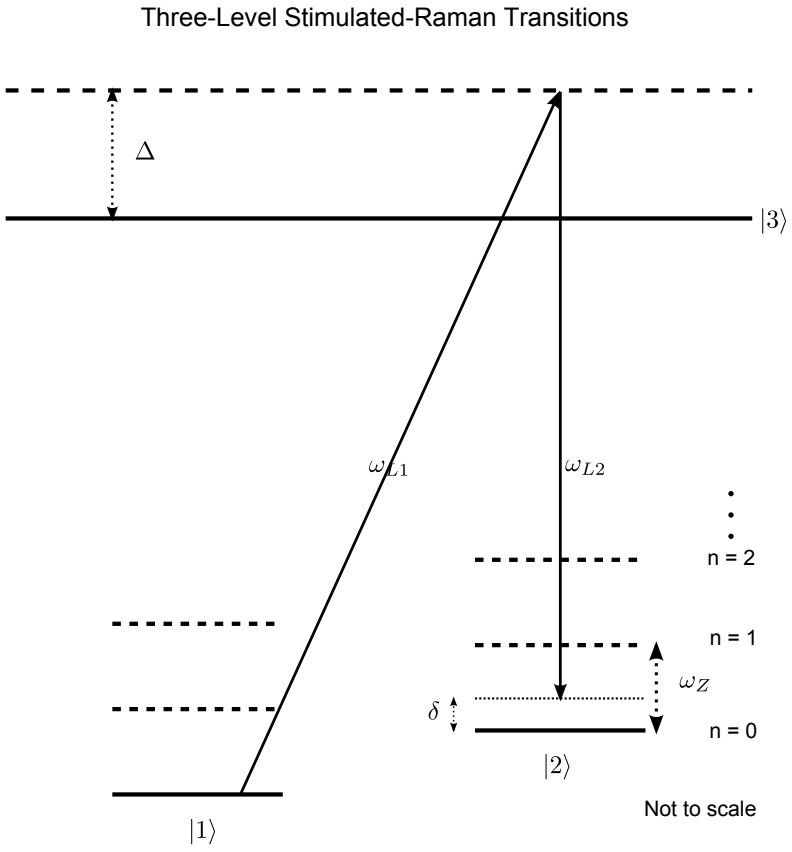

Figure 6.2: Energy level diagram illustrating stimulated Raman sideband transitions. The transitions are driven with two laser beams, which have frequencies ω_{L1} and ω_{L2} . Both beams are detuned from the excited state $|3\rangle$ by approximately Δ. We consider two internal ground states labeled $|1\rangle$ and $|2\rangle$, which have energies $\hbar\omega_1$ and $\hbar\omega_2$. The frequency difference between the the two beams is $\omega_{L1} - \omega_{L2} + \delta$. Superimposed on top of the two internal ground states are ladders of harmonic oscillator states, which represent the quantized motion. The values of n represents the Fock states. When there are multiple modes of motion then several sets of states must be superimposed; however, only one mode will be considered here.

ions spaced a few 10's of microns apart. Lasers offer the additional advantage that they can be steered with Acoustic Optic Modulators and move-able mirrors, which enables addressing different parts of the ion trap.

This section discusses how the two-photon stimulated-Raman transition gives the same results for coupling the two internal (qubit) levels to the motions as the pre-

vious section. This is also worked out in the thesis by Jonathan Home [Home 06b, Wineland 04]. Figure (6.2) shows the setup. There are three internal levels labeled $|1\rangle, |2\rangle,$ and $|3\rangle$, which have energies $\hbar\omega_1, \hbar\omega_2,$ and $\hbar\omega_3$ respectively. The splitting between levels $|1\rangle$ and $|2\rangle$ is on the order of 100 MHz or a 1 GHz for the hyperfine levels typically used in $^9Be^+$ at a magnetic field of $\sim$ 120 Gauss. The splitting between $|1\rangle$ and $|3\rangle$ or $|2\rangle$ and $|3\rangle$ is approximately 313 nm. For $^{24}Mg^+$ the splitting between levels $|1\rangle$ and $|2\rangle$ is about 300 MHz at a magnetic field of $\sim$ 120 Gauss, and around 280 nm for the difference between the excited state and ground states. The exact values for the splitting of the two ground states will depend on the value of the magnetic field used in the experiments.

One laser beam with a frequency ω_{L1} couples the states $|1\rangle \rightarrow |3\rangle$ with a detuning Δ. The second laser has a frequency ω_{L2}. It couples the states $|2\rangle \rightarrow |3\rangle$ with a detuning Δ from state $|3\rangle$ and a detuning δ from state $|2\rangle$, where $\delta \ll \Delta \ll \omega_{L1}, \omega_{L2}$. It should also be noted that for the case considered here $\Delta \gg \Gamma$ with Γ being the radiative line width of the excited state. The electric field of the lasers is given by $\vec{E}_i(t) = \hat{\epsilon}_i E_{o,i} \cos(k_i \cdot z - \omega_{L,i} t + \phi_i)$. Where the index $i \in 1, 2$ denotes the laser beam. The polarization is represented by $\hat{\epsilon}$ and the electric field magnitude by $E_{o,i}$. The radiation couples the ground to the excited states via an electric dipole transition given by

$$H_L = -\vec{\mu}_{ed}(\vec{E}_1(t) + \vec{E}_2(t)). \tag{6.40}$$

Substituting the oscillating electric field gives,

$$H_L = \hbar g_{13} \cos(k_1 \cdot z - \omega_{L1} t + \phi_1) |1\rangle \langle 3| + \hbar g_{23} \cos(k_2 \cdot z - \omega_{L2} t + \phi_2) |2\rangle \langle 3| + H.c.. \tag{6.41}$$

The coupling strengths g_{13} and g_{23} are

$$g_{13} = -\langle 3| \vec{\mu}_{ed} \cdot \hat{\epsilon}_1 |1\rangle \frac{E_{o,1}}{\hbar} \tag{6.42}$$

$$g_{23} = -\langle 3| \vec{\mu}_{ed} \cdot \hat{\epsilon}_2 |2\rangle \frac{E_{o,2}}{\hbar}. \tag{6.43}$$

The Hamiltonian for the internal state can be written in the form

$$H_a = \hbar\omega_1 |1\rangle\langle 1| + \hbar\omega_2 |2\rangle\langle 2| + \hbar\omega_3 |3\rangle\langle 3| . \tag{6.44}$$

As before it is convenient to move to an interaction picture where $H_o = H_a$ and $V_I = H_L$. The laser frequencies can be written in terms of the internal state energies and detunings as $\omega_{L1} = \omega_3 - \omega_1 + \Delta$ and $\omega_{L2} = \omega_3 - \omega_1 + \Delta - \delta$. Transforming to the interaction picture using equation (6.9) gives

$$\begin{aligned} H_I &= \frac{\hbar g_{13}}{2} e^{i(\vec{k}_1\cdot\vec{z}+\phi_1)} e^{-i\Delta t}\left(1 + e^{i2\omega_{L1}t}\right)|1\rangle\langle 3| && (6.45)\\ &\quad + \frac{\hbar g_{23}}{2} e^{i(\vec{k}_2\cdot\vec{z}+\phi_2)} e^{-i(\Delta-\delta)t}\left(1 + e^{i2\omega_{L2}t}\right)|2\rangle\langle 3| + H.c.. && (6.46)\end{aligned}$$

Looking at the time dependent terms, there is one that oscillates at Δ and another that oscillates at a much higher frequency $2\omega_{L,i}$. For typical experimental parameters Δ might range from 10 GHz to 100 GHz where $\omega_{l,i}$ is in the PHz regime. The position operator z has not been transformed to the interaction picture yet but this will be done later.

The wave function for the internal states can be written as

$$\Psi(t) = \sum_{i=1}^{3} C_i(t)|i\rangle . \tag{6.47}$$

Using this wave function and the interaction Hamiltonian (6.45), the Schrodinger equation (6.19) can be solved to find the time dependence of the coefficients $C_i(t)$. This gives

$$\begin{aligned} \dot{C}_1 &= -i\frac{g_{13}}{2} e^{i(\vec{k}_1\cdot\vec{z}+\phi_1)} e^{-i\Delta t} Cc && (6.48)\\ \dot{C}_2 &= -i\frac{g_{23}}{2} e^{i(\vec{k}_2\cdot\vec{z}+\phi_2)} e^{-i(\Delta-\delta)t} C_3 && (6.49)\\ \dot{C}_3 &= -i\frac{g^{\star}_{13}}{2} e^{-i(\vec{k}_1\cdot\vec{z}+\phi_1)} e^{+i\Delta t} C_1 + -i\frac{g^{\star}_{23}}{2} e^{-i(\vec{k}_1\cdot\vec{z}+\phi_1)} e^{+i(\Delta-\delta)t} C_2. && (6.50)\end{aligned}$$

This is coupled differential equation for the three level system. The goal is to make this set of equations look like that for a two level system. To do this it is necessary to

eliminate the third level. An approximate solution for $\dot{C}_3$ can be found by integrating by parts twice to give

$$C_3 = -i\frac{g_{13}^{\star}}{2}e^{-i(\vec{k}_1\cdot\vec{z}+\phi_1)}\left(\frac{C_1}{i\Delta}e^{i\Delta t} - \frac{1}{i\Delta}\left[\frac{\dot{C}_1}{i\Delta}e^{i\Delta t} - \int\frac{\ddot{C}_1}{i\Delta}e^{i\Delta t}dt\right]\right) \quad (6.51)$$

$$-i\frac{g_{23}^{\star}}{2}e^{-i(\vec{k}_2\cdot\vec{z}+\phi_2)}\left(\frac{C_2}{i\left(\Delta-\delta\right)}e^{i(\Delta-\delta)t}\right) \quad (6.52)$$

$$-i\frac{g_{23}^{\star}}{2}e^{-i(\vec{k}_2\cdot\vec{z}+\phi_2)}\left(-\frac{1}{i\left(\Delta-\delta\right)}\left[\frac{\dot{C}_2}{i\left(\Delta-\delta\right)}e^{i(\Delta-\delta)t} - \int\frac{\ddot{C}_2}{i\left(\Delta-\delta\right)}e^{i(\Delta-\delta)t}dt\right]\right) \quad (6.53)$$

An approximation can be made here to simplify things. Terms of order $\mathcal{O}\left(\frac{g_{13}}{\Delta^2}\right)$ and $\mathcal{O}\left(\frac{g_{123}}{(\Delta-\delta)^2}\right)$ can be dropped (note: $g_{13}, g_{23} \ll \Delta$) as long as C_1 and C_2 oscillate slowly. This means dropping the two terms in the square brackets, which gives

$$C_3 = -\frac{g_{13}^{\star}}{2\Delta}e^{-i(\vec{k}_1\cdot\vec{z}+\phi_1)}e^{i\Delta t}C_1 - \frac{g_{23}^{\star}}{2\left(\Delta-\delta\right)}e^{-i(\vec{k}_2\cdot\vec{z}+\phi_2)}e^{i(\Delta-\delta)t}C_2. \quad (6.54)$$

This equation can be plugged into the differential equations (6.50) to get a set of coupled differential equations that do not depend on the population in the excited state.

$$\dot{C}_1 = i\frac{|g_{13}|^2}{4\Delta}C_1 + i\frac{g_{23}^{\star}g_{13}}{4\left(\Delta-\delta\right)}e^{-i\delta t}e^{i(\Delta\vec{k}\cdot\vec{z}+\Delta\phi)}C_2 \quad (6.55)$$

$$\dot{C}_2 = i\frac{|g_{23}|^2}{4\left(\Delta-\delta\right)}C_2 + i\frac{g_{23}g_{13}^{\star}}{4\Delta}e^{i\delta t}e^{-i(\Delta\vec{k}\cdot\vec{z}+\Delta\phi)}C_1. \quad (6.56)$$

Now the terms in the exponentials depend on the difference of the wave vectors $\Delta k = k_1 - k_2$ and on the difference of the phases of the two laser beams $\Delta\phi = \phi_1 - \phi_2$. From this differential equation, it can be determined that the Hamiltonian that gives the same evolution is

$$H_I = -\hbar\frac{|g_{13}|^2}{4\Delta}|1\rangle\langle 1| - \hbar\frac{|g_{23}|^2}{4\left(\Delta-\delta\right)}|2\rangle\langle 2| \quad (6.57)$$

$$-\hbar\frac{g_{23}^{\star}g_{13}}{4\left(\Delta-\delta\right)}e^{-i\delta t}e^{i(\Delta\vec{k}\cdot\vec{z}+\Delta\phi)}|1\rangle\langle 2| \quad (6.58)$$

$$-\hbar\frac{g_{23}g_{13}^{\star}}{4\Delta}e^{i\delta t}e^{-i(\Delta\vec{k}\cdot\vec{z}+\Delta\phi)}|2\rangle\langle 1|. \quad (6.59)$$

The first two terms in the Hamiltonian are the Stark shifts of the levels as a result of the light fields. These do not depend on time and can be absorbed into the definition of H_o, which has the affect of redefining the energy of the two levels. Another approximation

that can be made is $\Delta - \delta \rightarrow \Delta$, which can be made for $\delta \ll \Delta$. With these assumptions the interaction Hamiltonian can be written as.

$$H_I = \hbar\Omega e^{-i\delta t} e^{i\left(\Delta\vec{k}\cdot\vec{z}+\Delta\phi\right)} |1\rangle\langle 2| + \hbar\Omega^{\star} e^{i\delta t} e^{-i\left(\Delta\vec{k}\cdot\vec{z}+\Delta\phi\right)} |2\rangle\langle 1| . \tag{6.60}$$

This has the same form as the Hamiltonian found for the case treated early where an oscillating magnetic field was use to couple the two levels. The difference here is that $\Omega = -\frac{g_{23}^{\star} g_{13}}{4(\Delta)}$, and the redefinition of $\vec{k} \rightarrow \Delta\vec{k}$ and $\phi \rightarrow \Delta\phi$.

The same types of transitions (MA, MS, and carrier) exist for the three level stimulated Raman transitions as those for the two level case depicted in figure (6.1). Figure (6.3) shows several of the possible transitions for the three level system. One additional transition not depicted in figure (6.1) is the second sideband transition. The main difference between this type of transition and the MA and MS transitions previously discussed is that two quanta of energy are added or removed. This is done by tuning the difference frequency to be $\delta = 2\omega_z$. The Rabi frequency equation (6.23) will also be different for these transitions.

6.4.1 Co-propagating Beam Transitions

In the above discussion of stimulated-Raman transitions, it was assumed that two beams are orthogonal to each other. The orientation of the two beams has important implications for whether or not the transitions are sensitive to the ions' motion. The sensitivity to motion enters through the term $\Delta\vec{k}\cdot\vec{z}$, where $\vec{k}$ is the effective wavevector and $\vec{z}$ represents the ions displacement from equilibrium. For the stimulated-Raman sideband transitions discussed above the two beams used are at UV wavelengths with wavevectors $\vec{k}_1$ and $\vec{k}_2$. The two beams are orthogonal to each other and at 45 degrees with respect to the trap axis. Only the transition's sensitivity to motion along the trap axis is considered. This is valid if $\Delta\vec{k} = \frac{1}{\sqrt{2}}\left(\vec{k}_1 - \vec{k}_2\right)$ lies along the trap axis. The other case to be considered is when the two beams are co-propagating and at 45 degrees

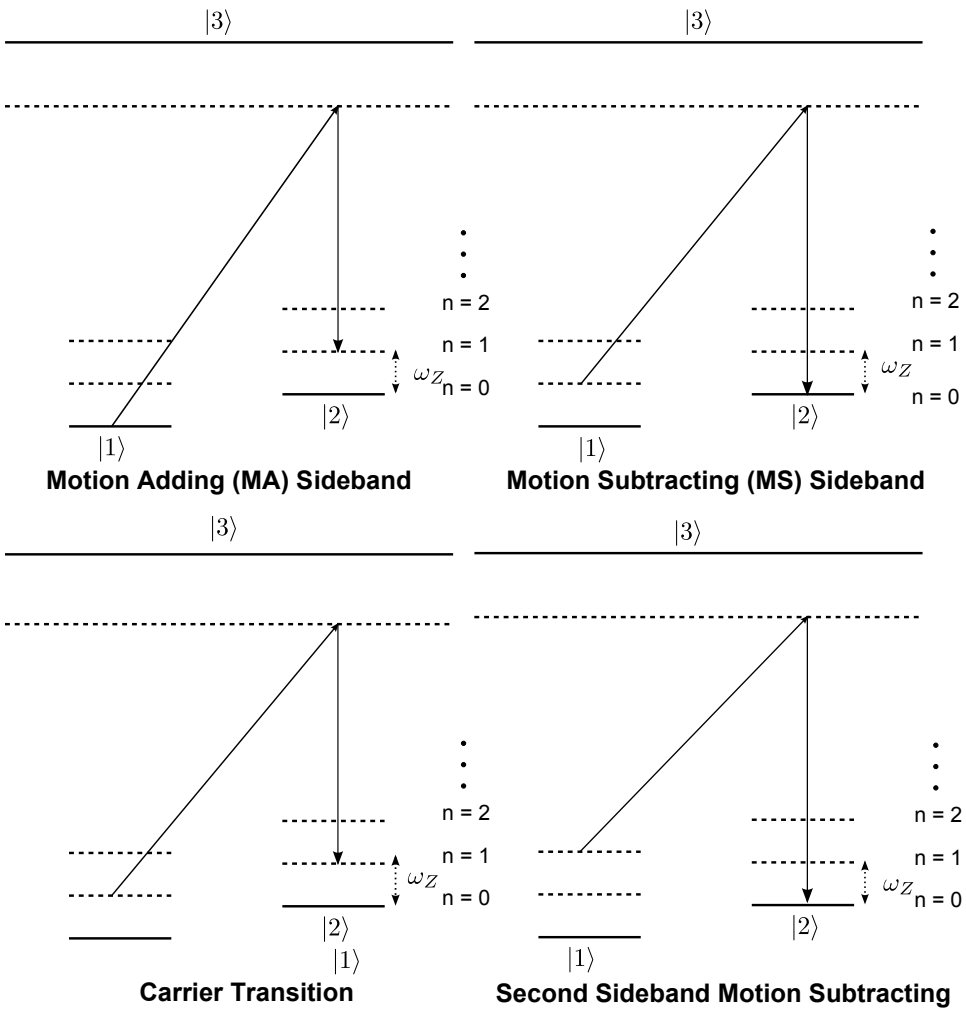

Figure 6.3: This figure depicts a few of the different types of stimulated Raman transitions that are possible. When one quanta of motional energy is added this called a motion adding (MA) transition. A transition where one quanta of energy is removed is called a motion subtracting (MS) transition. It is also possible to change the internal state without affecting the motion, which is called a carrier transition. The second sideband motion subtracting transition is relevant for the sideband cooling discussed in section (6.6). This transition removes two quanta of energy from the motion.

with respect to the trap axis. Now the magnitude of $\Delta\vec{k}$ is the small. For example, a single trapped $^9Be^+$ ion with a motional frequency of $\omega = 2\pi \times 3 \times 10^6$ Hz, the Lamb-Dicke parameter $\eta \sim 0.4$ for the orthogonal beam case and $\eta \sim 3 \times 10^{-8}$ for the

co-propagating case (It is assumed the stimulated-Raman transitions were made between the levels $|^2S_{\frac{1}{2}}, F = 2, m_F = 2\rangle \rightarrow |^2S_{\frac{1}{2}}, F = 2, m_F = 1\rangle$ at a field of ~ 120 Gauss giving rise to a splitting between the levels of ~ 100 MHz). The small Lamb-Dicke parameter for the co-propagating beams makes theses transitions insensitive to the motional state of the trapped ions. Thus, they can be used to perform coherent rotations between the internal states of the ions. These rotations are termed single qubit gates [Nielsen 00].

6.5 Motional State Analysis

The sensitivity of the Rabi frequency to the motional state and the presence of other modes provide a tool for determining the distribution motional energy states. Several types of distributions have been experimentally prepared. Reference [Meekhof 96] gives examples of sideband flopping (Sideband flopping refers to a scan measuring the fluorescence versus the duration of a MA or MS transition) on a single ion that has had its motional state prepared in either a thermal distribution, coherent state, or a squeezed state. Discussed the section on Doppler cooling of this dissertation is an example where sideband flopping is used to estimate the temperature of the two axial modes of a $^9Be^+ - ^{24}Mg^+$ ion pair. Also discussed in this section is another technique for estimating the temperature of a thermal distribution. This technique relies on measuring the relative probability of making a MA and MS transition [Monroe 95b, Turchette 00, Home 06b, Diedrich 89].

If the duration of the laser interaction is scanned and the internal state populations are measured, then a Rabi sideband flopping curve is obtained. For a single ion initialized in the state $|1, n\rangle$, the probability that the ion is found in state $|1\rangle$ is given by

$$P_{|1\rangle}(t) = \left|\cos\left(\Omega_{n',n}t\right)\right|^2. \tag{6.61}$$

This can be re-expressed as $P_{|1\rangle} = \frac{1}{2}\left(1 + \cos\left(2\Omega_{n',n}t\right)\right)$. Typically the ion's initial motional state will follow some distribution, where each motional state in the Fock basis

has some probability P_n of being occupied. The ion's motion is harmonic, so for a particular sideband transition all transitions between all the different Fock states will be driven. For example driving a MA transition causes all the transitions $n = 0 \rightarrow 1$, $n = 1 \rightarrow 2$, etc.... The only difference between all the transitions is that each has a different Rabi rate. Thus, each transition needs to be included in calculating the probability, but they will be weighted by a distribution.

$$P_{|1\rangle} = \frac{1}{2}\left(1 + \sum_{n_k=0}^{\infty} P_{n_k} \cos\left(2\Omega_{n'_k,n_k} t\right)\right). \tag{6.62}$$

A common distribution that occurs with trapped ions is a thermal distribution. Most of our ion experiments involve Doppler laser cooling, which to a good approximation leaves the ions motional state in a thermal distribution.

$$P_n^{thermal} = \frac{\bar{n}^n}{(1+\bar{n})^{n+1}}. \tag{6.63}$$

The average motional state is $\bar{n}$, and n represents the a particular Fock state. If there are multiple modes of motion, then the other modes will affect the Rabi rate as a result of the their Debye-Waller factors. A more general expression for the probability of finding the ion in state $|1\rangle$ is

$$P_{|1\rangle}(t) = \frac{1}{2}\left(1 + \left[\prod_{m=1,m\neq k}^{L} \sum_{n_m=0}^{\infty} P_{n_m}\right] \sum_{n_k=0}^{\infty} P_{n_k} \times \right. \tag{6.64}$$

$$\left. \cos\left(2\Omega \left| \langle n_{m\neq k}, n'_k | \, e^{i\eta_k\left(a+a^\dagger\right)} \left[\prod_{m=1,m\neq k}^{L} e^{i\eta_m\left(a+a^\dagger\right)}\right] |m_{p\neq k}, n_k\rangle \right| t\right)\right) \tag{6.65}$$

The terms in the brackets are the contributions from the other modes, which are represented by the index m, where $m \neq k$. The first bracket is the product of the sums over all the probability distributions. Each distribution is summed over all the Fock states for that mode. The second bracket, which appears inside the cosine term, is the product of all the Debye-Waller factors for the other modes.

Equation (6.64) can be used as a model for performing motional state analysis. This can be accomplished by tuning the laser interaction to the resonance of a particular mode of motion and scanning the interaction time. The resulting data can be fit to the

above model. Different probability distributions can be tried until an acceptable fit for the experimental data is obtained.

If it is known the ion's motion is in a thermal state, which it is to a good approximation after Doppler cooling, then there is another technique for estimating the temperature. This method relies on measuring the probability of making a MA and MS transition with fixed interaction time. If a ion is prepared in the $|1\rangle$ state, then the probability of making either a MS or MA transition to state $|2\rangle$ is given by equation

$$P_{|2\rangle}^{MS} = \sum_{n=1}^{\infty} P_n \sin^2\left(\Omega_{n-1,n} t_d\right) \tag{6.66}$$

$$P_{|2\rangle}^{MA} = \sum_{n=0}^{\infty} P_n \sin^2\left(\Omega_{n+1,n} t_d\right). \tag{6.67}$$

Note that the sums run over different n values. This is because the lowest $|n\rangle$ that a MS can be made from is the $|n=1\rangle$ state. Taking the ratio of these two probabilities gives

$$R = \frac{\sum_{n=1}^{\infty} P_n \sin^2\left(\Omega_{n-1,n} t_d\right)}{\sum_{n=0}^{\infty} P_n \sin^2\left(\Omega_{n+1,n} t_d\right)}, \tag{6.68}$$

where R is the ratio of the sideband amplitudes. Using the thermal distribution equation (6.63)for P_n and making the substitution $n \rightarrow n+1$ for the motion subtracting transition, allows the ratio to be rewritten as

$$R = \frac{\sum_{n=0}^{\infty} \frac{\bar{n}^{n+1}}{(1+\bar{n})^{n+2}} \sin^2\left(\Omega_{n,n+1} t_d\right)}{\sum_{n=0}^{\infty} \frac{\bar{n}^{n}}{(1+\bar{n})^{n+1}} \sin^2\left(\Omega_{n+1,n} t_d\right)}. \tag{6.69}$$

Noting that $\Omega_{n,n+1} = \Omega_{n+1,n}$, the ratio simplifies to

$$R = \frac{\bar{n}}{\bar{n}+1} \tag{6.70}$$

, which gives the expression for the $\bar{n}$

$$\bar{n} = \frac{R}{R+1}. \tag{6.71}$$

In order to measure the ratio, the signal strengths two sideband are measured by applying a fixed length Raman sideband pulse and scanning the frequency of the pulse δ_s across

the MA and MS resonances. This curve can be fit to the expected result for a two level system given by[Metcalf 99][Home 06b]

$$P_{|2,n'\rangle} = a\frac{\Omega_{n',n}^2}{\Omega_{n',n}^2+\delta_s^2}\sin^2\left(\frac{\sqrt{\Omega_{n',n}^2+\delta_s^2}}{2}t\right)+b. \tag{6.72}$$

After fitting experimental data and figuring out the amplitude and the baseline for each transition, the signal strength of the transition can be found. Taking the ratio of the two signal strengths gives the value of R. If the ion's motion is near the ground state of motion, then the signal strength of the MS transition will be quite small. In the ideal case where $|n=0\rangle$ then no MS transition can be driven. However, a MA transition can always be driven.

6.6 Sideband Cooling

One of the interesting features of trapped ions is the ability to accurately control the motional states. Most experiments require the ion to start in the motional ground state before some special motional state is prepared. Upon initially trapping an ion there is typically a large energy in the motion. We therefore perform Doppler cooling as an initial cooling stage, which can often cool the ions down to the level of a few motional quanta. For example, a single $^9Be^+$ ion with an axial frequency of 3 MHz would be Doppler cooled to an average motional Fock state $\bar{n}\sim 3$ with a thermal distribution. It should be noted that depending on the parameters an average motional state of a few tens of quanta is possible. Cooling to the Doppler limit, is sufficient for some quantum mechanical gate operations [Kirchmair 09]. However gates many require the motion to be initialized in the ground state to work [Cirac 95] or to minimize errors in the gate operations [Leibfried 03b]. In addition, one of the main focuses of this work, which is the entangled mechanical oscillators experiment discussed in chapter (8), requires the motion of two spatially separated pairs of $^9Be^+ - ^{24}Mg^+$ ions to be cooled to the ground state of motion. Stimulated Raman sideband cooling (Raman cooling) is the technique

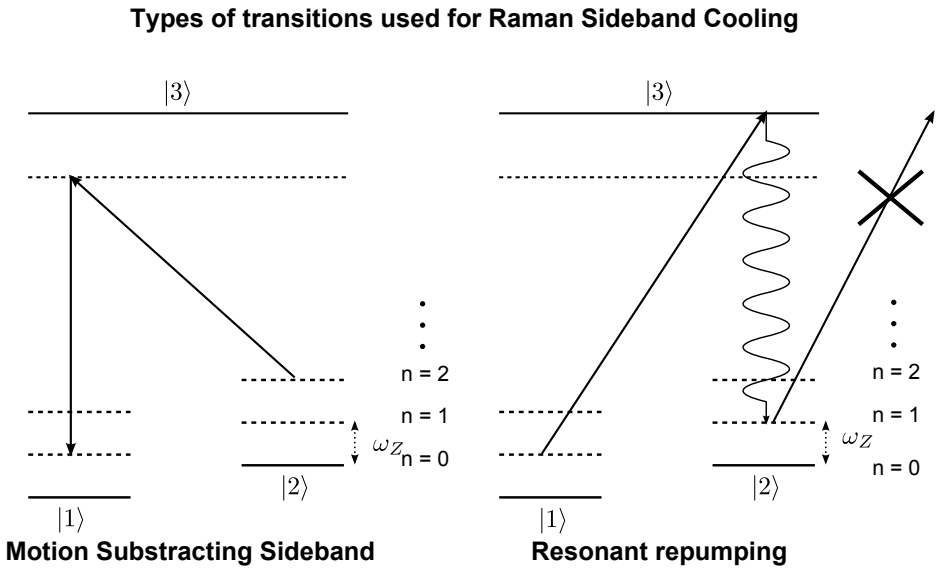

Figure 6.4: The two main types of transitions used in Raman sideband cooling. On the left part of the figure, the motion subtracting transition removes one quanta of energy from the motion. It should be noted that this transition was drawn differently from the one depicted in figure (6.3), where the only difference is the starting state. In this figure the ion's internal state starts in state $|2\rangle$, and in figure (6.3) it starts in state $|1\rangle$. On the right part of the figure, the resonant repumping transition transfers internal state population from $|1\rangle$ to $|2\rangle$ by scattering only a few photons, which leads to negligible heating. State $|2\rangle$ scatters no photons from this laser beam.

used in this work to cool the motion of trapped ions to very near the ground state.

In a simplified picture, the transitions used for Raman cooling are illustrated in figure (6.4). There are two types of transitions used: the MS sideband transition discussed in section (6.9) and a resonant electric dipole transition that performs optical pumping. The procedure begins with the ion being prepared in state $|2\rangle$ by optical pumping, which will also have some distribution of motional states. A MS transition is then performed, using a two-photon stimulated Raman transition. The time of the interaction is chosen such that all the population is transferred from $|2\rangle\,|n\rangle \rightarrow |1\rangle\,|n-1\rangle$., which is is called a π-pulse (See below for a discussion on choosing which $|n\rangle \rightarrow |n-1\rangle$ transition is driven.). The next step is apply a resonant interaction, which couples $|1\rangle \rightarrow |3\rangle$, referred to as repumping. The excited state will spontaneously emit a photon

and decay to either state $|1\rangle$ or $|2\rangle$. If it decays to state $|2\rangle$, then optical pumping shuts off, since it is no longer resonant or it is not possible to drive a transition with the polarization used. If the decay was back to state $|1\rangle$, then it will only take a few scattering events until all the population is in state $|2\rangle$. The scattering from repumping will cause the ions' motion to heat up but on average this is less than a motional quanta, because $\frac{(\hbar k)^2}{2m} < \hbar\omega_z$. Here the momenta of the absorbed/scattered photon are represented by $\hbar k$ and $\omega_z$is the motional frequency. Another way to say this is if the Lamb-Dicke parameter is less than one, then there will not be much heating from scattering. This is because $\eta^2 = \frac{(\hbar k)^2}{2m}/\hbar\omega_z$. This process is repeated many times until all the motion is cooled to the ground state. The sequence of a MS sideband followed by a repumping pulse and spontaneous emission will be referred to as a single Raman cooling cycle.

Other issues complicate the cooling beyond this simple picture. After Doppler cooling, the ions' motional state will be in a thermal distribution. This means that is possible for some of motional population to occupy Fock states with large values on $|n\rangle$. From equation (6.23) it can be seen that the Rabi frequency depends on the particular $|n\rangle$ state. Thus if the time of the interaction is chosen to drive a π-pulse on the $|n = 1\rangle$ to $|n = 0\rangle$ transition this will not drive a full π-pulse on the $|n = 10\rangle$ to $|n = 9\rangle$. A partial solution to this is to estimate the maximum Fock state with a non negligible population and start with a π- pulse that is optimized to make the transition $|n_{max}\rangle \rightarrow |n_{max} - 1\rangle$. Then for the next cycle, the time is chosen to optimize the $|n_{max} - 1\rangle \rightarrow |n_{max} - 2\rangle$ transition. During each pulse, partial π-pulses are driven between the other transitions between motional states. This process can be continued until reaching the $|n = 1\rangle \rightarrow |n = 0\rangle$ transition.

Trapped ions are sensitive to electric field noise, which couples to the ions motion and causes heating. One common source of noise is Johnson noise from the electrodes. In addition, sources of electric field noise are observed that have yet to be fully understood. This noise is commonly referred to as anomalous [Turchette 00, Epstein 07,

Labaziewicz 08a, Labaziewicz 08b]. For Raman cooling to be efficient, the heating rate in quanta per cooling-cycle duration must be much less than one. A typical heating rate for the ion trap discussed in this dissertation is on the order of 0.25 quanta/ms for a single $^9Be^+$ ion with a trap frequency of ~ 3 MHz. A typical Raman cooling cycle in the experiment requires a few ten's of microseconds. Several of the experiments discussed in this dissertation involve multiple ions where it is necessary to cool all axial modes. It would be possible to have separate dedicated laser beams to cool all the different modes in parallel, but this is not an efficient use of laser resources. Typically, a single set of Raman beams are used, and the frequency is changed to address the different modes in a serial fashion. One way to cool all the modes would be to cool them serially This has the disadvantage that many Raman cooling cycles are required to reach the ground state. If one mode is cooled completely before cooling another mode, then the cold mode may heat up during the time it takes to cool the other modes due to photon recoil. A better option is to interlace the Raman cooling cycles, applying one Raman cooling cycle to mode 1 then one Raman cooling cycle to mode 2 and so on. This prevents one mode from heating while the others are being cooled.

Another potential problem arises from the dependence of the Rabi frequency equation (6.23) on the motional state $|n\rangle$, which in part comes about through the generalized Laguerre polynomials $L_{n_<}^{|n'-n|}\left(\eta^2\right)$. For a a fixed value of η and $|n'-n|$ the Laguerre polynomials will have a value equal or near to 0 for some value of n_{L0}. This means that Rabi frequency will go to zero for this particular n_{L0} state and no transition can be driven. Thus, any motional population above n_{L0} will not be cooled to the ground state but will tend to collect in the $|n_{L0}\rangle$ state. This will not be a problem if n_{L0} is significantly larger the $\bar{n}$ reached after Doppler cooling. However the motional state follows a thermal distribution after Doppler cooling and there can be a significant amount of motional state population occupying large n states.

Figure (6.5) shows the thermal distribution of motional states equation (6.63) as-

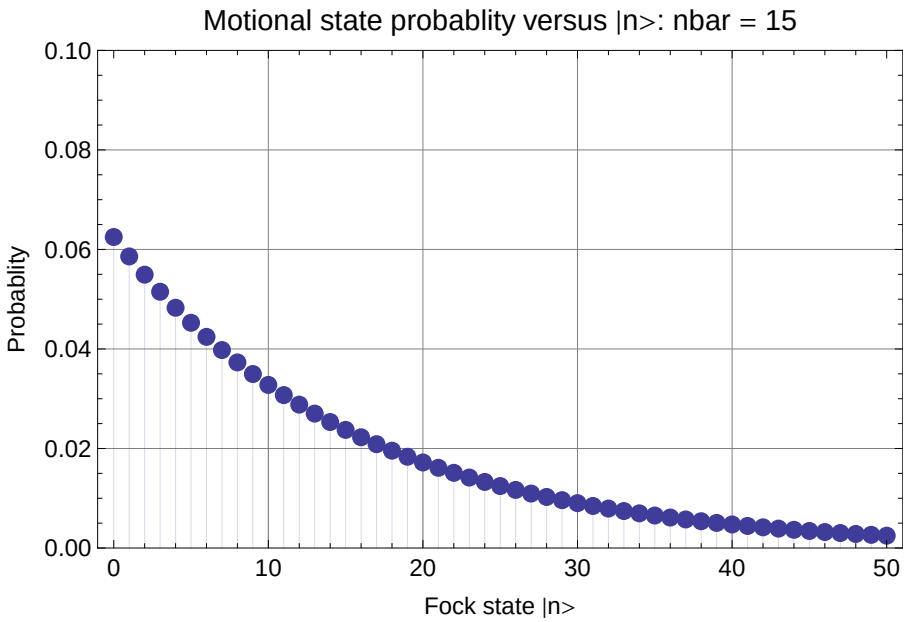

Figure 6.5: Probability for finding the ion in Fock state $|n\rangle$, assuming the ion's motional population follows a thermal distribution equation (6.63)with $\bar{n} = 15$.

suming a $\bar{n} = 15$. Typical Doppler cooling temperatures for $^{9}Be^{+}$ can be much lower than this temperature. However, (in chapter (5) Doppler cooling with $^{24}Mg^{+}$ is discussed) it is possible after $^{24}Mg^{+}$ Doppler cooling to have an $\bar{n} \sim 15$. It should be noted from the figure, that there is a significant population for $n > 15$. For the Raman cooling technique discussed earlier a particular initial $|n\rangle$ state is chosen and cooling proceeds until all the motional population with n equal to or less than this value is brought to the $|n = 0\rangle$ state. To capture 100% of motional population in theory it would require starting at $|n = \infty\rangle$. Obviously, this is not physically possible. Instead, some threshold needs to be established regarding what percentage of the motional population is required to be in the ground state. This will depend on the experiment, and what level of errors can be tolerated.

Figure (6.6) shows the largest $|n\rangle$ state that would have be cooled to get 95%, 99%, and 99.99% for a given $\bar{n}$. This assumes that the highest $|n\rangle$ is the starting state for Raman cooling and that the cooling continues from there, stepping down from that

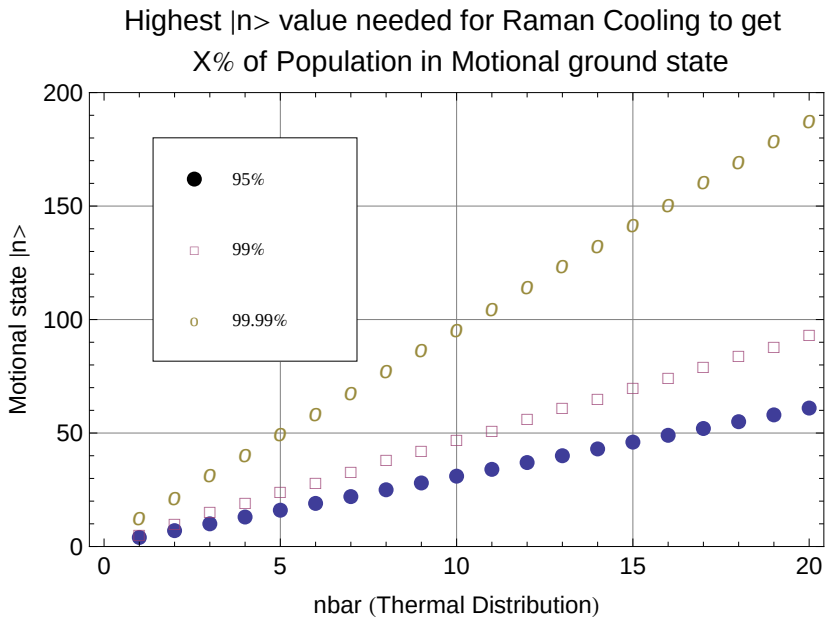

Figure 6.6: The largest motional state $|n\rangle$ that needs to be cooled in order to get X % of the motional population in the ground state for a range of $\bar{n}$. The figure shows the values for requiring 95%, 99%, and 99.99% of motional population to be cooled.

$|n\rangle$ all the way to the ground state. For example assuming $\bar{n} = 15$, the highest $|n\rangle$ state that would need to be cooled to capture 95%, 99%,or 99.99% of the motional population would be $|n = 46\rangle$, $|n = 71\rangle$, or $|n = 151\rangle$ respectively.

Now that it is clear that it is necessary to start cooling from reasonably high values of $|n\rangle$, let's examine where the zeros in the Laguerre polynomials occur. Figures (6.7) and (6.8) show the $|n\rangle$ values of the first zeros in the Laguerre polynomials as function of the Lamb-Dicke parameter for both first ($|n' - n| = 1$) and second ($|n' - n| = 2$) sidebands. For small values of η, the value of n for this first zero can be quite large. However, values of $\eta > 0.1$ are common in the trapped ion experiments discussed here. The zeros start to approach the regime, where they may cause problems for Raman cooling. For example the Lamb-Dicke parameters for the two axial modes of a $^{9}Be^{+} - ^{24}Mg^{+}$ pair discussed in the next section have the values $\eta \sim 0.28$ and $\eta \sim 0.08$. This would give the zeros for the first sidebands at $n \sim 46$ and $n \sim 156$ respectively and for the second sidebands

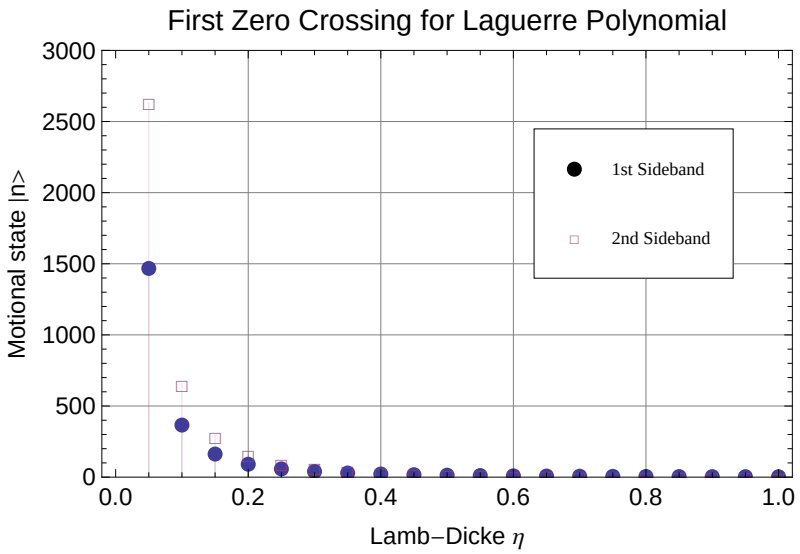

Figure 6.7: This figure shows the first zeros in the Laguerre polynomials as function of the Lamb-Dicke parameter η . The zeros are shown for both first ($|n' - n| = 1$) and second ($|n' - n| = 2$) sidebands. Note that the zeros of the second sidebands always occur at a larger value of $|n\rangle$ than the first sidebands.

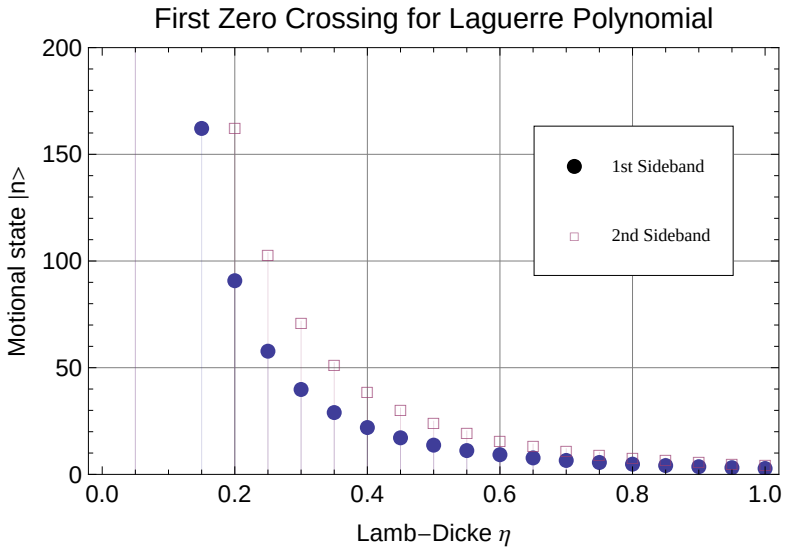

Figure 6.8: This figure is the same as figure (6.7), but with a different vertical scale

at $n \sim 83$ and $n \sim 1029$. (- The answer to the joke: It saw the salad dressing. The first part of the joke is somewhere in this thesis -) It was mentioned above that to cool 99% of the motional population to the ground state for $\bar{n} = 15$ the cooling would have to start

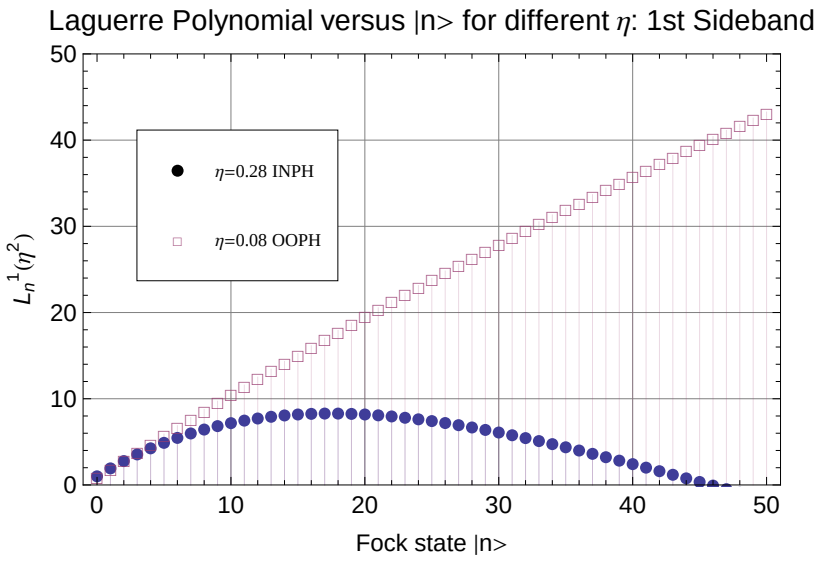

Figure 6.9: The value of the Laguerre Polynomials $L_n^{|n'-n|}\left(\eta^2\right)$ versus n for first sideband transitions, where $|n'-n|=1$. The values of $\eta=0.28$ and $\eta=0.08$ are plotted.

with $|n=71\rangle$ state. For a mode with a Lamb-Dicke parameter of $\eta=0.28$ not all of the motional population could be cooled using first sideband transitions alone. For this case, first sideband cooling would leave behind $\sim 5\%$ of the motional population. This problem can be solved if second sideband cooling is used in addition to first sideband cooling, since the location of the zeros in the Laguerre polynomials is sufficiently high.

As an example figures (6.9) and (6.10) show the value of the Laguerre polynomials for both the first and second sidebands where $\eta_{INPH}\sim 0.28$ and $\eta_{OOPH}\sim 0.08$. Also figures (6.11) and (6.12) show the scaled Rabi frequency $\Omega_{n',n}/\Omega$ from equation (6.23) for these two cases. There are regions in these last two plots where the Rabi frequency will be higher for second sideband transitions than for first sideband transitions for the same value of $|n\rangle$. Thus it may be possible to find mixture of first and second sideband cooling to optimize the amount of time it takes to Raman cool.

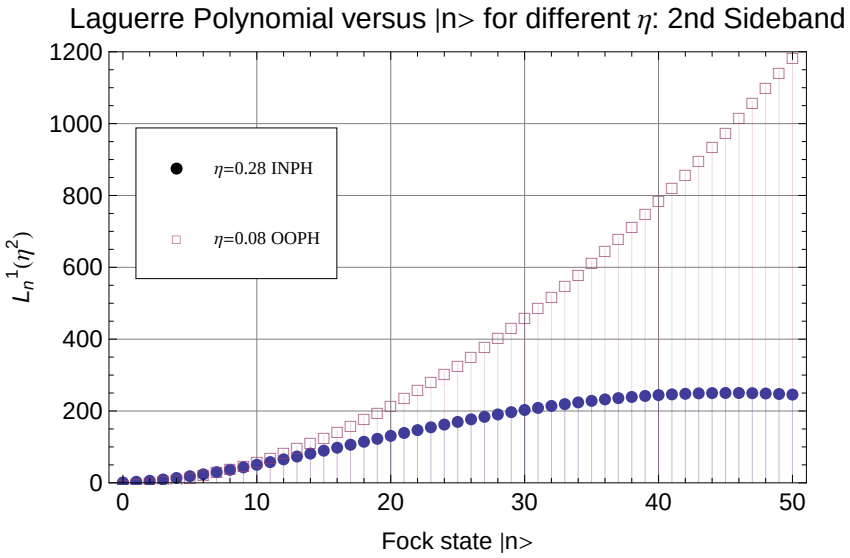

Figure 6.10: The value of the Laguerre Polynomials $L_n^{|n'-n|}\left(\eta^2\right)$ versus n for a sideband first stimulated-Raman transition, where $|n'-n| = 1$. The values of $\eta = 0.28$ and $\eta = 0.08$ are plotted.

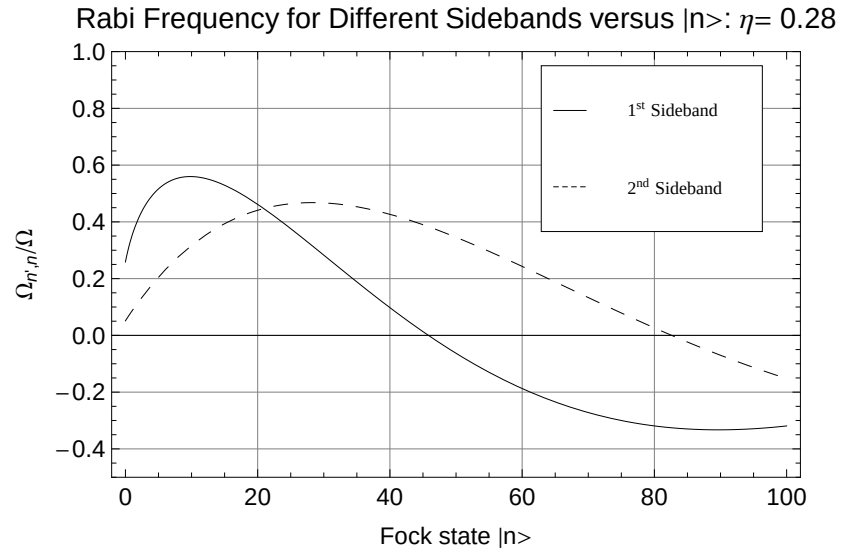

Figure 6.11: The scaled Rabi frequencies $\Omega_{n',n}/\Omega$ from equation 6.23 versus $|n\rangle$ for the first and second sidebands where η =0.28

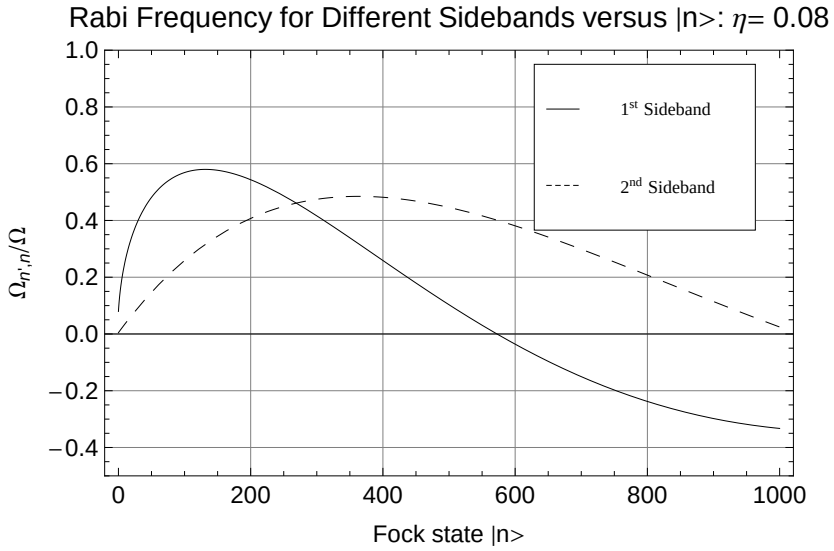

Figure 6.12: The scaled Rabi frequencies $\Omega_{n',n}/\Omega$ from equation 6.23 versus $|n\rangle$ for the first and second sidebands where η =0.08

6.7 Sideband Cooling Experiments

One of the approaches in ion trap quantum computing includes having the ability to move ions around an ion trap-array and to sympathetically recool them to the ground state of motion. This section describes an experiment demonstrating this capability. In addition this experiment served as a calibration experiment for a the entangled mechanical oscillators experiment[Jost 09] discussed in chapter (8).

The goal in the experiments described here is to take two $^{9}Be^{+}$ions that start in the same trapping region, separate them transfer them to different locations in an ion trap array, and show that their axial modes can be sympathetically recooled to ground state of motion after the transport and separation (separation tends to heat the ions). The recooling is performed with another species of ion $^{24}Mg^{+}$ that accompany the two $^{9}Be^{+}$ions, which allows any quantum information stored in the $^{9}Be^{+}$ions to be maintained. Only the details relevant to discussing the sideband cooling of the two pairs of $^{9}Be^{+} - {}^{24}Mg^{+}$ ions will be elaborated on here, and the other details are discussed elsewhere in this dissertation. Figure (6.15) shows the basic outline of the experiments. Several different experiments are required to demonstrate the sympathetic cooling of the axial modes of the two $^{9}Be^{+} - {}^{24}Mg^{+}$ pairs. Experiments will have to be done where MA and MS sideband transitions are performed on the $^{9}Be^{+}$ ions in both trapping locations, which allow the temperature after sympathetic recooling with $^{24}Mg^{+}$ to be determined. Due to technical limitations, the experiments for measuring the temperature in traps A and B are performed separately.

The experiment involves four trapped ions. These are loaded serially into the trap. The order of the ions is important, since it determines the normal mode frequencies of the ions [Jost 09]. Independent of the order they start in the ions are ordered [Jost 09] into the spatial sequence $^{9}Be^{+} - {}^{24}Mg^{+} - {}^{24}Mg^{+} - {}^{9}Be^{+}$ as shown in step 1. This is accomplished by applying a series of control potentials [Jost 09] combined with Doppler

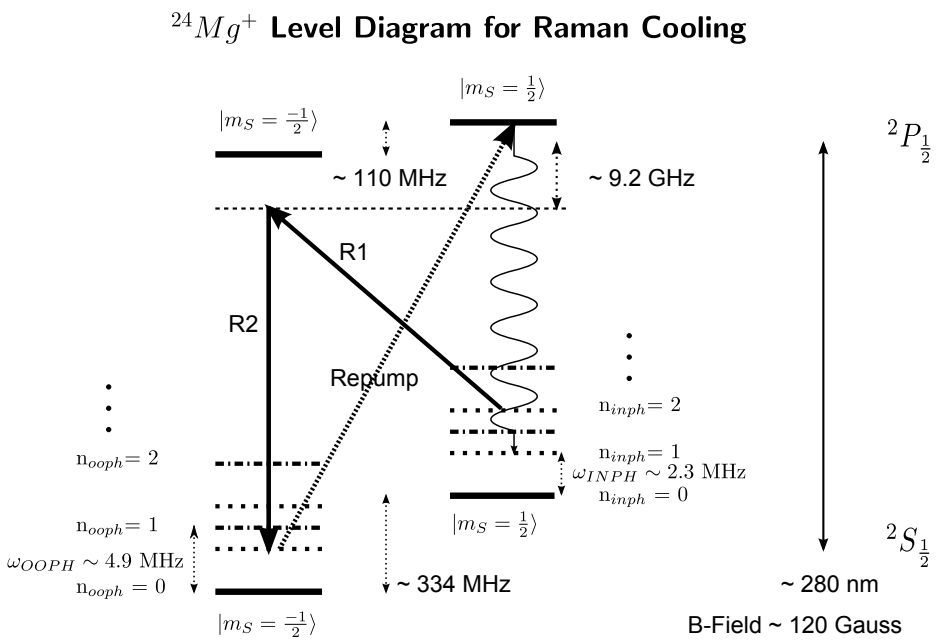

Figure 6.13: This figure depicts the relevant energy levels for Raman cooling with ^{24}Mg$^+$. The two beams used to make a MS sideband transition are labeled R1 and R2. The beam labeled repump is used for optical pumping, and the wavy line represents spontaneous emission. Superimposed on to the ground state internal levels $|m_s = \frac{1}{2}\rangle$ and $|m = -\frac{1}{2}\rangle$ are the harmonic oscillator levels for the INPH and OOPH modes (see text) for a pair of ^{9}Be$^+ - ^{24}$Mg$^+$ ions.

cooling on both the ^{9}Be$^+$ and ^{24}Mg$^+$ ions. In step 2 the four ions are Doppler cooled using a combination of both ^{24}Mg$^+$ and ^{9}Be$^+$ Doppler cooling. Combining these two types of cooling helps ensure all modes are well-cooled. For example, if the ^{9}Be$^+$ ions have a small motional amplitude on a mode they will not be efficiently cooled by ^{9}Be$^+$ Doppler cooling, but the ^{24}Mg$^+$ ions will have large amplitude and efficiently cooled. Next, the four axial modes are Raman cooled to very near the ground state by driving MS sidebands on the ^{9}Be$^+$ ions. (Subsequent experiments [Home 09, Hanneke 10] have performed this operation with only ^{24}Mg$^+$ cooling for both the Doppler component and the for the MS sidebands.)

The ions are then transported from the position near trap A in the figure to the separation region in front of electrode S.E.. This is accomplished by changing the

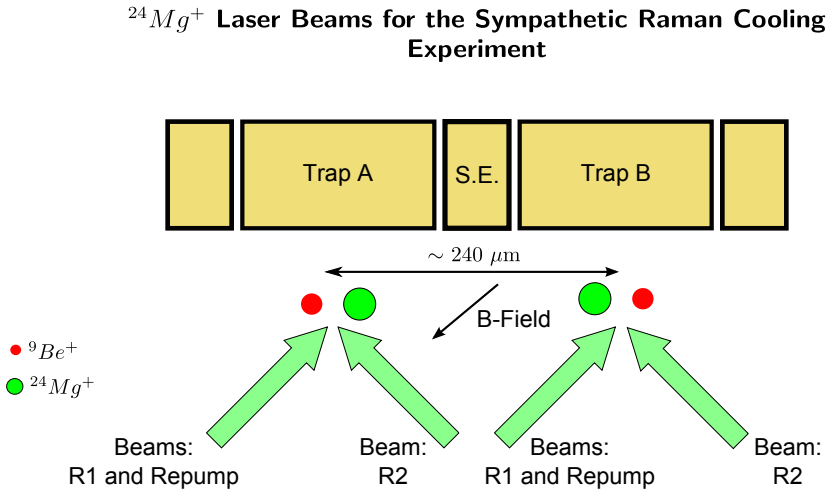

Figure 6.14: Laser Beams used for Raman cooling of ^{24}Mg$^+$ ions in traps A and B. The beams R1 and R2 comprise the two beams used for MS sideband transitions on ^{24}Mg$^+$. The repump beam is used for optical pumping. The two trapping locations A and B are located $\sim 240\ \mu m$ apart. The boxes represent the some of the electrodes, where S.E. stands for separation electrode.

control voltages on the electrodes [Rowe 02, Barrett 04, Reichle 06a]. The four ions can be separated into two pairs by changing the control voltages on the electrodes such that a potential wedge is inserted between the four ions to form two separate potential wells. The ion pairs are then moved to trap A and B, which are separated by about $240\ \mu m$. This is represented in the figure as step 3. The separation process typically heats the ions [Rowe 02, Barrett 04].

The two separate potential wells were designed to have approximately the same trap frequency. There are two normal modes along the axial direction: the in-phase (INPH) and the out-of-phase (OOPH). They have a frequency of $\sim$ 2.3 MHz [0.37, 0.93] and $\sim$ 4.9 MHz [-0.93, 0.37] respectively. The terms in the brackets are the normal mode amplitudes for the ^{9}Be$^+ - ^{24}$Mg$^+$ions respectively. In the experiment, the two trapping locations have slightly different axial frequencies. The INPH modes differ in frequency by $\sim$ 8 KHz, and the OOPH modes differ in frequency by $\sim$ 30 KHz. The

Lamb-Dicke parameters for $^{24}Mg^{+}$ for the two modes of motion in each trapping location are $\eta_{INPH} = 0.28$ and $\eta_{OOPH} = 0.08$.

Sympathetic cooling is performed to recool the ions in both locations, which is shown in step 5. The ions in both traps are simultaneously Doppler cooled for $\sim 400\mu s$ using the $^{24}Mg^{+}$ ions, which is shown in step 4 . The Doppler cooling used is discussed in chapter (5). The stimulated Raman sideband transitions on $^{24}Mg^{+}$ are performed on the $|m_s = \frac{1}{2}\rangle \rightarrow |m_s = -\frac{1}{2}\rangle$ transition see figure (6.13) of the $^2S_{\frac{1}{2}}$ ground state. A magnetic field of $\sim$ 120 Gauss is applied to the ions, which causes the two ground states to be split by $\sim$ 334 MHz. There is some uncertainty of the final temperature reached after Doppler cooling with $^{24}Mg^{+}$. It is possible that the temperature will reach a level that first sideband cooling is not sufficient to cool all the motional population. Thus second sideband cooling is initially performed. 40 Raman cooling cycles of second sideband cooling were applied to the $^{24}Mg^{+}$ ions in both trapping locations simultaneously. For the first sideband cooling, both traps are also simultaneously Raman cooled. However, the frequency of the MS sideband transitions are chosen to be resonant with the motional mode frequencies of the different traps. This means that four different Raman cooling cycles are applied to all the ions with the parameters optimized for the INPH mode in trap A, the INPH mode in trap B, the OOPH mode in trap A, and the OOPH mode in trap B. In total 30 interlaced Raman cooling cycles of first sideband cooling with $^{24}Mg^{+}$ are applied for each of the four modes. Both types of Raman cooling are performed in step 5.

At this point, both normal modes in both traps have been cooled to near the ground state. Due to technical limitations closed cycling transition in $^{24}Mg^{+}$ between the $^2S_{\frac{1}{2}} \rightarrow ^2 P_{\frac{3}{2}}$ levels is not used, the $^{24}Mg^{+}$ fluorescence cannot be probed directly. To diagnose the temperature, the ratio of driving MA and MS transitions on the $^{9}Be^{+}$ ions in each trapping location is measured, see section (6.5). To measure the temperature in trap A of the INPH and OOPH modes, both a MA and MS Raman side-

band transitions are driven (These two different probe pulses are performed in separate experiments on each mode) on the $|F = 2, m_F = 2\rangle \rightarrow |F = 2, m_F = 1\rangle$ transitions in $^9Be^+$(probe pulse). Any population in the $|F = 2, m_F = 1\rangle$ level is transferred to the $|F = 2, m_F = -2\rangle$ state prior to performing resonance fluorescence detection on the $^9Be^+$ion, using co-propagating Raman π-pulses. This is included in step 6a of figure (6.15) . The fluorescence is then plotted versus the frequency of the sideband pulse for both MA and MS transitions see figures (6.16), (6.17), (6.20), and (6.21), where each scan is a separate experiment (see the figures for the number of experiments performed). The ions are recombined in trap A after the detection and the experiments are repeated (step 7a). From the ratio of the two sidebands, $\bar{n}$ for each mode is estimated to be $\bar{n}_{INPH} = 0.095 \pm .022$ and $\bar{n}_{OOPH} = 0.063 \pm 0.018$, where the errors are one standard deviation.

Measurement of the temperature of the $^9Be^+ - ^{24}Mg^+$ ions in trapping region B, requires a slightly different procedure than above. This is due to the technical limitation of not being able to measure resonance fluorescence of the $^9Be^+$ ions in that location. The probe pulse is performed while the ion pair is still in trap B. To do the measurement, the ions have to be transferred back to trapping region A. The state of the $^9Be^+$ ion in trapping region A does not matter. The internal state of the $^9Be^+$ in trap A is optically pumped back to the bright state $|F = 2, m_F = 2\rangle$. Both of these processes are represented by step 6b. In step 7b the ions are recombined into trapping region A. Now resonance fluorescence detection is performed on both ions $^9Be^+$. The ion that was in trapping region A only contributes extra background photons to the data. Figures (6.18), (6.19), (6.22), and (6.23) show the result of scanning the frequency of the probe pulse in trapping region B over the MA and MS transition resonance on both modes, where each data point is a separate experiment repeated many times (see the figures for the number of experiments performed). By fitting the depths of the sidebands, the temperature is estimated to be $\bar{n}_{INPH} = 0.03 \pm 0.049$ and $\bar{n}_{OOPH} = 0.016 \pm 0.024$,

where the errors are one standard deviation.

The average $\bar{n}$ for all the modes is very near the ground state. The finite temperature could result from a number of imperfections. The beam that performs the repumping has a σ^- polarization component (not depicted in figure (6.13)) that is off resonant, but could optically pump the internal state of the $^{24}Mg^+$ ions. This would mean excess scattering events could occur that could heat the ions. Also if the optical power of the σ^- repumping beam is above saturation then this will increase the scattering rate of the off resonant σ^+component. The INPH mode is more sensitive to heating from ambient electric field noise than the OOPH [Kielpinski 00]. As a result, if the Raman cooling process takes longer than the time to gain one motional quantum from heating for this mode, then it will be difficult to cool to the ground state. An additional problem can arise from the separation process. During the separation the trap frequency decreases; this makes the ions more likely to acquire motional energy from ambient electric field noise. To separate the ions, a potential bump is brought up between the ions to create a double well potential. If the location of this potential bump is not located exactly between the ions, then one or more of the ions can effectively ride up this potential hill before eventually being dumped into one of the wells. This can leave the ions with a large amount of motional energy, which can be difficult to remove.

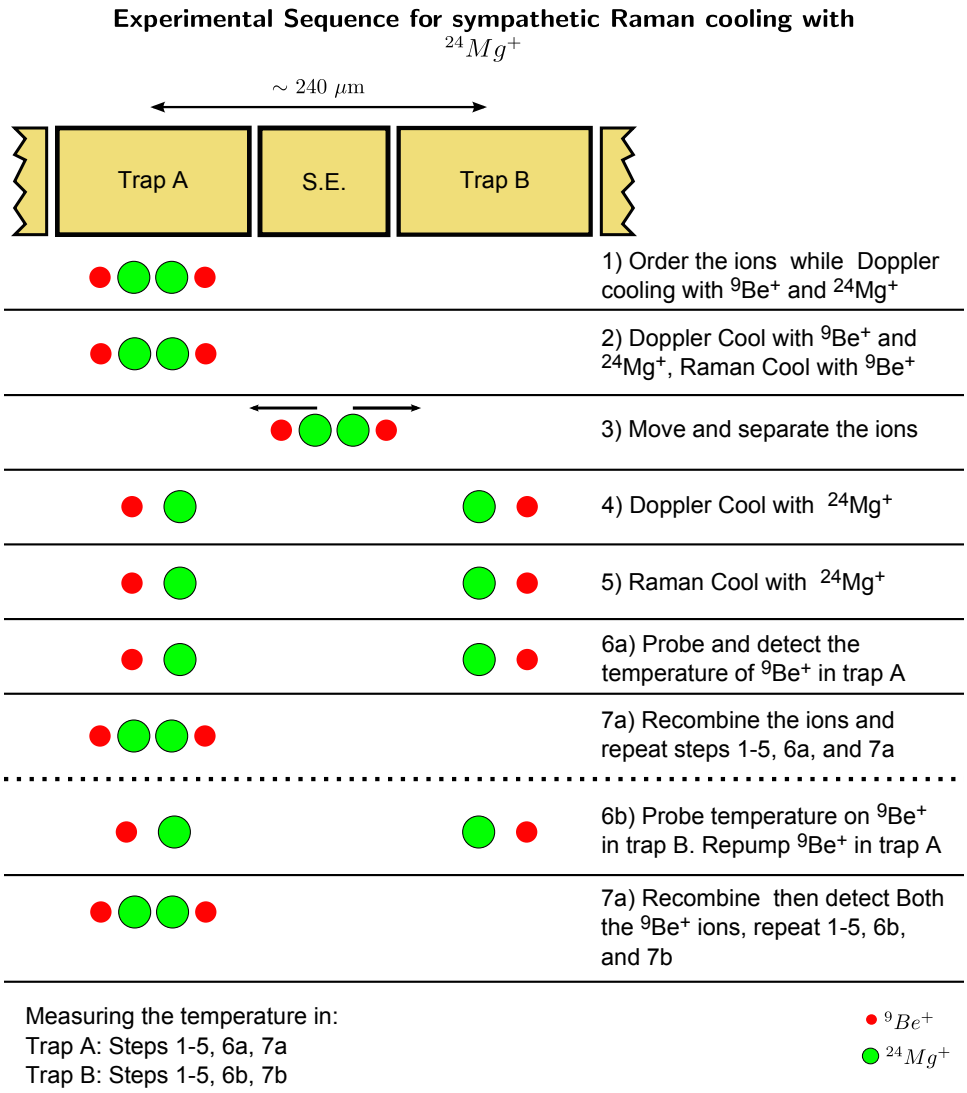

Figure 6.15: Experimental outline for performing and detecting sympathetic cooling on two pairs of trapped $^{9}\mathrm{Be}^{+} - {}^{24}\mathrm{Mg}^{+}$ ions. (More details are provided in the text.) This figure shows the steps for two different experiments. Steps 1-5, 6a, and 7a describes the procedure for sympathetic cooling of a pair of $^{9}\mathrm{Be}^{+} - {}^{24}\mathrm{Mg}^{+}$ ions in trap A and measuring the temperature of the two axial modes. Steps 1-5, 6b, and 7b describe the procedure for doing the same thing but with the pair of ions in trap B. The boxes represent one bank of electrodes in the ion trap. There are two main trapping locations separated by $\sim 240\ \mu$m, labeled trap A and B. There is a separation electrode (S.E.) used for separating the four ions into two pairs.

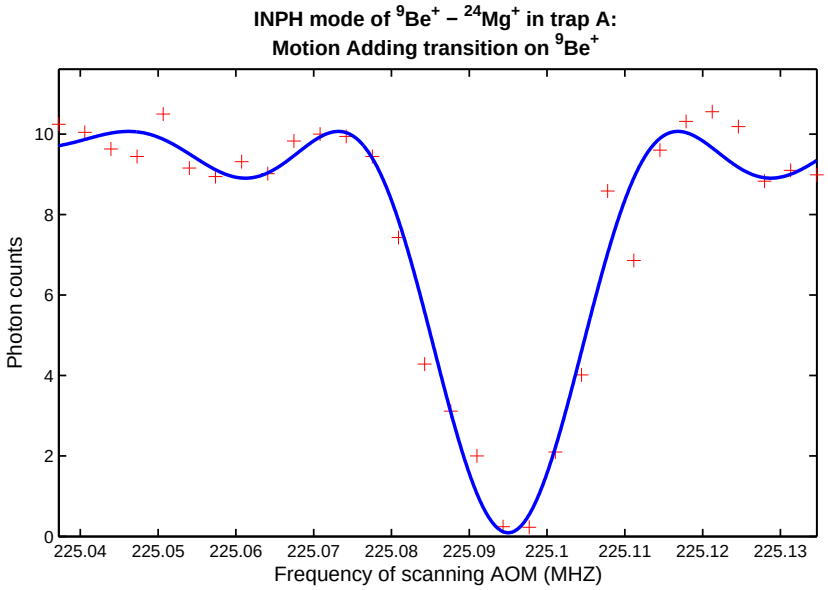

Figure 6.16: Frequency scan over the resonance of the MA transition on the INPH mode of the $^{9}Be^{+} - ^{24}Mg^{+}$ pair of ions in trap A. The horizontal axis is the frequency of an acoustic-optic modulator that is used to scan the frequency of the laser beam. The real frequency scale is is twice the value shown on the axis. The vertical axis shows the number of photons collected, during a single detection period of 200 μs. The line is the fit of a sinc function to the experimental data. Each data point is the average of 70 experiments.

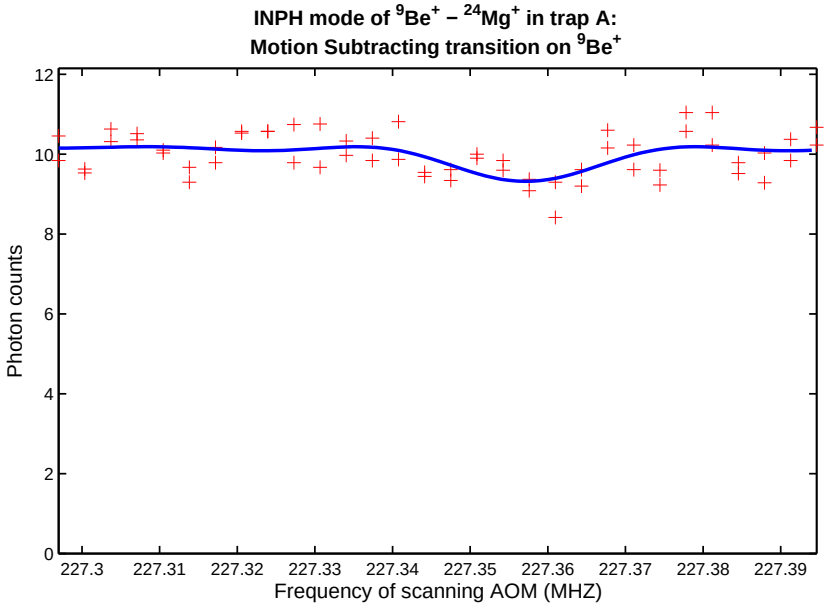

Figure 6.17: Frequency scan over the resonance of the MS transition on the INPH mode of the $^{9}Be^{+} - {}^{24}Mg^{+}$ pair of ions in trap A. The lack of strong resonance implies that the temperature is near the motional ground state. The horizontal axis is the frequency of an acoustic-optic modulator that is used to scan the frequency of the laser beam. The real frequency scale is is twice the value shown on the axis. The vertical axis shows the number of photons collected, during a single detection period of 200 μs. The line is the fit of a sinc function to the experimental data. Each data point is the average of 70 experiments, and two scans were performed.

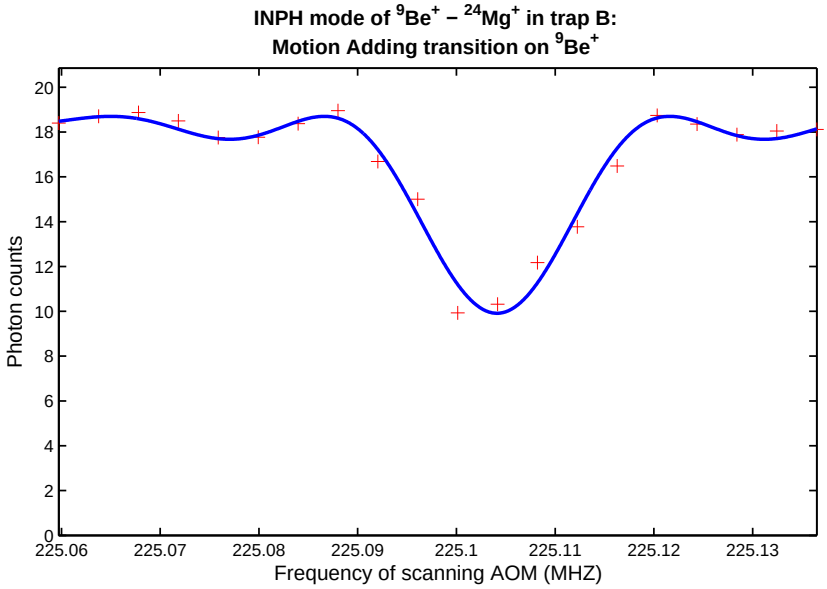

Figure 6.18: Frequency scan over the resonance of the MA transition on the INPH mode of the $^{9}Be^{+} - {}^{24}Mg^{+}$ pair of ions in trap B. The vertical axis shows the number of photons collected, during a single detection period of 200 μs. There is a $\sim$ 10 count background on the signal from the presence of another $^{9}Be^{+}$ ion, see the text for more detail. The horizontal axis is the frequency of an acoustic-optic modulator that is used to scan the frequency of the laser beam. The real frequency scale is is twice the value shown on the axis. The line is the fit of a sinc function to the experimental data. Each data point is the average of 210 experiments.

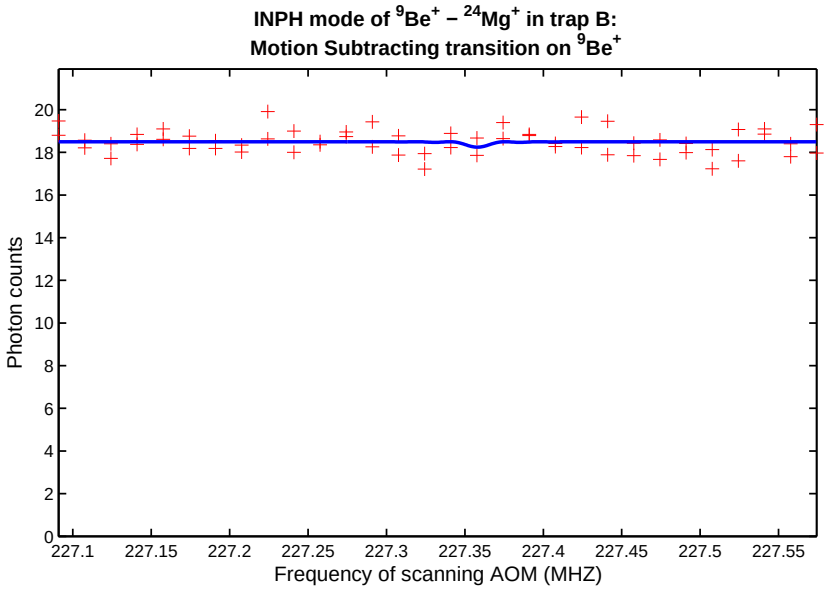

Figure 6.19: Frequency scan over the resonance of the MS transition on the INPH mode of the $^{9}Be^{+} - {}^{24}Mg^{+}$ pair of ions in trap B. The lack of an apparent strong resonance implies that $\bar{n}_{INPH}$ is near the ground state. The vertical axis shows the number of photons collected. There is a ~ 10 count background on the signal from the presence of another $^{9}Be^{+}$ ion, see the text for more detail. The horizontal axis is the frequency of an acoustic-optic modulator that is used to scan the frequency of the laser beam. The real frequency scale is is twice the value shown on the axis. The line is the fit of a sinc function to the experimental data. Each data point is the average of 70 experiments, and two scans were performed.

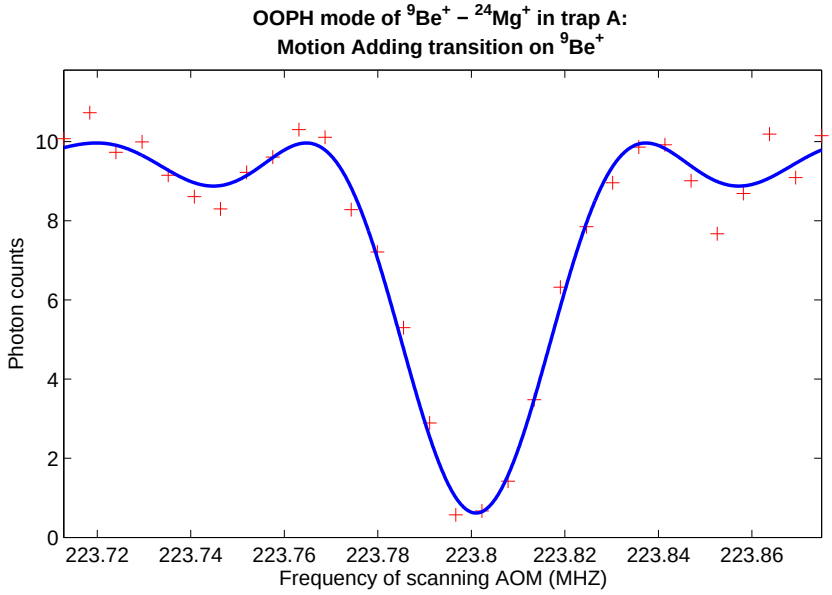

Figure 6.20: Frequency scan over the resonance of the MA transition on the OOPH mode of the $^{9}Be^{+} - ^{24}Mg^{+}$ pair of ions in trap A. The horizontal axis is the frequency of an acoustic optic modulator that is used to scan the frequency of the laser beam. The real frequency scale is is twice the value shown on the axis. The vertical axis shows the number of photons collected, during a single detection period of 200 μs. The line is the fit of a sinc function to the experimental data. Each data point is the average of 100 experiments.

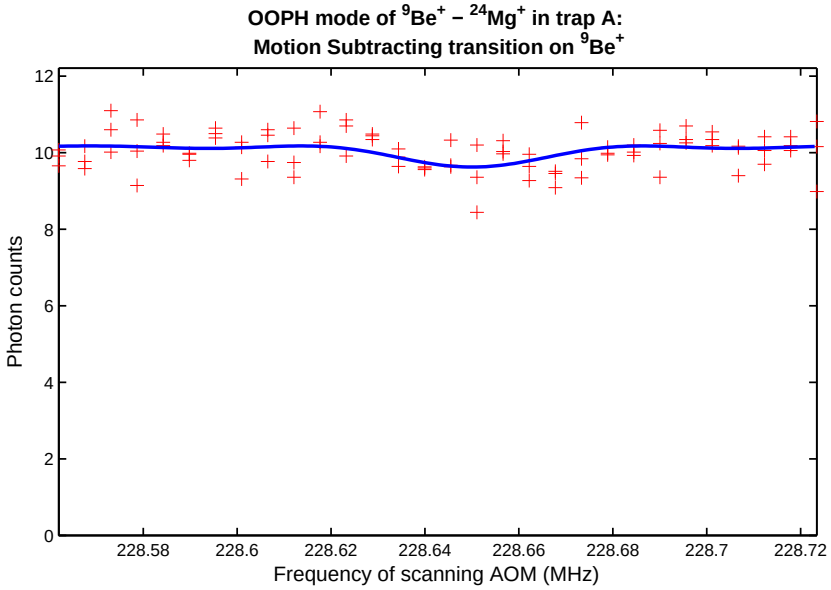

Figure 6.21: Frequency scan over the resonance of the MS transition on the OOPH mode of the $^{9}Be^{+} - {}^{24}Mg^{+}$ pair of ions in trap A. The lack of strong resonance implies that $\bar{n}_{OOPH}$ is near the ground state is near the motional ground state. The horizontal axis is the frequency of an acoustic-optic modulator that is used to scan the frequency of the laser beam. The real frequency scale is is twice the value shown on the axis. The vertical axis shows the number of photons collected, during a single detection period of 200 μs. The line is the fit of a sinc function to the experimental data. Each data point is the average of 70 experiments, and three scans were preformed.

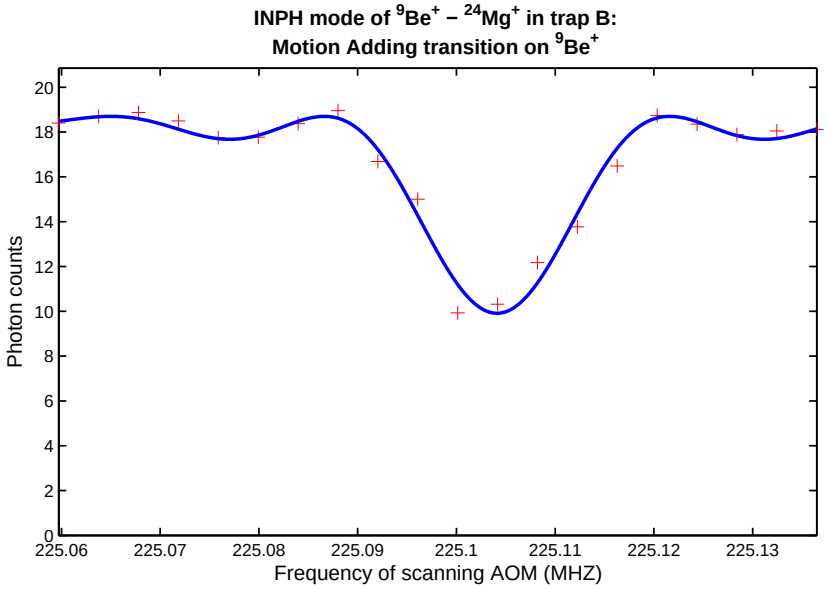

Figure 6.22: Frequency scan over the resonance of the MA transition on the OOPH mode of the $^{9}Be^{+} - {}^{24}Mg^{+}$ pair of ions in trap B. The vertical axis shows the number of photons collected, during a single detection period of 200 μs. There is a ~ 10 count background on the signal from the presence of another $^{9}Be^{+}$ ion, see the text for more detail. The horizontal axis is the frequency of an acoustic-optic modulator that is used to scan the frequency of the laser beam. The real frequency scale is is twice the value shown on the axis. The line is the fit of a sinc function to the experimental data. Each data point is the average of 100 experiments.

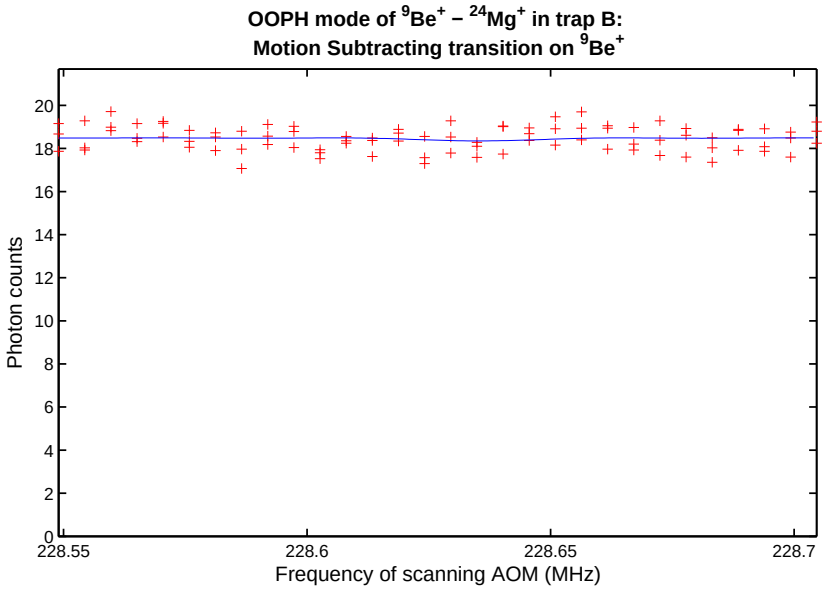

Figure 6.23: Frequency scan over the resonance of the MS transition on the OOPH mode of the $^{9}Be^{+} - {}^{24}Mg^{+}$ pair of ions in trap B. The lack of strong resonance implies that $\bar{n}_{OOPH}$ is near the ground state. The vertical axis shows the number of photons collected, during a single detection period of 200 μs. There is a ~ 10 count background on the signal from the presence of another $^{9}Be^{+}$ ion, see the text for more detail. The horizontal axis is the frequency of an acoustic-optic modulator that is used to scan the frequency of the laser beam. The real frequency scale is twice the value shown on the axis. The line is the fit of a sinc function to the experimental data. Each data point is the average of 70 experiments, and three scans were performed.

Chapter 7

Phase Gate

Two qubit gates are one of the essential components of QIP, since they are necessary along with single qubit rotations to make a universal gate set [Nielsen 00]. One of the early proposals for two qubit gates involved ions in a chain coupled via their Coulomb interaction [Cirac 95]. This proposal was followed quickly by the first demonstration of a two qubit gate using the internal state of a single ion and its quantized motion as the two qubits [Monroe 95a]. Although the first demonstration involved entanglement between the internal and external degrees of freedom, there have been many proposals to perform gates that entangle the internal states of multiple ions [Mølmer 99, Wang 01, Solano 99, Milburn 01, Cirac 95]. This entanglement is always mediated by the Coulomb interaction between the ions, since it is the strongest coupling. Several experimental demonstrations have also been implemented [Sackett 00, Leibfried 03b, Leibfried 04, Leibfried 05, Haljan 05, Häffner 05, Kirchmair 09, Roos 04]. These experiments used different types of ion species, but the demonstrations of entanglement were always between one type of ion. There also has been an experimental demonstration of the entanglement of the internals states of two different isotopes of Calcium ($^{40}Ca^{+}$and $^{43}Ca^{+}$)[Home]. One of the goals of ion trap QIP is to incorporate sympathetic cooling ions with the logical qubits [Kielpinski 00, Barrett 03, Rohde 01, Blinov 02]. For large scale QIP that incorporates sympathetic cooling ions, it will most likely be necessary to

perform entangling operations in the presence of these cooling ions. Prior to reference [Jost 09], which is the focus of this dissertation; this had not been demonstrated before. There was followed by experiments, which have also performed such entanglement [Home 09, Hanneke 10]. The experimental implementation, which discussed in section (7.6), is a tune-up experiment for the experimental work discussed in chapter (8) and reference [Jost 09].

The rest of this chapter provides a more detailed description of the geometrical phase gate [Leibfried 03b, Home 06b] used in reference [Jost 09]. The first section provides a general overview of entanglement and the phase gate. Discussed second is how a stimulated-Raman transition can be used to create a state dependent optical dipole force. A particular example is used to show the resulting force on two ions. Next properties of coherent states and the forced harmonic oscillator will be discussed. This is relevant, since the optical dipole force when acting on a Fock state behaves like a forced harmonic oscillator, creating a coherent state. Next, the amplitude of the coherent state and the phase, arising from the geometrical phase gate, will be derived. This followed by a step through of the implementation of a ideal geometric phase gate. The resulting quantum mechanical states at each point, and the analysis of the entanglement are highlighted. The last section goes through the experimental details for implementing the geometrical phase gate on two $^{9}\mathrm{Be}^{+}$ ions in the four-ion chain $^{9}\mathrm{Be}^{+} - {}^{24}\mathrm{Mg}^{+} - {}^{24}\mathrm{Mg}^{+} - {}^{9}\mathrm{Be}^{+}$.

7.1 Entanglement Overview

An entangled state is a quantum mechanical state of two or more systems that can not be written as a product state [Nielsen 00]. Let us consider two spin $\frac{1}{2}$ systems labeled A and B, where the possible states of each system are $\Psi_A = |\uparrow_A\rangle$, $\Psi_A = |\downarrow_A\rangle$, $\Psi_B = |\uparrow_B\rangle$, and $\Psi_B = |\downarrow_B\rangle$. It is possible to place each system in a quantum mechanical superposition $\Psi = |\uparrow\rangle + |\downarrow\rangle$ (The normalization constant is omitted.). The product state

of both systems can be written

$$\Psi_{A,B} = \Psi_A \otimes \Psi_B = \frac{1}{2}\left(|\uparrow\uparrow\rangle_{A,B} + |\uparrow\downarrow\rangle_{A,B} + |\downarrow\uparrow\rangle_{A,B} + |\downarrow\downarrow\rangle_{A,B}\right). \tag{7.1}$$

With product states the wave function can always be written as the outer product of the individual wave functions for each system. However, if a phase is introduce between some of the elements then the overall state is an entangled state, for example

$$\Psi_{A,B} = \frac{1}{2}\left(|\uparrow\uparrow\rangle_{A,B} + i\,|\uparrow\downarrow\rangle_{A,B} + i\,|\downarrow\uparrow\rangle_{A,B} + |\downarrow\downarrow\rangle_{A,B}\right). \tag{7.2}$$

This state cannot be written as the outer product of two individual wave functions. The systems can longer be thought of as separate and distinct.

Product states of the internal states of trapped ions are significantly easier to generate in the lab than entangled states. The product states are generated with an appropriately tuned co-carrier Raman pulse, see chapter (6). To create an entangled state of two trapped ions of the form in equation (7.2), a state dependent phase factor needs to be created. This is done in the experiments discussed in this dissertation, using a geometric phase gate [Leibfried 03b]. This gate uses a state dependent optical dipole force to excite a coherent state of motion of the ions in the selected states. The force is adjusted such that it drives the states around a loop in phase space see figure (7.1). This figure shows a possible path in phase space for the states of a product state when a geometric phase gate has been applied. The states where motion has been excited acquire a geometric phase that is proportional to area enclosed by the loop in phase space. In this case the states $|\uparrow\downarrow\rangle_{A,B}$ and $|\downarrow\uparrow\rangle_{A,B}$, acquire a phase $e^{i\frac{\pi}{2}}$, where the states $|\uparrow\uparrow\rangle_{A,B}$ and $|\downarrow\downarrow\rangle_{A,B}$ acquire no phase. This creates the state (7.3).

7.2 Optical Dipole Force

The optical dipole force is a conservative force that is uniform in space. As a result the potential giving rise to such a force depends on the position, so the Hamiltonian for

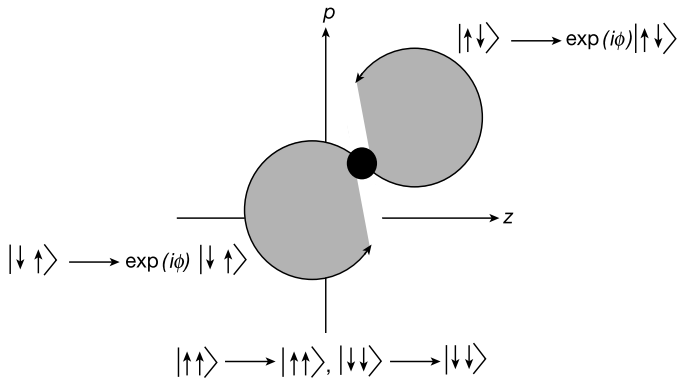

Figure 7.1: This shows possible paths in phase space for the states of a product state when a geometric phase gate has been applied. The states where motion has been excited acquire a geometric phase that is proportional to area enclosed by the loop in phase space. In this case the states $|\uparrow\downarrow\rangle_{A,B}$ and $|\downarrow\uparrow\rangle_{A,B}$ acquire a phase $e^{i\frac{\pi}{2}}$, where the states $|\uparrow\uparrow\rangle_{A,B}$ and $|\downarrow\downarrow\rangle_{A,B}$ acquire no phase (from reference [Leibfried 03b]).

a dipole like force in the linear approximation, takes the form

$$H_{dp} = -zf\left(t\right). \tag{7.3}$$

The position is represented by the coordinate z, since only one dimension will be considered here. The force can have a time dependence or be a constant and is represented by $f\left(t\right)$. The optical dipole force considered here will have a time dependence. This force arises from the ions interaction with the laser beams used for stimulated Raman transitions.

From section (6.4) equation (6.60) the Hamiltonian for a stimulated Raman transition is

$$H_I = \hbar\Omega e^{-i\delta t} e^{i(\Delta k \cdot z + \Delta\phi)} |1\rangle\langle 2| + H.C.. \tag{7.4}$$

It is assumed that the system is in the Lamb-Dicke regime. This allows the Hamiltonian to be simplified to

$$H_I = \hbar\Omega e^{-i(\omega t - \phi)} (1 + i\eta\hat{z}) |1\rangle\langle 2| + H.C.. \tag{7.5}$$

To simplify the notation a few replacements have been made. The difference phase $\Delta\phi$ between the two laser beams has been replaced with ϕ. The term $\Delta k \cdot z$ has been rewritten as $\eta\hat{z}$, where $\eta = \Delta k\, z_o$ and $\hat{z} = \left(a + a^\dagger\right)$. The difference frequency of the Raman beams δ in section (6.4) has been rewritten as ω to emphasis that a different type of transition is driven. For the Raman interaction considered in this section $\omega = \omega_z + \delta$, where ω_z is the axial frequency of one of the normal modes and δ is a small frequency detuning. In section (6.4) on stimulated Raman transitions, the transitions always involved driving a spin-flip transition. Here, no spin flip transitions are driven. The frequency difference between the two laser beams will be close to one of the motional frequencies (see figure (7.2)). This means the matrix elements $|1\rangle\langle 2|$ in equation (7.5) need to be replaced with $|1\rangle\langle 2| \rightarrow |1\rangle\langle 1|, |2\rangle\langle 2|$. Making these substitutions and rewriting equation (7.5), gives

$$H_I = \hbar\Omega e^{-i(\omega t - \phi)} (1 + i\eta\hat{z}) [|1\rangle\langle 1| + |2\rangle\langle 2|] + H.C.. \tag{7.6}$$

Also to make the notation a little less confusing since multiple ions will be considered, the following replacements will be made $|1\rangle \rightarrow |\downarrow\rangle$ and $|2\rangle \rightarrow |\uparrow\rangle$. Making these changes and collecting all the terms together, allows equation (7.6) to be rewritten as

$$H_g = \hbar\Omega \cos(\omega t - \phi) (|\downarrow\rangle\langle\downarrow| + |\uparrow\rangle\langle\uparrow|) - \hbar\Omega\eta\hat{z} \sin(\omega t - \phi) (|\downarrow\rangle\langle\downarrow| + |\uparrow\rangle\langle\uparrow|). \tag{7.7}$$

The first two terms, which do not depend on the position operator $\hat{z}$, behave as a Stark shift that oscillates in time. The shift can be canceled out by choosing the time the of interaction appropriately. Another possibility is to embed the gate interaction in the two

arms of a spin-echo sequence, which cancels the shift (see section 7.5). It will be ignored in the rest of the derivation. The last two terms show a position dependent force on both spin states. In general either the Rabi frequency or the phase will be different for the different spin states. The above Hamiltonian is for one ion, considering the general case for two ions gives

$$H_g = \sum_{j=1,2} \sum_{m_j=\uparrow,\downarrow} -\hbar\Omega^{m_j}\eta_j\hat{z}_j \sin\left(\omega t - \phi_{m_j}\right) |m_j\rangle \langle m_j| . \tag{7.8}$$

This Hamiltonian can be used to understand the force on multiple ions for different parameters and laser beam setups. The next section will go through a simple example. A more complicated example will discussed in the experimental section.

7.2.1 Example

One particular scenario is depicted in figure (7.2). This case is also discussed nicely in the dissertation by Jonathan Home [Home 06b]. In this case the two ground states are coupled via a two level excited state. The two Raman laser beams have a detuning Δ from the excited state, where Δ is much larger than the splittings between the ground state levels or the excited state levels. The two ground state levels are labeled by $|\uparrow\rangle$ and $|\downarrow\rangle$. The $|\downarrow\rangle$ state is coupled to the excited state only with σ^+ polarized light, and the $|\uparrow\rangle$ state is coupled with σ^- light. It has been assumed the Rabi frequency Ω is the same for all the different transitions and for both ions. The interference between two laser beams with orthogonal polarizations gives rise to the state dependent force. The interference creates a "walking standing wave" of the polarization. This is similar to the lin $\perp$ lin configuration discussed in reference [Metcalf 99]. In this case the resulting electric field is $E(z,t) = E_o[\hat{x}\cos(\omega_l t - k\cdot z) + \hat{y}\cos(\omega_l t + \omega t - k\cdot z)]$. Where E_o is the electric field amplitude of both beams and ω_l is the optical frequency of the laser beams. If $\omega = 0$, then a standing wave is created, where the polarization cycles from linear to circular to orthogonal linear to orthogonal circular over a distance of $\lambda_{eff}/2$. The effective

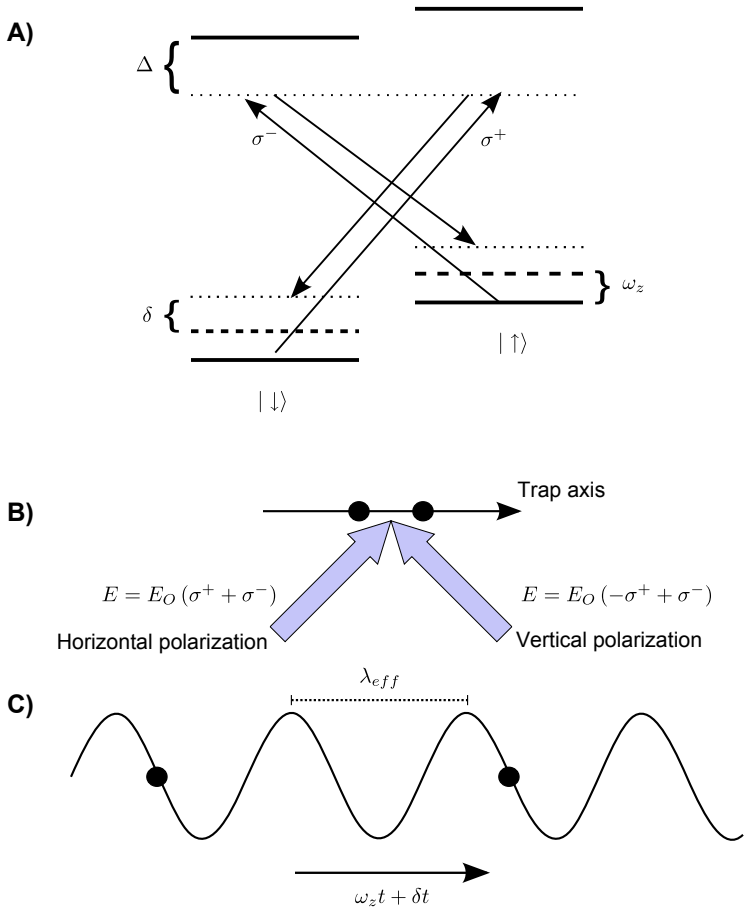

Figure 7.2: A) The level diagram for the phase gate considered in section (7.2.1). It is a four level system, where the coupling laser beams are detuned by Δ from the excited state, which is much larger than any of the other level splittings. Each of the ground states are coupled to one of the excited states with a stimulated-Raman transition. The difference frequency between the two beams that drive each transitions is $\omega_z + \delta$. The lower heavier dashed lines represent the one of the motional states of the pair of trapped ions. In this case it will represent the stretch mode of motion. B) This figure shows the polarization the laser beams used. C) The resulting polarization interference pattern from the two lasers beams used for the gate drive. They set up what is called a "walking standing wave" of the polarization.

wavelength λ_{eff} is related to the actual wavelength of the laser by $\lambda_{eff} = \frac{\lambda}{\sqrt{2}}$. The $\frac{1}{\sqrt{2}}$ factor comes from the projection of the laser's k-vector on to the trap axis, which is oriented at 45 degrees with respect to the trap axis. When the two lasers have a finite detuning $\omega \neq 0$ then polarization gradient changes at a rate ωt. This is what gives rise

to the "walking" part of the "walking standing wave."

The two ions are coupled via the Coulomb interaction and as such behave as two masses connected by a spring confined in an external harmonic well. Thus the position of ions can instead be written in terms of the their normal mode coordinates

$$z_1 = z_c + z_s \tag{7.9}$$

$$z_2 = z_c - z_s. \tag{7.10}$$

The normal mode coordinates z_c and z_s represent the center-of-mass and the stretch mode respectively. Substituting the normal mode coordinates into equation (7.8) and collecting like terms in the position coordinate gives

$$H_g = -\hbar\Omega[\eta_c\hat{z}_c\left(\sin\left(\omega t-\phi_{\uparrow_1}\right)|\uparrow_1\rangle\langle\uparrow_1| + \sin\left(\omega t-\phi_{\downarrow_1}\right)|\downarrow_1\rangle\langle\downarrow_1|\right) \tag{7.11}$$

$$-\eta_s\hat{z}_s\left(\sin\left(\omega t-\phi_{\uparrow_1}\right)|\uparrow_1\rangle\langle\uparrow_1| + \sin\left(\omega t-\phi_{\downarrow_1}\right)|\downarrow_1\rangle\langle\downarrow_1|\right) \tag{7.12}$$

$$+\eta_c\hat{z}_c\left(\sin\left(\omega t-\phi_{\uparrow_2}\right)|\uparrow_2\rangle\langle\uparrow_2| + \sin\left(\omega t-\phi_{\downarrow_2}\right)|\downarrow_2\rangle\langle\downarrow_2|\right) \tag{7.13}$$

$$+\eta_s\hat{z}_s\left(\sin\left(\omega t-\phi_{\uparrow_2}\right)|\uparrow_2\rangle\langle\uparrow_2| + \sin\left(\omega t-\phi_{\downarrow_2}\right)|\downarrow_2\rangle\langle\downarrow_2|\right)]. \tag{7.14}$$

The normal mode coordinates equation can be rewritten as $z_c \rightarrow z_c\hat{z}_c$ and $z_s \rightarrow z_s\hat{z}_s$. The terms with the $\hat{}$ represent the position operator $\left(a+a^\dagger\right)$ for that particular mode, and the other component is the magnitude. The form of the Hamiltonian can be made more intuitive rewriting it in terms of the basis states for two spin $\frac{1}{2}$ systems (two qubits): $|\uparrow\uparrow\rangle$, $|\downarrow\downarrow\rangle$, $|\uparrow\downarrow\rangle$, and $|\downarrow\uparrow\rangle$. Note that when two spins are represented in the same ket it is assumed the first ion corresponds to the spin state of ion 1 and the second spin is for ion 2. This helps reduce the number of subscripts, but they will be added if it helps with the clarity of a particular expression. The Hamiltonian in this basis can be determined from the above Hamiltonian by calculating all the matrix elements such as $\langle\uparrow\uparrow|\,H_g\,|\uparrow\uparrow\rangle$.

The Hamiltonian in this form is

$$\begin{aligned} H_g &= -2\hbar\Omega[\eta_c\hat{z}_c \sin(\omega t) |\uparrow\uparrow\rangle\langle\uparrow\uparrow| && (7.15)\\ &\quad +\eta_c\hat{z}_c \sin(\omega t - \Delta\phi) |\downarrow\downarrow\rangle\langle\downarrow\downarrow| && (7.16)\\ &\quad +\eta_c\hat{z}_c \cos\left(\frac{\Delta\phi}{2}\right) \sin(\omega t - \Delta\phi) [|\uparrow\downarrow\rangle\langle\uparrow\downarrow| + |\downarrow\uparrow\rangle\langle\downarrow\uparrow|] && (7.17)\\ &\quad +\eta_s\hat{z}_s \sin\left(\frac{\Delta\phi}{2}\right) \cos(\omega t - \Delta\phi) [|\uparrow\downarrow\rangle\langle\uparrow\downarrow| - |\downarrow\uparrow\rangle\langle\downarrow\uparrow|]. && (7.18) \end{aligned}$$

The phase difference between the spin states has been defined as $\Delta\phi \equiv \phi_\uparrow - \phi_\downarrow$, and it is adjusted to be the same for both ions. The first three lines represent a time dependent optical dipole force on the center-of-mass mode of motion. The last line represents a time dependent force on the stretch mode of motion. Note the sign difference between the matrix elements $|\uparrow\downarrow\rangle\langle\uparrow\downarrow|$ and $-|\downarrow\uparrow\rangle\langle\downarrow\uparrow|$. This implies that the sign of the force is different for the two different states. The frequency of the force will be chosen such that it is near the resonance with the stretch mode. This means all the terms in the Hamiltonian involving the center-of-mass mode of motion to a good approximation, be neglected, since they will be off resonance. The Hamiltonian can now be written as

$$H_g = -2\hbar\Omega\eta_s\hat{z}_s \sin\left(\frac{\Delta\phi}{2}\right) \cos(\omega t - \Delta\phi) [|\uparrow\downarrow\rangle\langle\uparrow\downarrow| - |\downarrow\uparrow\rangle\langle\downarrow\uparrow|]. \quad (7.19)$$

Transforming the position operator $\hat{z}_s$ into the interaction picture gives

$$\hat{z}_s = a_s e^{-i\omega_s t} + a_s^\dagger e^{-i\omega_s t}, \quad (7.20)$$

where a_s and $a_s^\dagger$ are the annihilation and the creation operators for the stretch mode of motion. The frequency of the this mode is ω_s. Taking equation (7.20) and inserting into equation (7.19) gives a version of the Hamiltonian that will be convenient for seeing the connection to coherent states discussed in a later section. A rotating-wave approximation is made to simplify the Hamiltonian, where terms that oscillate a $\omega + \omega_z$ are dropped.

$$H_g = -\hbar\eta_s\Omega \sin\left(\frac{\Delta\phi}{2}\right) a_s e^{i\left(\omega t - \frac{\Delta\phi}{2}\right)} e^{-i\omega_s t} [|\uparrow\downarrow\rangle\langle\uparrow\downarrow| - |\downarrow\uparrow\rangle\langle\downarrow\uparrow|] + H.c.. \quad (7.21)$$

7.3 Coherent States and the Forced Harmonic Oscillator

In this section some basic properties of coherent states [Howard 87, Walls 94] and the quantum forced harmonic oscillator [Carruthers 65, Merzbacher 98] will be described. This is relevant because the oscillations of a pair of trapped ions are that of a harmonic oscillator. Also applying the interaction given by equation (7.21) to the stretch mode of a pair of ions, is equivalent to driving a harmonic oscillator with a time dependent force. In the first section a few of the relevant properties of coherent states will be mentioned. Then in the next section, the results of a forced harmonic will be given.

7.3.1 Coherent States

Typically when talking about the motion of trapped ions for quantum information processing, the Fock states (number basis) are used, since they form a complete orthonormal set of states for the harmonic oscillator. Also some quantum algorithms [Cirac 95] require the ability to put in a single quanta of energy into one of the motional modes, changing the Fock state by one, in order to perform a two qubit gate. The geometric phase gate [Leibfried 03b] can be used on any motional state as long as the ions are in the Lamb-Dicke regime. In the geometric phase gate experiments discussed in this dissertation, the ions' motion is cooled to the ground state and then an optical dipole force is applied. This has the effect of creating a coherent state of motion. A coherent state $|\alpha\rangle$ can be expanded in the Fock state basis [Walls 94]

$$|\alpha\rangle = e^{\frac{|\alpha|^2}{2}} \sum_{n=0}^{\infty} \frac{\alpha^n}{n!^{\frac{1}{2}}} |n\rangle . \tag{7.22}$$

A coherent state can be generated by applying a displacement operator to $|n=0\rangle$ Fock state. The form of the displacement operator is [Walls 94]

$$D(\alpha) = e^{\alpha a^\dagger - \alpha^\star a^\star}. \tag{7.23}$$

Applying this operator to the ground state, results in the creation of the coherent state

$$|\alpha\rangle = D(\alpha)|0\rangle . \tag{7.24}$$

7.3.2 Forced Harmonic Oscillator

As mention earlier the Hamiltonian equation (7.21) derived in section (7.2) is the same Hamiltonian that gives rise to a forced harmonic oscillator (FHO). This section describes a few of the FHO's relevant properties. The text book by Merzbacher [Merzbacher 98] has a good discussion of the subject, and this section follows that discussion closely. The Hamiltonian for a FHO is

$$H_{fho} = \frac{p^2}{2m} + \frac{1}{2}m\omega z^2 - zf(t) . \tag{7.25}$$

Using the annihilation and creation operator form of the position and momentum operators and going to an interaction picture where $H_o = \hbar\omega(a^\dagger a + \frac{1}{2})$ the interaction Hamiltonian is

$$H^I_{fho}(t) = -f(t)\, a e^{-i\omega t} - f^\star(t)\, a^\dagger e^{i\omega t}. \tag{7.26}$$

To understand the time development of this system, the Schrodinger equation for the time-evolution operator will be used [Merzbacher 98]

$$i\hbar\frac{\partial T(t,t_1)}{\partial t} = H^I_{fho}(t)\, T(t,t_1) , \tag{7.27}$$

where the solution for time-evolution operator is

$$T(t,t_1) = -\frac{i}{\hbar}\int_{t_1}^{t} dt' H^I_{fho}(t)\, T(t,t_1) . \tag{7.28}$$

The solution depends on the structure of the Hamiltonian $H^I_{fho}(t)$. It will be seen later that for the case considered here the Hamiltonian at different times does not commute with itself. This leads to following solution [Merzbacher 98] for $T(t,t_1)$.

$$T(t,t_1) = e^{\left[\frac{-i}{\hbar}\int_{t_1}^{t} dt'\left(f(t')ae^{-i\omega t'} + f^\star(t')a^\dagger e^{i\omega t'}\right)\right]} \tag{7.29}$$

$$\times e^{\frac{-1}{2\hbar^2}\int_{t_1}^{t} dt'\int_{t_1}^{t} dt''\left[H^I_{fho}(t'),H^I_{fho}(t'')\right]}. \tag{7.30}$$

The first term has the form of the displacement operator, which can be seen if the following substitutions are made

$$\alpha(t) = \frac{-i}{\hbar}\int_{t_1}^{t} dt' f\left(t'\right) e^{-i\omega t'} \tag{7.31}$$

and

$$\alpha^{\star}(t) = \frac{i}{\hbar}\int_{t_1}^{t} dt' f^{\star}\left(t'\right) e^{i\omega t'}. \tag{7.32}$$

The argument of the second term of equation (7.30) is the phase acquired during the application of the interaction, which will be called $\Phi(t)$. The commutator $\left[H^I_{fho}(t'), H^I_{fho}(t'')\right]$ can be evaluated using equation (7.26) and the commutation relations for the a and $a^{\dagger}$ [Sakurai 94]. Working through the algebra gives for the phase

$$\Phi(t) = \frac{-1}{2\hbar^2}\int_{t_1}^{t} dt' \int_{t_1}^{t} dt'' \left(f\left(t'\right) f^{\star}\left(t''\right) e^{i\omega(t''-t')} - f^{\star}\left(t'\right) f\left(t''\right) e^{-i\omega(t''-t')}\right). \tag{7.33}$$

Now the time evolution operator equation (7.30) can be rewritten in the form

$$T(t,t_1) = e^{\left(\alpha(t)a^{\dagger} - \alpha^{\star}(t)a^{\star}\right)} e^{\Phi(t)}. \tag{7.34}$$

From this it can been seen what happens to harmonic oscillator subject to time dependent dipole force. If the system starts in a Fock state, then it will evolve to coherent state that acquires a phase $\Phi(t)$.

7.4 Geometric Phase and Coherent State Amplitude

Now that the general form of the coherent state amplitude and phase acquired during the phase gate interaction has been derived, the results can applied to the specific case of the Hamiltonian in equation (7.21). The coherent state amplitude as a function of time is given by equation (7.31). By inspection of equation (7.21) the time dependent force can be written as

$$f(t) = -\hbar\eta_s \sin\left(\frac{\Delta\phi}{2}\right) e^{i\left(\omega t - \frac{\Delta\phi}{2}\right)}. \tag{7.35}$$

The frequency ω used in the general expression for $\alpha(t)$ will be replaced by ω_z, making these substitutions leads to

$$\alpha(t) = i\eta_s\Omega \int_{t_1}^{t} dt' \sin\left(\frac{\Delta\phi}{2}\right) e^{i\left(\omega t' - \frac{\Delta\phi}{2}\right)} e^{-i\omega_s t'}. \tag{7.36}$$

Integrating this expression and making the definition $\delta \equiv \omega - \omega_s$ gives the expression

$$\alpha(t) = 2\eta_s\Omega \sin\left(\frac{\Delta\phi}{2}\right) e^{i\left(\frac{\delta}{2}t - \frac{\Delta\phi}{2}\right)} \frac{\sin\left(\frac{\delta}{2}t\right)}{\delta}. \tag{7.37}$$

There are a few interesting things to note about this expression. The coherent state amplitude oscillates in time, and after a time $t = \frac{2n\pi}{\delta}$ $(n = 0, 1, 2...)$ the coherent state amplitude returns to zero. This is important, because if some other time is chosen for the length of the interaction, then the spin states are entangled with the motion. This is undesirable in some circumstances and should be avoided for the phase gate. It could lead to excess decoherence as a result of the motion being sensitive to decoherence from ambient electric field noise. Also it should be noted the detuning δ influences the magnitude of the coherent state obtained. Smaller detunings lead to larger amplitude coherent states, which follows from the fact that as the detuning decreases the drive frequency approaches the resonance of the motion.

The next important term is the geometrical phase equation (7.33) acquired during the gate interaction. To calculate the phase the commutator

$$\left[H_{fho}^{I}(t'), H_{fho}^{I}(t'')\right] \tag{7.38}$$

needs to be calculated using equation (7.21). Using the commutator relations for a and $a^{\dagger}$ [Sakurai 94], gives the result

$$\left[H_g(t'), H_g(t'')\right] = 2i\hbar^2\eta_s^2\Omega^2 \sin^2\left(\frac{\Delta\phi}{2}\right) \sin\left(\delta\left(t'' - t'\right)\right). \tag{7.39}$$

The phase as function of the interaction time can now be written as, plugging equation (7.39) into equation 7.33,

$$\Phi(t) = \frac{i}{2}\eta_s^2\Omega^2 \sin^2\left(\frac{\Delta\phi}{2}\right) \int_{t_1}^{t} dt' \int_{t_1}^{t} dt'' \sin\left(\delta\left(t'' - t'\right)\right). \tag{7.40}$$

Integrating this expression gives

$$\Phi(t) = -\eta_s^2 \Omega^2 \sin^2\left(\frac{\Delta\phi}{2}\right) \frac{(\sin(\delta t) - \delta t)}{\delta^2}. \tag{7.41}$$

Now if the time is chosen such that the coherent state returns to its starting state at $t = \frac{2n\pi}{\delta}$ then the phase acquired will be

$$\Phi\left(t = \frac{2n\pi}{\delta}\right) = \eta_s^2 \Omega^2 \sin^2\left(\frac{\Delta\phi}{2}\right) \frac{(2n\pi)}{\delta^2}. \tag{7.42}$$

In order to get $\Phi = \frac{\pi}{2}$, the experiment parameters such as the phase $\Delta\phi$, the Rabi frequency Ω, and the detuning δ can be adjusted.

7.5 Ideal Gate Implementation

This section describes how the geometrical phase gate is implemented. The effect of the phase gate is to imprint a phase on some of the states of a superposition. However this phase cannot be directly observed in our experiments. With trapped ions, the measurable quantity is the ion's fluorescence. By embedding the phase gate drive into a Ramsey experiment [Ramsey 63] enables the creation of states with different parity, which can be distinguished via resonance fluorescence techniques.

This implementation assumes that two ions are confined in a linear radio-frequency Paul trap, and the motion along the trap axis has been cooled to the ground state. Figure (7.3) shows the sequence of pulses used in performing the gate operations. The first step is to prepare the ions via optical pumping techniques [Wineland 98] to create the state

$$\Psi = |\uparrow\uparrow\rangle. \tag{7.43}$$

The motional state has been left out of the wave function. The next step is to create a equal superposition of all the states. This is accomplished by applying a co-carrier rotation to both ions. Applying the rotation $R\left(\frac{\pi}{2}, 0\right)$(note $\sigma_x = iR(\pi, 0)$ and $\sigma_y = iR\left(\pi, \frac{\pi}{2}\right)$), creates the superposition

$$\Psi = \frac{1}{2}\left(|\uparrow\uparrow\rangle - i|\uparrow\downarrow\rangle - i|\downarrow\uparrow\rangle - |\downarrow\downarrow\rangle\right). \tag{7.44}$$

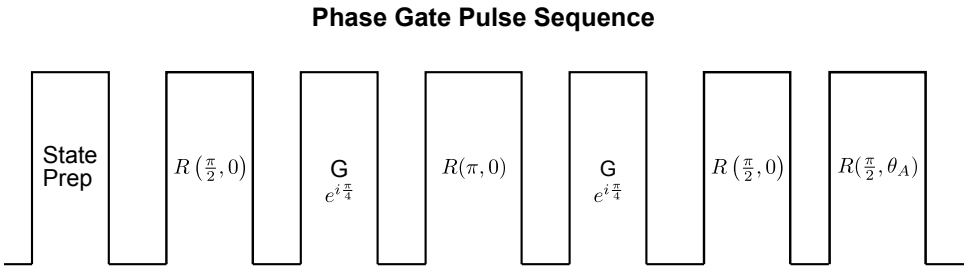

Figure 7.3: Phase gate pulse sequence. The state preparation includes everything required to create state (7.43). This includes things such as Doppler cooling, Raman cooling, etc.. The phase gate operator is represented by G, and the phase acquired during each application is adjusted to be $e^{i\frac{\pi}{4}}$. The drive is embedded in a spin echo pulse sequence composed of the rotations $R\left(\frac{\pi}{2},0\right)$, $R\left(\pi,0\right)$, and $R\left(\frac{\pi}{2},0\right)$. Theses rotations are co-carrier stimulated Raman transitions applied to both ions. The last pulse is the analysis pulse for the phase gate given by $R\left(\frac{\pi}{2},\theta_A\right)$.

At this point, the phase gate interaction could be applied to imprint the necessary phase. However the phase gate drive is embedded in a spin echo sequence [Vandersypen 04]. This has a number of advantages. It makes the gate resistant to uniform magnetic field changes that are slow compared to the length of the arms of the spin echo sequence[Leibfried 03b]. By splitting up the phase gate interaction so that half the phase is acquired in the first half of the spin-echo sequence and the rest acquired in the second half, residual stark shifts resulting from the gate interaction are canceled. One possibility is to choose the detuning such that each half of the gate drive takes you half way around a loop in phase space. This has the disadvantage that there is additionally time where the spin and motion are in entangled. If the motional decoherence rate is larger than the spin decoherence, which is often the case, then the decoherence will be larger. Therefore it is more desirable for each half of the gate drive to make one complete smaller loop in phase space. Thus at the end of each drive the spin and motion are unentangled. The gate is applied for a time that imprints the phase $e^{i\frac{\pi}{4}}$. In particular this would be applied near the resonance of the stretch mode of motion for the two ions. This is equivalent to

applying the operation

$$G\left(\frac{\pi}{4}\right) = \begin{bmatrix} 1 & 0 & 0 & 0 \\ 0 & e^{i\frac{\pi}{4}} & 0 & 0 \\ 0 & 0 & e^{i\frac{\pi}{4}} & 0 \\ 0 & 0 & 0 & 1 \end{bmatrix} \tag{7.45}$$

to the spin states of the two ions. This changes the state to

$$\Psi = \frac{1}{2}\left(|\uparrow\uparrow\rangle - ie^{i\frac{\pi}{4}}|\uparrow\downarrow\rangle - ie^{i\frac{\pi}{4}}|\downarrow\uparrow\rangle - |\downarrow\downarrow\rangle\right). \tag{7.46}$$

The next pulse is the refocusing pulse. This is implemented by applying the operation $R(\pi, 0)$ to both ions, which gives

$$\Psi = \frac{1}{2}\left(i|\uparrow\uparrow\rangle - e^{i\frac{\pi}{4}}e|\uparrow\downarrow\rangle - e^{i\frac{\pi}{4}}|\downarrow\uparrow\rangle - i|\downarrow\downarrow\rangle\right). \tag{7.47}$$

In the second half of the spin-echo sequence, the second part of the phase gate interaction is applied, so the another loop in phase space is driven. This gives the state

$$\Psi = \frac{1}{2}\left(|\uparrow\uparrow\rangle - |\uparrow\downarrow\rangle - |\downarrow\uparrow\rangle - |\downarrow\downarrow\rangle\right). \tag{7.48}$$

Next in the sequence, is the final pulse in the Ramsey experiment. The rotation applied is $R\left(\frac{\pi}{2}, 0\right)$.

$$\Psi = \frac{1}{\sqrt{2}}\left(|\uparrow\uparrow\rangle + i|\downarrow\downarrow\rangle\right). \tag{7.49}$$

The state at this point is a more obvious entangled state and happens to be similar to one of the Bell states[Nielsen 00] (It will be referred to as a Bell state)ξ. However just measuring the resonant fluorescence at this point would not give any information about the entanglement phase. In order show the entanglement, a final analysis pulse $R\left(\frac{\pi}{2}, \theta_A\right)$ with a variable phase is applied, which results in creating

$$\begin{aligned} \Psi_g &= \frac{1}{2}e^{i\theta_A}\left(\cos(\theta_A) - \sin(\theta_A)\right)|\uparrow\uparrow\rangle && (7.50) \\ &+\frac{1}{2}\left(\cos(\theta_A) + \sin(\theta_A)\right)|\uparrow\downarrow\rangle && (7.51) \\ &+\frac{1}{2}\left(\cos(\theta_A) + \sin(\theta_A)\right)|\downarrow\uparrow\rangle && (7.52) \\ &\frac{\sqrt{2}}{4}e^{i\frac{5\pi}{4}}\left(e^{-i\frac{3\pi}{2}} + e^{i2\theta_A}\right)|\downarrow\downarrow\rangle. && (7.53) \end{aligned}$$

It may be difficult to see how this state makes it possible to analyze the entanglement. Let's examine the resulting state for a couple choices of the phase θ_A.

$$\Psi_g\left(\theta_A = \frac{\pi}{4}\right) = \frac{1}{\sqrt{2}}\left(|\uparrow\downarrow\rangle + |\downarrow\uparrow\rangle\right) \tag{7.54}$$

$$\Psi_g\left(\theta_A = \frac{3\pi}{4}\right) = \frac{1}{\sqrt{2}}\left(|\uparrow\uparrow\rangle + i\,|\downarrow\downarrow\rangle\right) \tag{7.55}$$

$$\Psi_g\left(\theta_A = \frac{5\pi}{4}\right) = \frac{-1}{\sqrt{2}}\left(|\uparrow\downarrow\rangle + |\downarrow\uparrow\rangle\right) \tag{7.56}$$

$$\Psi_g\left(\theta_A = \frac{7\pi}{4}\right) = \frac{1}{\sqrt{2}}\left(|\uparrow\uparrow\rangle + i\,|\downarrow\downarrow\rangle\right). \tag{7.57}$$

The result of varying the phase θ_A between 0 and 2π is that the state oscillates between the state (7.54) and the state (7.55) and a rate of $2\theta_A$. The state in equation (7.54) is an example of a decoherence-free subspace (DFS) state [Kielpinski 01] (also called a triplet state). The DFS state is very useful for its resistance to decoherence from uniform magnetic field noise, and will be used in the entangled mechanical oscillators experiment discussed in chapter (8). These two different states can be distinguished via resonance fluorescence, since they have a different parity. In this context the parity refers to the number of ions in the $|\uparrow\rangle$ state (strongly fluorescing state). The Bell state equation (7.55) has even parity, since a measurement of this state will always result in measuring two or zero ions fluorescing. The DFS state is an odd parity state since only one ion is measured in the $|\uparrow\rangle$. The populations P (for example $P_{|\uparrow\uparrow\rangle} = \langle\Psi_g\,|\uparrow\uparrow\rangle\,\langle\uparrow\uparrow|\,\Psi_g\rangle$) of the for the various spin states are

$$P_{|\uparrow\uparrow\rangle} = P_{|\downarrow\downarrow\rangle} = \frac{1}{4}\left(1 - \sin\left(2\theta_A\right)\right) \tag{7.58}$$

$$P_{|\uparrow\downarrow\rangle} = P_{|\downarrow\uparrow\rangle} = \frac{1}{4}\left(1 + \sin\left(2\theta_A\right)\right). \tag{7.59}$$

The parity signal $\Pi\left(\theta_A\right)$ is defined as

$$\Pi\left(\theta_A\right) = P_{|\uparrow\uparrow\rangle} + P_{|\downarrow\downarrow\rangle} - \left[P_{|\uparrow\downarrow\rangle} + P_{|\downarrow\uparrow\rangle}\right] \tag{7.60}$$

$$= -\sin\left(2\theta_A\right). \tag{7.61}$$

The parity signal can be used to verify that entanglement is present by looking at the

amplitude of the oscillation. The parity can be written as $\Pi(\theta_A) = -C\sin(\theta_A)$, where C characterizes the contrast of the oscillation. In the ideal case $C = 1$. Having a contrast greater than 50% shows that entanglement is present [Sackett 00, Leibfried 03b]. Also the contrast is a lower bound on the fidelity F, which is a standard measure of the amount of entanglement[Nielsen 00].

$$F = \langle \Psi_{ideal} | \rho | \Psi_{ideal} \rangle . \tag{7.62}$$

This can be understood as the overlap of the created state with the ideal state. The density matrix of the system is represented by ρ. The fidelity of creating the Bell state equation (7.55) is

$$F = \frac{1}{2}\left(P_{|\uparrow\uparrow\rangle} + P_{|\downarrow\downarrow\rangle}\right) + |\rho_{\uparrow\uparrow,\downarrow\downarrow}| . \tag{7.63}$$

The density matrix element $|\rho_{\uparrow\uparrow,\downarrow\downarrow}| = \langle \Psi_{ideal} | \uparrow\uparrow \rangle \langle \downarrow\downarrow | \Psi_{ideal} \rangle$ and also note that $\rho_{\uparrow\uparrow,\downarrow\downarrow} = \rho^{\star}_{\downarrow\downarrow,\uparrow\uparrow}$. The fidelity of creating the DFS state (7.54) is

$$F = \frac{1}{2}\left(P_{|\uparrow\downarrow\rangle} + P_{|\downarrow\uparrow\rangle}\right) + |\rho_{\uparrow\downarrow,\downarrow\uparrow}| . \tag{7.64}$$

Assuming the fidelity of creating either state is the same, then equations (7.64) and (7.63) can be inserted into equation to (7.60) to give

$$\frac{\Pi(\theta_A)}{2} = -\frac{C}{2}\sin(\theta_A) = |\rho_{\uparrow\downarrow,\downarrow\uparrow}| - |\rho_{\uparrow\uparrow,\downarrow\downarrow}| . \tag{7.65}$$

Thus when the phase is chosen such that the Bell state is created then contrast can be related to off diagonal density matrix elements $|\rho_{\uparrow\uparrow,\downarrow\downarrow}| = \frac{C}{2}$. This allows for a more experimentally convenient definition of the fidelity

$$F = \frac{1}{2}\left(P_{|\uparrow\uparrow\rangle} + P_{|\downarrow\downarrow\rangle}\right) + \frac{C}{2}. \tag{7.66}$$

The contrast can be experimentally determined from a parity measurement. The populations can be determined from a separate experiment, where the analysis pulse is omitted and the populations are measured.

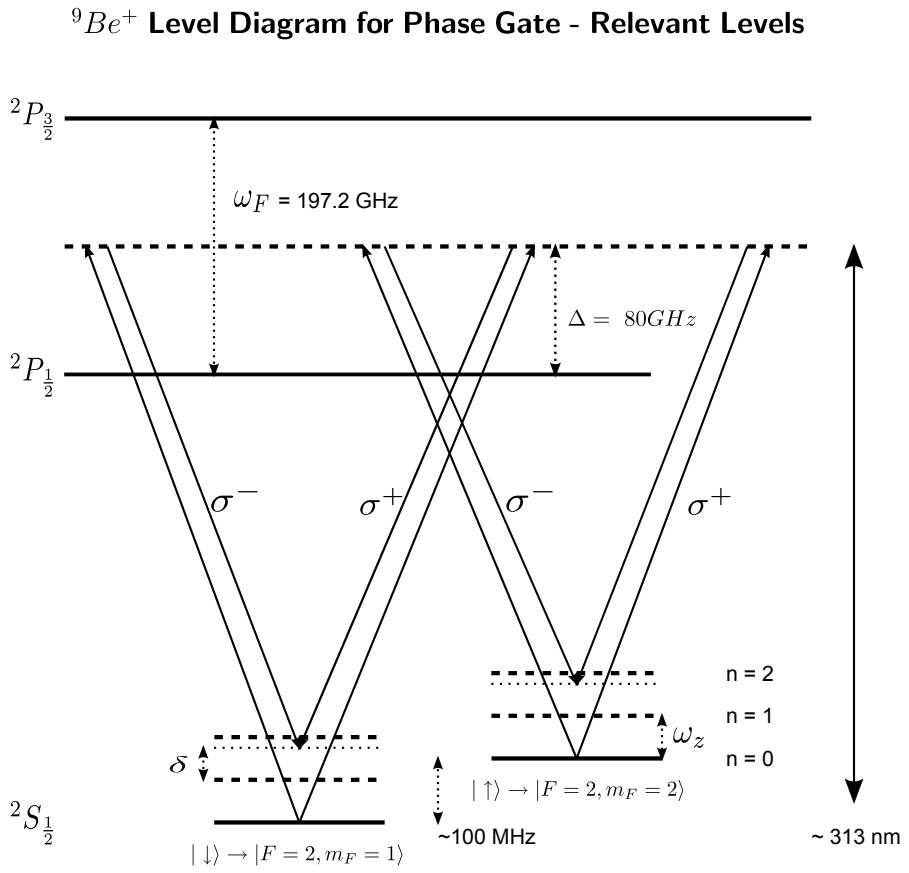

Figure 7.4: Experimental level diagrams for a phase gate on ^{9}Be$^+$ ions. This figure shows the relevant levels. Only two of the $S_{\frac{1}{2}}$ ground state hyperfine levels play a role in the gate; these are split by ~ 100 MHz. The fine structure splitting of the excited states is 197.2 GHz [Langer 06]. Each of the spin states is off resonantly coupled to both of the excited states with σ^- and σ^+ polarized light, except there is no state in the $P_{\frac{1}{2}}$ level for $|\uparrow\rangle$ to couple to with σ^+ polarized light. The detuning of the Raman laser beams from the $P_{\frac{1}{2}}$ is given by Δ, which is ~ 80 GHz. Superimposed on top of the spin states are the harmonic oscillator states for one of the normal modes, which is labeled by ω_z. The detuning of the difference frequency of the Raman beams from being on resonance with the motional states is δ.

7.6 Phase Gate Entanglement Experiment

7.6.1 Theory

The theory for the experimental implementation of the phase gate discussed in section (7.6) is more complicated than the example discussed above. In this section some of the differences are highlighted. The phase gate will be between two $^9Be^+$ ions, whose relevant energy levels are shown in figure (7.4). The two ground state levels are coupled to the excited states with both types of circular polarizations. For each ion the $|\uparrow\rangle$ and the $|\downarrow\rangle$ states will not have the same Rabi frequency and each ion will see different laser beam phases. The stimulated Raman transition Rabi frequency for each state will be given by [Wineland 03]

$$\Omega_i^{m_i} = \frac{e^{i(\phi_1-\phi_2)}}{4\hbar^2}\sum_j \frac{\langle m_i|\,\vec{d}\cdot\vec{E}_n\,|j\rangle\,\langle j|\,\vec{d}\cdot\vec{E}_c\,|m_i\rangle}{\Delta_j}. \tag{7.67}$$

In this expression i represents the ion number and m_i is the spin state for ion i. It is often convenient to use the low magnetic field notation for the labeling of the spin states. In general the states at intermediate magnetic fields will be a superposition of these states. The experiment discussed in the next section uses the states $|\downarrow\rangle = |F=2, m_F=1\rangle$ and $|\uparrow\rangle = |F=2, m_F=2\rangle$ states of $^9Be^+$ at a field of ~ 120 Gauss. The two levels are split by ~ 100 MHz. In the $|m_I, m_j\rangle$ basis we have $|\downarrow\rangle = \alpha\,|m_I=\frac{1}{2}, m_J=\frac{1}{2}\rangle + \beta\,|\frac{3}{2}, \frac{-1}{2}\rangle$ and $|\uparrow\rangle = |m_I=\frac{3}{2}, m_J=\frac{1}{2}\rangle$. These ground state levels are coupled to the excited states by the electric fields $\vec{E}_n = E_n\left(\hat{\sigma^+} + \hat{\sigma^-}\right)$ and $\vec{E}_c = E_c\left(-\hat{\sigma}^+ + \hat{\sigma^-}\right)$ see part B and C of figure (7.2). The term in the denominator Δ_i is the detuning from the excited states, and the sum is over all the possible excited states, and in $^9Be^+$these would be the $P_{\frac{1}{2}}$ and $P_{\frac{3}{2}}$ states. Both Raman beams can be considered to have the same detuning from an excited state if the detuning Δ is much larger than the splitting between the spin states. In the experiment discussed below the splitting between the excited states is 197.2 GHz [Langer 06] and the two Raman beams are detuned 80 GHz from the $P_{\frac{1}{2}}$

level.

The phase gate Hamiltonian (7.8) can be used to write the Hamiltonian for this case. Again it will be assumed there are only two ions being used and two axial normal modes, which can be written in terms of the individual ion positions as equation (7.9). The Hamiltonian becomes

$$\begin{aligned} H_g &= -\hbar[\eta_c\hat{z}_c\left(\sin\left(\omega t-\phi_1\right)\left(\Omega^{\uparrow}\left|\uparrow_1\right\rangle\left\langle\uparrow_1\right|+\Omega^{\downarrow}\left|\downarrow_1\right\rangle\left\langle\downarrow_1\right|\right)\right) && (7.68)\\ &\quad \eta_s\hat{z}_s\left(\sin\left(\omega t-\phi_1\right)\left(\Omega^{\uparrow}\left|\uparrow_1\right\rangle\left\langle\uparrow_1\right|+\Omega^{\downarrow}\left|\downarrow_1\right\rangle\left\langle\downarrow_1\right|\right)\right) && (7.69)\\ &\quad +\eta_c\hat{z}_c\left(\sin\left(\omega t-\phi_2\right)\left(\Omega^{\uparrow}\left|\uparrow_2\right\rangle\left\langle\uparrow_2\right|+\Omega^{\downarrow}\left|\downarrow_2\right\rangle\left\langle\downarrow_2\right|\right)\right) && (7.70)\\ &\quad -\eta_s\hat{z}_s\left(\sin\left(\omega t-\phi_2\right)\left(\Omega^{\uparrow}\left|\uparrow_2\right\rangle\left\langle\uparrow_2\right|+\Omega^{\downarrow}\left|\downarrow_2\right\rangle\left\langle\downarrow_2\right|\right)\right)]. && (7.71)\end{aligned}$$

This Hamiltonian can be written in terms of the two qubit basis states: $|\uparrow\uparrow\rangle$, $|\downarrow\downarrow\rangle$, $|\uparrow\downarrow\rangle$, and $|\downarrow\uparrow\rangle$ as

$$\begin{aligned} H_g &= -\hbar[2\eta_c\hat{z}_c\sin\left(\omega t-\frac{1}{2}\left(\phi_1+\phi_2\right)\right)\cos\left(\frac{-\Delta\phi}{2}\right) && (7.72)\\ &\quad \times\left[\Omega^{\uparrow}\left|\uparrow\uparrow\right\rangle\left\langle\uparrow\uparrow\right|+\Omega^{\downarrow}\left|\downarrow\downarrow\right\rangle\left\langle\downarrow\downarrow\right|\right] && (7.73)\\ &\quad +\eta_c\hat{z}_c\sin\left(\omega t-\phi_1\right)\left[\Omega^{\downarrow}\left|\downarrow\uparrow\right\rangle\left\langle\downarrow\uparrow\right|+\Omega^{\uparrow}\left|\uparrow\downarrow\right\rangle\left\langle\uparrow\downarrow\right|\right] && (7.74)\\ &\quad +\eta_c\hat{z}_c\sin\left(\omega t-\phi_2\right)\left[\Omega^{\uparrow}\left|\downarrow\uparrow\right\rangle\left\langle\downarrow\uparrow\right|+\Omega^{\downarrow}\left|\uparrow\downarrow\right\rangle\left\langle\uparrow\downarrow\right|\right] && (7.75)\\ &\quad +2\eta_s\hat{z}_s\cos\left(\omega t-\frac{1}{2}\left(\phi_1+\phi_2\right)\right)\sin\left(\frac{-\Delta\phi}{2}\right) && (7.76)\\ &\quad \times\left[\Omega^{\uparrow}\left|\uparrow\uparrow\right\rangle\left\langle\uparrow\uparrow\right|+\Omega^{\downarrow}\left|\downarrow\downarrow\right\rangle\left\langle\downarrow\downarrow\right|\right] && (7.77)\\ &\quad +\eta_s\hat{z}_s\sin\left(\omega t-\phi_1\right)\left[\Omega^{\downarrow}\left|\downarrow\uparrow\right\rangle\left\langle\downarrow\uparrow\right|+\Omega^{\uparrow}\left|\uparrow\downarrow\right\rangle\left\langle\uparrow\downarrow\right|\right] && (7.78)\\ &\quad -\eta_s\hat{z}_s\sin\left(\omega t-\phi_2\right)\left[\Omega^{\uparrow}\left|\downarrow\uparrow\right\rangle\left\langle\downarrow\uparrow\right|+\Omega^{\downarrow}\left|\uparrow\downarrow\right\rangle\left\langle\uparrow\downarrow\right|\right]. && (7.79)\end{aligned}$$

This Hamiltonian simplifies when looking at a few special cases. The interaction is usually tuned to be near resonance with only one of the motional modes. Most commonly this will be the stretch mode, since it has a reduced sensitivity to heating from stray electric fields [Kielpinski 00]. Choosing the ion spacing see part C of figure (7.2) such that the phase difference between two ions is an integer multiple of 2π and that one ion

has a phase of zero, (i.e. $\phi_1 = 0$ and $\phi_2 = \phi_1 + 2\pi$), the Hamiltonian simplifies to

$$H_g = -\hbar\eta_s\hat{z}_s \sin(\omega t)\left(\Omega^{\uparrow} - \Omega^{\downarrow}\right)\left[|\downarrow\uparrow\rangle\langle\downarrow\uparrow| - |\uparrow\downarrow\rangle\langle\uparrow\downarrow|\right]. \tag{7.80}$$

In this case only the states $|\uparrow\downarrow\rangle$, and $|\downarrow\uparrow\rangle$ will acquire a motional dependent phase, which is proportional to the difference in the Rabi frequency between the spin states. Another case worth considering is the one where the ions are spaced by $\lambda_{eff}/2$ in the interference pattern, which corresponds to having a phase difference between the ions of π (i.e. $\phi_1 = 0$ and $\phi_2 = \phi_1 + \pi$)

$$\begin{aligned} H_g &= -\hbar\eta_s\hat{z}_s \sin(\omega t)\left[2\Omega^{\uparrow}|\uparrow\uparrow\rangle\langle\uparrow\uparrow| + 2\Omega^{\downarrow}|\downarrow\downarrow\rangle\langle\downarrow\downarrow|\right. & (7.81)\\ &\quad \left. + \left(\Omega^{\uparrow} + \Omega^{\downarrow}\right)|\uparrow\downarrow\rangle\langle\uparrow\downarrow| - \left(\Omega^{\uparrow} + \Omega^{\downarrow}\right)|\downarrow\uparrow\rangle\langle\downarrow\uparrow|\right]. & (7.82)\end{aligned}$$

Here all the states are driven and pick up a phase. If the Rabi frequencies are different, then a differential phase between the states is produced, which leads to entanglement. However, if $\Omega^{\uparrow} = \Omega^{\downarrow}$ then the force on all the states is the same and no entanglement will occur.

Well if you read this part then you must be really into ion trapping. Send me an email at john.d.jost@gmail.com and let me know you got this far. (It would be cool to know if after a few years have past since the writing of this thesis if anyone is actually still looking at it.)

7.6.2 Determining the Phase - Ion Spacing

Determining the phase of the ions in the interference pattern is crucial to being able to apply a known state dependent force. A calibration experiment can be performed to determine the relative phase and adjust it. This calibration experiment will be explained in the context of dealing with two $^9Be^+$ions, but the same procedure applies to the four ion mixed species crystal entanglement discussed in section (7.6.4). After cooling the two ions to the ground state see chapter (3) the ions are prepared in the $|\uparrow\uparrow\rangle$ state using

optical pumping. Then the laser beams that give rise to the gate interaction equation (7.79) are applied for a fixed length of time. In the examples discussed above it is assumed that the difference frequency of the laser is detuned by δ from the resonance of the one of the modes. In this experiment the difference frequency is set to be resonant with the stretch mode of motion. If the two ions have a spacing such that there is a phase difference of 2π, then the ions experience the Hamiltonian given by equation (7.80). In this case the ions experience no force. However if the phase difference is π then they do experience a force given by equation (7.82). This the force is on resonance with the mode of motion, and the ions' motional state is driven to a coherent state see section 7.3.2. Then a motion subtracting (MS) Raman transition (see section (6)) is performed. If the ions' motion has been excited, then this transition gets driven, but no transition is driven if the motional state is still in the ground state. When a transition is driven the ions internal state is put into a non-fluorescing state. Thus using resonance fluorescence detection [Langer 06] it can be determined if the motional state was excited. The ion spacing can be varied by changing the potentials on the electrodes, which also changes the mode frequencies. This can be done and the experiment repeated until the correct spacing is obtained. The goal is to apply the Hamiltonian in equation (7.80), which occurs when no force is applied to the ions in this calibration experiment.

7.6.3 Determining the Detuning

It is often difficult to know the exact magnitude the of Rabi frequency and other parameters that will determine the required detuning for the phase gate, see equation (7.3). This means it is necessary to determine it experimentally, and a separate tune-up experiment accomplishes this. In the gate sequence depicted in figure (7.3) the gate interaction is chosen such that a total phase of $e^{i\frac{\pi}{2}}$ is acquired on two of the two states $|\uparrow\downarrow\rangle$ and $|\downarrow\uparrow\rangle$. If the gate interaction is chosen to induce a phase factor of $e^{i\pi}$, then the result of the gate sequence is not an entangled state, but the state $|\downarrow\downarrow\rangle$. The

experiment works by applying the gate sequence (7.3) and scanning the detuning δ. The interaction time is proportional to the inverse of the detuning. For each value of the detuning an experiment is performed and then the internal state populations are measured using resonance fluorescence [Langer 05]. When the detuning is such that the both ions internal state populations are measured to be in the state $|\downarrow\downarrow\rangle$, then the right detuning has been found.

7.6.4 Entanglement in a Mixed Species Crystal

This section discusses experimentally demonstrating entanglement of the internal spin states of two ions in a four ion mixed species chain $^{9}\mathrm{Be}^{+} - {}^{24}\mathrm{Mg}^{+} - {}^{24}\mathrm{Mg}^{+} - {}^{9}\mathrm{Be}^{+}$ [Jost 09]. The ions are confined in one trapping zone of the linear radio frequency Paul trap as discussed in chapter (2). The ions to be entangled are two $^{9}\mathrm{Be}^{+}$ ions, which could serve as logical qubits in QIP applications. The other two ions are $^{24}\mathrm{Mg}^{+}$ ions, which are used as sympathetic cooling ions. Although the theory in the previous section was for two ions, it applies here as well. There are several possible orders of the four ion mixed species crystal. This experiment uses one particular order: $^{9}\mathrm{Be}^{+}-{}^{24}\mathrm{Mg}^{+}-{}^{24}\mathrm{Mg}^{+}-{}^{9}\mathrm{Be}^{+}$. There are four axial modes, which we designate with these names: in-phase mode (INPH) (frequency $\sim$ 2.0 MHz, mode vector: [0.32, 0.63, 0.63, 0.32]), the out-of-phase mode (OOPH) ($\sim$ 4.1 MHz, [-0.47, - 0.53, 0.53, 0.47]), the Egyptian mode ($\sim$ 5.5 MHz, [0.63, -0.32, -0.32, 0.63]) and the Funk ($\sim$ 5.7 MHz, [0.53, -0.47, 0.47, -0.53]). The amplitudes given in the mode vectors (written in ion order from left to right) are related to each ion's root-mean-squared ground state wave function size by multiplying by $\sqrt{\hbar/2M\omega}$, with M the mass of the relevant ion and ω the mode frequency in angular units. The gate drive will use the OOPH mode, which resembles the stretch like motion of two ions, where the $^{9}\mathrm{Be}^{+}$ ions move in opposite directions but with equal amplitudes. All other modes will be off resonance with the gate drive. The gate interaction will also only address the internal states of the $^{9}\mathrm{Be}^{+}$ ions and these levels are the same as discussed

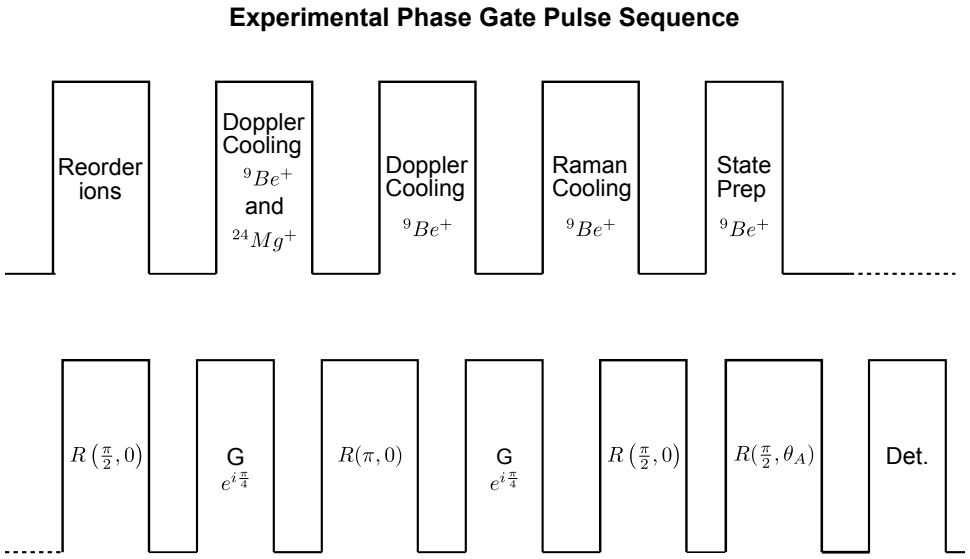

Figure 7.5: Experimental pulse sequence for performing the geometric phase gate on the four ion mixed species chain $^9\mathrm{Be}^+ - {}^{24}\mathrm{Mg}^+ - {}^{24}\mathrm{Mg}^+ - {}^9\mathrm{Be}^+$. The sequence is explained in more detail in the text. The first line is everything involved in the initial state preparation: Ordering the ions to create $^9\mathrm{Be}^+ - {}^{24}\mathrm{Mg}^+ - {}^{24}\mathrm{Mg}^+ - {}^9\mathrm{Be}^+$, a sequence of Doppler and Raman cooling to initialize the axial motion to near the ground state, and a state preparation pulse that optically pumps the $^9\mathrm{Be}^+$ ions to the $|\uparrow\uparrow\rangle$ state. The second line contains the phase gate sequence. The phase gate drive is represented by G, and the phase acquired during each drive is $e^{i\frac{\pi}{4}}$. The drive is embedded in a spin echo pulse sequence composed of the rotations $R\left(\frac{\pi}{2},0\right)$, $R\left(\pi,0\right)$, and $R\left(\frac{\pi}{2},0\right)$. Theses rotation are co-carrier stimulated Raman transitions applied to both ions. The last pulse is the analysis pulse for the phase gate given by $R\left(\frac{\pi}{2},\theta_A\right)$. The last pulse is the resonance fluorescence detection.

in section (7.6). This means the $^{24}\mathrm{Mg}^+$ ions internal states will not be affected by the gate drive, and the Hamiltonian derived in section (7.6)still applies. The $^{24}\mathrm{Mg}^+$ions are used when initially Doppler cooling (see chapter (2)) the four ion crystal.

The experimental pulse sequence is depicted in figure (7.5). If the ions have a different order from $^9\mathrm{Be}^+ - {}^{24}\mathrm{Mg}^+ - {}^{24}\mathrm{Mg}^+ - {}^9\mathrm{Be}^+$, then the normal mode frequencies will change. Thus it is necessary to ensure the ions always start in this particular order. The ions can be forced into this order using time varying potentials and laser cooling [Jost 09], which is done before each experiment.

After the ordering, Doppler cooling is performed using a combination of both

$^9Be^+$ and $^{24}Mg^+$(see chapter (5)) Doppler cooling. Both types of cooling are used because the Doppler cooling only efficiently cools the modes where that type of ion has large motional amplitude. The $^{24}Mg^+$cooling is especially important; because there are radial modes with frequencies comparable to the axial ones. If these modes have a large amount of energy, then this can lead to off resonant coupling of the radial modes to the axial modes of motion if micromotion is not well compensated. The Doppler cooling used on $^9Be^+$ is a combination of both far off resonance cooling (~ -400 MHz) and cooling where the frequency is tuned to near the optimum $-\frac{\Gamma}{2}$ point. The far off resonance cooling is used to cool instances where the ions are highly excited (from for example a background gas collision) and cool these ions to a regime where the near resonance cooling is effective. This combined Doppler cooling lasts for 3500 μs. When this experiment was initially performed it was believed the $^9Be^+$ Doppler cooling would provide the lowest possible temperatures. Also in subsequent experiments [Home 09, Hanneke 10] the Doppler cooling of the four crystal has been performed with only $^{24}Mg^+$ Doppler cooling. The combined Doppler cooling is followed by 500 μs. of near resonance Doppler cooling with $^9Be^+$. This brings the temperature of the axial modes to a low enough $\overline{n}$ to be efficiently Raman cooled to the ground state.

Before Raman cooling is performed, the $^9Be^+$ ions are optically pumped to the $|\uparrow\uparrow\rangle$ state (The same is done with the $^{24}Mg^+$ ions, but this just part of a protocol that is performed for subsequent experiments). After Doppler cooling, the state of the $^9Be^+$ions should be well initialized, but the last optical pumping step helps to ensure this. Raman cooling (6) is performed using the $^9Be^+$ states $|\downarrow\rangle = |F = 2, m_F = 1\rangle$ and $|\uparrow\rangle = |F = 2, m_F = 2\rangle$. Twenty interlaced cooling cycles are performed on each of the axial modes of motion, which takes 2800 μs in total. After this cooling all the motional modes have been cooled to $\overline{n} < 0.2$[Jost 09].

Now that the $^9Be^+$ ions have been prepared, the gate sequence discussed in section (7.5) can be implemented, see figure (7.5). The co-carrier Raman transitions that

perform the single qubit rotations $R(\theta,\phi)$ are implemented on the same internal transitions as the Raman cooling. The first step is to implement the rotation $R\left(\frac{\pi}{2},0\right)$ (takes approximately 1.5 μs), which prepares the two $^9Be^+$ ions in the superposition state given by equation (7.44). It should be noted that the internal states of $^{24}Mg^+$ ions are omitted since they no longer play a role. The next step in the sequence is to apply the first half of the gate drive. The detuning of the gate drive is 40 KHz, which makes a one loop in phase space in a duration of $\sim 25\mu s$. This leaves the system in the state (7.46). The next step is to apply the refocusing pulse of the spin echo sequence, where a co-carrier pulse implements the rotation $R(\pi,0)$ (takes approximately 3 μs) on both $^9Be^+$ ions, which produces the state (7.47). Now the second half of the gate drive is applied, which drives the motion around another loop in phase space to give (7.48). The final pulse in the spin echo sequence applies the rotation $R\left(\frac{\pi}{2},0\right)$ and creates the Bell like state (7.49) . Next the variable phase analysis pulse $R\left(\frac{\pi}{2},\theta_A\right)$ applied to both $^9Be^+$ ions, which creates the phase dependent state (7.52).

After the final analysis pulse, shelving is performed see chapter (3) on the $|\downarrow\downarrow\rangle$ state. This transfers the population of both ions in the state $|\downarrow\rangle = |F=2,m_F=1\rangle$ to the state $|F=2,m_F=-2\rangle$, which helps distinguish the fluorescing state $|\uparrow\rangle$ from the other spin state [Langer 06]. Finally a 200 μs pulse of resonant detection light is applied to the $^9Be^+$ ions and photons are collected and counted. The resulting histograms are fit to a sum of Poissonian distributions to extract the populations for a given data point, where the data in figure (7.6) is composed of 500 experiments per point. From the these populations, the parity (7.60) for a given phase can be determined. The scan of analysis phase θ_A is shown in figure (7.6). The resulting curve is fit using a non-linear curve fitting routine in Matlab to the function $C_2\cos(2\theta_A+\phi_2)+C_1\cos(\theta_A+\phi_1)+C_0$. From the fit, the values for the amplitudes are $C_2 = 0.84\pm0.015$, $C_1 = 0.03\pm0.015$, and $C_0 = -0.012\pm0.011$ [1] . The value of C_2 is greater than the 0.5 necessary to show

[1] Parity data was taken on 10/10/08 at 19:17:28

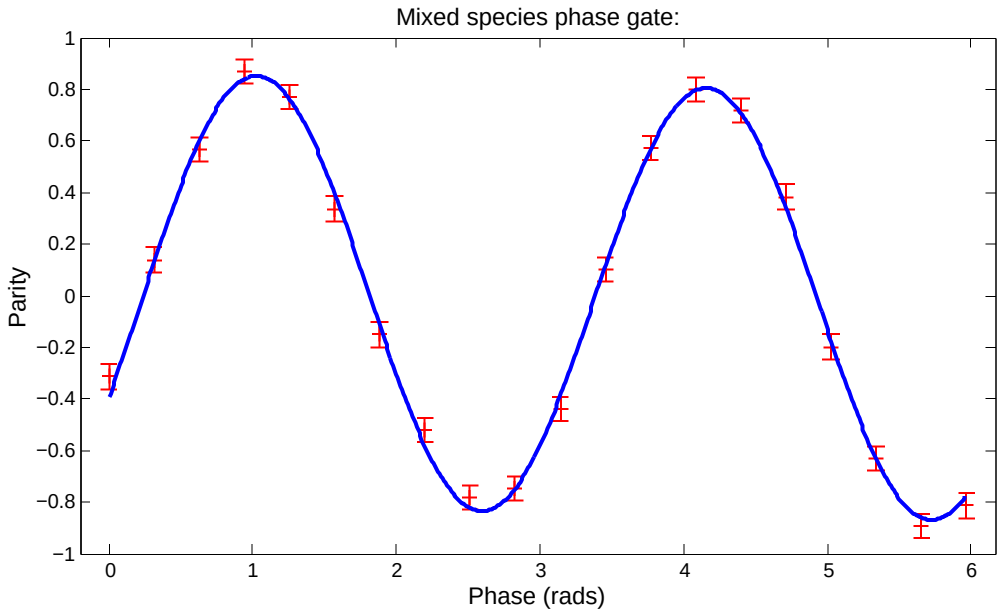

Figure 7.6: Parity flopping on the two $^{9}Be^{+}$ ions in the four ion chain $^{9}Be^{+} - {}^{24}Mg^{+} - {}^{24}Mg^{+} - {}^{9}Be^{+}$. A parity of value of 1 corresponds to the state $\frac{1}{\sqrt{2}}(|\uparrow\uparrow\rangle + i|\downarrow\downarrow\rangle)$, and a value of -1 corresponds to creating the state $\frac{1}{\sqrt{2}}(|\uparrow\downarrow\rangle + |\downarrow\uparrow\rangle)$. The flopping signal data is fit to a $C_2\cos(2\theta_A + \phi_2) + C_1\cos(\theta_A + \phi_1) + C_0$ function and is shown by the solid line. The amplitude $C_2 = 0.84 \pm 0.015$ is the important quantity, since a value > 0.5 shows there is entanglement. Each data point is composed of 500 experiments. The vertical error bars represent one standard deviation.

entanglement.

In order to obtain the populations required for calculating the fidelity a separate almost identical experiment is performed, where the only difference is that the analysis pulse is excluded[2] . The resulting histograms are and fit to a sum of Poissonian distributions to extract the populations for $P_{|\uparrow\uparrow\rangle} = 0.46 \pm 0.02$, $P_{|\downarrow\downarrow\rangle} = 0.45 \pm 0.02$, and $P_{|\uparrow\downarrow\rangle+|\downarrow\uparrow\rangle} = 0.09 \pm 0.01$. The fidelity from equation (7.63) is found to be $F = 0.876 \pm 0.015$. There are several possible sources of the errors in the phase gate that prevent the fidelity from being higher. Spontaneous emission from the finite detuning of the Raman beams from the excited state is one such source of error [Leibfried 03b, Ozeri 07, Jost 09].

[2] Population data was taken on 10/10/08 at 19:20:03

Many laser pulses are required to implement the phase gate and the rotations. These pulses often have intensity noise leading to a loss in fidelity [Leibfried 03b, Jost 09].

Chapter 8

Entangled Mechanical Oscillators

This chapter discusses the experiments [Jost 09] performed to entangle two spatially separated mechanical oscillators and to entangle the internal electronic state of an ion with a spatially separate mechanical oscillator.

8.1 Motivation

Hallmarks of quantum mechanics include superposition and entanglement. In the context of large complex systems, these features should lead to situations like Schrödinger's cat [Schrödinger 35], which exists in a superposition of alive and dead states entangled with a radioactive nucleus. Such situations are not observed in nature. This may simply be due to our inability to sufficiently isolate the system of interest from the surrounding environment [Ball 08, Schlosshauer 08] – a technical limitation. Another possibility is some as-of-yet undiscovered mechanism that prevents the formation of macroscopic entangled states [Bassi 03]. Such a limitation might depend on the number of elementary constituents in the system [Leggett 02b] or on the types of degrees of freedom that are entangled. Tests of the latter possibility have been made with photons, atoms, and condensed matter devices [Southwell 08, Aspelmeyer 08a]. One system ubiquitous to nature where entanglement has not been previously demonstrated is distinct mechanical oscillators. Here we demonstrate deterministic entanglement of separated mechanical oscillators, consisting of the vibrational states of two pairs of atomic ions

held in different locations. We also demonstrate entanglement of the internal states of an atomic ion with a distant mechanical oscillator. These results show quantum entanglement in a degree of freedom that pervades the classical world. Such experiments may provide pathways towards generation of entangled states of larger-scale mechanical oscillators [Mancini 02, Schwab 05, Kippenburg 08], and offer possibilities for testing non-locality with mesoscopic systems [Milman 05]. In addition, the control developed in these experiments is an important ingredient to scale up quantum information processing based on trapped atomic ions [Wineland 98, Cirac 00, Kielpinski 02a].

Mechanical oscillators pervade nature; examples include the vibrations of violin strings, the oscillations of quartz crystals used in clocks, and the vibrations of atoms in a molecule. Independent of the size of the system, each mode of vibration can be described by the same equations that describe the oscillations of a mass attached to a fixed object by a spring. For very low energy oscillations, quantum mechanics is needed for a correct description: the energy is quantized and the motion can be described generally by superpositions of wavefunctions corresponding to each quantum level. Coherent states behave very much like classical oscillators, while other states have properties with distinctly non-classical features [Schleich 01]. Quantum mechanics also permits superposition states of multiple systems called entangled states, where the measured properties of the systems are correlated in ways that defy our every-day experience [Aspect 02, Southwell 08, Pan 08, Matsukevich 08, Aspelmeyer 08a]. When extended to macroscopic scales, situations akin to Schrödinger's cat should appear. Our inability to produce such macroscopic entanglement may be just a question of technical difficulty. However, there might be a more fundamental cause, such as the inability to entangle certain types of degrees of freedom.

Figure 8.1: $^{9}Be^{+} - {}^{24}Mg^{+}$ mechanical oscillators. Simplified depiction of the two mechanical oscillators indicating motion in the stretch mode of each $^{9}Be^{+} - {}^{24}Mg^{+}$ ion pair, held in separate locations (not to scale). The pairs – spaced by $\simeq 0.24$ mm – each behave as two masses spaced by ~ 4 μm, connected by a spring.

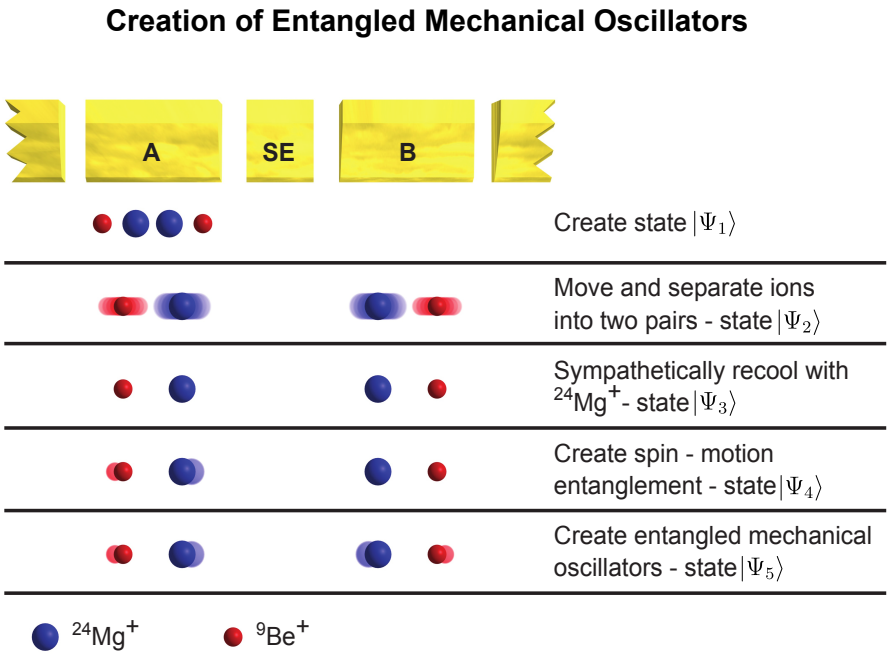

Figure 8.2: Creation of entangled mechanical oscillators. Schematic showing the ions' positions with respect to the ion trap electrodes (A, X, and B) and the quantum states at key points in the experiments (not to scale). After entangling the $^{9}Be^{+}$ ions' spins in a single well, the ions are separated into two pairs by electrode X and distributed to different wells. Laser cooling of $^{24}Mg^{+}$ removes motional excitation incurred during separation. A $^{9}Be^{+}$ laser pulse in well A entangles the motion in well A with the $^{9}Be^{+}$ spin in well B. A subsequent pulse in well B entangles the two mechanical oscillators.

8.2 Experiment

To explore the latter territory in a new regime, we demonstrate entanglement of two separated mechanical oscillators. Here each oscillator is comprised of a pair of ions -

one $^{9}Be^{+}$ and one $^{24}Mg^{+}$ - confined in a potential well. In the context of the experiment described below, each pair behaves like two masses connected by a spring of length ~ 4 μm, undergoing vibrational motion (figure (8.1)). The two pairs are separated by 0.24 mm such that the coupling between them can be neglected. To create the entangled state of the oscillators, we start with all four ions in one location and entangle the internal states of the two $^{9}Be^{+}$ ions [Leibfried 03b]. We then separate the four ions into two pairs, each containing one of the entangled $^{9}Be^{+}$ ions. Finally, we transfer the entanglement from the $^{9}Be^{+}$ ions' internal states to the motion of the separated ion pairs, creating the desired motional entanglement.

Initially, all the ions are held in a single potential well of a multi-zone linear Paul trap [Rowe 02, Barrett 04]. The potential well is configured to locate the ions along a line corresponding to the axis of weakest confinement, which we call the axial direction. We will be concerned only with motional modes along this axis. While applying continuous laser cooling, we initialize the ions in a particular order, $^{9}Be^{+} - ^{24}Mg^{+} - ^{24}Mg^{+} - ^{9}Be^{+}$, by first increasing the axial confinement until no linear arrangement is stable. The axial potential is independent of ion mass while the radial potential strength scales inversely with the mass [Wineland 98], thus there exist axial potentials where the heavier $^{24}Mg^{+}$ ions are displaced from the axis and must reside between the $^{9}Be^{+}$ ions. We then relax the axial confinement giving the desired order [Rosenband]. The four ions are located in one well in the configuration $^{9}Be^{+} - ^{24}Mg^{+} - ^{24}Mg^{+} - ^{9}Be^{+}$, which has four axial modes of motion. In order of ascending frequency, we designate them as the in-phase mode (frequency $\simeq$ 2.0 MHz, mode vector: [0.32, 0.63, 0.63, 0.32]), the out-of-phase mode (4.1 MHz, [-0.47, -0.53, 0.53, 0.47]), a third mode (5.5 MHz, [0.63, -0.32, -0.32, 0.63]) and the Funk mode (5.7 MHz, [0.53, -0.47, 0.47, -0.53]). The amplitudes given in the mode vectors (written in ion order from left to right) are related to each ion's root-mean-squared ground state wavefunction size by multiplying by $\sqrt{\hbar/(2M\omega)}$, with M the mass of the relevant ion and ω the mode frequency in angular units.

In addition to comprising part of the mechanical oscillators, the $^{24}Mg^+$ ions serve as a tool to provide sympathetic cooling of the $^9Be^+$ ions [Barrett 03]. Doppler cooling of $^{24}Mg^+$ is accomplished by driving transitions between the ground $^2S_{1/2}$ states and excited $^2P_{1/2}$ states, which have a radiative linewidth of 41 MHz [Herrmann 09]. In the 0.012 T applied magnetic field, the ground Zeeman states $|m_J = \pm 1/2\rangle$ are split by 334 MHz, hence efficient Doppler cooling requires an additional repump beam to prevent optical pumping.

Lasers provide control of the ions' motion and internal states through laser cooling and stimulated-Raman carrier or sideband transitions [King 98, Wineland 98] [Southwell 08]. Doppler cooling is performed on the $^9Be^+$ and $^{24}Mg^+$ ions. There are radial modes that have small amplitudes for $^9Be^+$ but large amplitudes for $^{24}Mg^+$. This means $^9Be^+$ cooling is inefficient for these modes, hence we also cool these modes using $^{24}Mg^+$ Doppler cooling. This is followed by sideband cooling on the $^9Be^+$ ions, which prepares the motion of each of the four axial normal modes to an average motional occupation of $\langle n \rangle \leq 0.17$. By applying a magnetic field of 0.012 T, we spectrally isolate two internal (hyperfine) states in each $^9Be^+$ ion, which we call "spin" states, and label $|\uparrow\rangle \equiv |F = 2, m_F = 2\rangle$ and $|\downarrow\rangle \equiv |F = 2, m_F = 1\rangle$. These states are split by 102 MHz. Using a spin rotations and a geometric phase gate [Leibfried 03b] operation, which implements a $^9Be^+$ state-dependent motional displacement on the out-of-phase mode, we create the decoherence-free-subspace entangled state

$$|\Psi_1\rangle = \frac{1}{\sqrt{2}} \left[|\uparrow\downarrow\rangle + |\downarrow\uparrow\rangle\right] \tag{8.1}$$

of the two $^9Be^+$ ions. This state is resistant to decoherence from spatially uniform magnetic field noise [Kielpinski 01].

Time-varying axial potentials move and separate [Rowe 02, Barrett 04] the four ions into two $^9Be^+ - {}^{24}Mg^+$ pairs in different wells, which are spaced by ~ 0.24 mm (see figure (8.2)). Each pair of ions has two axial normal modes: the "stretch" mode

(frequency $\simeq$ 4.9 MHz, mode vector $\simeq$ [-0.93, 0.37]) in which the two ions oscillate out-of-phase and the "common" mode (frequency $\simeq$ 2.3 MHz, mode vector $\simeq$ [0.37, 0.93] MHz) where they oscillate in-phase. The experiment involves the ground $|n=0\rangle_j$ and first excited $|n=1\rangle_j$ states of the stretch modes, where $j \in \{A, B\}$ refers to the well. In general, the separation process excites the motional modes into unknown states. The wavefunction of the $^9Be^+$ spin states after separation is \k

$$|\Psi_2\rangle = \frac{1}{\sqrt{2}}\left[|\uparrow\rangle_A|\downarrow\rangle_B + e^{i\xi(t)}|\downarrow\rangle_A|\uparrow\rangle_B\right] \tag{8.2}$$

where $\xi(t)$ is a phase that accumulates through the course of the experiment due to a small difference in magnetic field between wells A and B.

To create the motional entangled state we first prepare the stretch modes close to $|0\rangle_A|0\rangle_B$ (see appendix (C) for a detailed pulse sequence). For this, Doppler and sideband laser cooling on the $^{24}Mg^+$ ions in both wells sympathetically cools [Barrett 03] the $^9Be^+$ ions. One cycle of the pulsed $^{24}Mg^+$sideband cooling [Barrett 03] uses stimulated-Raman transitions on a motional sideband of the $|+1/2\rangle \rightarrow |-1/2\rangle$ ground state transition (duration ~ 5 μs), followed by application of the repumping beam to reprepare $|+1/2\rangle$ (~ 2 μs). The $^{24}Mg^+$ sideband laser cooling uses 40 cooling cycles per mode on the second motional sideband and then 60 cycles per mode on the first sideband. This prepares the stretch modes to mean occupation numbers of $\langle n_A\rangle = 0.06(2)$ and $\langle n_B\rangle = 0.02(2)$ where the uncertainties are standard errors (s.e.m.). We also cool the common mode in each well to $\langle n\rangle \leq 0.13$. The cooling does not affect the spin states of the $^9Be^+$ ions [Barrett 03], thereby approximating the state

$$|\Psi_3\rangle = \frac{1}{\sqrt{2}}\left[|\uparrow\rangle_A|\downarrow\rangle_B + e^{i\xi(t)}|\downarrow\rangle_A|\uparrow\rangle_B\right]|0\rangle_A|0\rangle_B \tag{8.3}$$

We transfer the entanglement from the spin to the motion with a sequence of laser pulses on the $^9Be^+$ ions. Carrier transitions (labeled with superscript c, duration $\simeq 4$ μs) only affect the spin states, and sideband transitions (superscript m, referred to as

spin $\leftrightarrow$ motion transfer pulses, duration $\simeq 13$ μs) couple the spin and motion. These can be described as generalized rotations:

$$R_j^{c,m}(\theta,\phi) = \begin{pmatrix} \cos\frac{\theta}{2} & -ie^{-i\phi}\sin\frac{\theta}{2} \\ -ie^{i\phi}\sin\frac{\theta}{2} & \cos\frac{\theta}{2} \end{pmatrix}, \tag{8.4}$$

where $j \in \{A, B\}$. Carrier transitions correspond to rotations in the basis

$$\begin{pmatrix} 1 \\ 0 \end{pmatrix} = |\uparrow\rangle, \begin{pmatrix} 0 \\ 1 \end{pmatrix} = |\downarrow\rangle,$$

and sideband transitions correspond to rotations in the basis

$$\begin{pmatrix} 1 \\ 0 \end{pmatrix} = |\uparrow\rangle|1\rangle, \begin{pmatrix} 0 \\ 1 \end{pmatrix} = |\downarrow\rangle|0\rangle.$$

The rotation angle θ is proportional to the intensity and duration of the pulses, and the phase ϕ is determined by the phase difference between the two optical Raman fields [Wineland 98, King 98] at the position of the ion. We individually address the $^9Be^+$ ions in each well using acousto-optic modulators to shift the positions of the laser beams.

Applying $R_A^m(\pi, 0)$ to state (8.3) entangles the $^9Be^+ - {}^{24}Mg^+$ motion in well A with the $^9Be^+$ spin in well B, creating the state

$$|\Psi_4\rangle = \tfrac{1}{\sqrt{2}}|\uparrow\rangle\left[|\downarrow\rangle|0\rangle_A - ie^{i\xi(t)}|\uparrow\rangle|1\rangle_A\right]|0\rangle_B. \tag{8.5}$$

After this spin $\rightarrow$ motion transfer, the spin in well B is sensitive to decoherence from fluctuating magnetic fields. To minimize this effect, we apply a spin-echo pulse [Vandersypen 04], $R_B^c(\pi, 0)$, $T \simeq 40$ μs after the previous pulse. After a second delay T, we apply a second spin $\rightarrow$ motion transfer pulse $R_B^m(\pi, 0)$ in well B, producing the state

$$|\Psi_5\rangle = \tfrac{1}{\sqrt{2}}|\uparrow\rangle|\uparrow\rangle\left[|0\rangle_A|0\rangle_B - e^{i\xi(t)}|1\rangle_A|1\rangle_B\right]. \tag{8.6}$$

This state is an entangled superposition of both stretch modes in the ground and first excited states. The entanglement now resides only in the mechanical oscillator states of both wells. We leave the system in this state for ~ 50 μs before beginning our analysis.

We are not able to directly measure the entangled motional state. The analysis proceeds by basically reversing the steps used to create state (8.6) and characterizing the resulting spin state. We transfer the motional state back into the spins using the pulse sequence: $R^m_B(\pi,0), T, R^c_B(\pi,0), T, R^m_A(\pi,\phi_A)$. We then recombine all the ions into a single potential well, to ideally reproduce the state $|\Psi_1\rangle$, having chosen ϕ_A to compensate for the phase $\xi(t)$.

Imperfect creation of the state (8.6) could leave entanglement in the spin states, which could mimic motional entanglement in the analysis. To prevent this, we transfer residual populations $\epsilon_{A,B}$ of states $|\downarrow\rangle_{A,B}$ into auxiliary internal (hyperfine) states prior to performing the motion $\rightarrow$ spin transfers (discussed more below). Moreover, since all experiments are used in the analysis, this transfer process does not constitute post-selection and cannot enhance the deduced entanglement.

Our detection relies on analyzing the state $|\Psi_f\rangle = \frac{1}{\sqrt{2}}[|\uparrow\uparrow\rangle + i\,|\downarrow\downarrow\rangle]$, which we create by applying a common rotation $R^c(\frac{\pi}{2}, -\frac{3\pi}{4})$ to both spins. We verify the entanglement created in state (8.6) by measuring the off-diagonal element $|\rho_{\downarrow\downarrow,\uparrow\uparrow}| = |\langle\downarrow\downarrow|\,\rho_f\,|\uparrow\uparrow\rangle|$ of the density matrix ρ_f corresponding to our approximation to the state $|\Psi_f\rangle$. We determine $|\rho_{\downarrow\downarrow,\uparrow\uparrow}|$ by applying a final analysis pulse, $R^c(\frac{\pi}{2}, \phi_p)$, to both $^9Be^+$ ions with a phase ϕ_p and measuring the parity[Sackett 00], $P_{\downarrow\downarrow} + P_{\uparrow\uparrow} - (P_{\downarrow\uparrow} + P_{\uparrow\downarrow})$, for different values of ϕ_p, where $P_{\downarrow\downarrow}, P_{\uparrow\uparrow}, P_{\downarrow\uparrow}$, and $P_{\uparrow\downarrow}$ are the populations of the spin states $|\downarrow\downarrow\rangle, |\uparrow\uparrow\rangle, |\downarrow\uparrow\rangle$, and $|\uparrow\downarrow\rangle$. The entanglement is revealed by the component of the parity signal that oscillates as $C_2\cos(2\phi_p)$, where $C_2 = |\rho_{\downarrow\downarrow,\uparrow\uparrow}|$. A value of $C_2 > 0.5$ verifies the spin entanglement of $|\Psi_f\rangle$ and thus the motional entanglement in state (8.6).

To deduce the spin populations, we use state-dependent resonance fluorescence [Wineland 98, Southwell 08]. The $|\uparrow\rangle$ state strongly fluoresces. Prior to final spin population measurement, the $|\downarrow\rangle$ population is transferred to the dark state $|F=2, m_F=-2\rangle$ using carrier π pulses $R(\pi,0)$ on the sequence of transitions $|2,1\rangle \rightarrow |2,0\rangle$, $|2,0\rangle \rightarrow |2,-1\rangle$, $|2,-1\rangle \rightarrow |2,-2\rangle$. The number of photons measured per $^9Be^+$ ion if all the pop-

ulation were in the $|2,-2\rangle$ dark state during the 200 μs detection period approximates a Poisson distribution with a mean of 0.2. For the fluorescing state $|\uparrow\rangle$, we observe a Poisson distribution, with a mean number of photons $\simeq 10$ per $^9Be^+$ ion.

As described in the main text, we move populations $\epsilon_{A,B}$ of the spin states $|\downarrow\rangle_{A,B}$ to the auxiliary hyperfine state $|2,0\rangle$, so they do not contribute to entanglement verification. To ensure that the $\epsilon_{A,B}$ populations end in dark states for the measurements, we precede the transfer pulses described in the previous paragraph with transfer of the $|2,0\rangle$ populations to $|2,-2\rangle$ using a sequence of carrier π pulses on the $|2,0\rangle \rightarrow |2,-1\rangle$ and $|2,-1\rangle \rightarrow |2,-2\rangle$ transitions. Since the last pulse of the final transfer sequence is also a carrier π pulse on the $|2,-2\rangle \leftrightarrow |2,-1\rangle$ transition, this leads to the populations $\epsilon_{A,B}$ ending in $|2,-1\rangle$. If all the population is in this state, it would give a mean fluorescence value per $^9Be^+$ ion of ~ 1 photon during detection. This fluorescence falsely contributes to $P_{\downarrow\downarrow}$ but in a way that does not depend on ϕ_p, and hence does not contribute to C_2. We fit the data in the top plot of figure (8.3) with $C_2\cos(2\phi_p+\phi_2)+C_1\cos(\phi_p+\phi_1)+C_0$ and extract $C_2 = 0.57(2)$. This demonstrates that entanglement was present in the motion after the steps to create state (8.6).

The intermediate state (8.5) is itself a novel "spin – motion" entangled state, where the spin state of the $^9Be^+$ ion in well B is entangled with the motion of the stretch mode of the ion pair in well A. We characterize this state in a separate set of experiments. After creating state (8.5), we allow it to persist for 176 μs. Following the analysis described above (omitting the spin $\leftrightarrow$ motion transfer steps in well B), we measure the parity (bottom plot in figure (8.3)) and find $C_2 = 0.65(2)$.

To provide partial checks of the spin $\rightarrow$ motion transfer steps, we perform separate experiments to determine the spin populations after the transfer. In the first check experiment, we follow the steps used to create state (8.5) then implement the above hyperfine state transfer sequences (omitting the ϵ_B population transfer process) and measure the spin populations. The populations are determined to be $P_{\uparrow\uparrow} = 0.47(1), P_{\downarrow\downarrow} = 0.04(1)$,

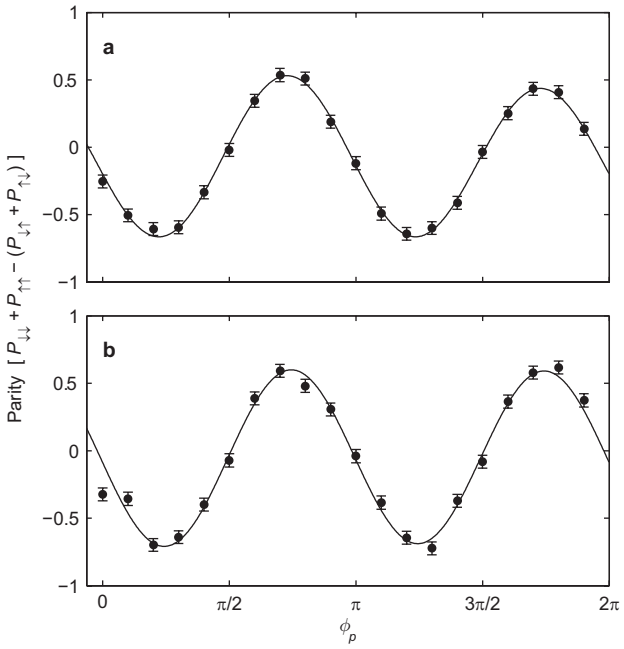

Figure 8.3: Entanglement demonstration through parity oscillation. Parity data obtained from **a**, the entangled mechanical oscillators and **b**, the spin – motion entanglement experiments. Each point is calculated using the maximum-likelihood method on the fluorescence data from running the experiment 500 times and is plotted with standard error bars (s.e.m.). The solid curve is a fit to the data. Two-ion entanglement is verified by an amplitude greater than 0.5 for the component of the parity signal that oscillates at twice the analysis pulse phase ϕ_p [Sackett 00]. For the data shown, this amplitude is **a**, 0.57(2) and **b**, 0.65(2).

and $P_{\downarrow\uparrow} + P_{\uparrow\downarrow} = 0.49(2)$. Ideally we would expect $P_{\uparrow\uparrow} = 1/2, P_{\downarrow\downarrow} = 0$, and $P_{\downarrow\uparrow} + P_{\uparrow\downarrow} = 1/2$. Similarly, after the step used to create state (8.6), and following the transfer procedure, we determine $P_{\uparrow\uparrow} = 0.86(2), P_{\downarrow\downarrow} = 0.01(1)$, and $P_{\downarrow\uparrow} + P_{\uparrow\downarrow} = 0.13(2)$. Ideally we should find $P_{\uparrow\uparrow} = 1$.

Significant sources of infidelity are spontaneous photon scattering [Ozeri 07] and motional decoherence. The fidelity with which we initially create $|\Psi_1\rangle$ is $\simeq 0.88$. Motional state superpositions of the stretch mode in each well were independently measured to have a coherence time of ~ 800 μs, which is consistent with a model of decoherence due to couplings to thermally occupied radial modes [Roos 08]. In the entangled mechanical oscillators experiment, the motional superpositions are occupied for $\simeq 250$ μs and $\simeq 50$

μs in wells A and B respectively; we estimate a decrease in C_2 from this source to be $\sim$ 5 %. In the spin – motion entanglement experiment, we estimate a decrease in C_2 of $\sim$ 3 % from this source. Non-zero temperature also reduced the fidelity of motional state initialization. We estimate that this would reduce the fidelity for producing the states (8.6) and (8.5) by 8 % and 6 % respectively. Intensity fluctuations at the few percent level reduce the accuracy of all rotations.

The Coulomb coupling between the ion pairs in wells A and B could lead to an entangled state of their stretch modes. However, the resonant exchange rate is 5 Hz, which leads to negligible entanglement for the experimental time scales. Furthermore, the stretch mode frequencies in wells A and B differ by $\sim$ 25 kHz, which would yield negligible entanglement for all time scales.

In summary, we have created two novel entangled states of separated systems involving mechanical oscillators, extending the regime where entanglement has been observed in nature. Implementing these experiments required deterministic ion ordering and the ability to separate and recool ions while preserving entanglement and performing subsequent coherent operations. This is the first demonstration of these techniques combined. Some of these methods could apply to similar experiments with nano- and micro-mechanical resonators [Schwab 05, Kippenburg 08, Mancini 02]. The states created could be used to extend tests of nonlocality in ion traps in a manner analogous to that proposed for the electromagnetic fields of separated cavities [Milman 05]. The control developed for these experiments also represents an important step towards large-scale trapped-ion quantum information processing [Kielpinski 02a, Wineland 98].

Well thanks for actually looking at my thesis. I would be curious to know who found this work interesting so send me an email if you like at john.d.jost@gmail.com. Also it would be cool to know if after a few years have past since the writing of this thesis that there is someone actually still looking at it. Thanks.

Bibliography

[Antohi 09] P. B. Antohi, D. Schuster, G. M. Akselrod, J. Labaziewicz, Y. Ge, Z. Lin, W. S. Bakr & I. L. Chuang. Cryogenic ion trapping systems with surface-electrode traps. Review of Scientific Instruments, vol. 80, no. 1, page 013103, 2009.

[Arcizet 06] O. Arcizet, P.-F. Cohadon, T. Briant, M. Pinard & A. Heidmann. Radiation-pressure cooling and optomechanical instability of a micromirror. Nature, vol. 444, pages 71–74, 2006.

[Aspect 02] A. Aspect. Bell's Theorem : The Naive View of an Experimentalist. In R. A. Bertlmann & A. Zeilinger, editeurs, Quantum [Un]speakables - From Bell to Quantum information. Springer, 2002.

[Aspelmeyer 08a] M. Aspelmeyer & A. Zeilinger. A Quantum Renaissance. Physics World, vol. July, pages 22–28, 2008.

[Aspelmeyer 08b] Markus Aspelmeyer & Keith Schwab. Focus on Mechanical Systems at the Quantum Limit. New Journal of Physics, vol. 10, no. 9, page 095001, 2008.

[Ball 08] P. Ball. Quantum all the way. Nature, vol. 453, pages 22–25, 2008.

[Barenco 95] A Barenco, C H Bennett, R Cleve, D P DiVincenzo, N Margolus, P Shor, T Sleator, J Smolin & H Weinfurter. Elementary gates for quantum computation. Phys. Rev. A, vol. 52, pages 3457–3467, 1995.

[Barrett 03] M D Barrett, B DeMarco, T Schaetz, V Meyer, D Leibfried, J Britton, J Chiaverini, W M Itano, B Jelenković, J D Jost, C langer, T Rosenband & D J Wineland. Sympathetic cooling of $^{9}Be^{+}$ and $^{24}Mg^{+}$ for quantum logic. Phys. Rev. A, vol. 68, pages 042302–1–8, 2003.

[Barrett 04] M D Barrett, J Chiaverini, T Schätz, J Britton, W M Itano, J D Jost, E Knill, C Langer, D Leibfried, R Ozeri & D J Wineland. Deterministic quantum teleportation of atomic qubits. Nature, vol. 429, pages 737–739, 2004.

[Bassi 03] A. Bassi & G. Ghiradi. Dynamical Reduction Models. Phys. Rept., vol. 379, page 257, 2003.

[Bell 64] J S Bell. On the Einstein-Podolsky-Rosen paradox. Physics, vol. 1, no. 6/7, pages 195–488, 1964.

[Benvenuti 01] C. Benvenuti, P. Chiggato, P. Costa Pinto, A. Escudeiro Santana, T. Hedley, A. Mongelluzzo, V. Ruzinov & I. Wevers. Vacuum properties of TiZrV non-evaporable getter films. Vacuum, vol. 60, pages 57–65, 2001.

[Bergquist 86] J C Bergquist, R G Hulet, W M Itano & D J Wineland. Observation of Quantum Jumps in a Single Atom. Phys. Rev. Lett., vol. 57, no. 14, pages 1699–1702, October 1986.

[Berkeland 98] D J Berkeland, J D Miller, J C Bergquist, W M Itano & D J Wineland. Minimization of ion micromotion in a Paul trap. J. Appl. Phys., vol. 83, no. 10, pages 5025–5033, 1998.

[Bertelsen 04] A. Bertelsen, I. S. Vogelius, S. Jørgensen, R. Kosloff & M. Drewsen. Photo-dissociation of Cold MgH^+ ions: Towards rotational temperature measurements and controlled dissociation. Eur. J. Phys. D., vol. 31, pages 403–408, 2004.

[Blakestad 09] R. B. Blakestad, C. Ospelkaus, A. P. VanDevender, J. M. Amini, J. Britton, D. Leibfried & D. J. Wineland. High fidelity transport of trapped-ion qubits through an X-junction trap array. Phys. Rev. Lett., vol. 102, page 153002, 2009.

[Blatt 90] R. Blatt. Laser Cooling of Trapped Ions. In J.Dalibard, J. M. Raimond & J. Zinn-Justin, editeurs, Les Houche, Session LIII, Fundamentl Systems in Quantum Optics, chapitre 4, page 255. Elsevier Science, 1990.

[Blinov 02] B B Blinov, L Deslauriers, P Lee, M J Madsen, R Miller & C Monroe. Sympathetic cooling of trapped Cd^+ isotopes. Phys. Rev. A, vol. 65, pages 040304–1–4, 2002.

[Blinov 04] B B Blinov, D L Moehring, L M Duan & C Monroe. Observation of entanglement between a single trapped atom and a single photon. Nature, vol. 428, pages 153–157, 2004.

[Bollinger 85] J. J. Bollinger, J. S. Wells, D. J. Wineland & Wayne M. Itano. Hyperfine structure of the $2p^2P_{1/2}$ state in $^9Be^+$. Phys. Rev. A, vol. 31, no. 4, pages 2711–2714, 1985.

[Bollinger 91] J J Bollinger, D J Heinzen, W M Itano, S L Gilbert & D J Wineland. A 303-MHz Frequency Standard Based on Trapped $^9Be^+$ Ions. IEEE Trans. Instr. Meas., vol. 40, no. 2, pages 126–128, April 1991.

[Bollinger 96] J J Bollinger, W M Itano, D J Wineland & D J Heinzen. Optimal Frequency Measurements with Maximally Correlated States. Phys. Rev. A, vol. 54, no. 6, pages R4649–R4652, December 1996.

[Boyd 68] G. D. Boyd & D. A. Kleinman. Parametric Interaction of Focused Gaussian Light Beams. J. Appl. Phys., vol. 39, page 3597, 1968.

[Brandsden 03] B.H. Brandsden & C.J. Joachain. Physics of atoms and molecules. Prentice Hall, 2003.

[Burrell 09] A. H. Burrell, D. J. Szwer, S. C. Webster & D. M. Lucas. Scalable simultaneous multi-qubit readout with 99.99single-shot fidelity. arXiv:0906.3304v1 [quant-ph], 2009.

[Carruthers 65] P. Carruthers & M. N. Nieto. Coherent States and the Forced Harmonic Oscillators. Am. J. Phys., vol. 33, pages 537–544, 1965.

[Chang 10] D. E. Chang, C. A. Regal, S. B. Papp, D. J. Wilson, J. Ye, O. Painter, H. J. Kimble & P. Zoller. Cavity opto-mechanics using an optically levitated nanosphere. Proc. Nat. Acad. Sci. USA, vol. 107, pages 1005–1010, 2010.

[Chen 00] Gang Chen, N. H. Bonadeo, D. G. Steel, D. Gammon, D. S. Katzer, D. Park & L. J. Sham. Optically Induced Entanglement of Excitons in a Single Quantum Dot. Science, vol. 289, no. 5486, pages 1906–1909, 2000.

[Chiaverini 04] J Chiaverini, D Leibfried, T Schaetz, MD Barrett, RB Blakestad, J Britton, WM Itano, JD Jost, E Knill, C Langer, R Ozeri & DJ Wineland. Realization of quantum error correction. Nature, vol. 432, no. 7017, pages 602 – 605, 2004.

[Chiaverini 05] J Chiaverini, J Britton, D Leibfried, E Knill, M D Barrett, R B Blakestad, W M Itano, J D Jost, C Langer, R Ozeri, T Schaetz & D J Wineland. Implementation of the semiclassical quantum Fourier transform in a scalable system. Science, vol. 308, pages 997–1000, 2005.

[Chiaverini 06] J Chiaverini, M D Barrett, R B Blakestad, J Britton, W Itano, J D Jost, E Knill, C Langer, D Leibfried, R Ozeri, T Schaetz & D J Wineland. Recent experiments in trapped-ion quantum information processing at NIST. In Han A. Bachor et al., editeur, Proc. of SPIE, volume 6256, pages 625610–1–12, Bellingham, Washington, 98227, 2006. SPIE.

[Cirac 95] J I Cirac & P Zoller. Quantum Computation with Cold, Trapped Ions. Phys. Rev. Lett., vol. 74, no. 20, pages 4091–4094, May 1995.

[Cirac 96a] J. I. Cirac, A. S. Parkins, R Blatt & P. Zoller. Non-classical states of motion in ion traps. Adv. At. Mol. Phys., vol. 37, pages 238–96, 1996.

[Cirac 96b] J. I. Cirac, T. Pellizzari & P. Zoller. Enforcing coherent evolution in dissipative quantum dynamics. Science, vol. 273, page 1207, 1996.

[Cirac 00] J I Cirac & P Zoller. A scalable quantum computer with ions in an array of microtraps. Nature, vol. 404, pages 579–581, 2000.

[Cohen-Tannoudji 92] C Cohen-Tannoudji, J Dupont-Roc & G Grynberg. Atom-photon interactions. John Wiley & Sons, New York, 1992.

[Corbitt 07] Thomas Corbitt, Yanbei Chen, Edith Innerhofer, Helge Müller-Ebhardt, David Ottaway, Henning Rehbein, Daniel Sigg, Stanley Whitcomb, Christopher Wipf & Nergis Mavalvala. An All-Optical Trap for a Gram-Scale Mirror. Phys. Rev. Lett., vol. 98, no. 15, page 150802, Apr 2007.

[Dalton 82] B. J. Dalton & P. L. Knight. The effects of laser field fluctuations on coherent population trapping. J. Phys. B: At. Mol. Phys., vol. 15, pages 3997–4015, 1982.

[Dehmelt 75] H. G. Dehmelt. Proposed 1014 Dv < v Laser Fluorescence Spectroscopy on Tl+ Mono-Ion Oscillator II (spontaneous quantum jumps). Bull. Am. Phys. Soc., vol. 20, page 60, 1975.

[Deutsch 89] D Deutsch. Quantum Computational Networks. Proc. Roy. Soc. London A, vol. 425, no. 1868, pages 73–90, September 1989.

[Diedrich 89] F Diedrich, J C Bergquist, W M Itano, & D J Wineland. Laser Cooling to the Zero Point Energy of Motion. Phys. Rev. Lett., vol. 62, pages 403–406, 1989.

[DiVincenzo 01] D P DiVincenzo. The physical implementation of quantum computation. In S L Braunstein, H -K Lo & P Kok, editeurs, Scalable Quantum Computers, pages 1–13, Berlin, 2001. Wiley-VCH.

[Drees 64] J Drees & W Paul. Beschleunigung von elektronen in einem plasmabetatron. Z. Phys., vol. 180, pages 340–361, 1964.

[Edmonds 96] A. R. Edmonds. Angular momentum in quantum mechanics. Princeton University Press, 1996.

[Einstein 35] A Einstein, B Podolsky & N Rosen. Can Quantum-Mechanical Description of Physical Reality Be Considered Complete? Phys. Rev., vol. 47, pages 777–780, 1935.

[Epstein 07] R J Epstein, S Seidelin, D Leibfried, J H Wesenberg, J J Bollinger, J M Amini, R B Blakestad, J Britton, J P Home, W M Itano, J D Jost, E Knill, C Langer, R Ozeri, N shiga & D J Wineland. Simplified motional heating rate measurements of trapped ions. Phys. Rev. A, vol. 76, pages 033411–1–5, 2007.

[Feynman 81] R P Feynman. Simulating Physics with Computers. Int. J. Th. Phys., vol. 21, no. 6/7, pages 467–488, 1981.

[Feynman 85] R P Feynman. Quantum Mechanical Computers. Optics News, vol. 11, pages 11–20, February 1985.

[Foot 05] Christopher J. Foot. Atomic physics. Oxford University Press, 2005.

[Ghosh 95] P K Ghosh. Ion traps. Clarendon Press, Oxford, 1995.

[Gigan 06] S. Gigan, H. R. Böhm, M. Paternostro, F. Blaser, G. Langer, J. B. Hertzberg, K. C. Schwab, D. Bäuerle, M. Aspelmeyer & A. Zeilinger. Self-cooling of a micromirror by radiation pressure. Nature, vol. 444, pages 67–70, 2006.

[Griffiths 95] David J. Griffiths. Introduction to quantum mechanics. Prentice Hall, 1995.

[Grover 97] L K Grover. Quantum mechanics helps in searching for a needle in a haystack. Phys. Rev. Lett., vol. 79, no. 2, pages 325–328, 1997.

[Häffner 05] H Häffner, W Hänsel, C F Roos, J Benhelm, D Chek-al-kar, M Chwalla, T Körber, U D Rapol, M Riebe, P O Schmidt, C Becher, O Gühne, W Dür & R Blatt. Scalable multiparticle entanglement of trapped ions. Nature, vol. 438, pages 643–646, 2005.

[Haljan 05] P C Haljan, P J Lee, K A Brickman, M Acton, L Deslauriers & C Monroe. Entanglement of trapped-ion clock states. Phys. Rev. A, vol. 72, pages 062316–1–5, 2005.

[Hanneke 10] D. Hanneke, J. P. Home, J. D. Jost, J. M. Amini, D. Leibfried & D. J. Wineland. Realization of a programmable two-qubit quantum processor. Nature Physics, vol. 1, pages 13–16, 2010.

[Hänsch 75] T. Hänsch & A. Schawlow. Cooling of gases by laser radiation. Opt. Commun., vol. 13, page 68, 1975.

[Hansch 80] T. W. Hansch & B. Couillaud. Laser frequency stabilization by polarization spectroscopy of a reflecting reference cavity. Opt. Commun., vol. 35, page 441, 1980.

[Haroche 06] Serge Haroche & Jean-Michel Raimond. Exploring the quantum atoms, cavities, and photons. Oxford Graduate Texts, 2006.

[Hecht 04] Eugene Hecht. Optics. Pearson Education, 2004.

[Heinzen 90] D J Heinzen & D J Wineland. Quantum-Limited Cooling and Detection of Radio-Frequency Oscillations by Laser-Cooled Ions. Phys. Rev. A, vol. 42, no. 5, pages 2977–2994, Sept. 1990.

[Herrmann 09] M. Herrmann, V. Batteiger, S. Knünz, G. Saathoff, Th. Udem & T. W. Hänsch. Frequency Metrology on Single Trapped Ions in the Weak Binding Limit: The $3s_{1/2}$ - $3p_{3/2}$ Transition in $^{24}Mg^{+}$. Phys. Rev. Lett., vol. 102, page 013006, 2009.

[Häffner 08] H. Häffner, C.F. Roos & R. Blatt. Quantum computing with trapped ions. Physics Reports, vol. 469, Issue 4, pages 155–203, 2008.

[Hollberg 90] L. Hollberg. Dye laser principles: With applications. Academic Press, Inc., 1990.

[Home] Johnathan Home. Private communication.

[Home 06a] J P Home & A M Steane. Electrode configurations for fast separation of trapped ions. Quant. Inform. Comp., vol. 6, pages 289–325, 2006.

[Home 06b] Jonathan Home. Entanglement of Two Trapped-Ion Spin Qubits. PhD thesis, Linace College, Oxford, 2006.

[Home 09] J. P. Home, D. Hanneke, J. D. Jost, J. M. Amini, D. Leibfried & D. J. Wineland. Complete Methods Set for Scalable Ion Trap Quantum Information Processing. Science, vol. 308, pages 997–1000, 2009.

[Howard 87] Stephen Howard & Sanat K. Royer. Coherent states of a harmonic oscillator. Am. J. Phys., vol. 55, pages 1109–1117, 1987.

[Hume 07] D. B. Hume, T. Rosenband & D. J. Wineland. High-Fidelity Adaptive Qubit Detection through Repetitive Quantum Nondemolition Measurements. Phys. Rev. Lett., vol. 99, no. 12, page 120502, Sep 2007.

[Itano 82] W M Itano & D J Wineland. Laser cooling of ions stored in harmonic and Penning traps. Phys. Rev. A, vol. 25, no. 1, pages 35–54, 1982.

[J. C. Bergquist 87] W. M. Itano J. C. Bergquist & D. J. Wineland. Recoilless Optical Absorbtion and Doppler Sidebands of a Single Trapped Ion. Phys. Rev. A, vol. 436, page 428, 1987.

[Jackson 99] John David Jackson. Classical electrodynamics. John Wiley & Sons, 1999.

[Jaynes 63] E T Jaynes & F W Cummings. Comparison of quantum and semiclassical radiation theories with application to the beam maser. Proceedings of the IEEE, vol. 51, pages 89–109, January 1963.

[Jefferts 95] S R Jefferts, C Monroe, E Bell & D J Wineland. Coaxial-Resonator Driven rf (Paul) Trap for Strong Confinement. Phys. Rev. A, vol. 51, no. 4, pages 3112–3116, April 1995.

[Jost 09] J. D. Jost, J. P. Home, J. M. Amini, D. Hanneke, R. Ozeri, C. Langer, J. J. Bollinger, D. Leibfried & D. J. Wineland. Entangled Mechanical Oscillators. Nature, vol. 459, pages 683–685, 2009.

[Julsgaard 01] B. Julsgaard, A. Kozhekin & E. S. Polzik. Experimental long-lived entanglement of two macroscopic objects. Nature, vol. 413, pages 400–403, 2001.

[Kahill 69] K. E. Kahill & R. J. Glauber. Phys. Rev., vol. 177, page 1857, 1969.

[Kielpinski 00] D Kielpinski, B E King, C J Myatt, C A Sackett, Q A Turchette, W M Itano, C Monroe & D J Wineland. Sympathetic cooling of trapped ions for quantum logic. Phys. Rev. A, vol. 61, pages 032310–1–8, 2000.

[Kielpinski 01] D Kielpinski, V Meyer, M A Rowe, C A Sackett, W M Itano, C Monroe & D J Wineland. A Decoherence-Free Quantum Memory Using Trapped Ions. Science, vol. 291, pages 1013–1015, 2001.

[Kielpinski 02a] D. Kielpinski, C.Monroe & D. Wineland. Architecture for a large-scale ion-trap quantum computer. Nature, vol. 417, pages 709–711, 2002.

[Kielpinski 02b] D Kielpinski, C Monroe & D J Wineland. Architecture for a large-scale ion-trap quantum computer. Nature, vol. 417, pages 709–711, 2002.

[Kim 09] K. Kim, M.-S. Chang, R. Islam, S. Korenblit, L.-M. Duan & C. Monroe. Entanglement and Tunable Spin-Spin Couplings between Trapped Ions Using Multiple Transverse Modes. Physical Review Letters, vol. 103, no. 12, page 120502, 2009.

[King 98] B E King, C S Wood, C J Myatt, Q A Turchette, D Leibfried, W M Itano, C Monroe & D J Wineland. Cooling the Collective Motion of Trapped Ions to Initialize a Quantum Register. Phys. Rev. Lett., vol. 81, pages 1525–1528, 1998.

[King 99] B. E. King. Quantun State Engineering and Information Processing with Trapped Ions. PhD thesis, University of Colorado at Boulder, 1999.

[King 08] Brian King. Angular Momentum Coupling and Rabi Frequencies for Laser-Coolers. arXiv:0804.4528v1 [physics.atom-ph], 2008. Submitted to the American Journal of Physics.

[Kippenberg 05] T. J. Kippenberg, H. Rokhsari, T. Carmon, A. Scherer & K. J. Vahala. Analysis of Radiation-Pressure Induced Mechanical Oscillation of an Optical Microcavity. Phys. Rev. Lett., vol. 95, no. 3, page 033901, Jul 2005.

[Kippenburg 08] T. J. Kippenburg & K. J. Vahala. Cavity Optomechanics: Back-Action at the Mesoscale. Science, vol. 321, page 1172, 2008.

[Kirchmair 09] G. Kirchmair, J. Benhelm, F. Zhäringer, R. Gerritsma, C. F. Roos & R. Blatt. Deterministic entanglement of ions in thermal states of motion. New J. Phys., vol. 11, page 023002, 2009.

[Kitaev 97a] A. Y. Kitaev. Quantum computation: algorithms and error correction. Russ. Math. Surv., vol. 52(6), pages 1191–1249, 1997.

[Kitaev 97b] A. Y. Kitaev. Quantum error correction with imperfect gates. Plenum Press, 1997.

[Knill 05] E. Knill. Quantum computing with realistically noisy devices. nature, vol. 434, pages 39–44, 2005.

[Labaziewicz 08a] J Labaziewicz, Y Ge, P Antohi, C Leibrandt, K R Brown & I L Chuang. Suppression of heating rates in cryogenic surface-electrode ion traps. Phys. Rev. Lett., vol. 100, pages 013001–1–4, 2008.

[Labaziewicz 08b] J. Labaziewicz, Y. Ge, R. Shewmon D. R. Leibrant S. X. Wang & I. L. Chuang. Temperature Dependence of Electric Field Noise above Gold Surfaces. Phys. Rev. Lett., vol. 101, page 180602, 2008.

[Ladd 10] T. D. Ladd, F. Jelezko, R. Laflamme, Y. Nakamura, C. Monroe & J. L. O'Brien. Quantum computers. Nature, vol. 464, pages 45–53, 2010.

[Langer 05] C Langer, R Ozeri, J D Jost, J Chiaverini, B DeMarco, A Ben-Kish, R B Blakestad, J Britton, D B Hume, W M Itano, D Leibfried, R Reichle, T Rosenband, T Schaetz, P O Schmidt & D J Wineland. Long-lived qubit memory using atomic ions. Phys. Rev. Lett., vol. 95, pages 060502–1–4, 2005.

[Langer 06] Christopher E. Langer. High Fidelity Quantum Information Processing with Trapped Ions. PhD thesis, University of Colorado at Boulder, 2006.

[Leggett 02a] A J Leggett. Testing the limits of quantum mechanics: motivation, state of play, prospects. J. Phys.: Condens. Matter, vol. 14, pages R415–R451, 2002.

[Leggett 02b] A. J. Leggett. Testing the limits of quantum mechanics: motivation, state of play, prospects. J. Phys.: Condens. Matter., vol. 14, pages R415–R451, 2002.

[Leibfried 96] D Leibfried, D M Meekhof, B E King, C Monroe, W M Itano & D J Wineland. Experimental Determination of the Motional Quantum State of a Trapped Atom. Phys. Rev. Lett., vol. 77, no. 21, pages 4281–4285, November 1996.

[Leibfried 03a] D Leibfried, R Blatt, C Monroe & D Wineland. Quantum dynamics of single trapped ions. Rev. Mod. Phys., vol. 75, pages 281–324, 2003.

[Leibfried 03b] D Leibfried, B DeMarco, V Meyer, D Lucas, M Barrett, J Britton, W M Itano, B Jelenković, C Langer, T Rosenband & D J Wineland. Experimental demonstration of a robust, high-fidelity geometrical two ion-qubit phase gate. Nature, vol. 422, pages 412–415, 2003.

[Leibfried 04] D Leibfried, M D Barrett, T Schätz, J Britton, J Chiaverini, W M Itano, J D Jost, C Langer & D J Wineland. Toward Heisenberg-limited spectroscopy with multiparticle entangled states. Science, vol. 304, pages 1476–1478, 2004.

[Leibfried 05] D Leibfried, E Knill, S Seidelin, J Britton, R B Blakestad, J Chiaverini, D Hume, W M Itano, J D Jost, C Langer, R Ozeri, R Reichle & D J Wineland. Creation of a six-atom 'Schrödinger cat' state. Nature, vol. 438, pages 639–642, 2005.

[Lin 09] G. D. Lin, S.-L. Zhu, R. Islam, K. Kim, M.-S. Chang, S. Korenblit, C. Monroe & L.-M. Duan. Large-scale quantum computation in an anharmonic linear ion trap. EPL, vol. 86, page 60004, 2009.

[Lindberg 86] M. Lindberg & J. Javaninen. Temperature of a laser-cooled trapped three-level ion. J. Opt. Soc. Am. B, vol. 3, no. 7, page 1008, 1986.

[Madsen 00] D. N. Madsen, S. Balslev, M. Drewsen, N. Kjærgaard, Z. Videsen & J. W. Thomsen. Measurement of photo-ionization of $3s3p\,^1P_1$ magnesium atoms. J. Phys. B., vol. 33, page 4981, 2000.

[Major 05] F G Major, V N Gheorghe & G Werth. Charged particle traps. Springer, Berlin, Heidelberg, 2005.

[Mancini 02] S. Mancini, V.Giovannetti, D. Vitali & P. Tombesi. Entangling Macroscopic Oscillators Exploiting Radiation Pressure. Phys. Rev. Lett., vol. 88, page 120401, 2002.

[Mathematica] Mathematica. Wolfram Research Inc.

[Matlab] Matlab. The Mathworks Inc.

[Matsukevich 08] D. N. Matsukevich, P. Maunz, D. L. Moehring, S. Olmschenk & C. Monroe. Bell inequality violation with two remote atomic qubits. Phys. Rev. Lett., vol. 100, page 150404, 2008.

[McDonnell 03] Matthew McDonnell. Two-Photon Readout Methods for an Ion Trap Quantum Information Processer. PhD thesis, Keble College, Oxford, 2003.

[Meekhof 96] D M Meekhof, C Monroe, W M Itano, B E King & D J Wineland. Generation of Nonclassical Motional States of a Trapped Atom. Phys. Rev. Lett., vol. 76, no. 11, pages 1796–1799, March 1996.

[Merzbacher 98] Eugen Merzbacher. Quantum mechanics. John Wiley & Sons, 1998.

[Metcalf 99] Harold J. Metcalf & Peter van der Straten. Laser cooling and trapping. Springer, 1999.

[MgI] Lawrence Berkeley National Labs Isotope Project.

[Milburn 01] G J Milburn, S Schneider & D F V James. Ion trap quantum computing with warm ions. In S L Braunstein, H -K Lo & P Kok, editeurs, Scalable Quantum Computers, pages 31–40, Berlin, 2001. Wiley-VCH.

[Milman 05] P. Milman, A. Auffeves, F. Yamaguchi, M. Brune, J. M. Raimond & S. Haroche. A proposal to test Bell's inequalities with mesoscopic non-local states in cavity QED. Eur. J. Phys., vol. 32, pages 233–239, 2005.

[Mintert 01] F Mintert & C Wunderlich. Ion-trap quantum logic using long-wavelength radiation. Phys. Rev. Lett., vol. 87, no. 25, pages 257904–1–4, 2001.

[Moehring 07] D L Moehring, P Maunz, S Olmschenk, K C Younge, D N Matsukevich, L M Duan & C Monroe. Entanglement of single-atom quantum bits at a distance. Nature, vol. 449, pages 68–71, 2007.

[Mølhave 00] K Mølhave & M Drewsen. Formation of translationally cold MgH^+ and MgH^+ molecules in an ion trap. Phys. Rev. A, vol. 62, pages 011401–1–4, 2000.

[Mølmer 99] K Mølmer & A Sørensen. Multiparticle entanglement of hot trapped ions. Phys. Rev. Lett., vol. 82, pages 1835–1838, 1999.

[Monroe 95a] C Monroe, D M Meekhof, B E King, W M Itano & D J Wineland. Demonstration of a fundamental quantum logic gate. Phys. Rev. Lett., vol. 75, no. 25, pages 4714–4717, December 1995.

[Monroe 95b] C Monroe, D M Meekhof, B E King, S R Jefferts, W M Itano, D J Wineland & P Gould. Resolved-Sideband Raman Cooling of a Bound Atom to the 3D Zero-point Energy. Phys. Rev. Lett., vol. 75, no. 22, pages 4011–4014, 1995.

[Monroe 96] C Monroe, D M Meekhof, B E King & D J Wineland. A "Schrödinger cat" superposition state of an atom. Science, vol. 272, pages 1131–1136, May 1996.

[Myerson 08] A. H. Myerson, D. J. Szwer, S. C. Webster, D. T. C. Allcock, M. J. Curtis, G. Imreh, J. A. Sherman, D. N. Stacey, A. M. Steane & D. M. Lucas. High-Fidelity Readout of Trapped-Ion Qubits. Phys. Rev. Lett., vol. 100, no. 20, page 200502, May 2008.

[Nägerl 99] H C Nägerl, D Leibfried, H Rohde, G Thalhammer, J Eschner, F Schmidt-Kaler & R Blatt. Laser addressing of individual ions in a linear trap. Phys. Rev. A, vol. 60, no. 1, pages 145–148, 1999.

[Nagourney 86] W Nagourney, J Sandberg & H G Dehmelt. Shelved Optical Electron Amplifier: Observation of Quantum Jumps. Phys. Rev. Lett., vol. 56, no. 26, pages 2797–2799, June 1986.

[Neuhauser 78] W. Neuhauser, M. Hohenstatt, P. Toschek & H. Dehmelt. Optical-Sideband Cooling of Visible Atom Cloud Confined in Parabolic Well. Phys. Rev. Lett., vol. 41, page 233, 1978.

[Nielsen 00] M A Nielsen & I L Chuang. Quantum computation and quantum information. Cambridge Univ. Press, Cambridge, 1st edition, 2000.

[O'Connell 10] A. D. O'Connell, M. Hofheinz, M. Ansmann, R. C. Bialczak, M. Lenander, E. Lucero, M. Neeley, D. Sank, H. Wang, M. Weides, J. Wenner, J. M. Martinis & A. N. Cleland. Quantum ground state and single-phonon control of a mechanical resonator. Nature, 2010.

[O'Hanlon 89] J. F. O'Hanlon. A users guide to vacuum technology. John Wiley & Sons, 1989.

[Ospelkaus 08] C. Ospelkaus, C. E. Langer, J. M. Amini, K. R. Brown, D. Leibfried & D. J. Wineland. Trapped-Ion Quantum Logic Gates Based on Oscillating Magnetic Fields. Phys. Rev. Lett., vol. 101, page 090502, 2008.

[Ozeri 05] R Ozeri, C Langer, J D Jost, B L DeMarco, A Ben-Kish, B R Blakestad, J Britton, J Chiaverini, W M Itano, D Hume, D Leibfried, T Rosenband, P Schmidt & D J Wineland. Hyperfine coherence in the presence of spontaneous photon scattering. Phys. Rev. Lett., vol. 95, pages 030403–1–4, 2005.

[Ozeri 07] R. Ozeri, W. M. Itano, R.B. Blakestad, J. Britton, J. Chiaverini, J.D. Jost, C. Langer, D. Leibfried, R. Reichle, S. Seidelin, J. H. Wesenberg & D.J. Wineland. Errors in trapped-ion quantum gates due to spontaneous photon scattering. Phys. Rev. A, vol. 75, page 042329, 2007.

[Pan 08] J-W. Pan, Z-B. Chen, M. Zukowski, H. Weinfurter & A. Zeilinger. Multi-photon entanglement and interferometry. arxiv:0805.2853, 2008.

[Paul 90] W Paul. Electromagnetic traps for charged and neutral particles. Rev. Mod. Phys., vol. 62, pages 531–540, 1990.

[Petta 05] J. R. Petta, A. C. Johnson, J. M. Taylor, E. A. Laird, A. Yacoby, M. D. Lukin, C. M. Marcus, M. P. Hanson & A. C. Gossard. Coherent Manipulation of Coupled Electron Spins in Semiconductor Quantum Dots. Science, vol. 309, no. 5744, pages 2180–2184, 2005.

[Poulsen 75] O. Poulsen, T. Andersen & N. J. Skouboe. Fast-beam, zero-field level-crossing measurements of radiative lifetimes, fine and hyperfine structures in excited states of ionic and neutral beryllium. J. of Phys. B: Atom. Mole Phys., vol. 8, no. 9, pages 1393–1405, 1975.

[Raizen 93] M G Raizen, J M Gilligan, J C Bergquist, W M Itano & D J Wineland. Ionic crystals in a linear Paul trap. Phys. Rev. A, vol. 45, no. 9, pages 6493–6501, May 1993.

[Ramsey 63] N F Ramsey. Molecular beams. Oxford University Press, London, 1963.

[Regal 08] C. A. Regal, J. D. Teufel & K. W. Lehnert. Measuring nanomechanical motion with a microwave cavity interferometer. Nature Physics, vol. 4, pages 555–560, 2008.

[Reichle 06a] R Reichle, D Leibfried, R B Blakestad, J Britton, J D Jost, E Knill, C Langer, R Ozeri, S Seidelin & D J Wineland. Transport dynamics of single ions in segmented microstructured Paul trap arrays. Fortschr. Phys., vol. 54, pages 666–685, 2006.

[Reichle 06b] R Reichle, D Leibfried, E Knill, J Britton, R B Blakestad, J D Jost, C Langer, R Ozeri, S Seidelin & D J Wineland. Experimental purification of two-atom entanglement. Nature, vol. 443, pages 838–841, 2006.

[Riebe 04] M Riebe, H Häffner, C F Roos, W Hänsel, J Benhelm, G P T Lancaster, T W Körber, C Becher, F Schmidt-Kaler, D F V James & R Blatt. Deterministic quantum teleportation with atoms. Nature, vol. 429, pages 734–737, 2004.

[Rohde 01] H Rohde, S T Gulde, C F Roos, P A Barton, D Leibfried, J Eschner, F Schmidt-Kaler & R Blatt. Sympathetic ground-state cooling and coherent manipulation with two-ion crystals. J. Opt. B: Quantum Semiclass. Opt., vol. 3, pages S34–S41, 2001.

[Roos 04] C F Roos, M Riebe, H Häffner, W Hänsel, J Benhelm, G P T Lancaster, C Becher, F Schmidt-Kaler & R Blatt. Control and measurement of three-qubit entangled states. Science, vol. 304, pages 1478–1480, 2004.

[Roos 08] C. F. Roos, T. Monz, K. Kim, M. Riebe, H. Häffner, D. F. V. James & R. Blatt1. Nonlinear coupling of continuous variables at the single quantum level. Phys. Rev. A., vol. 77, page 040302(R), 2008.

[Rosenband] T. Rosenband. private communication.

[Rowe 01] M A Rowe, D Kielpinski, V Meyer, C A Sackett, W M Itano, C Monroe & D J Wineland. Experimental violation of a Bell's inequality with efficient detection. Nature, vol. 409, pages 791–794, 2001.

[Rowe 02] M A Rowe, A Ben-Kish, B DeMarco, D Leibfried, V Meyer, J Beall, J Britton, J Hughes, W M Itano, B Jelenković, C Langer, T Rosenband & D J Wineland. Transport of quantum states and separation of ions in a dual RF ion trap. Quant. Inform. Comp., vol. 2, no. 4, pages 257–271, 2002.

[Sackett 00] C A Sackett, D Kielpinski, B E King, C Langer, V Meyer, C J Myatt, M Rowe, Q A Turchette, W M Itano, D J Wineland & C Monroe. Experimental entanglement of four particles. Nature, vol. 404, pages 256–258, 2000.

[Sakurai 94] J. J. Sakurai. Modern quantum mechanics. Addison-Wesley, 1994.

[Sauter 86] Th Sauter, W Neuhauser, R Blatt & P E Toschek. Observation of Quantum Jumps. Phys. Rev. Lett., vol. 57, no. 14, pages 1696–1698, October 1986.

[Schaetz 04] T Schaetz, M D Barrett, D Leibfried, J Chiaverini, J Britton, W M Itano, J D Jost, C Langer & D J Wineland. Quantum dense coding with atomic qubits. Phys. Rev. Lett., vol. 93, no. 4, pages 040505–1–4, 2004.

[Schaetz 05] T Schaetz, M D Barrett, D Leibfried, , J Britton J Chiaverini, W M Itano, J D Jost, E Knill, C Langer & D J Wineland. Enhanced quantum state detection efficiency through quantum information processing. Phys. Rev. Lett., vol. 94, pages 010501–1–4, 2005.

[Schleich 01] W. P. Schleich. Quantum optics in phase space. Wiley-VCH, Berlin, 1st edition, 2001.

[Schlosshauer 08] M. Schlosshauer. Lifting the fog from the north. Nature, vol. 453, page 39, 2008.

[Schrödinger 35] E. Schrödinger. Die Gegenwärtige Situation in der Quantunmechanik. Naturwissenschaften, vol. 23, pages 807–812; 823–828; 844–849, 1935.

[Schwab 05] K. C. Schwab & M. L. Rourkes. Putting Mechanics into Quantum Mechanics. Physics Today, vol. 58, page 36, 2005.

[Seidelin 06] S Seidelin, J Chiaverini, R Reichle, J J Bollinger, D Leibfried, J Britton, J H Wesenberg, R B Blakestad, R J Epstein, D B Hume, W M Itano, J D Jost, C Langer, R Ozeri, N Shiga & D J Wineland. A microfabricated surface-electrode ion trap for scalable quantum information processing. Phys. Rev. Lett., vol. 96, pages 253003–1–4, 2006.

[Shor 94] P W Shor. Algorithms for quantum computation: discrete logarithms and factoring. In S Goldwasser, editeur, Proceedings of the 35th Annual Symposium on the Foundations of Computer Science, volume 35, page 124, Los Alamitos, CA, 1994. IEEE Computer Society Press.

[Shor 95] P W Shor. Scheme for reducing decoherence in quantum computer memory. Phys. Rev. A, vol. 52, no. 4, pages R2493–R2496, October 1995.

[Shor 96] P. W. Shor. Fault-tolerant quantum computation. In Proceedings, 37th Annual Symposium on Fundamentals of Computer Science, pages 56–65. IEEE Press, 1996.

[Sleator 95] Tycho Sleator & Harald Weinfurter. Realizable Universal Quantum Logic Gates. Phys. Rev. Lett., vol. 74, no. 20, pages 4087–4090, May 1995.

[Solano 99] E Solano, R L de Matos Filho & N Zagury. Deterministic Bell states and measurement of the motional state of two trapped ions. Phys. Rev. A, vol. 59, pages 2539–2542, 1999.

[Sørensen 99] Anders Sørensen & Klaus Mølmer. Quantum Computation with Ions in Thermal Motion. Phys. Rev. Lett., vol. 82, no. 9, pages 1971–1974, Mar 1999.

[Sørensen 00] A Sørensen & K Mølmer. Entanglement and quantum computation with ions in thermal motion. Phys. Rev. A, vol. 62, pages 02231–1–11, 2000.

[Southwell 08] K. Southwell. Nature Insight: Quantum coherence. Nature, vol. 453, page 1003, 2008.

[Steane 96] A Steane. Error Correcting Codes in Quantum Theory. Phys. Rev. Lett., vol. 77, no. 5, pages 793–796, 1996.

[Steane 03a] A. Steane. How to Buila a 300 Bit, 1 Giga-Opertion Quantum Computer. Quantum Information and Computation, vol. 0, 2003.

[Steane 03b] A M Steane. Overhead and noise threshold of fault-tolerant quantum error correction. Phys. Rev. A, vol. 68, no. 4, pages 042322–1–19, 2003.

[Steffen 06] Matthias Steffen, M. Ansmann, Radoslaw C. Bialczak, N. Katz, Erik Lucero, R. McDermott, Matthew Neeley, E. M. Weig, A. N. Cleland & John M. Martinis. Measurement of the Entanglement of Two Superconducting Qubits via State Tomography. Science, vol. 313, no. 5792, pages 1423–1425, 2006.

[Steinbach 96] A. Steinbach, M. Rauner, F.C. Cruz & J. C. Bergquist. CW second harmonic generation with elliptical Gaussian beams. Optics Comm., vol. 123, page 207, 1996.

[Stenholm 86] Stig Stenholm. The semiclassical theory of laser cooling. Rev. Mod. Phys., vol. 58, pages 699–739, 1986.

[Tan 99] Sze M Tan. A computational toolbox for quantum and atomic opticss. J. Opt. B: Quantum Semiclass. Opt., vol. 1, pages 424–432, 1999.

[Thompson 08] J. D. Thompson, B. M. Zwickl, A. M. Jayich, F. Marquardt, S. M. Girvin & J. G. E. Harris. Strong dispersive coupling of a high-finesse cavity to a micromechanical membrane. Nature, vol. 452, pages 72–75, 2008.

[Turchette 00] Q A Turchette, D Kielpinski, B E King, D Leibfried, D M Meekhof, C J Myatt, M A Rowe, C A Sackett, C S Wood, W M Itano, C Monroe & D J Wineland. Heating of trapped ions from the quantum ground state. Phys. Rev. A, vol. 61, pages 063418–1–8, 2000.

[Vandersypen 04] L. M. K. Vandersypen & I. L. Chuang. NMR techniques for quantum control and computation. Rev. Mod. Phys., vol. 76, pages 1035–1069, 2004.

[Verdeyen 95] Joseph T. Verdeyen. Laser electronics. Prentice Hall, 1995.

[Walls 94] D F Walls & G J Milburn. Quantum optics. Springer, Berlin, 1st edition, 1994.

[Wang 01] X Wang, A Sørensen & K Mølmer. Mulitbit gates for quantum computing. Phys. Rev. Lett., vol. 86, pages 3907–3910, 2001.

[Wang 09] S. X. Wang, J. Labaziewicz, Y. Ge, R. Shewmon & I. L. Chuang. Individual addressing of ions using magnetic field gradients in a surface -electrode ion trap. Appl. Phys. Let., vol. 94, page 094103, 2009.

[Wineland 75] D. J. Wineland & H. Dehmelt. Bull. Am. Phys. Soc., vol. 20, page 637, 1975.

[Wineland 78] D. J. Wineland, R. E. Drullinger, & F. L. Walls. Radiation-Pressure Cooling of Bound Resonant Absorbers. Phys. Rev. Lett., vol. 40, pages 1639–1642, 1978.

[Wineland 79] D J Wineland & W M Itano. Laser cooling of atoms. Phys. Rev. A, vol. 20, no. 4, pages 1521–1540, October 1979.

[Wineland 80] D J Wineland, J C Bergquist, W M Itano & R Drullinger. Double-resonance and optical-pumping experiments on electromagnetically confined, laser-cooled ions. Opt. Lett., vol. 5, no. 6, pages 245–247, 1980.

[Wineland 83] D. J. Wineland, J. J. Bollinger & Wayne M. Itano. Laser-Fluorescence Mass Spectroscopy. Phys. Rev. Lett., vol. 50, no. 9, pages 628–631, 1983.

[Wineland 87] D J Wineland & W M Itano. Laser Cooling. Physics Today, vol. 40, no. 6, pages 2–8, June 1987.

[Wineland 98] D J Wineland, C Monroe, W M Itano, D Leibfried, B E King & D M Meekhof. Experimental issues in coherent quantum-state manipulation of trapped atomic ions. J. Res. Nat. Inst. Stand. Tech., vol. 103, pages 259–328, 1998.

[Wineland 03] D J Wineland, M Barrett, J Britton, J Chiaverini, B DeMarco, W M Itano, B. Jelenković, C Langer, D Leibfried, V Meyer, T Rosenband & T Schätz. Quantum information processing with trapped ions. Phil. Trans. R. Soc. Lond. A, vol. 361, pages 1349–1361, 2003.

[Wineland 04] D. J. Wineland. Quantum information processing in ion traps. In D. Estéve, J. M. Raimond & J. Dalibard, editeurs, Les Houches, Session LXXIX, 2003, Quantum Entanglement and Information Processing, pages 261–293. Elsevier, Amsterdam, 2004.

[Yu. 08] Ralchenko Yu., Kramida A.E., Reader J. & NIST ASD Team. NIST Atomic Spectra Database (version 3.1.5), [Online]. Available: http://physics.nist.gov/asd3 [2010, March 8]., 2008.

[Zhu 06] Shi-Liang Zhu, C Monroe & L M Duan. Arbitrary-speed quantum gates within large ion crystals through miminum control of laser beams. quant-ph/0508037, 2006.

[Zurek 96] W. H. Zurek & R. Laflamme. Quantum logical operations on encoded qubits. Phys. Rev. Lett., vol. 77(22), pages 4283–4686, 1996.

Appendix A

Calculating Rabi Frequencies

The Rabi frequency equation (5.27), which is rewritten here for convenience as

$$\Omega = -\frac{e}{\hbar} E_o \langle e | \vec{r} \cdot \vec{\epsilon} | g \rangle , \tag{A.1}$$

is a parameter that commonly shows up in atomic physics calculations. Here the states $|g\rangle$ and $|e\rangle$ represent the ground and excited states respectively. The Rabi frequency is usually defined in terms of the electric field strength of the laser beams and the dipole matrix operator. However this not all that useful of a quantity for experimentalists. Typically the information an experimentalist has at hand is the laser power, the polarization, a measurement of the beam waist, the excited state linewidth, and some Clebsch-Gordon tables. Equation (5.27) can be rewritten such that only that information is needed to come up with a value for the Rabi frequency to plug into our calculations.

The electric field for a Gaussian laser beam [Verdeyen 95] is

$$\vec{E}(x,y,z,t) = E_o \vec{\epsilon} \frac{\omega_o}{\omega(z)} e^{-\left(\frac{r}{\omega(z)}\right)^2} e^{\left(-ikz + i\tan\left(\frac{z}{z_0}\right)\right)} e^{-i\frac{kr^2}{2R(z)}} e^{i\omega t}, \tag{A.2}$$

where

$$\omega^2(z) = \omega_o^2 \left(1 + \left(\frac{z}{z_o}\right)^2\right) \tag{A.3}$$

$$R(z) = z\left(1 + \left(\frac{z_o}{z}\right)^2\right) \tag{A.4}$$

$$z_o = \frac{\pi n \omega_o}{\lambda}. \tag{A.5}$$

This describes the electric field and the phase in the radial direction of the beam as it travels in the z direction. The beam waist ω_o is defined as the $\frac{1}{e}$ point, so this is a radius. The wavelength and the index of refraction are given by λ and n respectively. The polarization vector is given by $\vec{\epsilon}$. The intensity in the beam can be calculated from the poynting vector[Hecht 04] $\vec{S}$

$$I = \left\langle \vec{S} \right\rangle_T = c^2 \epsilon_o \left| \vec{E} \times \vec{B} \right|, \tag{A.6}$$

where $\left\langle \vec{S} \right\rangle_T$represents the time average. Substituting equation (5.25) and $\vec{B} = \frac{\vec{E}}{c}$ into the above equation gives

$$I = \left\langle \vec{S} \right\rangle_T = c\epsilon_o E_o^2 \frac{\omega_o}{\omega(z)} e^{-\left(\frac{2r}{\omega(z)}\right)^2} \left\langle \left(e^{\left(-ikz + i\tan\left(\frac{z}{z_0}\right)\right)} e^{-i\frac{kr^2}{2R(z)}} e^{i\omega t} \right)^2 \right\rangle_T . \tag{A.7}$$

With an optical power-meter the instantaneous power is not measured but rather the time averaged power. The time average of the oscillating field[Hecht 04] is $\frac{1}{2}$. This gives a more convenient expression for the intensity.

$$I = c\epsilon_o \frac{E_o^2}{2} \frac{\omega_o}{\omega(z)} e^{-\left(\frac{2r}{\omega(z)}\right)^2}. \tag{A.8}$$

However with the lab tools you are not going to measure the intensity but rather the total power in the beam and its waist. Assuming the ion is at the beam waist, $\omega(z) = \omega_o$ the power in the beam can be expressed as

$$P = \int I dA = c\epsilon_o \frac{E_o^2}{2} \int_0^\infty \int_0^{2\pi} r e^{-\left(\frac{2r}{\omega_o}\right)^2} dr d\phi = c\epsilon_o \frac{E_o^2}{2} \frac{\pi\omega_o^2}{2}. \tag{A.9}$$

Now the electric field can be written in terms of things measurable in the lab

$$E_o = \sqrt{\frac{4P}{c\epsilon_o \pi \omega_o^2}}. \tag{A.10}$$

The next thing that needs to be cast in a more useful form is the dipole matrix element $\langle e| \vec{r} \cdot \vec{\epsilon} |g\rangle$. The Wigner-Eckart theorem can be used to simplify this, using the

convention of Edmonds [Edmonds 96]

$$\begin{aligned}\langle \gamma', j', m' | \, T(k,q) \, | \gamma, j, m \rangle &= (-1)^{j'-m'} \begin{pmatrix} j' & k & j \\ m' & q & m \end{pmatrix} && \text{(A.11)} \\ &\times \left\langle \gamma' j' \right\| T(k,q) \left\| \gamma j \right\rangle && \text{(A.12)} \\ &= (-1)^{k-j+j'} \frac{\langle k, q, j, m | \, k, q, j', m' \rangle}{\sqrt{2j'+1}} \times && \text{(A.13)} \\ &\langle \gamma' j' \| \mathrm{T}(k,q) \, \| \gamma j \rangle. && \text{(A.14)}\end{aligned}$$

The matrix $\begin{pmatrix} j' & k & j \\ m' & q & m \end{pmatrix}$ is the Wigner 3-j symbol and $\langle k, q, j, m | \, k, q, j', m' \rangle$ represents the Clebsch-Gordon coefficient. The values can be looked up in tables or calculated using several common math programs. The term $\left\langle \gamma' j' \right\| T(k,q) \left\| \gamma j \right\rangle$ is the reduced density matrix element, where $T(k,q)$ is the tensor operator that connects the two states. The rank of the tensor is given by k, which is 1 for an electric dipole transition. The parameter q represents the quantum number, and for electric dipole transitions it can take on values of -1, 0, and 1, which corresponds to light with polarization of σ^-, π, and σ^+ polarizations respectively. The value for the reduced density matrix can only be calculated for a few special cases. However, it can be related to the spontaneous decay rate, which is a measurable quantity in most systems. Reference [King 08] has a derivation and discussion of this. It gives as a result the relation for the reduced density matrix element to the spontaneous emission rate as

$$\left\langle \gamma' j' \right\| T(k,q) \left\| \gamma j \right\rangle = (-1)^{j+j_>} \sqrt{2j'+1} \sqrt{\frac{3\epsilon_o \hbar \lambda^3 \Gamma}{8\pi^2 e^2}}, \qquad \text{(A.15)}$$

where $j_>$ is the larger of j and j'. The wavelength of the transition is given by λ, and the spontaneous decay rate is in Γ (units of radians per second). Equations (A.1),(A.10),(A.11), and(A.15)can be combined to give the following expression for the Rabi frequency

$$\Omega = \sqrt{\frac{3\lambda \Gamma P}{2\hbar c \pi^3 \omega_0^2}} \, (-1)^{j'+j+j_>-m} \sqrt{2j'+1} \begin{pmatrix} j' & k & j \\ m' & q & m \end{pmatrix} \qquad \text{(A.16)}$$

.

Appendix B

Determining the Average Motional State

It is not strictly correct to refer to the temperature of an ion since it is not in contact with a thermal reservoir but it is still commonplace to do so. If we assume an ion's motion has a thermal distribution, an expression can be found for the mean occupation number $\langle n \rangle$ (This is equivalent to $\bar{n}$ in the text) of the ion's quantized harmonic motion for a given temperature. The resulting distribution is a Bose-Einstein distribution. Here the case of a harmonic oscillator including the zero-point energy is derived.

The energy of a harmonic oscillator Fock state is given by $E = \hbar\omega(n + 1/2)$. Where ω is the frequency of the harmonic oscillator and n is the quantized motional state of the oscillator. The average energy for a particular mode is

$$\langle E \rangle = \hbar\omega \langle n + 1/2 \rangle . \tag{B.1}$$

The average for a distribution of states can be calculated by summing over all the possible n states times the probability p_n of being in that state for a given energy, which is given by

$$\langle n + 1/2 \rangle = \sum_{n=0}^{\infty} (n + 1/2)\, p_n. \tag{B.2}$$

The probability for being in a particular state is

$$p_n = \frac{e^{\frac{-E_n}{k_b T}}}{Z} = \frac{e^{\frac{-\hbar\omega(n+1/2)}{k_b T}}}{Z}. \tag{B.3}$$

The partition function Z is a sum over the energy states, which gives

$$Z = \sum_{n=0}^{\infty} e^{-\frac{E_n}{k_b T}} = e^{-\frac{\hbar\omega}{2k_b T}} \sum_{n=0}^{\infty} e^{-\frac{n\hbar\omega}{2k_b T}}. \tag{B.4}$$

This series can be summed using a geometric series to give

$$Z = \frac{e^{-\frac{\hbar\omega}{2k_b T}}}{1 - e^{-\frac{\hbar\omega}{k_b T}}} = \frac{1}{2}\mathrm{csch}\left(\frac{\hbar\omega}{2k_b T}\right). \tag{B.5}$$

Plugging equations (B.5) and (B.3) into (B.2) gives

$$\langle n + 1/2\rangle = \frac{1}{\frac{1}{2}\mathrm{csch}\left(\frac{\hbar\omega}{2k_b T}\right)} \sum_{n=0}^{\infty} (n+1)\, e^{\frac{-\hbar\omega(n+1/2)}{k_b T}}. \tag{B.6}$$

The sum in the above equation can be evaluated using the trick

$$\sum_n n e^{-nx} = -\frac{d}{dx}\sum_n e^{-nx} = -\frac{d}{dx}\left(\frac{1}{1-e^{-x}}\right). \tag{B.7}$$

Making use of this trick and simplifying give the following expression for equation on the preceding page

$$\langle n + 1/2\rangle = \frac{1}{2}\coth\left(\frac{\hbar\omega}{2k_b T}\right). \tag{B.8}$$

Subtracting $1/2$ from each side of the above expression gives

$$\langle n\rangle = \frac{1}{2}\coth\left(\frac{\hbar\omega}{2k_b T}\right) - \frac{1}{2}. \tag{B.9}$$

This is the same expression obtained it is assumed there is no zero point energy to begin with, which is a slightly simpler calculation.

Appendix C

Pulse Sequence for the Entangled Mechanical Oscillators Experiment

The following table is the pulse sequence for the entangled mechanical oscillators experiment. This table is reproduced from reference [Jost 09]. As a NIST publication it is not subject to US Copyright.

Supplementary Table 1: **Detailed procedure for the entangled mechanical oscillators experiment.** Rotations are defined in the text; those without superscripts are carrier rotations between hyperfine pairs other than $\{|\uparrow\rangle, |\downarrow\rangle\}$. These auxiliary states are indicated with $|F, m_F\rangle$. Times are rounded to the nearest microsecond. Steps without an explicit operation typically involve laser frequency changes and intensity stabilization. The procedure for the spin–motion entanglement experiment is identical except the seven steps between the spin-echo pulses in well B are replaced with a single 90 μs delay.

Operation	Ideal State after Operation	Time (μs)	Notes
Order ions	–	935	Order the ions to $^9\mathrm{Be}^+$ –$^{24}\mathrm{Mg}^+$ –$^{24}\mathrm{Mg}^+$ –$^9\mathrm{Be}^+$
Lock the laser intensity	–	380	–
–	–	26	–
Doppler cool ($^9\mathrm{Be}^+$ & $^{24}\mathrm{Mg}^+$)	–	3500	–
Doppler cool ($^9\mathrm{Be}^+$ only)	–	500	–
–	–	2	–
Repump $^{24}\mathrm{Mg}^+$	–	2	–
Repump $^9\mathrm{Be}^+$	$\|\uparrow\uparrow\rangle$	25	–
$^9\mathrm{Be}^+$ sideband cool	$\|\uparrow\uparrow\rangle\|0\rangle$	2753	Ground-state cool the four axial modes (20 cooling pulses per mode). From this point on, all $^9\mathrm{Be}^+$ interactions are coherent.
Prepare $\|\Psi_1\rangle$	$\frac{1}{\sqrt{2}}\left[\|\uparrow\downarrow\rangle + \|\downarrow\uparrow\rangle\right]$	266	–
Separate	$\frac{1}{\sqrt{2}}\left[\|\uparrow\rangle_A\|\downarrow\rangle_B + e^{i\phi_g(t)}\|\downarrow\rangle_A\|\uparrow\rangle_B\right]\|\Lambda\rangle_A\|\Upsilon\rangle_B$	819	Unknown motional state after separation (state $\|\Psi_2\rangle$)
$^{24}\mathrm{Mg}^+$ Doppler cool	–	400	Cool in both wells simultaneously; $^9\mathrm{Be}^+$ coherence undisturbed
$^{24}\mathrm{Mg}^+$ 2nd sideband cool	–	539	20 cooling pulses on the second sideband of each of the two axial modes; cool both wells simultaneously
$^{24}\mathrm{Mg}^+$ 2nd sideband cool	–	539	Repeat the previous step.
$^{24}\mathrm{Mg}^+$ sideband cool	$\frac{1}{\sqrt{2}}\left[\|\uparrow\rangle_A\|\downarrow\rangle_B + e^{i\phi_g(t)}\|\downarrow\rangle_A\|\uparrow\rangle_B\right]\|0\rangle_A\|0\rangle_B$	1277	Account for the slight difference in mode frequencies between the two wells by applying 30 cooling pulses resonant with each mode (4 modes total). Final $\langle n\rangle < 0.1$ on the stretch modes. (state $\|\Psi_3\rangle$)

Continued on next page

Supplementary Table 1: (continued)

Operation	Ideal State after Operation	Time (μs)	Notes
–	–	22	–
$R_A^m(\pi,0)$	$\frac{1}{\sqrt{2}}\left\|\uparrow\right\rangle_A\left[\left\|\downarrow\right\rangle_B\left\|0\right\rangle_A - ie^{i\phi_g(t)}\left\|\uparrow\right\rangle_B\left\|1\right\rangle_A\right]\left\|0\right\rangle_B$	12	Spin→motion transfer pulse in well A (state $\left\|\Psi_4\right\rangle$)
–	–	14	*At this point, we have entangled a mechanical oscillator with the spin of a separated ion.*
$R_A(\pi,0)$	$\epsilon_A\left\|\downarrow\right\rangle_A \Rightarrow \epsilon_A\left\|2,0\right\rangle_A$	3	Shelve residual amplitude ϵ_A of $\left\|\downarrow\right\rangle_A$ ($\epsilon_A \neq 0$ only if there is an error in the spin→motion transfer)
–	–	22	This step and the previous two constitute T of the first spin-echo sequence.
$R_B^c(\pi,0)$	$\frac{1}{\sqrt{2}}\left\|\uparrow\right\rangle_A\left[\left\|\uparrow\right\rangle_B\left\|0\right\rangle_A - ie^{i\phi_g(t)}\left\|\downarrow\right\rangle_B\left\|1\right\rangle_A\right]\left\|0\right\rangle_B$	4	First spin-echo pulse in well B
–	–	38	Second T delay of the first spin-echo sequence
$R_B^m(\pi,0)$	$\frac{1}{\sqrt{2}}\left\|\uparrow\right\rangle_A\left\|\uparrow\right\rangle_B\left[\left\|0\right\rangle_A\left\|0\right\rangle_B - e^{i\phi_g(t)}\left\|1\right\rangle_A\left\|1\right\rangle_B\right]$	14	Spin→motion transfer pulse in well B (state $\left\|\Psi_5\right\rangle$)
–	–	24	*At this point, we have entangled separated mechanical oscillators.*
$R_B(\pi,0)$	$\epsilon_B\left\|\downarrow\right\rangle_B \Rightarrow \epsilon_B\left\|2,0\right\rangle_B$	4	Shelve residual amplitude ϵ_B of $\left\|\downarrow\right\rangle_B$. As above, this removes any residual spin entanglement for the remainder of the experiment.
–	–	24	–
$R_B^m(\pi,0)$	$\frac{1}{\sqrt{2}}\left\|\uparrow\right\rangle_A\left[\left\|\uparrow\right\rangle_B\left\|0\right\rangle_A + ie^{i\phi_g(t)}\left\|\downarrow\right\rangle_B\left\|1\right\rangle_A\right]\left\|0\right\rangle_B$	14	Motion→spin transfer pulse in well B
–	–	38	First T delay of the second spin-echo sequence
$R_B^c(\pi,0)$	$\frac{1}{\sqrt{2}}\left\|\uparrow\right\rangle_A\left[\left\|\downarrow\right\rangle_B\left\|0\right\rangle_A + ie^{i\phi_g(t)}\left\|\uparrow\right\rangle_B\left\|1\right\rangle_A\right]\left\|0\right\rangle_B$	4	Second spin-echo pulse in well B
–	–	39	Second T delay of the second spin-echo sequence
$R_A^m(\pi,\phi_A)$	$\frac{1}{\sqrt{2}}\left[\left\|\uparrow\right\rangle_A\left\|\downarrow\right\rangle_B + e^{i\left(\phi_g(t)+\phi_A\right)}\left\|\downarrow\right\rangle_A\left\|\uparrow\right\rangle_B\right]\left\|0\right\rangle_A\left\|0\right\rangle_B$	11	Motion → spin transfer pulse in well A
Recombine	$\frac{1}{\sqrt{2}}\left[\left\|\uparrow\downarrow\right\rangle + \left\|\downarrow\uparrow\right\rangle\right]$	1219	Recombine all ions to the same well
$^{24}Mg^+$ Doppler cool	$\frac{1}{\sqrt{2}}\left[\left\|\uparrow\downarrow\right\rangle + \left\|\downarrow\uparrow\right\rangle\right]$	400	–
–	–	22	–
$R(\pi,0)$	$\epsilon_A\epsilon_B\left\|2,0\right\rangle\left\|2,0\right\rangle \Rightarrow \epsilon_A\epsilon_B\left\|2,-1\right\rangle\left\|2,-1\right\rangle$	3	Further shelve the residual spin amplitudes

Continued on next page

Supplementary Table 1: (continued)

Operation	Ideal State after Operation	Time (μs)	Notes
–	–	22	–
$R(\pi, 0)$	$\epsilon_A\epsilon_B \left\|2,-1\right\rangle \left\|2,-1\right\rangle \Rightarrow \epsilon_A\epsilon_B \left\|2,-2\right\rangle \left\|2,-2\right\rangle$	4	Further shelve the residual spin amplitudes
–	–	22	–
$R^c(\frac{\pi}{2}, \phi_D)$	$\frac{1}{\sqrt{2}}\left[\left\|\uparrow\uparrow\right\rangle + i\left\|\downarrow\downarrow\right\rangle\right]$	1	Rotate into the detection basis ($\phi_D \approx -\frac{3\pi}{4}$)
–	–	6	–
$R^c(\frac{\pi}{2}, \phi_p)$	$\frac{1}{2}\Big[(\cos\phi_p - \sin\phi_p)\left(e^{-i\phi_p}\left\|\uparrow\uparrow\right\rangle - e^{i\phi_p}\left\|\downarrow\downarrow\right\rangle\right) + (\cos\phi_p + \sin\phi_p)\left(\left\|\uparrow\downarrow\right\rangle + \left\|\downarrow\uparrow\right\rangle\right)\Big]$	1	Analysis pulse with variable phase ϕ_p
–	–	79	–
$R(\pi, 0)$	$\left\|\downarrow\right\rangle \Rightarrow \left\|2,0\right\rangle$	3	Shelve any $\left\|\downarrow\right\rangle$ (dark) population
–	–	22	–
$R(\pi, 0)$	$\left\|2,0\right\rangle \Rightarrow \left\|2,-1\right\rangle$	3	Further shelve the dark population
–	–	22	–
$R(\pi, 0)$	$\left\|2,-1\right\rangle \Leftrightarrow \left\|2,-2\right\rangle$	4	Further shelve the dark population (and make any residual spin population ϵ_A and ϵ_B less dark)
–	–	43	–
Detect	$P_{\uparrow\uparrow}, P_{\downarrow\downarrow}, P_{\uparrow\downarrow} + P_{\downarrow\uparrow}$	200	Determine the spin populations
Total Time		$\approx$14 ms	$\approx$600 laser pulses

Appendix D

Ion Trap Wafer Dimensions

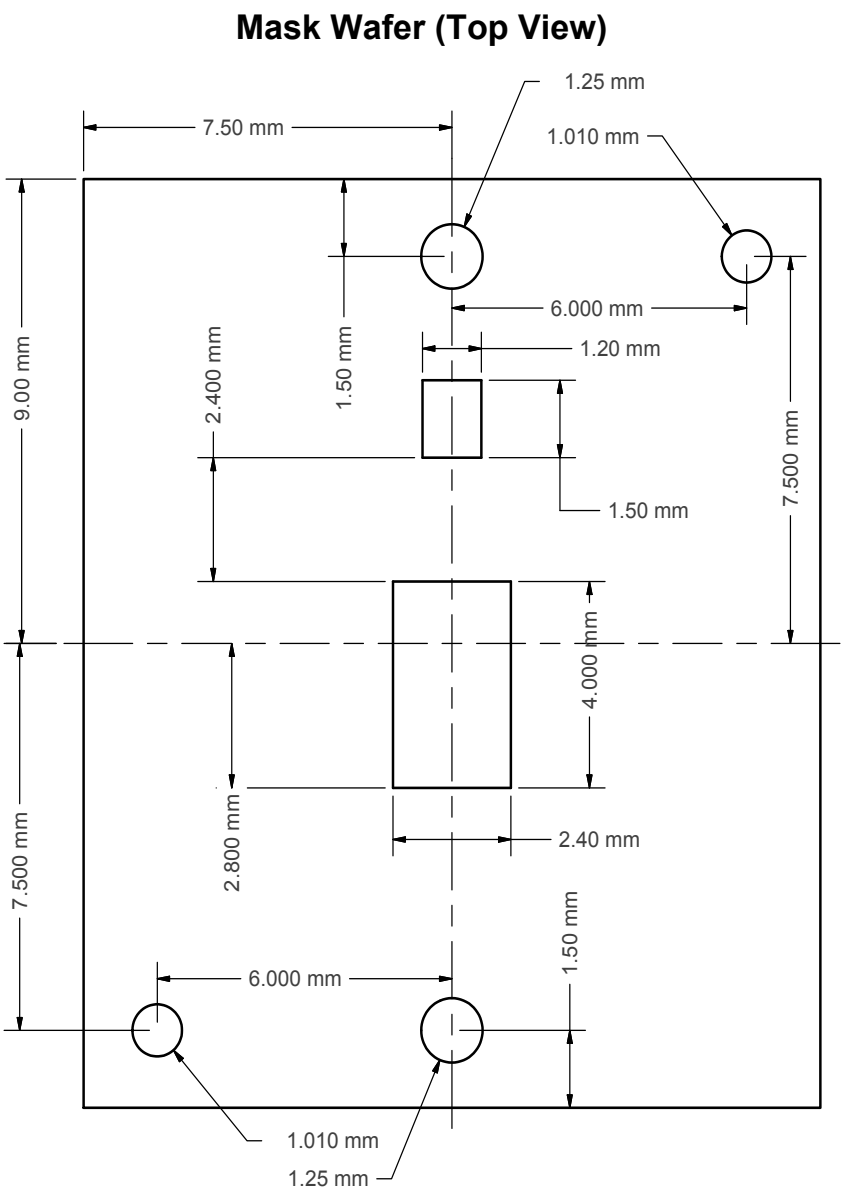

Bias Board (Top View)

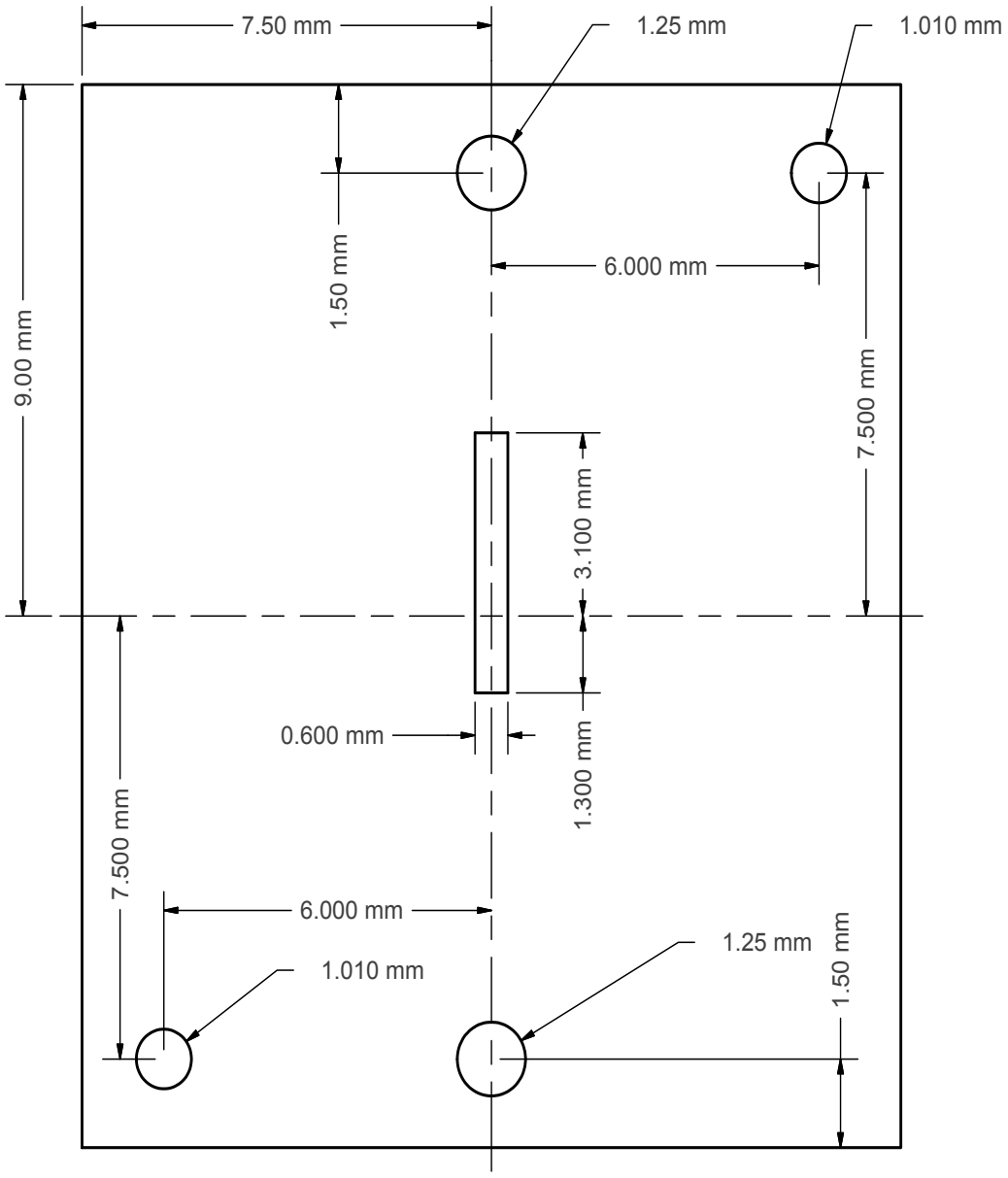

Fliter Board 1 (Top View)

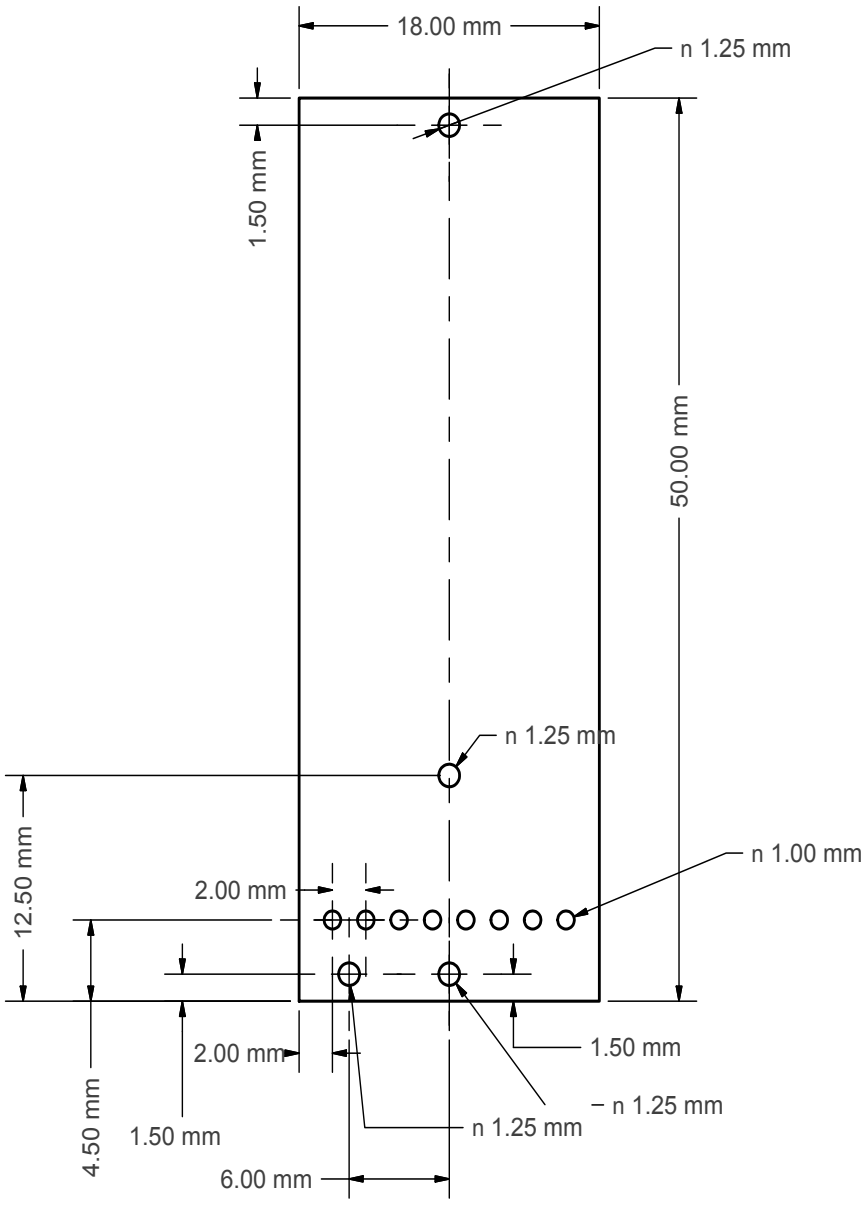

1.5 m5m thick alumia

Filter Board 2 and Spacers (Top View)

Filter Board - 0.5mm thick alumina wafer

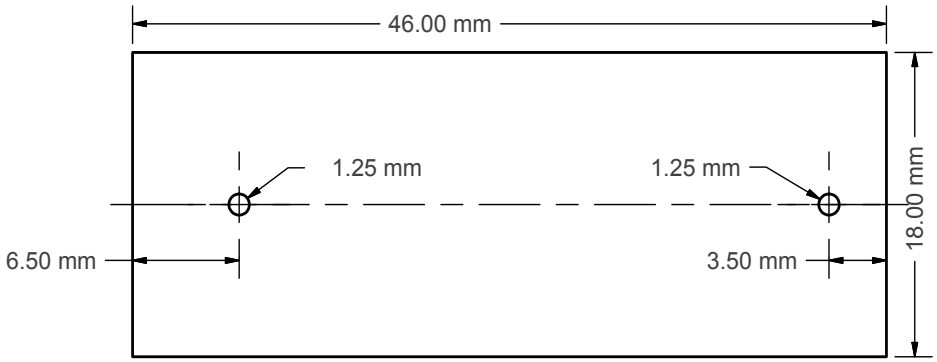

Spacers : alumina

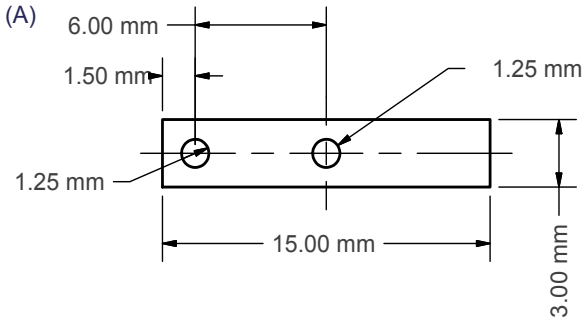

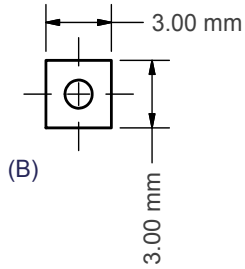

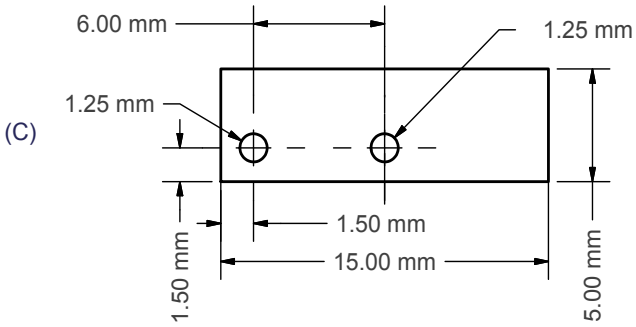

Appendix E

Other Contributions

This section contains the other work not highlighted in this disseration where I was one of the lead co-authors.

- **Realization of a programmable two-qubit quantum processor** , Hanneke D., Home J. P., Jost J. D., Amini J. M., Leibfried D. & Wineland D. J. , *Nature Physics*, 2010, 1, 13-16

- **Complete Methods Set for Scalable Ion Trap Quantum Information Processing**, Home J. P., Hanneke D., Jost J. D., Amini J. M., Leibfried D., & Wineland D. J., *Science*, 2009, 308, 997-1000

- **Long-lived qubit memory using atomic ion**, Langer C., Ozeri R., Jost J. D., Chiaverini J., DeMarco B., Ben-Kish A., Blakestad R. B., Britton J., Hume D. B., Itano W. M., Leibfried D., Reichle R., Rosenband T., Schaetz T., Schmidt P. O., & Wineland D. J., *Phys. Rev. Lett.*, 2005, 95, 060502-1-4

- **Hyperfine coherence in the presence of spontaneous photon scattering**, Ozeri R., Langer C., Jost J. D., DeMarco B. L., Ben-Kish A., Blakestad B. R., Britton J., Chiaverini J., Itano W. M., Hume D., Leibfried D., Rosenband T., Schmidt P, & Wineland D. J., *Phys. Rev. Lett.*, 2005, 95, 030403-1-4

This section contains the other work not highlighted in this disseration where I was one of the co-authors.

- **Randomized benchmarking of quantum gates**, E. Knill, D. Leibfried, R. Reichle, J. Britton, R. B. Blakestad, J. D. Jost, C. Langer, R. Ozeri, S. Seidelin, and D. J. Wineland, *Phys. Rev. A* 77, 012307-1 - 012307-7 (2008).

- **Towards scaling up trapped ion quantum information processing**, D. Leibfried, D. J. Wineland, R. B. Blakestad, J. J. Bollinger, J. Britton, J. Chiaverini, R. J. Epstein, W. M. Itano, J. D. Jost, E. Knill, C. Langer, R. Ozeri, R. Reichle, S. Seidelin, N. Shiga, and J. H. Wesenberg, Hyperfine Interactions 174, 1 - 7 (2007). Proc. 4th Int. Conf. Trapped Charged Particles and Fundamental Physics (TCP 2006), Parksville, Canada 3-8 Sept. 2006.

- **Simplified motional heating rate measurements of trapped ions**, R. J. Epstein, S. Seidelin, D. Leibfried, J. H. Wesenberg, J. J. Bollinger, J. M. Amini, R. B. Blakestad, J. Britton, J. P. Home, W. M. Itano, J. D. Jost, E. Knill, C. Langer, R. Ozeri, N. Shiga, and D. J. Wineland, *Phys. Rev. A* 76, 033411-1 - 033411-5 (2007).

- **Fluorescence during Doppler cooling of a single trapped atom**, J. H. Wesenberg, R. J. Epstein, D. Leibfried, R. B. Blakestad, J. Britton, J. P. Home, W. M. Itano, J. D. Jost, E. Knill, C. Langer, R. Ozeri, S. Seidelin, and D. J. Wineland, *Phys. Rev. A* 76, 053416-1 - 053416-11 (2007).

- **Errors in trapped-ion quantum gates due to spontaneous photon scattering**, R. Ozeri, W. M. Itano, R.B. Blakestad, J. Britton, J. Chiaverini, J.D. Jost, C. Langer, D. Leibfried, R. Reichle, S. Seidelin, J. H. Wesenberg, and D.J. Wineland, *Phys. Rev. A* 75, 042329-1 - 042329-14 (2007).

- **Trapped atomic ions and quantum information processing**, D. J. Wineland, D. Leibfried, J. C. Bergquist, R. B. Blakestad, J. J. Bollinger, J. Britton, J. Chiaverini, R. J. Epstein, D. B. Hume, W. M. Itano, J. D. Jost, M. Knill, J. C.

J. Koelemeij, C. Langer, R. Ozeri, R. Reichle, T. Rosenband, T. Schaetz, P. O. Schmidt, S. Seidelin, N. Shiga, and J. H. Wesenberg, in Atomic Physics 20, Proceedings of the International Conference (ICAP 2006), Innsbruck, Austria, 16-21 July 2006, edited by C. Roos, H. Haffner, and R. Blatt, AIP COnf. Proc. 869 (American Institute of Physics, 2006) p. 103 - 110.

- **Transport dynamics of single ions in segmented microstructured Paul trap arrays**, R. Reichle, D. Leibfried, R.B. Blakestad, J. Britton, J.D. Jost, E. Knill, C. Langer, R. Ozeri, S. Seidelin, and D.J. Wineland, *Fortschr. Phys.* 54, 666 - 685 (2006).

- **Experimental purification of two-atom entanglement**, R. Reichle, D. Leibfried, E. Knill, J. Britton, R.B. Blakestad, J. Jost, C. Langer, R. Ozeri, S. Seidelin, and D.J. Wineland, *Nature.* 443, 838 - 841 (2006).

- **A microfabricated surface-electrode ion trap for scalable quantum information processing**, S. Seidelin, J. Chiaverini, R. Reichle, J.J. Bollinger, D. Leibfried, J. Britton, J. Wesenberg, R.B. Blakestad, R. J. Epstein, D. Hume, W. M. Itano, J. D. Jost, C. Langer, R. Ozeri, N. Shiga, and D.J. Wineland, *Phys. Rev. Lett.* 96, 253003-1 - 253003-4 (2006).

- **Recent experiments in trapped-ion quantum information processing at NIST**, J. Chiaverini, M. D. Barrett, R. B. Blakestad, J. Britton, W. Itano, J. D. Jost, E. Knill, C. Langer, D. Leibfried, R. Ozeri, T. Schaetz, and D.J. Wineland, *Proc. SPIE* 6256, 625610-1 - 625610-12 (2006).

- **Quantum control, quantum information processing, and quantum-limited metrology with trapped ions**, D. J. Wineland, D. Leibfried, M. D. Barrett, A. Ben-Kish, J. C. Bergquist, R. B. Blakestad, J. J. Bollinger, J. Britton, J. Chiaverini, B. DeMarco, D. Hume, W. M. Itano, M. Jensen, J. D.

Jost, E. Knill, J. Koelemeij, C. Langer, W. Oskay, R. Ozeri, R. Reichle, T. Rosenband, T. Schaetz, P. O. Schmidt, and S. Seidelin, in Laser Spectroscopy, Proceedings of the 17th International Conference, Aviemore, Scotland, 19-24 June 2005, edited by E. A. Hinds, A. Ferguson, and E. Riis (World Scientific, Singapore 2005) p. 393 - 402.

- **Creation of a six-atom 'Schroedinger cat' state,** D. Leibfried**,** E. Knill, S. Seidelin, J. Britton, R. B. Blakestad, J. Chiaverini, D. B. Hume, W. M. Itano, J. D. Jost, C. Langer, R. Ozeri, R. Reichle, and D. J. Wineland, *Nature.* 438, 639-642 (2005).

- **Surface-electrode architecture for ion-trap quantum information processing**, J. Chiaverini, R. B. Blakestad, J. Britton, J. D. Jost, C. Langer, D. Leibfried, R. Ozeri, and D.J. Wineland, *Quantum Information and Computation* 5, 419-439 (2005).

- **Implementation of the semiclassical quantum Fourier transform in a scalable system**, J. Chiaverini, J. Britton, D. Leibfried, E. Knill, M. D. Barrett, R. B. Blakestad, W.M. Itano, J.D. Jost, C. Langer, R. Ozeri, T. Schaetz, and D.J. Wineland, *Science* 308, 997-1000 (2005).

- **Enhanced quantum state detection efficiency through quantum information processing**, T. Schaetz, M. D. Barrett, D. Leibfried, J. Britton, J. Chiaverini, W.M. Itano, J.D. Jost, E. Knill, C. Langer, and D.J. Wineland, *Phys. Rev. Lett.* 94, 010501-1 - 010501-4 (2005).

- **Quantum information processing with trapped ions**, M. D. Barrett, T. Schaetz, J. Chiaverini, D. Leibfried, J. Britton, W. M. Itano, J. D. Jost, E. Knill, C. Langer, R. Ozeri, and D.J. Wineland, in Atomic Physics 19, Proceedings of the International Conference (ICAP 2004), edited by L. G. Marcassa, K.

Helmerson, and V. S. Bagnato (American Institute of Physics, 2005) p. 350 - 358.

- **Towards a scalable quantum computer/simulator based on trapped ions**, T. Schaetz, D. Leibfried, J. Chiaverini, M. D. Barrett, J. Britton, B. DeMarco, W. M. Itano, J.D. Jost, C. Langer, and D.J. Wineland, *Appl. Phys. B* 79, 979-986 (2004).

- **Realization of quantum error correction**, J. Chiaverini, D. Leibried, T. Schaetz, M. D. Barrett, R. B. Blakestad, J. Britton, W.M. Itano, J.D. Jost, E. Knill, C. Langer, R. Ozeri, and D.J. Wineland, *Nature* 432, 602-605 (2004).

- **Deterministic quantum teleportation of atomic qubits**, M. D. Barrett, J. Chiaverini, T. Schaetz, J. Britton, W.M. Itano, J.D. Jost, E. Knill, C. Langer, D. Leibfried, R. Ozeri, and D.J. Wineland, *Nature* 429, 737-739 (2004).

- **Quantum dense coding with atomic qubits**, T. Schaetz, M. D. Barrett, D. Leibfried, J. Chiaverini, J. Britton, W.M. Itano, J.D. Jost, C. Langer, and D.J. Wineland, *Phys. Rev. Lett.* 93, 040505-1 - 040505-4 (2004).

- **Toward Heisenberg-limited spectroscopy with multiparticle entangled states**, D. Leibfried, M. D. Barrett, T. Schaetz, J. Britton, J. Chiaverini, W.M. Itano, J.D. Jost, C. Langer, and D.J. Wineland, *Science* 304, 1476-1478 (2004).

- **Building blocks for a scalable quantum information processor based on trapped ions**, D. Leibfried, M. D. Barrett, A. Ben-Kish, J. Britton, J. Chiaverini, B. DeMarco, W.M. Itano, B. Jelenkovic, J. D. Jost, C. Langer, D. Lucas, V. Meyer, T. Rosenband, M. A. Rowe, T. Schaetz, and D.J. Wineland, in Laser Spectroscopy, Proceedings of the 16th International Conference, Palm Cove, Australia, 13-18 July, 2003, edited by P. Hannaford, A. Sidorov, H. Bacher, and K. Baldwin (World Scientific, Singapore, 2004) p. 295 - 303.

- **Sympathetic cooling of 9Be+ and 24Mg+ for quantum logic**, M. Barrett, B.L. DeMarco, T. Schaetz, V. Meyer, D. Leibfried, J. Britton, J. Chiaverini, W.M. Itano, B.M. Jelenkovic, J.D. Jost, C. Langer, T. Rosenband, and D.J. Wineland, *Phys. Rev. A* 68, 042302-1 - 042302-7 (2003).